UNIVERSITY OF CALIFORNIA SAN DIEGO

Analytical, computational, and reduced-order modeling of vortical and turbulent flows

A dissertation submitted in partial satisfaction of the
requirements for the degree Doctor of Philosophy

in

Engineering Sciences (Mechanical Engineering)

by

Tianyi Chu

Committee in charge:

Professor Oliver T. Schmidt, Chair
Professor Stefan G. Llewellyn Smith, Co-Chair
Professor Melvin Leok
Professor Antonio L. Sánchez
Professor Sutanu Sarkar

2023

The Dissertation of Tianyi Chu is approved, and it is acceptable in quality and form for publication on microfilm and electronically.

University of California San Diego

2023

DEDICATION

Dedicated to my family and my beloved.

TABLE OF CONTENTS

LIST OF FIGURES

LIST OF TABLES

ACKNOWLEDGEMENTS

Firstly, I would like to convey my deepest gratitude and utmost respect to my esteemed advisor, Professor Oliver T. Schmidt, for his unwavering support throughout my Ph.D. journey. Under his expert guidance, I gained far more than just research insights. I acquired invaluable life lessons and a profound understanding of the academic world.

In addition, I would like to extend my heartfelt appreciation to Professor Stefan G. Llewellyn Smith, who served as my co-advisor and co-chair of my committee. He led me into the realm of research when I was a novice. Without his insightful guidance, I would have encountered far more detours in my academic journey.

I am also profoundly grateful to the other members of my dissertation committee, namely Prof. Antonio L. Sánchez, Prof. Sutanu Sarkar, and Prof. Melvin Leok. It is my great honor to have these distinguished experts from various fields as part of my dissertation committee. Their collective expertise and unwavering support offered me invaluable assistance in successfully completing this dissertation.

I would like to thank my dedicated lab mates, Nekkanti Akhil, Edward Lowell, Brandon Yeung, and Cong Lin. Their invaluable support and collaboration have been instrumental in shaping my research journey.

I would like to extend my warm appreciation to my roommates, Jiajie Shi and Muhan Zhao, for their support in various aspects of my life beyond research. Their friendship and companionship have been a source of strength throughout my academic journey. We also have three feline friends: Naomi, Luna, and Clay. Their presence and affection provided solace and joy during the challenging moments of my academic pursuit. The support from my other friends, including Haotian Mao, Jian Zeng, and Tuo Lin, was instrumental in helping me navigate the most challenging period during the COVID-19 pandemic.

Lastly, I would like to express my deepest gratitude to my family for their boundless support and love. My family has consistently been the cornerstone of my life. Especially, I want to express my appreciation to my love, Zixin Ma. We crossed paths at the onset of my Ph.D.

journey, and I owe my current achievements to her unwavering patience and love.

In this dissertation, some materials have been published, submitted for publication, or prepared for submission.

Chapter 1, in part, and chapter 8, in part, are reprints of the material as they appear in Philosophical Transactions of the Royal Society A 2022. Llewellyn Smith, Stefan G.; Chu, Tianyi; Hu Zinan, The Royal Society, 2022. The dissertation author was one of the primary investigators and authors of this paper.

Chapter 2, in part, chapter 3, in part, and chapter 5, in full, have been submitted for publication of the material as they may appear in Journal of Computational Physics 2024, Chu, Tianyi; Schmidt, Oliver T., Elsevier, 2024. The dissertation author was the primary investigator and author of this paper.

Chapter 2, in part, and chapter 6, in full, are reprints of the material as they appear in Theoretical and Computational Fluid Dynamics 2021, Chu, Tianyi; Schmidt, Oliver T., Springer, 2021. The dissertation author was the primary investigator and author of this paper.

Chapter 3, in part, and chapter 4, in full, are reprints of the material as they appear in Journal of Computational Physics 2023, Chu, Tianyi; Schmidt, Oliver T., Elsevier, 2023. The dissertation author was the primary investigator and author of this paper.

Chapter 7, in full, is currently being prepared for submission for publication of the material. The dissertation author was the primary investigator and author of this paper.

VITA

2017	Bachelor of Science, Shanghai Jiao Tong University (SJTU)
2018–2021	Teaching Assistant, University of California San Diego
2019	Master of Science, University of California San Diego
2023	Doctor of Philosophy, University of California San Diego

PUBLICATIONS

Chu, T. & Schmidt, O. T. 2021 "A stochastic SPOD-Galerkin model for broadband turbulent flows" *Theor. Comput. Fluid. Dyn.*, 35(6), 759-782.
Llewellyn Smith, S. G., **Chu, T.** & Hu, Z. 2022 "Equations of motion for weakly compressible point vortices" *Philos. Trans. R. Soc. A*, 20210052.
Chu, T. & Schmidt, O. T. 2023 "RBF-FD discretization of the Navier-Stokes equations on scattered but staggered nodes" *J. Comput. Phys.*, 111756.
Chu, T. & Schmidt, O. T. "Mesh-free hydrodynamic stability" Submitted to *J. Comput. Phys.* Available at *arXiv:2308.06840.*

FIELDS OF STUDY

Major Field: Mechanical Engineering

Studies in Engineering Sciences
Professors Oliver T. Schmidt and Stefan G. Llewellyn Smith

ABSTRACT OF THE DISSERTATION

Analytical, computational, and reduced-order modeling of vortical and turbulent flows

by

Tianyi Chu

Doctor of Philosophy in Engineering Sciences (Mechanical Engineering)

University of California San Diego, 2023

Professor Oliver T. Schmidt, Chair
Professor Stefan G. Llewellyn Smith, Co-Chair

This work delves into three fundamental aspects of fluid dynamics: (i) theoretical investigation, (ii) computational methodologies, and (iii) reduced-order modeling. The starting point is the near-perfect model for general fluid flows: the Navier-Stokes equations. For the first part, we investigate the motion of point vortices under the assumption of small Mach number ($M \ll 1$). We use a Rayleigh–Jansen expansion and the method of Matched Asymptotic Expansions to analyze the motion of the vortices at different time scales. Our study shows the motion undergoes modifications over long time scales $O(M^2 \log M)$ and $O(M^2)$.

Generally, the Navier-Stokes equations require the application of accurate, high-fidelity

computational methods for their solutions. To this end, we explore the use of radial basis function-based finite difference (RBF-FD) discretizations for both flow simulations and hydrodynamic stability analysis, which comprise the core of the second part. Polyharmonic spline functions with polynomial augmentation (PHS+poly) are used to construct the global differentiation matrices and the discrete linearized Navier-Stokes operators on scattered nodes. A systematic parameter study is carried out to identify a set of parameters that guarantee stability while balancing accuracy and computational efficiency. Based on this, we develop a mesh-free semi-implicit fractional-step Navier-Stokes solver that uses a staggered node layout. We employ classical linear stability (LST) analysis and state-of-the-art resolvent analysis (RA) to identify flow instabilities.

An alternative way to extract large-scale coherent structures from flow-field data is the utilization of modal decomposition techniques. In the third part, we revisit the connection between spectral proper orthogonal decomposition (SPOD) and other techniques while demonstrating its theoretical correspondence to time-delay analysis. Using SPOD modes, we establish two model order-reduction techniques, namely the operator-based Galerkin projection and the data-driven time-delay Koopman approach. Following the core concept of Koopman theory that an infinite-dimensional linear operator can describe the nonlinear dynamics, we inflate the linear state with an exogenous forcing to account for the nonlinear interactions and background turbulence. Closure is achieved by modeling the remaining residue as stochastic noise. The result models accurately predict the initial transient dynamics and reproduce the second-order statistics of broadband turbulent flows.

Chapter 1

Governing equations

The cornerstone equations in fluid dynamics encompass the continuity, momentum, and energy equations, which serve as the mathematical expressions of three fundamental physical principles underpinning the entire field of fluid dynamics: mass conservation, Newton's second law, and energy conservation. The Navier-Stokes equations are known as a near-perfect model that accurately describes the motion of a fluid. In this chapter, we briefly introduce the governing equations for both incompressible and compressible flows, as well as point vortices.

1.1 Incompressible flows

The motion of a general incompressible Newtonian fluid is governed by the Navier-Stokes and continuity equations,

$$\frac{\partial \boldsymbol{u}}{\partial t} + (\boldsymbol{u}\cdot\nabla)\,\boldsymbol{u} = -\nabla p + \mathrm{Re}^{-1}\nabla^2\boldsymbol{u}, \tag{1.1a}$$

$$\nabla\cdot\boldsymbol{u} = 0. \tag{1.1b}$$

Here, all variables are nondimensionalized by the velocity scale $\boldsymbol{U}_\infty$ and the length scale L, and Re denotes the Reynolds number. Taken 2D Cartesian coordinates as an example, equation (1.1)

can be written as

$$\frac{\partial u}{\partial t} = -\left(u\frac{\partial u}{\partial x} + v\frac{\partial u}{\partial y}\right) - \frac{\partial p}{\partial x} + \frac{1}{\mathrm{Re}}\left(\frac{\partial^2 u}{\partial x^2} + \frac{\partial^2 u}{\partial y^2}\right), \tag{1.2a}$$

$$\frac{\partial v}{\partial t} = -\left(u\frac{\partial v}{\partial x} + v\frac{\partial v}{\partial y}\right) - \frac{\partial p}{\partial y} + \frac{1}{\mathrm{Re}}\left(\frac{\partial^2 v}{\partial x^2} + \frac{\partial^2 v}{\partial y^2}\right), \tag{1.2b}$$

$$\frac{\partial u}{\partial x} + \frac{\partial v}{\partial y} = 0. \tag{1.2c}$$

Upon appropriate discretizations, the above equations can be solved to simulate the motion of general incompressible flows.

1.2 Compressible flows

The compressible Navier-Stokes equations govern the motion of a general, compressible Newtonian fluid,

$$\begin{aligned}
\frac{\partial \rho}{\partial t} &= -\nabla\cdot\rho\mathbf{u}, \\
\frac{\partial \rho\mathbf{u}}{\partial t} &= -\frac{1}{2}\nabla\cdot(\mathbf{u}:\rho\mathbf{u}+\rho\mathbf{u}:\mathbf{u}) - \nabla p + \frac{1}{\mathrm{Re}}\nabla\cdot\boldsymbol{\tau}, \\
\frac{\partial \rho e}{\partial t} &= -\nabla\cdot\rho e\mathbf{u} + \frac{1}{(\gamma-1)\mathrm{RePrMa}_\infty^2}\nabla\cdot k\nabla T - \nabla\cdot p\mathbf{u} + \frac{1}{\mathrm{Re}}\nabla\cdot\boldsymbol{\tau}\mathbf{u},
\end{aligned} \tag{1.3}$$

where e is the total energy. For a Newtonian fluid, the viscous stress tensor is $\boldsymbol{\tau} = \mu\left(\nabla\mathbf{u} + \nabla\mathbf{u}^T\right) - \frac{2}{3}\mu(\nabla\cdot\mathbf{u})\mathrm{I}$. All flow quantities are non-dimensionalized by their dimensional free-stream values, denoted by $(\cdot)_\infty^*$, and the coordinates by the diameter D. The dimensionless Reynolds number $\mathrm{Re} = \rho_\infty u_\infty D/\mu_\infty$, Prandtl number $\mathrm{Pr} = \mathrm{c_p}\mu_\infty/k_\infty$, and Mach number $M = u_\infty/a_\infty$ then fully describe the flow. Here, $\mu_\infty, k_\infty, c_p, \gamma, a_\infty$ are the free-stream values of the dynamic viscosity, heat conductivity, heat capacity at constant pressure, heat capacity ratio, and speed of sound, respectively. Closure of the equations is achieved under the assumption of an ideal gas, and using Sutherland's law to compute the dynamic viscosity from the local temperature.

1.3 Point vortices

The majority of the work to date on point vortices has been for plane incompressible flows [223]. Attempting to extend the notion of a point vortex to plane compressible flows is a daunting task in the general case, but for the case of low-Mach number flows, a Rayleigh–Jansen expansion in Mach number provides one approach. With the Mach number used in the expansion defined by the velocities induced by the vortices' motion and the speed of sound, the $O(1)$ incompressible velocity field increases so as to become supersonic near the location of a point vortex. One needs to consider further physics near the vortex location, i.e. the vortices have a small core region. Barsony-Nagy, Er-El & Yungster (hereafter BNEEY) [18] showed how to obtain steady point vortex configurations in this manner, relating the core behaviour to a solution obtained by Taylor [266]. Since then, there have been a few similar studies. These have examined the translating vortex pair [101, 153, 185], for which it was found in Leppington [153] that the speed of propagation was unchanged at $O(M^2)$, and the von Kármán vortex street [58], for which the speed of propagation for both staggered and unstaggered streets can either increase or decrease depending on parameters of the flow. (There have also been works on steady weakly compressible hollow vortices, as in [7, 57, 174], but these do not consider point vortices.)

As pointed out by Moore & Pullin [185], the existence of a family of continuous shock-free transonic compressible flows with embedded vortices is of intrinsic interest, given that similar flows for transonic aerofoils do not persist under small perturbations. Our goal is to extend the work on weakly compressible point vortices to the unsteady case. We extend the approach of BNEEY [18] to obtain equations of motion for the positions of the vortices up to $O(M^2)$. Our approach is based on conservation of momentum, which has been used for incompressible constant-density flows and which we now review (see Llewellyn Smith [157]). We compute the rate of change of momentum inside a moving closed contour $\mathscr{C}$ from Newton's

Second Law in complex notation,

$$\frac{\mathrm{d}P}{\mathrm{d}t} = \mathrm{i}\oint_{\mathscr{C}} p\,\mathrm{d}z - \frac{\mathrm{i}}{2}\oint_{\mathscr{C}} \rho\overline{w}[(\overline{w}-\overline{W})\,\mathrm{d}\overline{z} - (w-W)\,\mathrm{d}z]. \tag{1.4}$$

where $\mathscr{C}$ is described in the positive sense, the complex momentum inside $\mathscr{C}$ is given by the area integral $P = \int_{\mathscr{S}} \rho\overline{w}\,\mathrm{d}S$, the complex position and velocity are $z = x + \mathrm{i}y$ and $w = u - \mathrm{i}v$ respectively, and the velocity of $\mathscr{C}$ is given by $W = U - \mathrm{i}V$. Using Bernoulli's equation and taking the limit as the contour shrinks down to the vortex, gives $\overline{\zeta}_t = W = \tilde{w}$, since the contour moves with the vortex. Here $\tilde{w}$ is the desingularized velocity at the vortex: physically a point vortex moves with the local desingularized flow.

We next consider irrotational adiabatic compressible flow in the plane. The adiabatic relation between pressure, p^*, and density, ρ^*, takes the form $p^*/p_0^* = (\rho^*/\rho_0^*)^\gamma$, where γ is the constant ratio of specific heats, and p_0^* and ρ_0^* are reference values for pressure and density, taken to be the values at infinity where the flow is at rest. The momentum equation can be transformed into the unsteady Bernoulli equation,

$$\frac{\partial\phi^*}{\partial t} + \frac{1}{2}|\nabla\phi^*|^2 + \int\frac{\mathrm{d}p^*}{\rho^*} = \frac{\partial\phi^*}{\partial t} + \frac{1}{2}|\nabla\phi^*|^2 + \frac{c^2}{\gamma-1} = \frac{c_0^2}{\gamma-1}, \tag{1.5}$$

where ϕ^* is the velocity potential and the speed of sound (squared) is given by $c^2 = \mathrm{d}p^*/\mathrm{d}\rho^*|_{s^*} = \gamma p^*/\rho^*$ with constant value $c_0^2 = \gamma p_0^*/\rho_0^*$ at infinity. It is convenient to combine the above equation and the continuity equation into a single equation for the velocity potential, the Blokhintsev equation [27, 153]. We non-dimensionalize using a length characteristic of the distance between vortices L, a typical velocity V induced by one vortex on another, the resulting time scale L/V, as well as the value of density at large distances, ρ_0 and the dynamic pressure scale $\rho_0 V^2$. Then the Mach number is $M = V/c_0$, and the Blokhintsev equation becomes, dropping the stars and using the summation convention with subscripts running from 1 to 2,

$$\nabla^2\phi = M^2\left\{(\gamma-1)\left(\frac{\partial\phi}{\partial t}+\frac{1}{2}|\nabla\phi|^2\right)\nabla^2\phi+\frac{\partial^2\phi}{\partial t^2}+2\frac{\partial\phi}{\partial x_i}\frac{\partial^2\phi}{\partial x_i\partial t}+\frac{\partial\phi}{\partial x_i}\frac{\partial\phi}{\partial x_j}\frac{\partial^2\phi}{\partial x_i\partial x_j}\right\}, \quad (1.6)$$

along with

$$p = \frac{1}{\gamma M^2}\left[1-(\gamma-1)M^2\left(\frac{\partial\phi}{\partial t}+\frac{1}{2}|\boldsymbol{\nabla}\phi|^2\right)\right]^{\gamma/(\gamma-1)}, \quad (1.7)$$

$$\rho = \left[1-(\gamma-1)M^2\left(\frac{\partial\phi}{\partial t}+\frac{1}{2}|\boldsymbol{\nabla}\phi|^2\right)\right]^{1/(\gamma-1)}. \quad (1.8)$$

The above equations are valid in the region of length scale L between vortices, which we call the vortex region. They break down near the vortex cores, as pointed out by BNEEY [18] and also examined by Leppington [153]. To understand the flow behaviour in a vortex core and its impact on the subsequent matching process, we work in a reference frame co-moving with the vortex, so that for a vortex at location $\boldsymbol{X}$ moving with velocity $\boldsymbol{U}$, one has

$$\boldsymbol{x} = \hat{\boldsymbol{x}}+\boldsymbol{X}, \qquad \boldsymbol{u} = \hat{\boldsymbol{u}}+\boldsymbol{U}, \qquad t = \hat{t}, \qquad \phi = \hat{\Phi}+\boldsymbol{U}\cdot\hat{\boldsymbol{x}}, \quad (1.9)$$

where $\hat{\boldsymbol{x}}$ and $\hat{\boldsymbol{u}}$ are the position and velocity with respect to the vortex core in the moving frame, respectively. Here $\hat{t}$ is used to emphasize that partial time- and space-derivatives in the core frame are taken with constant $\hat{\boldsymbol{x}}$ and $\hat{t}$ respectively. The velocity potential in the core frame is $\hat{\Phi}$. Following previous authors, we now define an appropriately scaled variable in the core region using $\hat{\boldsymbol{x}} = M\boldsymbol{s}$, so that the radial coordinate measured from the vortex core is $r = Ms$. In terms of these variables, the Blokhintsev equation becomes

$$\begin{aligned}&\left[1-(\gamma-1)\left(M^2\frac{\partial\hat{\Phi}}{\partial\hat{t}}+\frac{1}{2}\frac{\partial\hat{\Phi}}{\partial s_j}\frac{\partial\hat{\Phi}}{\partial s_j}+M^3\dot{U}_j s_j-\frac{1}{2}M^2U_jU_j\right)\right]\frac{\partial^2\hat{\Phi}}{\partial s_i^2}\\ =&M^4\frac{\partial^2\hat{\Phi}}{\partial\hat{t}^2}+2M^2\frac{\partial\hat{\Phi}}{\partial s_i}\frac{\partial^2\hat{\Phi}}{\partial s_i\partial\hat{t}}+M^6\frac{\partial\hat{\Phi}}{\partial s_i}\frac{\partial\hat{\Phi}}{\partial s_j}\frac{\partial^2\hat{\Phi}}{\partial s_i\partial s_j}+M^5\ddot{U}_j s_j-M^4U_jU_j+M^3\dot{U}_j\frac{\partial\hat{\Phi}}{\partial s_j}, \quad (1.10)\end{aligned}$$

where dots above U_j indicate time derivatives.

Chapter 1, in part, is a reprint of the material as it appears in Philosophical Transactions of the Royal Society A 2022. Llewellyn Smith, Stefan G.; Chu, Tianyi; Hu Zinan, The Royal Society, 2022. The dissertation author was one of the primary investigators and authors of this paper.

Chapter 2

Modal analysis of fluid flows

Flow instabilities and large-scale coherent structures are ubiquitous phenomena in fluid mechanics that have been the focus of extensive research. Linear stability (LST) analysis is specifically designed to investigate the growth of small perturbations exclusively around laminar base flows, which are the steady-state solution to the Navier-Stokes equations. One-dimensional LST analysis was widely used in the past century, e.g., [26, 56, 103, 171]. Eriksson & Rizzi [66] and Tuckerman & Marcus [278] were the pioneers in conducting LST analysis in two-dimensional (2D). Subsequently, Jackson [114] and Zebib [306] examined the 2D nature of vortex shedding in the wakes of bluff bodies. Readers are referred to Huerre & Monkewitz [108] and Theofilis [267] for comprehensive reviews of the concept of 2D LST modes. The implementation of the 2D LST framework has enabled improved identification of flow instability in non-parallel flows, including cylinder wakes [91, 169, 189], aerofoil wakes [64, 298], boundary layers [1, 65], and jets in cross-flow [14, 198, 210]. Studies have demonstrated that an open flow can possess marginal stability despite exhibiting local convective instability. LST analysis around a steady laminar base flow, by its inherent nature, is not applicable to predict finite-amplitude flow instabilities arising from nonlinear interactions. The use of mean flow for LST analysis, despite violating the basic assumption of linear theory, has been used successfully to predict coherent flow features in diverse types of flows, including cylinder wakes [15, 203], open cavity flows [252, 253], mixing layers [89, 183, 294], and turbulent or transitional jets

[95, 190, 236]. Theoretical conditions required for the validity of mean flow stability analysis have been explored by [25]. Although beyond the scope of this work, it is noteworthy that the weakly-nonlinear extension of LST analysis has been successfully employed for studying the dynamics of non-parallel flows [50, 253]. The LST-based semi-empirical e^N method [258, 283] has succeeded in transition prediction for certain flows such as boundary layers. However, the prediction of disturbance behavior in more complex scenarios, such as crossflows or bypass transitions, falls outside the scope of LST theory.

Despite these limitations, resolvent, or input-output analysis, has recently emerged as a linear tool for accurately predicting large-scale coherent structures in fully turbulent flows. Resolvent analysis (RA) originally stems from the studies of transient growth [67, 207, 208, 276] and seeks the optimal pairs of inputs and corresponding outputs through the linearized system that maximizes the energy gain. Within the laminar regime, RA has been utilized to investigate the linear response to external body forces or perturbations for channel flows [124, 179, 216], boundary layers [3, 29, 41, 184, 200, 254, 274], and jets [88, 118, 239]. In contrast to classical LST analysis, the input-output perspective offers a mathematically rigorous framework for studying turbulent mean-flows by identifying the forcing as the Reynolds stresses in the perturbation-interaction terms in the Reynolds-decomposed Navier–Stokes equations [173, 247]. Applications include near-wall flows [1, 111, 247], boundary layers [10, 115, 214], incompressible [88, 154] or compressible jets [118, 237, 275], and airfoil wakes [212, 303]. The validation of fundamental relationships between RA and other modal decomposition techniques was facilitated by [275], establishing RA as a well-suited tool for turbulence modeling [201, 202].

2.1 Linear stability analysis

In the case of laminar flows, we can decompose the flow state around the steady-state solution of the Navier-Stokes equations (1.1) as

$$\boldsymbol{u} = \boldsymbol{U} + \boldsymbol{u}', \quad p = P + p', \tag{2.1}$$

where $(\boldsymbol{U}, P)$ represents the base flow that satisfies

$$(\boldsymbol{U} \cdot \nabla)\boldsymbol{U} = -\nabla P + \mathrm{Re}^{-1}\nabla^2 \boldsymbol{U}, \tag{2.2a}$$

$$\nabla \cdot \boldsymbol{U} = 0, \tag{2.2b}$$

and $(\cdot)'$ denotes the small fluctuating components. In turbulent flows, we take the Reynolds decomposition of the flow state into the temporal mean, $\overline{(\cdot)}$, and fluctuating components, given by

$$\boldsymbol{u} = \overline{\boldsymbol{u}} + \boldsymbol{u}', \quad p = \overline{p} + p'. \tag{2.3}$$

By generalizing the notation of the base state as $(\boldsymbol{u}_0, p_0)$, the resulting governing equations for the fluctuations take the form of

$$\frac{\partial \boldsymbol{u}'}{\partial t} + (\boldsymbol{u}_0 \cdot \nabla)\boldsymbol{u}' + \left(\boldsymbol{u}' \cdot \nabla\right)\boldsymbol{u}_0 = -\nabla p' + \mathrm{Re}^{-1}\nabla^2 \boldsymbol{u}' + \boldsymbol{f}', \tag{2.4a}$$

$$\nabla \cdot \boldsymbol{u}' = 0. \tag{2.4b}$$

Here, the term $\boldsymbol{f}'$ represents the remaining nonlinear interactions between the fluctuation components. Table 2.1 summarizes the two aforementioned decompositions.

Equation (2.4) can be written compactly in terms of the fluctuating state, $\boldsymbol{q}' = [u', v', p']^T$,

Table 2.1. Summary of flow state decompositions.

Base state	Description	Notation	Obtained from	Remaning forcing $\boldsymbol{f}'$
$(\boldsymbol{u}_0, p_0)$	Base flow	$(\boldsymbol{U}, P)$	equation (2.2)	$-(\boldsymbol{u}'\cdot\nabla)\boldsymbol{u}'$
	Mean flow	$(\overline{\boldsymbol{u}}, \overline{p})$	long-time average	$-(\boldsymbol{u}'\cdot\nabla)\boldsymbol{u}' + \overline{(\boldsymbol{u}'\cdot\nabla)\boldsymbol{u}'}$

as

$$\mathscr{P}\mathscr{P}^T\left(\frac{\partial}{\partial t}\boldsymbol{q}'\right) = \mathscr{L}\boldsymbol{q}' + \mathscr{P}\boldsymbol{f}', \tag{2.5}$$

where $\mathscr{P}$ is the prolongation operator that extends the velocity vector $[u, v]^T$ into $[u, v, 0]^T$, and its transpose is the restriction operator that extracts the velocity vector from the extended state vector [254]. The incompressible linearized Navier-Stokes (LNS) operator takes the form of

$$\mathscr{L} \equiv \begin{pmatrix} -(\boldsymbol{u}_0\cdot\nabla)() - [()\cdot\nabla]\boldsymbol{u}_0 + \mathrm{Re}^{-1}\nabla^2 & -\nabla \\ \nabla\cdot() & 0 \end{pmatrix}. \tag{2.6}$$

Beyond the linear dynamics, the remaining forcing $\boldsymbol{f}'$ in equation (2.5) comprises products of fluctuating quantities, as outlined in table 2.1. These terms will be either neglected or modeled. For compressible flows, we linearize the system described in equation (1.3) and the resulting governing equation for the fluctuating components takes the form

$$\frac{\partial}{\partial t}\boldsymbol{q}' = \mathscr{L}\boldsymbol{q}' + \boldsymbol{f}' \tag{2.7}$$

Equation (2.7) is formally equivalent to equation (2.5) when $\mathscr{P}$ is considered as the identity operator $\mathscr{I}$.

Classical (temporal) linear stability (LST) analysis investigates fluctuations with complex frequency $\lambda = \lambda_r + \mathrm{i}\lambda_i$, where λ_r is the exponential growth rate and λ_i the oscillation frequency. The fluctuations are assumed to be infinitesimally small, and the forcing term, $\boldsymbol{f}'$, is, therefore,

negligible at $O(1)$, see, e.g., Schmid & Henningson [231]. Substituting perturbations of the form $\boldsymbol{q}'(\boldsymbol{x},t) = \tilde{\boldsymbol{q}}(\boldsymbol{x})\mathrm{e}^{\lambda t}$ into the governing equations (2.4) yields the LST equation,

$$\lambda \mathscr{P}\mathscr{P}^T\tilde{\boldsymbol{q}} = \mathscr{L}\tilde{\boldsymbol{q}}. \tag{2.8}$$

Equation (2.8) is a generalized eigenvalue problem, and the eigenvector associated with the largest growth rate ought to predict the dominant flow instability mechanism.

2.2 Resolvent analysis

The nonlinear interactions in equation (2.5) are no longer negligible for general cases of finite amplitude fluctuations. Within the resolvent framework of turbulent flows, the nonlinear interactions, along with the background turbulence, can be interpreted as external forcing, $\boldsymbol{f}'$, to the otherwise linear dynamics. This interpretation was first proposed by Mckeon & Sharma [173]. By assuming a normal mode form for the fluctuating components,

$$[\boldsymbol{u}', \boldsymbol{q}', \boldsymbol{f}'](\boldsymbol{x},t) = [\hat{\boldsymbol{u}}, \hat{\boldsymbol{q}}, \hat{\boldsymbol{f}}](\boldsymbol{x})\mathrm{e}^{\mathrm{i}\omega t} + c.c., \tag{2.9}$$

where ω is the angular frequency, or equivalently by taking the Fourier transform, we obtain the linear time-invariant (LTI) representation of the governing equation (2.4) in the frequency domain,

$$\left(\mathrm{i}\omega\mathscr{P}\mathscr{P}^T - \mathscr{L}\right)\hat{\boldsymbol{q}} = \mathscr{P}\left(\mathscr{B}\hat{\boldsymbol{f}}\right), \tag{2.10a}$$

$$\hat{\boldsymbol{u}} = \mathscr{P}^T\left(\mathscr{C}\hat{\boldsymbol{q}}\right). \tag{2.10b}$$

The linear operators $\mathscr{B}$ and $\mathscr{C}$ are used to select spatial regions of particular interest. We write equations (2.10) in a compact form as

$$\hat{\boldsymbol{u}} = \mathscr{H}(\omega)\hat{\boldsymbol{f}}, \tag{2.11}$$

where $\mathscr{H}(\omega) = \mathscr{P}^T\mathscr{C}\left(\mathrm{i}\omega\mathscr{P}\mathscr{P}^T - \mathscr{L}\right)^{-1}\mathscr{P}\mathscr{B}$ is known as the resolvent operator.

In the absence of nonlinear interactions described in table (2.1), the application of input-output, or resolvent analysis (RA) provides a means to model them as optimal forcing inputs to the linear system in equation (2.11). The objective of resolvent analysis is to identify pairs of optimal forcings and their corresponding responses that maximize the gain, σ^2, defined as the ratio of the energy of the response to the energy of the forcing,

$$\sigma^2(\hat{\boldsymbol{f}};\omega) = \frac{\|\hat{\boldsymbol{u}}\|_u^2}{\|\hat{\boldsymbol{f}}\|_f^2} = \frac{\left\langle \mathscr{H}(\omega)\hat{\boldsymbol{f}}, \mathscr{H}(\omega)\hat{\boldsymbol{f}} \right\rangle_u}{\left\langle \hat{\boldsymbol{f}}, \hat{\boldsymbol{f}} \right\rangle_f}. \tag{2.12}$$

Refer to [231] for a detailed discussion. The energy of the response and the forcing are measured in the norms $\|\cdot\|_u$ and $\|\cdot\|_f$, induced by the inner products

$$\langle \hat{\boldsymbol{u}}_1, \hat{\boldsymbol{u}}_2 \rangle_u = \int_\Omega \hat{\boldsymbol{u}}_2^*(\boldsymbol{x},\omega)\boldsymbol{W}_u(\boldsymbol{x})\hat{\boldsymbol{u}}_1(\boldsymbol{x},\omega)\,\mathrm{d}\boldsymbol{x} \quad \text{and} \quad \left\langle \hat{\boldsymbol{f}}_1, \hat{\boldsymbol{f}}_2 \right\rangle_f = \int_\Omega \hat{\boldsymbol{f}}_2^*(\boldsymbol{x},\omega)\boldsymbol{W}_f(\boldsymbol{x})\hat{\boldsymbol{f}}_1(\boldsymbol{x},\omega)\,\mathrm{d}\boldsymbol{x} \tag{2.13}$$

on the output and input spaces, respectively. Here, $\boldsymbol{W}_u$ and $\boldsymbol{W}_f$ are weight matrices containing both the numerical quadrature weights and weights associated with these inner products, and $(\cdot)^*$ denotes the Hermitian transpose. Equation (2.12) is solved by the Schmidt decomposition to the resolvent operator

$$\mathscr{H}(\omega) = \sum_{j=1}^{\infty} \sigma_j(\omega)\hat{\boldsymbol{u}}_j(\boldsymbol{x},\omega) \otimes \hat{\boldsymbol{f}}_j(\boldsymbol{x},\omega) \tag{2.14}$$

in terms of the inner products (2.13), where $\otimes$ denotes the Kronecker product. In practice, that is for discrete data, it is solved by the singular value decomposition. The output modes, $\hat{\boldsymbol{u}}_j$, and input modes, $\hat{\boldsymbol{f}}_j$, are orthogonal in their respective inner products, that is, $\langle \hat{\boldsymbol{u}}_j, \hat{\boldsymbol{u}}_k \rangle_u = \left\langle \hat{\boldsymbol{f}}_j, \hat{\boldsymbol{f}}_k \right\rangle_f = \delta_{jk}$. The modes are ordered by the associated singular value, σ_j. It can be verified that the input and output modes are related through

$$\mathscr{H}(\omega)\hat{\boldsymbol{f}}_j = \sigma_j(\omega)\hat{\boldsymbol{u}}_j, \tag{2.15}$$

which provides a physical interpretation of the singular values and vectors.

2.3 Modal decomposition techniques

In addition to identifying flow instabilities through the governing equations, modal decomposition techniques offer an alternative data-driven approach for extracting energetically and dynamically significant features from flow-field data.

2.3.1 Proper orthogonal decomposition

In fluid mechanics, the most widely used approach for extracting the dominant features from a time-series data is proper orthogonal decomposition (POD); see Lumley [159, 160]. In other disciplines, POD is known as empirical orthogonal functions, principal component analysis, or Karhunen-Loève decomposition. POD modes are particularly suitable for Galerkin projection due to their optimality and orthogonality; see, e.g., [188, 219]. Most commonly, the space-only POD modes are computed using the method of snapshots by Sirovich [256]. Consider a fluctuation data matrix consisting of N snapshots,

$$\boldsymbol{Q}' = [\boldsymbol{q}[1] - \overline{\boldsymbol{q}}, \boldsymbol{q}[2] - \overline{\boldsymbol{q}}, \cdots, \boldsymbol{q}[N] - \overline{\boldsymbol{q}}], \tag{2.16}$$

and the spatial inner product $\langle \cdot, \cdot \rangle$ that quantifies the energy of the flow field,

$$\langle \boldsymbol{q}_1, \boldsymbol{q}_2 \rangle \equiv \int_{\Omega} \boldsymbol{q}_1^*(\boldsymbol{x}) \boldsymbol{W}(\boldsymbol{x}) \boldsymbol{q}_2(\boldsymbol{x}) \mathrm{d}\boldsymbol{x}, \tag{2.17}$$

The space-only POD modes are obtained through the eigendecomposition of the spatial cross-correlation tensor $\boldsymbol{S} = \boldsymbol{Q}'\boldsymbol{Q}'^*$ as

$$\boldsymbol{S}\boldsymbol{W}\boldsymbol{\Psi} = \boldsymbol{\Psi}\boldsymbol{\Lambda}, \tag{2.18}$$

The resulting POD modes $\boldsymbol{\Psi}$ optimally represent the data and have orthogonality by definition.

2.3.2 Dynamical mode decomposition and Koopman analysis

As an alternative to POD, dynamic mode decomposition (DMD) developed by Schmid [229] aims at identifying coherent spatial modes that best describe the flow dynamics upon linearization. The temporal dynamics of the coefficients are described by complex exponentials, specifically involving frequency and growth/decay rate. The DMD method provides a spatiotemporal decomposition of data streams and is closely related to Koopman analysis [177, 178, 221]. The fundamental concept of Koopman analysis [140] is to use an infinite-dimensional linear operator $\mathscr{K}$ that advances observable functions ϕ forward in time to describe the finite-dimensional nonlinear dynamics of the flow state $\boldsymbol{q} \in \mathscr{M}$, where $\mathscr{M} \subseteq \mathbb{C}^{N_q}$ is the state space. Let $\boldsymbol{F} : \mathscr{M} \to \mathscr{M}$ be an evolution operator that describes the nonlinear dynamics of $\boldsymbol{q}$ with

$$\boldsymbol{q}[i+1] = \boldsymbol{F}(\boldsymbol{q}[i]). \tag{2.19}$$

The Koopman operator acts on functions of state space and is defined by

$$\mathscr{K}\boldsymbol{\phi}(\boldsymbol{q}[i]) \equiv \boldsymbol{\phi}(\boldsymbol{F}(\boldsymbol{q}[i])) = \boldsymbol{\phi}(\boldsymbol{q}[i+1]), \tag{2.20}$$

producing a new vector-valued function $\boldsymbol{\phi} \circ \boldsymbol{F}$. Here, the observable vector $\boldsymbol{\phi}$ is defined as

$$\boldsymbol{\phi}(\boldsymbol{q}) = \begin{bmatrix} \phi_1(\boldsymbol{q}) & \phi_2(\boldsymbol{q}) & \cdots & \phi_{N_k}(\boldsymbol{q}) \end{bmatrix}^T, \tag{2.21}$$

where $(\cdot)^T$ denotes the transpose. Each component of $\boldsymbol{\phi}$ is a scalar-valued observable with $\phi : \mathscr{M} \to \mathbb{C}$. For intuitive understanding, we recommend the notes by Brunton [35]. The most important property of the Koopman operator is that it linearly governs the evolution of observables in discrete time, i.e., $\mathscr{K}(c_1\boldsymbol{\phi}_1 + c_2\boldsymbol{\phi}_2) = c_1\mathscr{K}\boldsymbol{\phi}_1 + c_2\mathscr{K}\boldsymbol{\phi}_2$. In the following, we omit the dependence on $\boldsymbol{q}$, and use the notation $\boldsymbol{\phi}[i] \equiv \boldsymbol{\phi}(\boldsymbol{q}[i])$ for brevity.

In standard DMD [229], the full state observable vector is defined as the observable vector, that is, $\boldsymbol{\phi}(\boldsymbol{q}) = \boldsymbol{q}$. The most popular flavor of DMD is the so-called exact DMD method developed by Tu *et al.* [277], which is based on the eigendecomposition of the finite-dimensional DMD operator, defined as

$$\boldsymbol{K} \equiv \boldsymbol{Q}_2^N \left(\boldsymbol{Q}_1^{N-1}\right)^+. \tag{2.22}$$

Here, the notations, $(\cdot)_1^{N-1}$ and $(\cdot)_2^N$, represent the submatrices by excluding the last and the first columns, respectively. The DMD modes, also called dynamic modes, reduce to temporal discrete Fourier transform (DFT) modes if the data is periodic [221] and approximate the Koopman eigenfunctions if snapshots are independent [48]. For stationary flow, the physically relevant DMD modes often have nearly zero growth/decay rates, see, e.g., [48, 221, 229, 232, 238, 277]. It is commonly recommended not to subtract the mean when performing DMD for non-stationary flows to capture their dynamics. If one aims to recover Koopman modes of stationary flows with zero growth/decay rates, incorporating mean subtraction in DMD is beneficial [275].

As a generalization of the standard DMD, Williams *et al.* [295] proposed the extended DMD (EDMD) method for approximating the leading Koopman eigenvalues and eigenfunctions by using a dictionary of scalar observables. In EDMD, every function of the flow state can be

considered as observables, in particular, nonlinear observable functions, such as kernel functions [296], Hermite polynomials [155], and candidate functions obtained using sparse regression [37]. The EDMD operator then takes the form of

$$\boldsymbol{K} \equiv \boldsymbol{\Phi}_2^N \left(\boldsymbol{\Phi}_1^{N-1}\right)^+, \tag{2.23}$$

where $\boldsymbol{\Phi}$ represents the data matrix for observables, $\boldsymbol{\phi}$. Koopman theory guarantees the convergence of the EDMD operator to the Koopman operator in the limit of infinite observables [141]. It also converges to a Galerkin method in the large-data limit ($N \to \infty$) and recovers the action of the Koopman operator on the N_k-dimensional subspace of observables [138, 295].

2.3.3 Time-delay embedding and space-time POD

While (E)DMD focuses on embedding the state dynamics onto (non)linear manifolds in space, the time-delay embedding of data sequences provides a different perspective for identifying dominant spatiotemporal structures. Arbabi & Mezić [5] introduced the Hankel-DMD algorithm to obtain the Koopman spectrum by performing the DMD of a Hankel data matrix. This Hankelized approach is guaranteed to retrieve Koopman eigenfunctions for ergodic systems when an infinite amount of data is available. Le Clainche & Vega [147] proposed the higher-order DMD (HODMD) to address high spectral complexity. This approach has been successfully demonstrated on a range of flows characterized by a broadband spectrum, including a jet [149], a cylinder wake [148], and an airfoil wake [142]. The reader is referred to Vega & Le Clainche [286] for more applications. The above variants of DMD are summarized in the recent review by Schmid [230].

In addition to these DMD-based methods, an alternative approach to identifying spatiotemporal structures from data is space-time POD, which originates from the most general version of POD and describes the time evolution of the flow over a specified time window [160]. Schmidt & Schmid [235] proposed the conditional space-time POD to identify acoustic

intermittency in a jet. Recently, Frame & Towne [86] demonstrated that discrete space-time POD modes can be obtained through the singular value decomposition (SVD) of a block Hankel matrix. These Hankel singular vectors form the modal basis of the Hankel alternative view of Koopman (HAVOK) model by Brunton *et al.* [36]. As shown by Frame & Towne [86], they converge to space-only POD modes in the short-time limit and to spectral POD (SPOD) modes in the long-time limit. The common idea behind these time-delay decomposition techniques is the SVD of a Hankel matrix, which is closely related to the singular spectral analysis (SSA) [285] and the eigensystem realization algorithm (ERA) [125]. Naturally, their computational cost depends on the spatial and spectral complexities of the data sequence. This bottleneck can be circumvented by using convolutional coordinates that readily encapsulate time-delay embedding [129]. In particular, SPOD can be alternatively viewed as a time-delay technique, specifically through the Fourier convolution, due to the inherent relationship between the Hankel singular vectors and SPOD modes [86].

2.3.4 Spectral proper orthogonal decomposition

SPOD, the frequency-domain variant of POD, identifies large coherent structures in stationary flows by decomposing the data set into energy-ranked, monochromatic modes [237, 275]. The resulting modes evolve coherently in both space and time, and optimally represent the second-order space-time flow statistics. Analogous to the eigendecomposition of the cross-covariance matrix, which constitutes POD, SPOD is computed from the eigendecomposition of the cross-spectral density matrix. For statistically stationary flows, the fluctuation component $\boldsymbol{q}'$ can be decomposed into temporal Fourier modes $\hat{(\cdot)}_{\omega_k}$ of angular frequency ω_k as

$$\boldsymbol{q}' = \sum_k \hat{\boldsymbol{q}}_{\omega_k} \mathrm{e}^{\mathrm{i}\omega_k t}. \tag{2.24}$$

SPOD is performed for each frequency independently. For a given frequency ω_k, the SPOD modes are found as the eigenvectors $\boldsymbol{\Psi}_{\omega_k} = \left[\boldsymbol{\psi}^{(1)}_{\omega_k}, \boldsymbol{\psi}^{(2)}_{\omega_k}, \cdots, \boldsymbol{\psi}^{(N_b)}_{\omega_k}\right]$, and the modal energy as the

descending eigenvalues $\boldsymbol{\Lambda}_{\omega_k} = \mathrm{diag}\left(\lambda_{\omega_k}^{(1)}, \lambda_{\omega_k}^{(2)}, \cdots, \lambda_{\omega_k}^{(N_b)}\right)$ of the cross-spectral density tensor $\hat{\boldsymbol{S}}_{\omega_k} = \hat{\boldsymbol{Q}}_{\omega_k}\hat{\boldsymbol{Q}}_{\omega_k}^{*}$ as

$$\hat{\boldsymbol{S}}_{\omega_k}\boldsymbol{W}\boldsymbol{\Psi}_{\omega_k} = \boldsymbol{\Psi}_{\omega_k}\boldsymbol{\Lambda}_{\omega_k}, \tag{2.25}$$

where $\hat{\boldsymbol{Q}}_{\omega_k} = \left[\hat{\boldsymbol{q}}_{\omega_k}^{(1)}, \hat{\boldsymbol{q}}_{\omega_k}^{(2)}, \cdots, \hat{\boldsymbol{q}}_{\omega_k}^{(N_b)}\right]$ is the matrix of Fourier realizations, and the weight matrix $\boldsymbol{W}$ enters through the definition of the inner product in the equation (2.17). Here, $\hat{\boldsymbol{q}}_{\omega_k}^{(i)}$ is the i-th realization of the Fourier transform which we obtain by segmenting the data into N_b blocks under the ergodicity hypothesis. A periodic Hamming window is used to minimize spectral leakage. The resulting SPOD modes $\boldsymbol{\Psi}_{\omega_k}$ are discretely orthogonal with $\langle \boldsymbol{\psi}_{\omega_k}^{(i)}, \boldsymbol{\psi}_{\omega_k}^{(j)} \rangle_E = \delta_{ij}$, where δ_{ij} is the Kronecker delta function. Expanding the SPOD modes in time, $\{\boldsymbol{\psi}_j^{(\alpha)} \mathrm{e}^{\mathrm{i}\omega_j t}\}$, achieves the space-time orthogonality by construction, which permits their interpretation as physical large-scale structures [275]. A large separation between the first and the remaining eigenvalues of the SPOD eigenspectra reveals low-rank dynamics associated with prevalent flow structures [237]. For the same method, Nekkanti & Schmidt [186] proposed a convolution-based approach to obtain discrete time-continuous expansion coefficients, and facilitate time-local analyses, such as frequency-time diagrams. Besides optimally accounting for the second-order statistics, the SPOD modes are also dynamically significant as they are optimally averaged ensemble DMD modes [275] and are formally equivalent to the spectral expansion of the stochastic Koopman operator [6, 177] for stationary flows. These properties leverage the potential of modeling turbulent flows through Koopman theory using SPOD-based convolutional coordinates, see §7.

The aforementioned modal decomposition/analysis techniques and other related methods are summarized in figure 2.1. Three modeling perspectives are used to categorize these methods. Note that all the methods here are applied to analyze general nonlinear fluid flows. The terminology 'linear,' 'forced linear,' and 'nonlinear' pertains to the state vector under analysis.

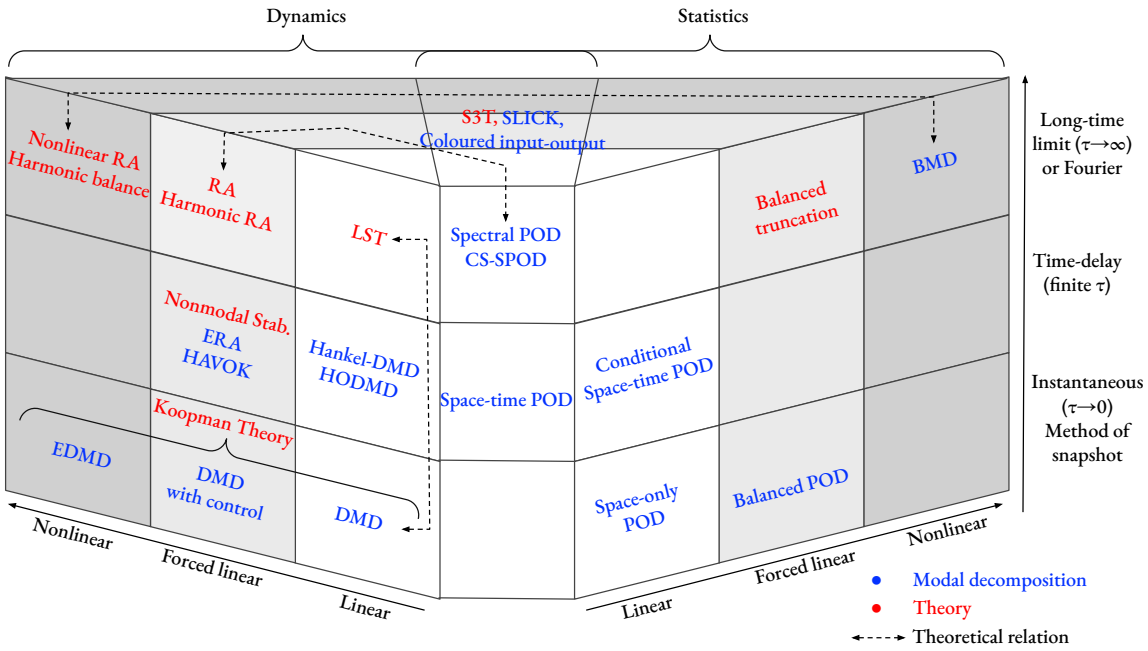

Figure 2.1. Summary of modal decomposition/analysis techniques for general fluid flows. These techniques are categorized due to three modeling perspectives: state vector (linear → forced linear → nonlinear), time-delay horizon (instantaneous → finite → long-time limit), and physical aspects (statistics or dynamics).

Example of a turbulent jet

SPOD has been applied to a variety of turbulent flows, including wall-bounded shear flows such as boundary layers [280], as well as bluff-body flows such as the wake behind a disk [281]. For turbulent jets, the use of SPOD was pioneered by Glauser, Leib, & George [93]. Later, different authors linked coherent structures identified by SPOD to concepts from linear stability theory for both experimental data [46, 94, 95] and large eddy simulation (LES) data [236, 273, 275].

Take as an example of a statistically stationary flow, a turbulent, iso-thermal jet at Mach number, based on the jet velocity and the far-field speed of sound, of $M = 0.9$ and Reynolds number, based on the nozzle diameter and the jet velocity, of $\mathrm{Re} \approx 10^6$. The state vector

$$\boldsymbol{q} = [\rho, u_x, u_r, u_\theta, T]^T, \tag{2.26}$$

comprises the density ρ, temperature T, and cylindrical velocity components u_x, u_r and u_θ in the streamwise, x, radial, r, and circumferential, θ, directions, respectively. The LES data is generated using the unstructured flow solver 'Charles'. Further details about the dataset can be found in Brès *et al.* [33]. Owing to the rotational symmetry of the jet, we may decompose the data, without loss of generality, into azimuthal Fourier components, m. Consequently, $\bar{\boldsymbol{q}} = [\bar{\rho}, \bar{u}_x, \bar{u}_r, 0, \bar{T}]^T$ is the long-time mean of the primitive state, whose azimuthal velocity component is zero for the round jet. We then interpolate the data on a 950×195 Cartesian mesh that includes the physical domain $x, r \in [0, 30] \times [0, 6]$. For more details, the reader is referred to Schmidt *et al.* [236]. To quantify the flow energy, we use the compressible energy inner product

$$\langle \boldsymbol{q}_1, \boldsymbol{q}_2 \rangle_E = \int_\Omega \boldsymbol{q}_1^* \mathrm{diag}\left(\frac{\overline{T}}{\gamma \bar{\rho} M^2}, \bar{\rho}, \bar{\rho}, \bar{\rho}, \frac{\bar{\rho}}{\gamma(\gamma-1)\overline{T}M^2} \right) \boldsymbol{q}_2 \mathrm{d}\boldsymbol{x} = \boldsymbol{q}_1^* \boldsymbol{W} \boldsymbol{q}_2, \tag{2.27}$$

devised by Chu [51], in equation (2.17). The same dataset is later used for resolvent analysis in §5.4.3 and SPOD-based reduced-order models in §6.4 and §7.

We compute the SPOD from the 10,000 snapshots of the turbulent jet by partitioning the data into $N_b = 77$ blocks of 256 snapshots with an overlap of 50%. These spectral estimation parameter are obtained following the best practices outlined in [234, 275]. Owing to the rotational and temporal symmetry of the jet, it suffices to consider the $N_f = 129$ non-negative frequency components.

Figure 2.2(a) shows the instantaneous streamwise fluctuating velocity, u_x', and its symmetric component (azimuthal wavenumber $m_\theta = 0$), $\hat{u}_x$, of the turbulent jet. The wide range of time and length scales of this fully developed turbulent flow becomes apparent from the velocity field. Figure 2.2(b) shows the SPOD eigenvalue spectra of the axisymmetric component.

Figure 2.3 shows the first, the second, and the 10th of the SPOD modes that constitute the basis of our models. The frequency is reported in terms of the Strouhal number $\mathrm{St} = \omega/(2\pi M)$, where ω is the non-dimensionalized frequency. Three representative frequencies are presented. Large-scale coherent structures associated with Kelvin-Helmholtz instability waves are observed

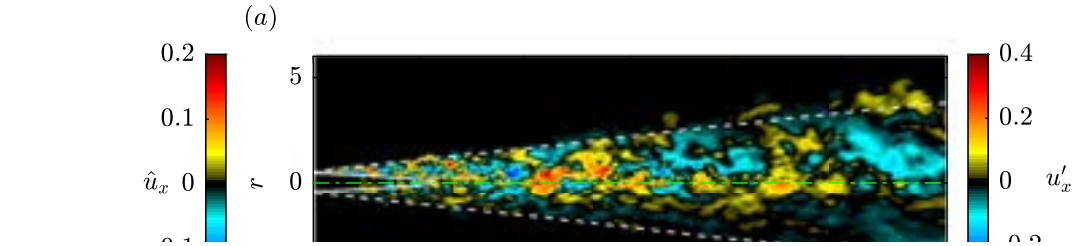

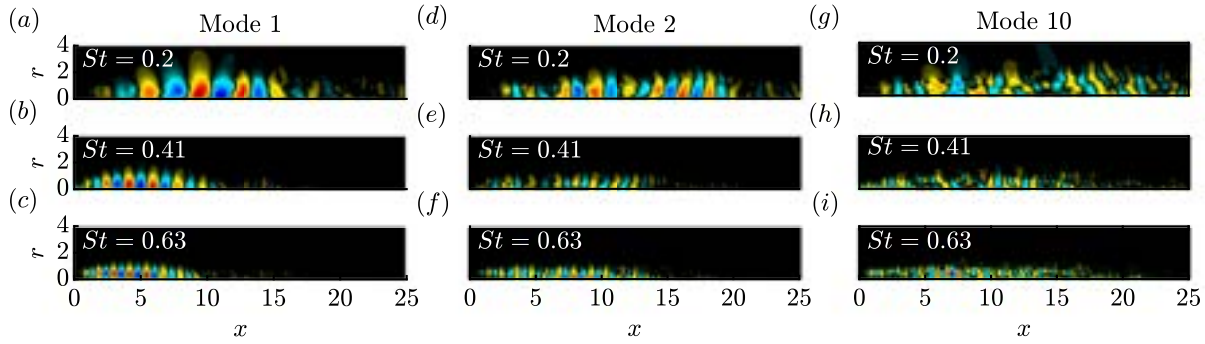

Figure 2.3. Examples of SPOD modes of the turbulent jet: (a,d,g) $St = 0.2$; (b,e,h) $St = 0.41$; (c,f,i) $St = 0.63$. The normalized pressure components of the 1st, 2nd, 10th modes are shown in $x, r \in [0, 25] \times [0, 4]$.

in the leading modes. Referred to Schmidt *et al.* [237] for more details on the physical interpretation of SPOD modes.

Chapter 2, in part, is a reprint of the materials as it appears in Theoretical and Computational Fluid Dynamics 2021, Chu, Tianyi; Schmidt, Oliver T., Springer, 2021 and Journal of

Computational Physics 2023, Chu, Tianyi; Schmidt, Oliver T., Elsevier, 2023. The dissertation author was the primary investigator and author of these two papers.

Chapter 3

Numerical discretization: radial basis functions (RBFs)

In the realm of Computational fluid dynamics (CFD), the fundamental task involves the discretization of the Navier-Stokes equations. In the past two decades, radial basis functions (RBF)–based discretizations have emerged as a viable alternative to established approaches [80]. RBF-based methods are often referred to as *mesh-free* as they facilitate the discretization of partial differential operators directly on a set of scattered nodes, i.e., without the need of local elements. The main promise of RBF-based methods is that they can combine the ease of implementation and high order of accuracy of finite differences (FD) with the geometrical flexibility of finite volume (FV), finite element (FE), and discontinuous Galerkin (DG) methods.

RBF approximations provide high-order accuracy, flexibility, and ease of implementation for interpolation and differentiation. Historically, RBFs were often used as global interpolants over all nodes. These global RBF methods with spectral-like nominal accuracy have been applied to a variety of flow problems [73, 75, 77, 78, 130, 131, 300] including Lagrangian fluid mechanics [291]. Other applications of global RBFs include solid mechanics [289, 290]. They are, however, computationally expensive for large problems and often suffer from ill-conditioning and numerical instability. Remedies to these problems have been found in the form of regularizations like hyperviscosity [76, 82] and preconditioners [132]. The use of local RBF stencils was pioneered by [249, 271, 288, 299] and yields a class of so-called RBF-FD

methods that are named in reference to classical finite differences. Just like classical FDs, RBF-FD methods generate sparse differentiation matrices. The level of sparsity depends on the local stencil size, which in turn is determined by the desired order of accuracy. Common choices of RBFs for fluid flow problems are Gaussians (GA), multiquadrics (MQ), and inverse multiquadrics (IMQ). Flyer *et al.* [76], for example, demonstrated the use of GA-type RBFs for solving the shallow water equations on a sphere and compared the performance to other high-order numerical methods. Applications to the incompressible Navier-Stokes equations (NSE) include the local MQ-differential quadrature (DQ) method by Shu, Ding, & Yeo [250], its extension to 3D by Ding *et al.* [61], the compact RBF-FD scheme by Chinchapatnam *et al.* [49], which in turn is based on the work by Wright & Fornberg [301], and the method by [302], who introduced a regularization term for IMQ RBFs and a semi-Lagrangian scheme for transient simulations. Incompressible flow solvers with convective heat transfer have been implemented by [249, 293, 304].

All these implementations use infinitely smooth RBFs that are characterized by a shape parameter. This shape parameter, in turn, significantly impacts both accuracy and stability, and extensive works, most empirical, have been devoted to investigating its effect [45, 70, 85, 87, 98, 215]. Good accuracy is often associated with near-flat RBFs. RBFs in this flat limit, however, often yield ill-conditioned discretizations and suffer from stagnation, or saturation, errors [74]. Numerical schemes that address these problems include Contour-Padé [85], RBF-QR [81, 84, 145], and RBF-GA [83] methods. More recently, RBF-FDs based on polyharmonic splines augmented with polynomials (PHS+poly), that do not require a shape parameter were introduced by Flyer, Barnett, & Wicker [72]. Later, Flyer *et al.* [74] demonstrated the use of higher-order polynomial augmentations, which improve the accuracy of derivative approximations of local RBF stencils and mitigate the stagnation error under node refinement. Bayona *et al.* [23] used PHS+poly for solving elliptic PDEs and showed that a larger stencil size near domain boundaries helps to avoid the Runge phenomenon. Using closed-form RBFs, Bayona [21] later provided an analytical validation of this result. Numerical demonstrations for 2-D and 3-D examples were

presented in Bayona, Flyer, & Fornberg [22]. Several comparisons to other mesh-free approaches, including polynomial least-squares approximations [74], the RBF-GA method near the flat limit [225], and the moving least-squares (MLS) method [20] have confirmed the competitiveness of PHS+poly-based RBF-FDs in terms of accuracy, robustness, and computational efficiency.

3.1 RBF approximations

The underlying idea of radial basis functions (RBFs) is to approximate a given function $f(\boldsymbol{x})$ using a smooth radial function $\phi(r)$. For a set of n scattered nodes, $\{\boldsymbol{x}\}_{j=1}^{n}$, we seek the interpolant

$$s(\boldsymbol{x}) = \sum_{j=1}^{n} \lambda_j \phi(\|\boldsymbol{x} - \boldsymbol{x}_j\|) \tag{3.1}$$

that satisfies $s(\boldsymbol{x}_i) = f(\boldsymbol{x}_i)$ for $i = 1, 2, \ldots, n$, where $\|\cdot\|$ denotes the standard Euclidean norm. The interpolation coefficients $\lambda_1, \cdots, \lambda_n$ can be found as the solution of the linear system

$$\underbrace{\begin{bmatrix} \phi(\|\boldsymbol{x}_1 - \boldsymbol{x}_1\|) & \phi(\|\boldsymbol{x}_1 - \boldsymbol{x}_2\|) & \cdots & \phi(\|\boldsymbol{x}_1 - \boldsymbol{x}_n\|) \\ \phi(\|\boldsymbol{x}_2 - \boldsymbol{x}_1\|) & \phi(\|\boldsymbol{x}_2 - \boldsymbol{x}_2\|) & \cdots & \phi(\|\boldsymbol{x}_2 - \boldsymbol{x}_n\|) \\ \vdots & \vdots & & \vdots \\ \phi(\|\boldsymbol{x}_n - \boldsymbol{x}_1\|) & \phi(\|\boldsymbol{x}_n - \boldsymbol{x}_2\|) & \cdots & \phi(\|\boldsymbol{x}_n - \boldsymbol{x}_n\|) \end{bmatrix}}_{\boldsymbol{A}} \begin{bmatrix} \lambda_1 \\ \lambda_2 \\ \vdots \\ \lambda_n \end{bmatrix} = \begin{bmatrix} f(\boldsymbol{x}_1) \\ f(\boldsymbol{x}_2) \\ \vdots \\ f(\boldsymbol{x}_n) \end{bmatrix}, \tag{3.2}$$

where $\boldsymbol{A}$ is the interpolation matrix. The RBF interpolant $s(\boldsymbol{x})$ based on these coefficients can then be used to approximate the function $f(\boldsymbol{x})$ in the local region described by the set of nodes, $\{\boldsymbol{x}\}_{j=1}^{n}$. Common choices for RBFs include Gaussian (GA), multiquadrics (MQ), and inverse multiquadrics (IMQ). See Fornberg & Flyer [80] for a comprehensive overview. These RBF types are known to suffer from the stagnation (or saturation) error under refinement and have a free shape parameter that significantly impacts their accuracy and stability. In this work, we use

polyharmonic splines (PHS),

$$\phi(r) = r^m, \qquad \text{where } m \text{ is an odd positive integer,} \tag{3.3}$$

as the basis functions. This choice is motivated by recent studies [22, 23, 72, 74], which highlight the advantageous properties of the PHS-type RBFs for discretizations, described next.

3.2 RBF-FD method and augmentation with polynomials

A direct approach for the generation of RBF-based differentiation operations is the RBF-FD method, which approximates the action of any linear operator, $\mathscr{D}$, as a linear combination of the function values, $f(\boldsymbol{x}_j)$, such that

$$\mathscr{D}f(\boldsymbol{x}_0) = \sum_{j=1}^{n} w_j f(\boldsymbol{x}_j). \tag{3.4}$$

Here, x_0 is a given location, and w_j are the unknown differentiation weights. Using equation (3.1), the function value $f(\boldsymbol{x})$ can be approximated by the RBF interpolant $s(\boldsymbol{x})$ and the corresponding weight vector $\boldsymbol{w} = (w_1, \cdots, w_n)^T$ is then obtained by solving the linear system

$$\begin{bmatrix} & & \\ & \boldsymbol{A} & \\ & & \end{bmatrix} \begin{bmatrix} w_1 \\ w_2 \\ \vdots \\ w_n \end{bmatrix} = \begin{bmatrix} \mathscr{D}\phi(\|\boldsymbol{x}-\boldsymbol{x}_1\|)|_{\boldsymbol{x}=\boldsymbol{x}_0} \\ \mathscr{D}\phi(\|\boldsymbol{x}-\boldsymbol{x}_2\|)|_{\boldsymbol{x}=\boldsymbol{x}_0} \\ \vdots \\ \mathscr{D}\phi(\|\boldsymbol{x}-\boldsymbol{x}_n\|)|_{\boldsymbol{x}=\boldsymbol{x}_0} \end{bmatrix}. \tag{3.5}$$

An implicit assumption of the RBF-FD method is that the derivative of the basis functions, $\mathscr{D}\phi$, is continuous.

A commonly used extension of equation (3.4) to enforce consistency with Taylor expansion-based FD approximations is polynomial augmentation [72, 80, 82, 145, 301]. For 2D

problems, this RBF-FD method with polynomial augmentation up to degree q takes the form

$$\mathscr{D}f(\boldsymbol{x}_0) = \sum_{j=1}^{n} w_j f(\boldsymbol{x}_j) + \sum_{i=1}^{(q+1)(q+2)/2} c_i P_i(\boldsymbol{x}_0). \tag{3.6}$$

The use of multivariate polynomial terms, $P_i(\boldsymbol{x})$, to match the local Taylor series introduces the additional constraints

$$\sum_{j=1}^{n} w_j P_i(\boldsymbol{x}_j) = \mathscr{D}P_i(\boldsymbol{x}_0), \qquad \text{for } 1 \le i \le \frac{(q+1)(q+2)}{2}, \tag{3.7}$$

also known as the vanishing momentum conditions [113], for the differentiation weights. These constraints ensure that the RBF approximations reproduce locally polynomial behaviour up to degree q [74] and appropriately decay in the far-field [79]. As an example, consider the linear system for $q = 1$,

$$\left[\begin{array}{ccc:ccc} & & & 1 & x_1 & y_1 \\ & \boldsymbol{A} & & \vdots & \vdots & \vdots \\ & & & 1 & x_n & y_n \\ \hdashline 1 & \cdots & 1 & & & \\ x_1 & \cdots & x_n & & \boldsymbol{0} & \\ y_1 & \cdots & y_n & & & \end{array}\right] \left[\begin{array}{c} w_1 \\ \vdots \\ w_n \\ \hdashline c_1 \\ c_2 \\ c_3 \end{array}\right] = \left[\begin{array}{c} \mathscr{D}\phi(\|\boldsymbol{x}-\boldsymbol{x}_1\|)|_{\boldsymbol{x}=\boldsymbol{x}_0} \\ \vdots \\ \mathscr{D}\phi(\|\boldsymbol{x}-\boldsymbol{x}_n\|)|_{\boldsymbol{x}=\boldsymbol{x}_0} \\ \hdashline \mathscr{D}1|_{\boldsymbol{x}=\boldsymbol{x}_0} \\ \mathscr{D}x|_{\boldsymbol{x}=\boldsymbol{x}_0} \\ \mathscr{D}y|_{\boldsymbol{x}=\boldsymbol{x}_0} \end{array}\right]. \tag{3.8}$$

The interpolation matrix $\boldsymbol{A}$ is the same one defined in equation (3.5). A more general and compact expression for equation (3.8) takes the form

$$\underbrace{\begin{bmatrix} \boldsymbol{A} & \boldsymbol{P} \\ \boldsymbol{P}^T & \boldsymbol{0} \end{bmatrix}}_{\boldsymbol{A}_{\text{aug}}} \begin{bmatrix} \boldsymbol{w} \\ \boldsymbol{c} \end{bmatrix} = \begin{bmatrix} \mathscr{D}\boldsymbol{\phi} \\ \mathscr{D}\boldsymbol{P} \end{bmatrix}. \tag{3.9}$$

This procedure ensures consistency with the local expansion, but equation (3.4) is used to

approximate the actual differentiation operations. The use of polynomial augmentation for PHS RBFs has shown to improve the accuracy for interpolation and derivative approximations [74], numerical solutions of elliptic PDE problems [23], and approximations near domain boundaries [22]. Our practical implementation follows Flyer, Barnett, & Wicker [72].

3.3 Global differentiation operators

Differentiation matrices provide a straightforward and flexible way to discretize partial differential equations (PDEs). The use of global RBFs leads to full matrices, which are computationally expensive and require a lot of memory. To obtain sparse matrices instead, we seek local differentiation operators that utilize a smaller number of neighboring nodes. Assume the given domain is discretized by two sets of scattered nodes, $\{\boldsymbol{x}_i^{(\alpha)}\}_{i=1}^N$ and $\{\boldsymbol{x}_j^{(\beta)}\}_{j=1}^M$. Given the function values at node set β, $f(\boldsymbol{x}^{(\beta)})$, we seek a differentiation matrix such that $\boldsymbol{D}_{\mathscr{D}}^{(\alpha,\beta)} f(\boldsymbol{x}^{(\beta)})$ approximates the derivatives, $\mathscr{D}f(\boldsymbol{x}^{(\alpha)})$, at node set α. The differentiation matrix $\boldsymbol{D}_{\mathscr{D}}^{(\alpha,\beta)}$ must hence satisfy

$$\underbrace{\begin{bmatrix} w_{11} & w_{12} & \cdots & w_{1N} \\ w_{21} & w_{22} & \cdots & w_{2N} \\ \vdots & \vdots & & \vdots \\ w_{M1} & w_{M2} & \cdots & w_{MN} \end{bmatrix}}_{\boldsymbol{D}_{\mathscr{D}}^{(\alpha,\beta)}} \begin{bmatrix} f(\boldsymbol{x}_1^{(\beta)}) \\ f(\boldsymbol{x}_2^{(\beta)}) \\ \vdots \\ f(\boldsymbol{x}_N^{(\beta)}) \end{bmatrix} = \begin{bmatrix} \mathscr{D}f(\boldsymbol{x})|_{\boldsymbol{x}=\boldsymbol{x}_1^{(\alpha)}} \\ \mathscr{D}f(\boldsymbol{x})|_{\boldsymbol{x}=\boldsymbol{x}_2^{(\alpha)}} \\ \vdots \\ \mathscr{D}f(\boldsymbol{x})|_{\boldsymbol{x}=\boldsymbol{x}_M^{(\alpha)}} \end{bmatrix}. \tag{3.10}$$

Note that for collocated grids, we have $\alpha = \beta$. For this arrangement, the jth row of the matrix $\boldsymbol{D}_{\mathscr{D}}^{(\alpha,\beta)}$ approximates the derivative at node $\boldsymbol{x}_j^{(\alpha)}$ using the $n \ll N$ nearest nodes of the β-grid as the stencil for equation (3.9). The remaining weights are set to zero. As argued in Flyer *et al.* [74], the use of local RBF-FD approximations has the additional advantage that each stencil has its own supporting polynomial that can be locally adjusted. The fully assembled matrix, $\boldsymbol{D}_{\mathscr{D}}^{(\alpha,\beta)}$, is sparse with $M \times n$ nonzero elements.

3.4 Accuracy and error analysis

We use modified wavenumber diagrams, as known from classical FD analysis, to gauge the accuracy of the PHS+poly RBF-FDs on the staggered nodes. Modified wavenumber analysis was originally designed to examine the truncation error of FD methods on lattice-based grids but has also been applied to unstructured FD discretizations [187, 193]. Accuracy and error analysis for RBF approximations are not straightforward and often done in a problem-specific manner. For PHS+poly RBF-FDs, for example, test problems such as the summation of sinusoids [72, 74], Poisson's equation [23], Kovasznay flow, and cylindrical Couette flow [241] were considered. These studies mainly focused on the discretization error under grid refinement and have demonstrated that the convergence rate is determined by the degree of the polynomial augmentation. Here, we first conduct a systematic parameter study to identify a set of parameters, i.e., stencil size, PHS exponent, and polynomial degree, that minimizes the relative error for a wave-like test function on a representative, highly heterogeneous grid. We proceed with a two-dimensional modified wavenumber analysis to quantify the order of accuracy on the staggered grids. The analysis shows that the selected 28-point stencil PHS+poly RBF-FDs provide accuracy comparable to 6th-order Padé-type FDs.

Panels 3.1(a,b) shows this unstructured staggered node arrangement for the example of a cylinder in a rectangular domain with increased resolution close to the cylinder and in the wake region. For each set of nodes that form a local stencil, a characteristic length Δr can be determined as the locally averaged distance between adjacent nodes. The histograms of Δr for the $V-$ and $P-$grids, shown in figure 3.1(c), indicate that the two grids are highly heterogeneous. The smallest characteristic spacing used to resolve the boundary layer near the cylinder differs by about one order of magnitude from the largest spacing in the far-field.

Specifically, we are interested in the accuracy of four types of differentiation matrices for flow simulations:

1. $\boldsymbol{D}_x^{(V,V)}$, $\boldsymbol{D}_y^{(V,V)}$, and $\boldsymbol{D}_\Delta^{(V,V)}$ with dimension $N \times N$ from V-grid to V-grid;

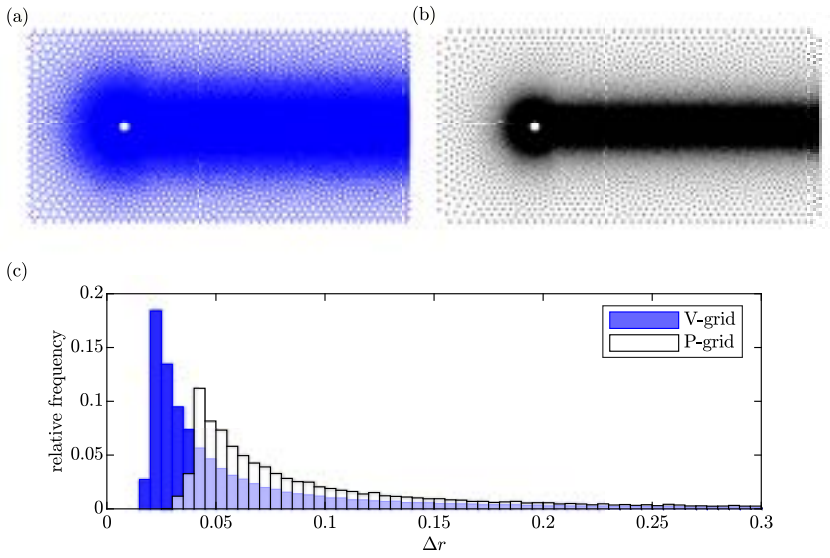

Figure 3.1. Unstructured staggered node layout for flow around a cylinder: (a) V-grid; (b) P-grid; (c) grid spacing histograms. This grid is used for both the accuracy and error analyses and the simulations of the cylinder wake in §4.2.2.

2. $\boldsymbol{D}_x^{(P,V)}$, $\boldsymbol{D}_y^{(P,V)}$ with dimension $M \times N$ from V-grid to P-grid;

3. $\boldsymbol{D}_\Delta^{(P,P)}$ with dimension $M \times M$ from P-grid to P-grid;

4. $\boldsymbol{D}_x^{(V,P)}$, $\boldsymbol{D}_y^{(V,P)}$ with dimension $N \times M$ from P-grid to V-grid.

Refer to the numerical scheme introduced in §4.1 below for more details.

Refer to figure 3.1 for the grid topology. For any given node, the RBF stencil consists of the nearest n nodes acquired through a k-nearest neighbor (kNN) search. For $n = 28$, figure 3.2 shows examples of stencils used for the four different cases. In panels 3.2(a) and (b), $\alpha = \beta$ and the node of interests hence is a node on the grid. In panels 3.2(c) and (d), on the other hand, the nodes comprising the stencil are from different grids.

In the following, we propose an error analysis strategy that minimizes the truncation error of the spatial derivatives on the staggered grid by selecting an appropriate combination of the stencil size, n, the exponent of the PHS, m, and the degree of polynomials, q. In previous studies, the discretization error for the augmented RBF-PHS method has been examined in terms of the convergence rate under grid refinement [23, 72, 74, 241]. A general observation is that the error

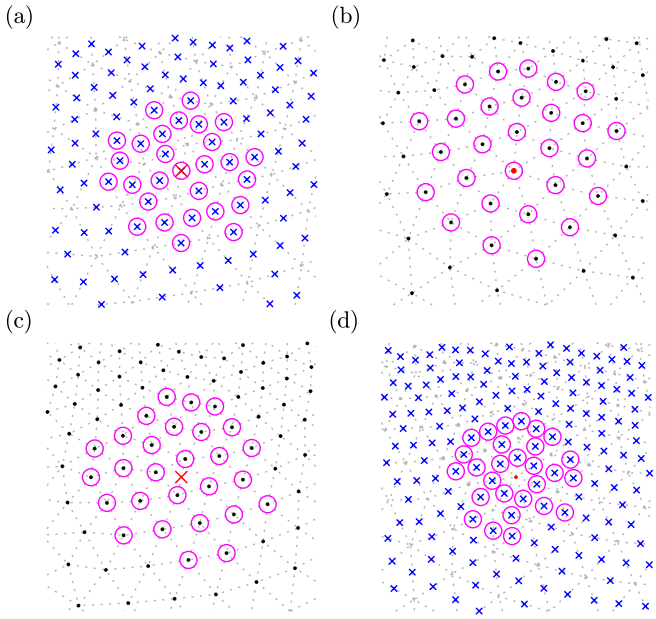

Figure 3.2. Stencils (magenta circles) for differentiation matrices: (a) $\boldsymbol{D}^{(V,V)}$; (b) $\boldsymbol{D}^{(P,P)}$; (c) $\boldsymbol{D}^{(V,P)}$; (d) $\boldsymbol{D}^{(P,V)}$. A constant stencil size $n = 28$ is used to approximate the derivatives at given nodes (red). Referred to figure 3.1 for the markers. The underlying triangular mesh is shown as gray dotted lines.

convergence depends on the degree of the polynomial, and a minimum stencil size is required for numerical stability. In this work, we propose the use of modified wavenumber analysis, which we generalize to scattered nodes. Classical modified wavenumber analysis for lattice-based node sets is commonly used to measure the accuracy of finite difference schemes, see e.g., Moin [182]. For a given lattice with grid spacing Δx, the modified wavenumber, k^*, is computed by applying the finite difference to the discretized sinusoidal function $g(x) = \mathrm{e}^{\mathrm{i}kx}$. The difference between $k^*\Delta x$ and $k\Delta x$ indicates the numerical error as a function of wavenumber. To be able to investigate the discretization error as a function of the wave angle, $\theta = \arctan(k_y/k_x)$, relative to the fixed set of scattered nodes, we define the transformed radial coordinate $\tilde{r} = (k_x x + k_y y)/\tilde{k}$, where $\tilde{k} = \sqrt{k_x^2 + k_y^2}$ is the radial wavenumber. As in [240, 265], the radial modified wavenumber

is then given as

$$k^* = -\mathrm{i}\delta_{\tilde{r}}\left\{\mathrm{e}^{\mathrm{i}\tilde{k}\tilde{r}}\right\}\mathrm{e}^{-\mathrm{i}\tilde{k}\tilde{r}}, \tag{3.11}$$

where $\delta_{\tilde{r}}$ is the discrete RBF-FD differentiation operator. Equation (3.11) reduces to the standard one-dimensional case for $k_x = 0$ or $k_y = 0$. Prior to performing the modified wavenumber analysis, we first identify the optimal parameters using a fixed nondimensional wavenumber, $k\Delta r = \sqrt{2}$, highlighted in figures 3.5 and 3.9. This specific value is chosen to guarantee the 'spectral-like resolution' [152] that is achieved by higher-order Padé-type compact finite differences, and that has made the latter a popular choice for direct numerical simulation (DNS) [52, 123, 137, 151, 224, 263].

The test function takes the form

$$g_j(\boldsymbol{x}) = \cos\left(\frac{x}{\Delta r_j}\right)\cos\left(\frac{y}{\Delta r_j}\right), \tag{3.12}$$

where j is the node index. The corresponding wavelength is $\lambda = \sqrt{2}\pi\Delta r_j$. The average relative error of the augmented RBF-PHS method is determined as

$$E^{(\alpha,\beta)} = \frac{1}{N}\sum_{j=1}^{N}\frac{|\delta_j^{(\alpha,\beta)} g_j(\boldsymbol{x}^{(\beta)}) - \mathscr{L} g_j(\boldsymbol{x}^{(\alpha)})|}{\max\{|\mathscr{L} g_j(\boldsymbol{x})|\}}, \tag{3.13}$$

where δ_j represents the local RBF differentiation operation at the jth node. The local minima of the error guide the selection of parameters: n, the stencil size, m, the exponent of the PHS, and q, the polynomial degree. It has been shown by [23, 72, 74, 241] that q determines the overall order of accuracy.

In the remainder of this section, we use as the test mesh for the error analysis the `distmesh` grid shown in figure 3.1 above. Due to its highly non-uniform node distribution and large variation of Δr, $0.03 < \Delta r < 0.79$, it is representative of meshes used to discretize complex

geometries. This ensures that the error estimates are conservative and applicable to non-generic scenarios.

Our requirements for the Navier-Stokes solver are:

1. compact stencil size of $n \lesssim 30$ for numerical efficiency,
2. formal order-of-accuracy of $q \geq 2$ for physical accuracy,
3. small relative error,
4. stability (requires $n \gtrsim (q+1)(q+2)$ for scattered nodes, see e.g. [21, 23, 22, 72]).

To meet these criteria, we vary the different parameters and conduct detailed error analyses for the (V,V)- and (P,P)-grids, reported in §3.4.1 and §3.4.2, respectively. The analyses for the remaining combinations are reported in A.2, and a comparison with the established RBF-QR implementation by Fornberg & Lehto [82] and the RBF-GA implementation by Bollig, Flyer, & Erlebacher [28] is shown in A.3.

3.4.1 V-grid to V-grid

We first consider the differentiation matrices $\boldsymbol{D}_x^{(V,V)}$ and $\boldsymbol{D}_\Delta^{(V,V)}$, which operate on the (V,V)-grid shown in figure 3.2(a). Figure 3.3 shows the average relative errors, equation (3.13), computed for the first derivative in the x-direction for the test function, equation (3.12). By comparing the different subplots of figure 3.3, we observe that the relative error for $m = 5$ is largely independent of the polynomial order, q. For $q \leq 3$, the relative error for $m = 5$ is larger than for $m = 7$ and 9, and we hence do not further consider $m = 5$. A general trend is that the truncation error decreases with increasing stencil size and then stagnates. Similar results are also found in [23]. The last observation is that for $q = 5$, the relative error has increased for all m. To avoid the Runge phenomenon near the domain boundary, a smaller value of q is favored for a fixed stencil size [21, 23, 22]. With the goal to minimize both the stencil size error, we identify $n = 28$, $m = 7$, and $q = 3$ as the best combination. Note that the order of accuracy is not

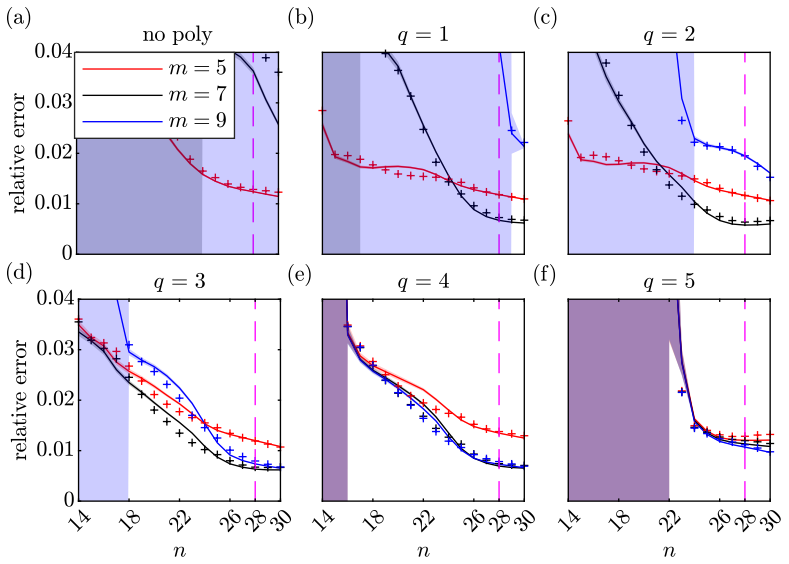

Figure 3.3. Relative error for $\boldsymbol{D}_x^{(V,V)}$ for different combinations of PHS exponents, m, and polynomial orders, q: (a) no polynomial augmentation; (b) $q = 1$; (c) $q = 2$; (d) $q = 3$; (e) $q = 4$; (f) $q = 5$. The results for the y-derivatives ('+') are almost indistinguishable. Shaded areas of the same color show the standard deviation (overlapping regions appear purple).

reflected in this analysis of the relative error for a fixed $k\Delta r$. The modified wavenumber analysis (shown in figures 3.5 and A.1 below) will, however, show that increasing q beyond 3 does not improve the order of accuracy for a fixed stencil size, $n = 28$.

Figure 3.4 shows the relative error for the second derivatives contained in the Laplacian, $\boldsymbol{D}_\Delta^{(V,V)}$. We repeat the same analysis as for the first derivative, and similar trends are observed. Following the same arguments stated above, and for consistency, we proceed with $(n,m,q) = (28,7,3)$ for the Laplacian as well.

Figure 3.5 shows the modified wavenumber diagrams for the differentiation matrices $\boldsymbol{D}^{(V,V)}$ with the corresponding standard deviations. Results for the standard 2nd-order central, and 4th- and 6th-order Padé-type methods are shown for comparison. Despite the inhomogeneity of the mesh, the truncation errors in the x and y directions are very similar. The accuracy of the first and second derivatives is almost identical to the 6th-order Padé scheme up to $k\Delta r = 2$. Also shown is the standard deviation of the modified wavenumbers obtained from all grid points.

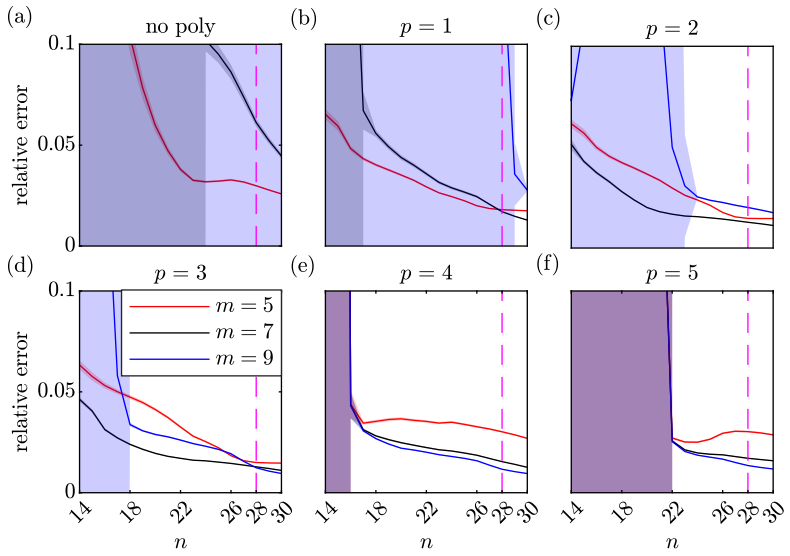

Figure 3.4. Relative error for $\boldsymbol{D}_{\wedge}^{(V,V)}$ for different combinations of PHS exponents, m, and polynon f) $q = 5$. Shaded a purple).

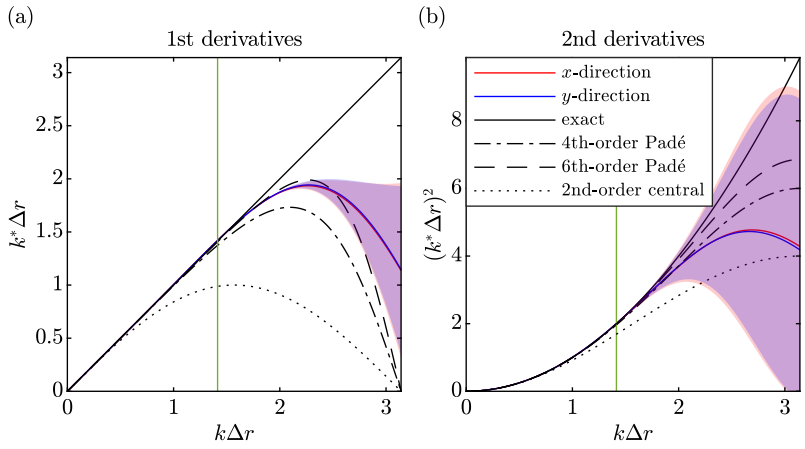

Figure 3.5. Modified wavenumber diagrams for the differentiation matrices $\boldsymbol{D}^{(V,V)}$ with $(n,m,q) = (28,7,3)$ for: (a) the first; (b) the second derivatives. Shaded areas represent the standard deviations for the results in the x- (red) and y- (blue) directions, respectively (overlapping regions appear purple). Results for Padé-type methods are shown for comparison. The recommended maximum modified wavenumber of $k\Delta r = \sqrt{2}$ is highlighted in green.

The important observation is that the standard deviation is negligible until the mean modified wavenumber deviates from the theoretical curve. Wavenumbers beyond this point have to be

considered underresolved and have to be filtered out or, ideally, avoided entirely through grid refinement. The proposed maximum modified wavenumber of $k\Delta r = \sqrt{2}$ (green lines in figure 3.5) ensures the spectral-like accuracy, which exceeds the second-order accuracy (dotted lines) of mc

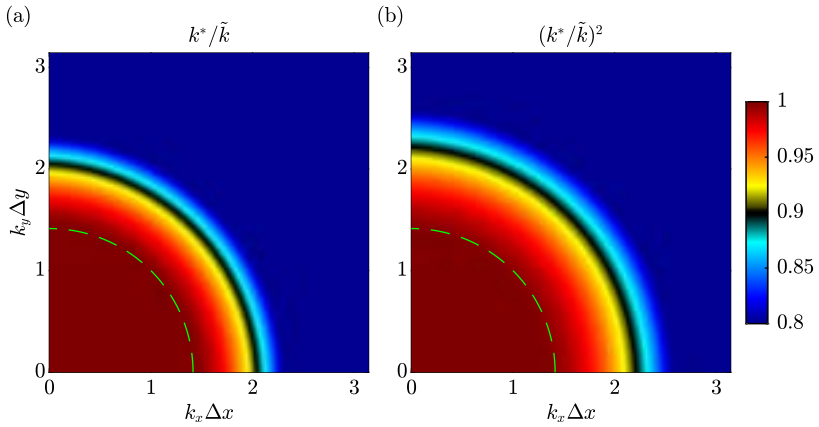

Figure 3.6. 2D modified wavenumber diagrams (normalized) for the differentiation matrices $\boldsymbol{D}^{(V,V)}$ with $(n,m,q) = (28,7,3)$: (a) first and (b) second derivatives. The recommended maximum modified wavenumber of $\tilde{k}\Delta r = \sqrt{2}$ is highlighted in green.

To assess the inhomogeneity of the computational grid, we extend the modified wavenumber analysis to two dimensions by plotting the ratio $k^*/\tilde{k}$, where $\tilde{k} = \sqrt{k_x^2 + k_y^2}$, in the x-y wavenumber plane. This is shown in figure 3.6. An important observation is that the normalized modified wavenumbers are almost independent of the direction of the wave. This finding is encouraging since the local topology of an unstructured mesh, in principle, can have arbitrary orientations. At the proposed maximum modified wavenumber of $\tilde{k}\Delta r = \sqrt{2}$ (green lines), the ratio deviates from the spectral limit by at most 0.6% and 0.2% for the first and second derivatives, respectively. These observations suggest that the 28-point PHS+poly RBF-FD discretization provides high-order accuracy independent of grid orientation if the nodes are taken as the midpoints of a `DistMesh` grid, see figure 3.1.

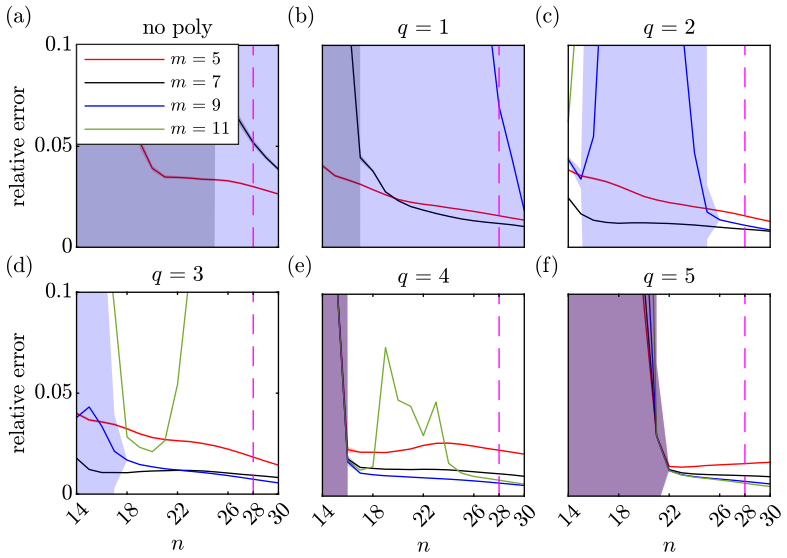

Figure 3.7. Relative error for $\boldsymbol{D}_{\Delta}^{(P,P)}$ for different combinations of PHS exponents, m, and polynomial orders, q: (a) no polynomial; (b) $q = 1$; (c) $q = 2$; (d) $q = 3$; (e) $q = 4$; (f) $q = 5$. Shaded areas of the same color show the standard deviation (overlapping regions appear purple).

3.4.2 P-grid to P-grid

Next, we repeat the analysis of §3.4.1 for the differentiation matrix $\boldsymbol{D}_{\Delta}^{(P,P)}$, which operates on the (P,P)-grid shown in figure 3.2(b). We focus on the truncation error of the discretized Laplace operator that is used to solve the pressure Poisson problem, equation 4.5. Figure 3.7 shows the relative error for different parameters. The combination $(n,m,q) = (28,7,3)$ that was identified as optimal for the (V,V)-grid is taken as the baseline. Deviating from the baseline case, increasing m to $m = 9$ with q constant or increasing q to $q = 4$ with m constant yields a small decrease of the error. We choose consistency over these marginal gains and proceed with $(n,m,q) = (28,7,3)$ for $\boldsymbol{D}_{\Delta}^{(P,P)}$. Prior to making this choice, we confirmed that further increasing m does not further decrease the error significantly. In fact, letting $m = 11$ leads to numerical instability, as can be seen in figure 3.7(d).

To gauge the numerical stability of the local stencils, figure 3.8(a,b) show the histograms of the condition number of $\boldsymbol{A}_{\text{aug}}$, defined in equation (3.9), for $q = 3$ and $q = 4$ on $V-$ and

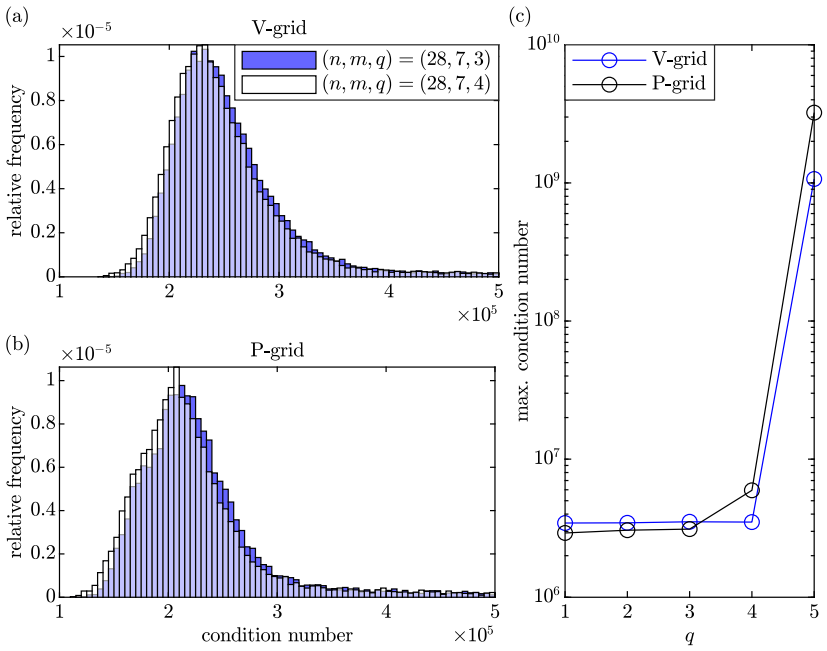

Figure 3.8. Histogram of the condition numbers of $\boldsymbol{A}_{\text{aug}}$: (a) V-grid and (b) P-grid; (c) maximum value for different polynomial degrees.

$P-$grids. While the histograms are comparable, the maximum condition number for $P-$grid shown in panel 3.8(c) reveals that the condition number starts to deteriorate for $q \geq 4$. This is in accordance with the findings of Flyer, Barnett, & Wicker [72] who found that lower polynomial degrees lead to more stable discretizations. We will show in the following that increasing q beyond 3 also does not increase the accuracy for a fixed stencil size.

The modified wavenumber diagrams for the differentiation matrices $\boldsymbol{D}^{(P,P)}$ are reported in figure 3.9. As before, the analytical results for the 2nd-order central, and 4th- and 6th-order Padé-type methods are shown for comparison. It is found that the modified wavenumber curves for the (P,P)-grid are as good or better as the 6th-order Padé scheme for both the first and second derivatives. Furthermore, the variances are much lower compared to the results for the (V,V)-grid, previously shown in figure 3.5. The likely reason is that the local topology of the (P,P)-grid is more evenly distributed in space. This becomes apparent when comparing figure 3.2(b,c) to (a,d) of the same figure. It is also observed that the modified wavenumber curves for the x- and y-directions, in particular for the second derivatives, differ. We suspect that this is due

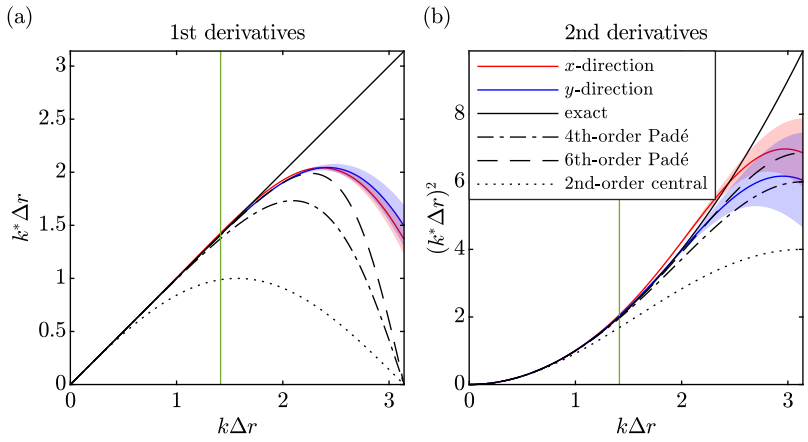

Figure 3.9. Same as figure 3.5 for $\boldsymbol{D}^{(P,P)}$ with $(n,m,q) = (28,7,3)$. Results for the combination $(28,7,4)$ are reported in panels A.1(c,d) with negligible difference.

to the inhomogeneity of the computational domain, which results from its elongated shape and the local grid refinement of the wake region that is also oriented in the $x-$direction. We conclude that the discretization is also robust in the presence of grid non-homogeneity while preserving highe

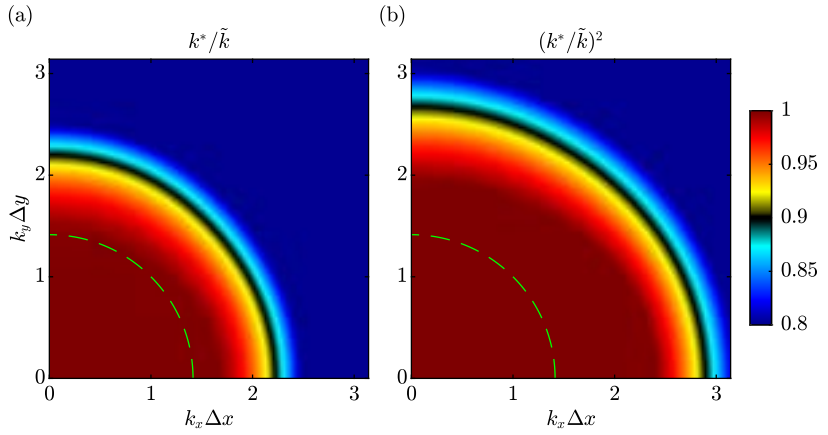

Figure 3.10. Same as figure 3.6 for $\boldsymbol{D}^{(P,P)}$ with $(n,m,q) = (28,7,3)$.

The effect of grid orientation is assessed for the first and second derivatives in terms of the two-dimensional modified wavenumber diagrams in panels 3.10(a) and (b), respectively. Similar to what was found for the $(V,V)-$grid in figure 3.6, no strong directional preference is observed. The direct comparison with figure 3.6 reveals that the modified wavenumber stays

closer to unity ccurate results over a wider w

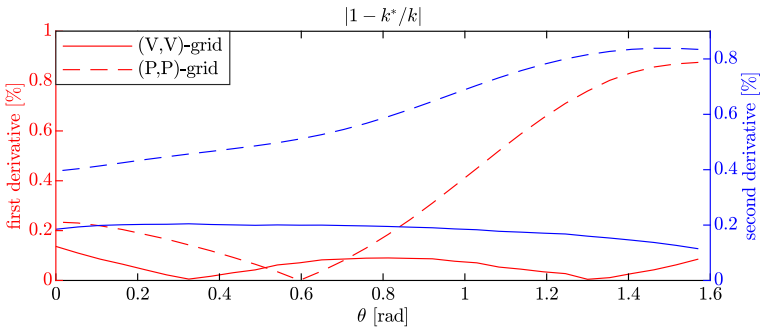

Figure 3.11. Relative error of the modified wavenumber at different wave angles.

Figure 3.11 shows a direct comparison of the error relative to the spectral limit at $\tilde{k}\Delta r = \sqrt{2}$ as a function of the wave angle for both grids and derivatives. The errors for the (P,P)-grid is around 0.4% and 0.6% for first and second derivatives, respectively. The values for (V,V)-grid are generally lower. This shows that, despite the heterogeneous grid, the dependence on the wave angle is low.

The relative error analyses for $\boldsymbol{D}^{(V,P)}$ and $\boldsymbol{D}^{(P,V)}$, that is, cases (c) and (d) in figure 3.2, are reported in A.2. The results are similar to those of the non-mixed grids above. To maintain the overall accuracy of the numerical scheme, which involves combinations of all grids, we hence retain the recommended value of $\tilde{k}\Delta r = \sqrt{2}$.

3.5 Numerical stability analysis

The stability of numerical methods plays an important role in hydrodynamic stability analysis. Numerical instabilities may lead to spurious eigenvalues and modes. The local $\mathscr{D}$-Lebesgue function proposed by Shanker & Fogelson [245] provides a measure of the eigenvalue stability of the RBF-FD method. For a given linear operator $\mathscr{D}$, the local Lebesgue function

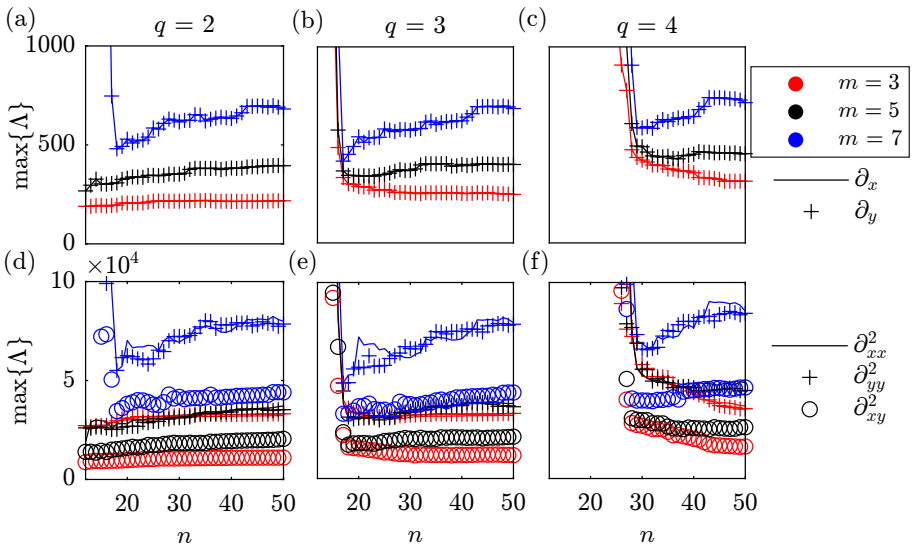

Figure 3.12. Maximum local $\mathscr{L}$-Lebesgue function for different combinations of PHS exponents, m, and polynomial orders, q for the first (a-c) and second derivatives (d-f) in the x- (solid line), y- ('+') and xy-directions (circle).

takes the form of the 1-norm of the RBF-FD weight in equation (3.4), that is

$$\Lambda_{\mathscr{D}}(\boldsymbol{x}_0; \{\boldsymbol{x}_j\}_{j=1}^n) = \|\boldsymbol{w}\|_1 = \sum_{j=1}^{n} |w_j|. \tag{3.14}$$

Larger values of the local Lebesgue function indicate an increased susceptibility to numerical instability in the assembled global differentiation matrix. Figure 3.12 shows the maximum value of the local Lebesgue function across various parameter combinations based on the test grid shown in figure 5.2. Refer to the accompanying context of figure 5.2 for more details of the grid. For all considered stencil sizes, polynomial degrees, and relevant operators, the minimax value is consistently achieved at $m = 3$, suggesting its suitability for hydrodynamic stability analysis.

For two-dimensional problems, it has been suggested that the stencil size should satisfy $n \gtrsim (q+1)(q+2)$ [72, 74]. In practice, including a few additional nodes beyond the minimum requirement is often beneficial to improve performance. The specific choice of additional nodes may depend on the type of node sets used. For instance, a recommended formula for Halton nodes is $n = (q+1)(q+2) + \lfloor \ln[(q+1)(q+2)] \rfloor$ [146, 245]. We here select the stencil size n

based on the assumption of a perfectly arranged hexagonal node distribution comprising $q/2+1$ layers, despite the actual distribution of nodes being heterogeneous. For practical examples, refer to figure 5.1 and the surrounding context. The recommended parameter combinations are summarized in table 3.1. With these parameters, hyperviscosity or other means of regularization are not needed to stabilize the solution further.

Table 3.1. Summary of parameter selections.

	Shankar & Fogelson [245]	Le Borne & Leinen [146]	present
$q=2$	$(n,m)=(14,3)$	$(n,m)=(14,5)$	$(n,m)=(19,3)$
$q=3$	$(n,m)=(22,3)$	$(n,m)=(22,7)$	$(n,m)=(28,3)$
$q=4$	$(n,m)=(33,3)$	$(n,m)=(33,7)$	$(n,m)=(37,3)$

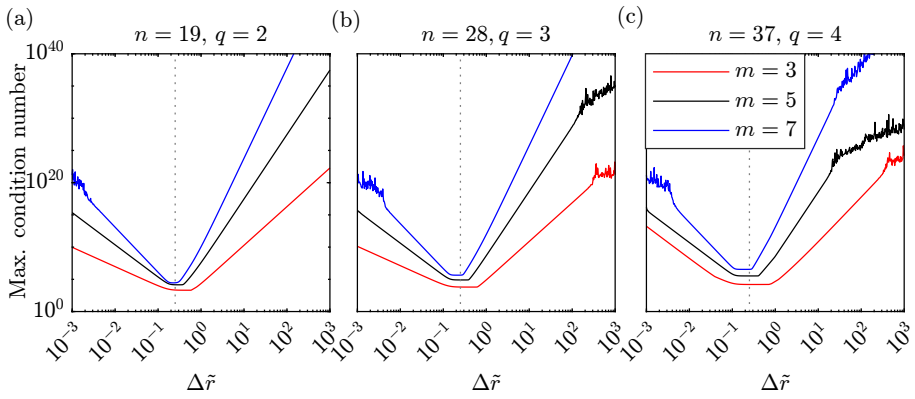

Figure 3.13. Maximum condition number of $\boldsymbol{A}_{\text{aug}}$ as a function of local grid spacing $\Delta\tilde{r}$: (a) $n=19$, $q=2$; (b) $n=28$, $q=3$; (c) $n=37$, $q=4$. The recommended local spacing of $\Delta\tilde{r}=0.25$ is highlighted as dashed lines.

The condition number of the augmented matrix $\boldsymbol{A}_{\text{aug}}$, defined in equation (3.9), affects the numerical stability in a similar way and hence needs to be considered separately. The condition number for various parameter combinations has been investigated and discussed in Le Borne & Leinen [146]. Independent of the parameter selection, Shahane, Radhakrishnan, & Vanka [241] demonstrated that scaling the local stencil to a unit length scale can improve the condition number. We further reveal the existence of an optimal range for the averaged local grid spacing, wherein the condition number of the augmented matrix $\boldsymbol{A}_{\text{aug}}$ reaches its minimum value.

For a given stencil $\{\boldsymbol{x}_j\}_{j=1}^n$, we perform scaling with respect to the location of $\boldsymbol{x}_0$ with a scaling factor κ such that

$$\{\tilde{\boldsymbol{x}}_j\}_{j=1}^n = \{\kappa(\boldsymbol{x}_j - \boldsymbol{x}_0)\}_{j=1}^n, \tag{3.15}$$

and the averaged local grid spacing becomes $\Delta\tilde{r} = \kappa\Delta r$. Figure 3.13 shows the maximum condition number within the test grid as a function of $\Delta\tilde{r}$ for the considered parameters. Optimal performance is consistently achieved within the range of $0.15 \lesssim \Delta\tilde{r} \lesssim 0.3$ across all examined parameter combinations. Based on this, we perform spatial scaling to ensure an averaged local spacing of $\Delta\tilde{r} = 0.25$ before solving the RBF-FD weights in equation (3.4). The chain rule is applied to transform the RBF weights back to the original grid.

Chapter 3, in part, is a reprint of the material as it appears in Journal of Computational Physics 2023, Chu, Tianyi; Schmidt, Oliver T., Elsevier, 2023. Chapter 3, in part, has been submitted for publication of the material as it may appear in Journal of Computational Physics 2024, Chu, Tianyi; Schmidt, Oliver T., Elsevier, 2024. The dissertation author was the primary investigator and author of these papers.

Chapter 4

An RBF-FD-based Navier-Stokes solver using scattered but staggered nodes

While there are numerous demonstrations of PHS+poly RBF-FDs for advection-diffusion problems [19, 96, 244, 245, 246, 261], their application to the incompressible Navier-Stokes equations has been explored only very recently. Shahane *et al.* [241], for example, simulated incompressible flows using an explicit fractional-step method and considered several test problems to gauge accuracy. A semi-implicit algorithm was proposed by Shahane & Vanka [243] and later implemented by Unnikrishnan *et al.* [282] to simulate Taylor-Couette flow. The consistency and convergence of this algorithm with respect to grid resolution were later examined in Shahane & Vanka [242].

We build on this successful combination of fractional-step methods with PHS+poly RBF-FD discretizations and make two main contributions, one in terms of improving computational efficiency and the other in terms of error analysis. A significant reduction in computational cost is achieved through the use of a staggered-grid arrangement that permits the use of smaller stencils and, at the same time, much coarser grids. The staggered grid arranges the velocity and pressure at different nodes to circumvent the numerical instability known as odd-even decoupling. While the idea of grid staggering originates from the classical FD Marker-And-Cell scheme by Harlow & Welch [99], staggering occurs naturally in finite volume methods that define velocity in terms of fluxes across cell faces. Similarly, the proposed staggering strategy is based on an

underlying triangular grid, generated using any standard grid generator, and defines the pressure at the vertices and velocities at the centers of the faces.

4.1 Numerical approach

Numerical instabilities are a known problem of standard FD methods that uses the Cartesian grid. This error can be traced back to central differencing schemes on collocated grids [194]. Similar grid oscillations are also observed on unstructured meshes. The arguably most common strategy to address this issue is the use of hyperviscosity [76, 80, 82, 245]. Instead of *ad-hoc* regularization, we propose the use of a staggered node arrangement that discretizes the pressure in the computational domain Ω by M scattered nodes that form the $P-$grid, and the velocity by N scattered nodes that form the $V-$grid. The $P-$grid is obtained using the Matlab algorithm `DistMesh` developed by Persson [199]. This algorithm generates unstructured triangular meshes in 2-D. Inspired by standard FV methods that define the flux across the cell boundaries, we arrange the velocity components at the midpoints of cell edges. The resulting N scattered nodes are the $V-$grid. This staggered node arrangement is different from the classical staggered grid, which evaluates the horizontal and vertical velocities at different locations, but is similar to that used in FV methods. The resulting ratio N/M is around 3. See figure 3.1 for an example of unstructured staggered node layout for flow around a cylinder.

Several variants of the original fractional-step method by Kim & Moin [136] using RBF-FD discretizations on collocated Cartesian grids [117, 302] and unstructured grids [241, 282] can be found in literature. These previous implementations do not require regularizations, but, as we will demonstrate, significant savings in terms of the total number of grid points and stencil size is achieved by using the staggered node layout. We propagate the flow field from $j-$th time step to $(j+1)-$th time step by the following three-stage semi-implicit approach. The primitive variables u, v, p are expressed in vector form as $\boldsymbol{u}, \boldsymbol{v}, \boldsymbol{p}$, respectively.

1. In the first stage, we use the second-order Adam-Bashforth method to discretize equations

(1.2a) and (1.2b) in time explicitly, yielding

$$\frac{\boldsymbol{u}^* - \boldsymbol{u}_j}{\Delta t} = \frac{3}{2}\boldsymbol{C}_j(\boldsymbol{u}_j) - \frac{1}{2}\boldsymbol{C}_{j-1}(\boldsymbol{u}_{j-1}), \qquad \frac{\boldsymbol{v}^* - \boldsymbol{v}_j}{\Delta t} = \frac{3}{2}\boldsymbol{C}_j(\boldsymbol{v}_j) - \frac{1}{2}\boldsymbol{C}_{j-1}(\boldsymbol{v}_{j-1}). \quad (4.1)$$

Here the convective term, $\boldsymbol{C}_j$, is defined as

$$\boldsymbol{C}_j(\boldsymbol{q}) = -\left[\boldsymbol{u}_j \circ \left(\boldsymbol{D}_x^{(V,V)}\boldsymbol{q}\right) + \boldsymbol{v}_j \circ \left(\boldsymbol{D}_y^{(V,V)}\boldsymbol{q}\right)\right], \quad (4.2)$$

where $\boldsymbol{q} \in \{\boldsymbol{u}, \boldsymbol{v}\}$, superscripts $(\cdot)^*$ and $(\cdot)^{**}$ denote intermediate, non-divergence-free velocity fields, and $\circ$ the Hadamard product.

2. In the second stage, the viscous terms are advanced by the second-order implicit Crank-Nicolson scheme in time as

$$\left(\boldsymbol{I} - \frac{\Delta t}{2\mathrm{Re}}\boldsymbol{D}_\Delta^{(V,V)}\right)\boldsymbol{u}^{**} = \left(\boldsymbol{I} + \frac{\Delta t}{2\mathrm{Re}}\boldsymbol{D}_\Delta^{(V,V)}\right)\boldsymbol{u}^*, \quad (4.3a)$$

$$\left(\boldsymbol{I} - \frac{\Delta t}{2\mathrm{Re}}\boldsymbol{D}_\Delta^{(V,V)}\right)\boldsymbol{v}^{**} = \left(\boldsymbol{I} + \frac{\Delta t}{2\mathrm{Re}}\boldsymbol{D}_\Delta^{(V,V)}\right)\boldsymbol{v}^*, \quad (4.3b)$$

where $\boldsymbol{I}$ denotes the identity matrix. The use of the Crank-Nicolson scheme eliminates the diffusive time-step constraint while maintaining second-order accuracy, see A.4 for more details.

3. In the third stage, incompressibility is enforced via pressure correction. First, we calculate the divergence of the intermediate velocity, $(\cdot)^{**}$, on the P-grid as

$$\boldsymbol{F}_{j+1} = \boldsymbol{D}_x^{(P,V)}\boldsymbol{u}^{**} + \boldsymbol{D}_y^{(P,V)}\boldsymbol{v}^{**}. \quad (4.4)$$

Upon solution of the pressure-Poisson equation,

$$\boldsymbol{D}_\Delta^{(P,P)}\tilde{\boldsymbol{p}}_{j+1} = \frac{1}{\Delta t}\boldsymbol{F}_{j+1}, \quad (4.5)$$

for the pressure correction, $\tilde{\boldsymbol{p}}$, the pressure is obtained as

$$\boldsymbol{p}_{j+1} = \tilde{\boldsymbol{p}}_{j+1} - \frac{\Delta t}{2\mathrm{Re}} \boldsymbol{D}_{\Delta}^{(P,P)} \tilde{\boldsymbol{p}}_{j+1}. \tag{4.6}$$

The velocity components at the $(j+1)$-th time step are then calculated as

$$\boldsymbol{u}_{j+1} = \boldsymbol{u}^{**} - \Delta t \boldsymbol{D}_x^{(V,P)} \tilde{\boldsymbol{p}}_{j+1}, \qquad \boldsymbol{v}_{j+1} = \boldsymbol{v}^{**} - \Delta t \boldsymbol{D}_y^{(V,P)} \tilde{\boldsymbol{p}}_{j+1}. \tag{4.7}$$

Following [136], the boundary conditions for the intermediate velocities are

$$\boldsymbol{u}^{**} = \boldsymbol{u}_{j+1} + \Delta t \boldsymbol{D}_x^{(V,P)} \tilde{\boldsymbol{p}}_j, \qquad \boldsymbol{v}^{**} = \boldsymbol{v}_{j+1} + \Delta t \boldsymbol{D}_y^{(V,P)} \tilde{\boldsymbol{p}}_j. \tag{4.8}$$

The matrix inversions in equations (4.3) and (4.5) are solved only once at the beginning using LU factorization with time complexity $\mathrm{O}(\frac{2}{3}N^3)$ and $\mathrm{O}(\frac{2}{3}M^3)$, respectively. At each time step, the time complexity is $\mathrm{O}(\max\{N^2, M^2\})$.

4.2 Applications

We demonstrate the viability, robustness, and flexibility of the fractional-step, staggered-node, PHS+poly RBF-FD algorithm on two examples, internal lid-driven cavity flow and the flow past a cylinder. Both test cases are established benchmark problems. The parameters identified from the error and accuracy analyses in the previous section, i.e., $(n, m, q) = (28, 7, 3)$, are used throughout, and it is ensured that the `DistMesh` grid properly resolves the flow by adhering to the $\tilde{k}\Delta r \lesssim \sqrt{2}$ recommendation.

4.2.1 Lid-driven cavity flows

The lid-driven cavity problem is often used to validate different implementations of RBF-FD methods. In the past, these implementations often used specific grid arrangements, such as Cartesian or quasi-uniform grids [226, 302], or locally orthogonal grids near the boundary

[49, 249, 250]. A notable exception is the vorticity/stream function-based steady-state solver by Bayona roblem on scat

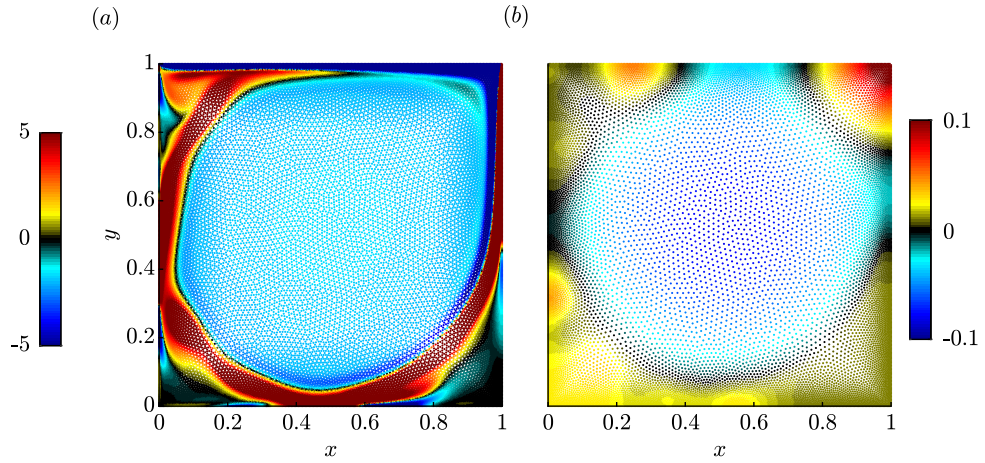

Figure 4.1. Computational domain and solution for the lid-driven cavity at Re = 10000: (a) V-grid with $N = 42799 \approx 207^2$ nodes, colored by vorticity; (b) P-grid with $M = 14606 \approx 121^2$ nodes, colored by pressure.

Figure 4.1 shows the discretization of the unit square cavity domain, $\Omega = [0,1] \times [0,1]$, with $N = 42799 \approx 207^2$ and $M = 14606 \approx 121^2$. The characteristic distance of the P-grid is 0.004 near the walls and averages at 0.008 for the whole domain. The flow inside the square cavity is driven by the motion of the top wall with unit velocity, $U_0 = 1$. No-slip boundary conditions are prescribed at all walls. The fluid is at rest at $t = 0$. A time step $\Delta t = 0.00125$, corresponding to a CFL number around 0.7, is used in the computation. Results at Reynolds numbers, $\mathrm{Re} = \frac{U_0}{\nu}$, ranging from 100 to 10000 are investigated for comparison with the benchmark results by [90]. While other RBF-based codes often rely on hyperviscosity or other means of regularization, the present implementation runs stably for the entire range of Reynolds numbers.

Figure 4.2(a) and (b) display the obtained velocity profiles through the horizontal and vertical centerlines of the cavity, respectively. The present results compare well with the benchmark data of Ghia *et al.* [90], who used 129^2 and 257^2 nodes for Reynolds numbers smaller and larger or equal than 5000, respectively. After reaching steady-state, a periodic solution

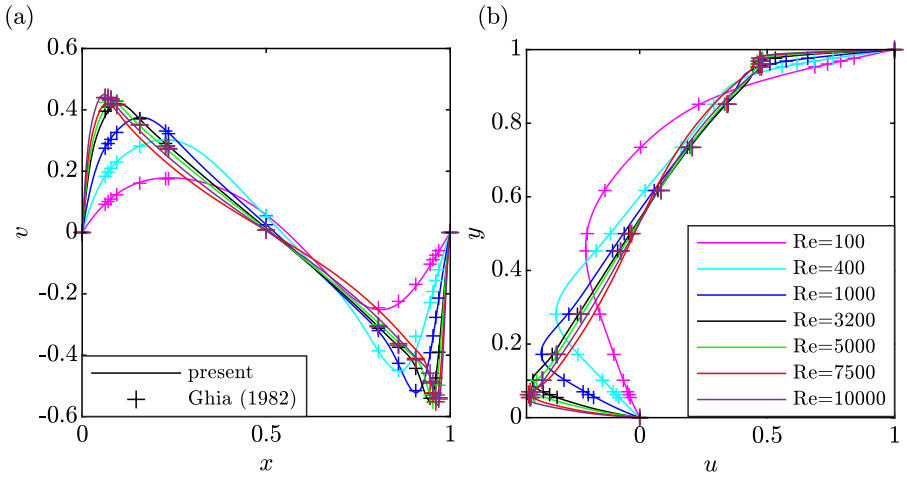

Figure 4.2. Velocity profiles for the lid-driven cavity flow at Re = 100 (magenta), Re = 400 (cyan), Re = 1000 (black), Re = 3200 (black), Re = 5000 (green) and Re = 7500 (red) through the: (a) horizontal centerline; (b) vertical centerline. Results at Re = 10000 (purple) are the time-averaged profiles. The obtained results (solid) are compared to those of [90] ('+').

with frequency $f = 0.63$ is found at Re = 10000. The corresponding curves in figure 4.2 are therefore time-averaged velocity profiles. The oscillation frequency varies in the literature, and the frequency obtained here falls well in the reported range [9, 34, 195, 268]. After confirming the quantitative agreement of our results with the literature, we next examine the corresponding flow fields.

Figure 4.3 shows the vorticity fields for the four highest Reynolds numbers. For Re $\leq$ 5000, the primary vortices seen in figure 4.3(a,b) evolve into the steady-state solutions shown in 4.3(e,f). Despite its more chaotic evolution, the flow at Re = 7500 also converges to a steady state. It is generally observed that the higher the Reynolds numbers, the longer it takes to reach steady-state. For Re = 10000, the flow-field is doe not possess a steady-state solution, and we hence show an instantaneous state within the limit-cycle. After confirming that the proposed scheme is well-suited for simulating this unsteady incompressible internal flow, we next focus on the more challenging example of open flow over a cylinder.

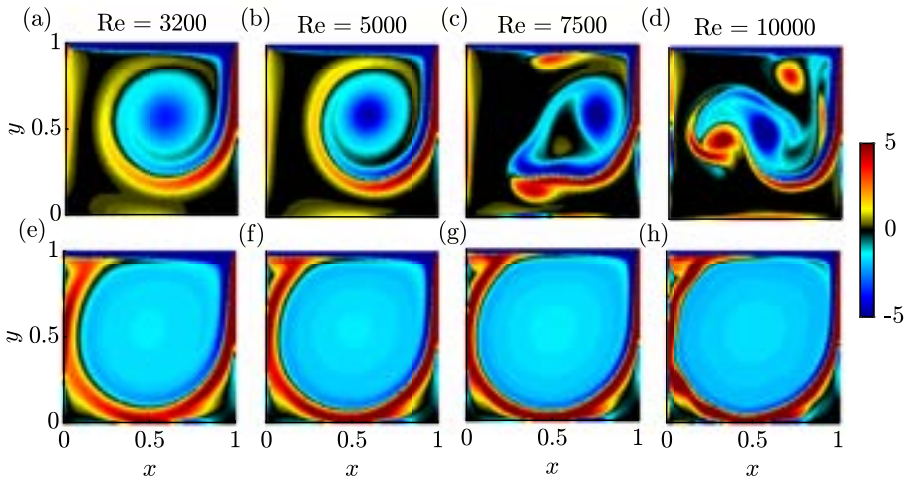

Figure 4.3. Vorticity fields for Re = 3200 (a, e), Re = 5000 (b, f), Re = 7500 (c, g) and Re = 10000 (d, h) at: (a-d) $t = 15$; (e-g) steady-state; (h) limit-cycle . The vorticity vector is calculated as $\boldsymbol{\omega} = \boldsymbol{D}_x^{(V,V)}\boldsymbol{v} - \boldsymbol{D}_y^{(V,V)}\boldsymbol{u}$.

4.2.2 Cylinder flow

Wakes behind bluff bodies are an ubiquitous phenomenon in engineering, and the flow over a circular cylinder is often used as an unsteady benchmark problem for numerical methods. RBF-based discretization facilitates easy local grid refinement near the solid boundaries and in the wake [illegible] have exclu [illegible] 302] (or ha [illegible] and previ

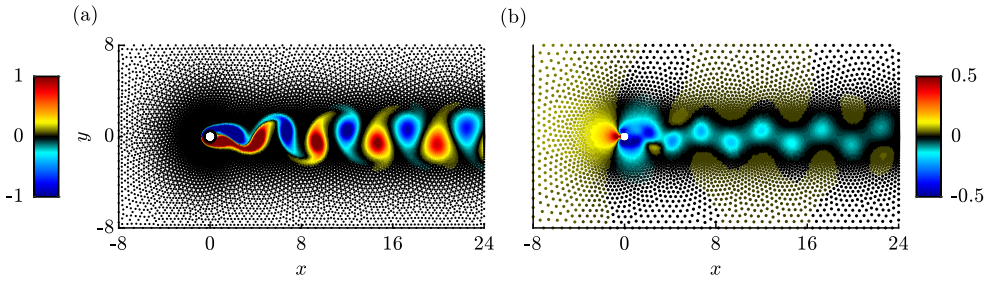

Figure 4.4. Computational grids for cylinder flow: (a) V-grid with $N = 55671$ nodes showing ω; (b) P-grid with $M = 18647$ nodes showing p at Re=100, respectively.

Following [43, 222], we take the computational domain Ω as the exterior of the cylinder

$r \geq D/2 = 0.5$ within the rectangle $-8 \leq x \leq 24$, $-8 \leq y \leq 8$. Local grid refinement is used to resolve the regions near the cylinder and the wake. Figure 4.4(a,b) show the V-grid with $N = 55671$ and P-grid with $M = 18647$, respectively. The characteristic distances of the P-grid are $\Delta r^{(p)} = 0.03$ near the cylinder, 0.04 on the wake centerline, $x > 0.5, y = 0$, and averaged at 0.123 in the whole domain. The inflow is uniform with $U_\infty = 1, V_\infty = 0$, symmetric boundary conditions with $v = \partial u/\partial y = 0$ are applied at the transverse boundaries, a no-slip condition is prescribed on the cylinder, and a stress-free outflow condition, $-p\boldsymbol{n} + \frac{1}{\mathrm{Re}}\nabla \boldsymbol{U} \cdot \boldsymbol{n} = 0$, where $\boldsymbol{n} = [1,0]^T$, is prescribed at the outlet. The flow field is initialized with $\boldsymbol{U}_0 = [\mathbf{1},\mathbf{0}]^T$. The

nbers,

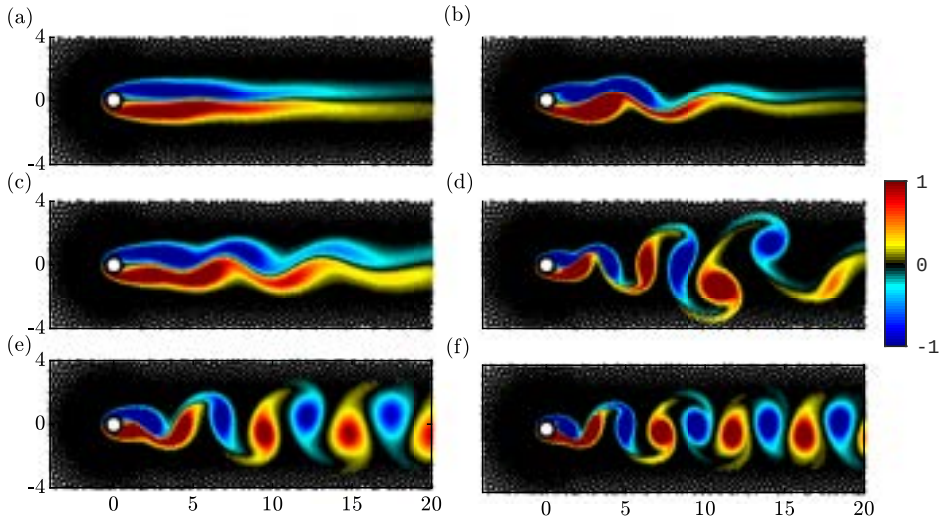

Figure 4.5. Instantaneous vorticity fields for Re = 100 (a, c, e), and Re = 200 (b, d, h) at: (a, b) $t = 25$; (c, d) $t = 40$; (e, f) limit-cycle .

Figure 4.5 shows the vorticity field at three different time instances for both Reynolds numbers. For both cases, these three time instances capture the gradual evolution of the unstable wake flow through a transient that finally results in the limit-cycle oscillation. This limit-cycle oscillation is the well-known periodic von Kármán vortex street seen in figures 4.5(e) and 4.5(f).

We next quantify these results by examining the drag and lift coefficients on the limit

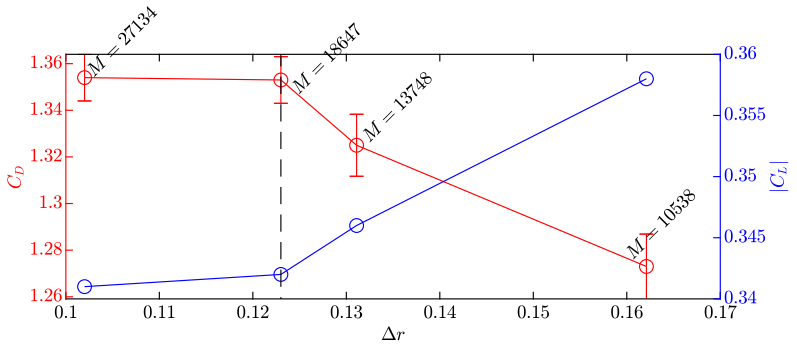

Figure 4.6. Drag (red) and lift (blue) coefficients for cylinder flow at Re = 100 for different grid resolutions. The vertical dashed line indicates the reference P-grid resolution $\Delta r = 0.123$ used in §4.2.2.

cycle, defined as

$$C_D = \frac{F_D}{\frac{1}{2}\rho U_\infty^2 D}, \qquad C_L = \frac{F_L}{\frac{1}{2}\rho U_\infty^2 D}, \tag{4.9}$$

respectively. The drag, F_D, and lift, F_L, forces are computed by integrating the pressure and wall-shear over the cylindrical surface using the Simpson's rule. The grid dependence of the lift and drag coefficients is investigated in figure 4.6 for Re = 100. The four grids are obtained by varying the initial edge length for `DistMesh` from 0.025 to 0.04. The differences in the drag and lift coefficients between the current (vertical dashed line) and the densest grid are 0.07% and 0.29%, respectively. This indicates that the present grid resolution is sufficient.

Table 4.1. Summary of results for drag, lift, and the fundamental vortex shedding frequency the flow behind a cylinder at Re = 100 and Re = 200.

	Re = 100			Re = 200		
	C_D	C_L	St	C_D	C_L	St
Braza *et al.* [32]	1.364 ± 0.015	± 0.25	-	1.40 ± 0.05	± 0.75	-
Calhoun [43]	1.330 ± 0.014	± 0.298	0.175	1.17 ± 0.058	± 0.67	0.202
Ding *et al.* [60]	1.325 ± 0.008	± 0.28	0.164	1.327 ± 0.045	± 0.60	0.196
Liu *et al.* [156]	1.350 ± 0.012	± 0.339	0.164	1.31 ± 0.049	± 0.69	0.192
Russell & Wang [222]	1.38 ± 0.007	± 0.300	0.169	1.29 ± 0.022	± 0.50	0.195
Shahane *et al.* [241]	1.354 ± 0.009	± 0.333	0.166	1.364 ± 0.045	± 0.690	0.197
Shu *et al.* [250]	1.362 ± 0.010	± 0.32	0.166	1.352 ± 0.049	± 0.62	0.192
Present	1.353 ± 0.010	± 0.342	0.171	1.382 ± 0.046	± 0.683	0.201

Table 4.1 compares previous results for both Reynolds numbers to the values obtained here. The vortex shedding frequency is reported in terms of the Strouhal number, $\mathrm{St} = fD/U_\infty$. It can be seen that our results fall well within the range of the previous results, which vary by as much as 16% at $\mathrm{Re} = 200$. Out of the reported literature, the work of Shahane *et al.* [241] is most closely related to the present study. Shahane *et al.* [241] report results for their collocated PHS-RBF method for two different grid resolutions. Their results on the finer grid are reported in table 4.1. The staggered-grid arrangement used here utilizes around 55% fewer nodes on the $V-$grid, or 85% on the $P-$grid, and an about one-third smaller RBF stencil.

Chapter 4, in full, is a reprint of the material as it appears in Journal of Computational Physics 2023, Chu, Tianyi; Schmidt, Oliver T., Elsevier, 2023. The dissertation author was the primary investigator and author of the paper.

Chapter 5

Mesh-free hydrodynamic stability

While RBF-FDs demonstrate the capability to construct sparse differentiation operators, the potential applications in hydrodynamic stability analysis have not been thoroughly explored. Both classical LST and RA require, in their most basic form, the construction of large matrices that have to be decomposed into their singular- or eigen-components. The construction and decomposition of these matrices are particularly challenging for flows in complex geometries. Previous studies [63, 213, 251, 303] have leveraged the flexibility of the FV methods on unstructured meshes. However, a downside of unstructured FV methods is that the accuracy is usually restricted to 2nd-order. Alternatively, the utilization of FE methods for spatial discretization provides high-order accuracy for flow instability analysis [168, 169, 214, 253]. The commonly employed weak formulation of governing equations in FE methods raises concerns regarding stability and convergence. FE methods offer the same flexibility, and the FreeFEM+ toolbox by Hecht [100] has been employed in a number of recent studies [168, 169, 214, 253]. Matrix-free methods, such as the time-stepper [11, 14, 279] and other related techniques [59, 170, 184, 192], provide an alternative approach where the decomposition of large matrix operations can be completely circumvented. Iterative Krylov subspace methods are commonly employed to obtain a partial eigendecomposition. However, their major limitation lies in their capacity to extract only a limited portion of the spectra at a time. Randomized approaches have also been explored as potential solutions to decrease the computational cost of the singular- or eigendecomposition

of large stability matrices [180, 212]. In this chapter, we demonstrate the capability and accuracy of RBFs in effectively addressing the aforementioned challenges. This work is the first demonstration of such applications.

5.1 Mesh-free linear stability analysis

Upon the use of these global RBF-FD-based differentiation matrices, we assemble the discrete global incompressible LNS operator from equation (2.6), taking the two-dimensional Cartesian coordinate system as an example, as

$$\boldsymbol{L} = \begin{pmatrix} \boldsymbol{S} - \mathrm{diag}\left(\boldsymbol{D}_x \boldsymbol{u}_0\right) + \mathrm{Re}^{-1}\left(\boldsymbol{D}_{xx} + \boldsymbol{D}_{yy}\right) & -\mathrm{diag}\left(\boldsymbol{D}_y \boldsymbol{u}_0\right) & -\boldsymbol{D}_x \\ -\mathrm{diag}\left(\boldsymbol{D}_x \boldsymbol{v}_0\right) & \boldsymbol{S} - \mathrm{diag}\left(\boldsymbol{D}_y \boldsymbol{v}_0\right) + \mathrm{Re}^{-1}\left(\boldsymbol{D}_{xx} + \boldsymbol{D}_{yy}\right) & -\boldsymbol{D}_y \\ \boldsymbol{D}_x & \boldsymbol{D}_y & \boldsymbol{0} \end{pmatrix}, \tag{5.1}$$

where $\boldsymbol{S} = -\left(\boldsymbol{u}_0 \circ \boldsymbol{D}_x + \boldsymbol{v}_0 \circ \boldsymbol{D}_y\right)$, and $\circ$ denotes the Hadamard product. For the case of compressible flows, we analogously replace all the differentiation operations in $\mathscr{L}$ with the RBF-FD-based differentiation matrices. In particular, we use $(n, m, q) = (37, 3, 4)$ for interior nodes and $(n, m, q) = (19, 3, 2)$ for nodes near boundaries in the construction of the discrete LNS operator, $\boldsymbol{L}$, as in table 3.1.

For a weighted inner product $\langle \boldsymbol{q}_1, \boldsymbol{q}_2 \rangle = \boldsymbol{q}_2^* \boldsymbol{W} \boldsymbol{q}_1$ that accounts for the non-uniformly distributed nodes, the discrete LST and its adjoint eigenvalue problems take the form of

$$\lambda \boldsymbol{P}\boldsymbol{P}^T \tilde{\boldsymbol{q}} = \boldsymbol{L}\tilde{\boldsymbol{q}}, \tag{5.2a}$$

$$\lambda^+ \boldsymbol{P}\boldsymbol{P}^T \tilde{\boldsymbol{q}}^+ = \boldsymbol{L}^+ \tilde{\boldsymbol{q}}^+, \tag{5.2b}$$

respectively, where

$$\boldsymbol{L}^{+} = \boldsymbol{W}^{-1}\boldsymbol{L}^{H}\boldsymbol{W} \tag{5.3}$$

is the discrete adjoint LNS operator. Here, the restriction matrix for two-dimensional incompressible flows takes the form of $\boldsymbol{P}^{T} = \begin{bmatrix} \boldsymbol{I} & \boldsymbol{0} & \boldsymbol{0} \\ \boldsymbol{0} & \boldsymbol{I} & \boldsymbol{0} \end{bmatrix}$, and $(\cdot)^{H}$ denotes the Hermitian transpose. The eigenvectors of these two generalized eigenvalue problems, $\tilde{\boldsymbol{q}} = [\tilde{\boldsymbol{u}}, \tilde{\boldsymbol{v}}, \tilde{\boldsymbol{p}}]^{T}$ and $\tilde{\boldsymbol{q}}^{+} = [\tilde{\boldsymbol{u}}^{+}, \tilde{\boldsymbol{v}}^{+}, \tilde{\boldsymbol{p}}^{+}]^{T}$, are referred to as the LST and adjoint modes, respectively.

The wavemaker (WM), introduced by Giannetti & Luchini [91], identifies the flow region with the strongest localized feedback, where the dominant instability mechanisms act. Based on the leading LST and adjoint modes, the WM is locally defined as

$$\zeta_{\mathrm{LST}}(x_1, x_2) = \frac{\|\boldsymbol{P}^{T}\tilde{\boldsymbol{q}}^{+}(x_1, x_2)\| \, \|\boldsymbol{P}^{T}\tilde{\boldsymbol{q}}(x_1, x_2)\|}{|\langle \tilde{\boldsymbol{q}}^{+}, \tilde{\boldsymbol{q}} \rangle|}, \tag{5.4}$$

where the norm $\|\cdot\|$ measures the localized energy. Referred to Luchini & Bottaro [158] for a comprehensive review. In addition to quantifying the receptivity, the wavemaker also indicates the non-normality level of the flow field [50]. Initially introduced for base flows, Meliga, Boujo, & Gallaire [175] extended the application of wavemaker as a sensitivity analysis technique for mean flows. We utilize this methodology to gauge the structural sensitivity of the RBF-FD-based global LNS operator, $\boldsymbol{L}$.

5.2 Mesh-free resolvent analysis (RA)

The construction of the global Jacobian, $\boldsymbol{L}$, leads to the direct discretization of the input-output system in equation (2.11), yielding

$$\hat{\boldsymbol{u}} = \boldsymbol{H}(\omega)\hat{\boldsymbol{f}}, \tag{5.5}$$

where

$$\boldsymbol{H}(\omega) = \boldsymbol{P}^T \boldsymbol{C} \left(\mathrm{i}\omega \boldsymbol{P}\boldsymbol{P}^T - \boldsymbol{L}\right)^{-1} \boldsymbol{P}\boldsymbol{B} \tag{5.6}$$

is referred to as the discrete resolvent operator. We further define the modified, or weighted, resolvent operator

$$\boldsymbol{R}(\omega) \equiv \boldsymbol{W}_u^{\frac{1}{2}} \boldsymbol{H}(\omega) \boldsymbol{W}_f^{-\frac{1}{2}} = \hat{\boldsymbol{U}} \boldsymbol{\Sigma} \hat{\boldsymbol{F}}^* \tag{5.7}$$

to account for the energy in the input and output spaces. The optimal responses $\hat{\boldsymbol{U}} = \left[\hat{\boldsymbol{u}}_1, \cdots, \hat{\boldsymbol{u}}_N\right]$ and the corresponding forcings $\hat{\boldsymbol{F}} = \left[\hat{\boldsymbol{f}}_1, \cdots, \hat{\boldsymbol{f}}_N\right]$ are obtained from the SVD of the modified resolvent operator and ranked by the energy gains $\Sigma = \left[\sigma_1, \cdots \sigma_N\right]$. The resulting modes are orthogonal in their respective inner products, that is, $\left\langle \hat{\boldsymbol{u}}_j, \hat{\boldsymbol{u}}_k \right\rangle_u = \left\langle \hat{\boldsymbol{f}}_j, \hat{\boldsymbol{f}}_k \right\rangle_f = \delta_{jk}$. The optimal input and output modes are related through

$$\boldsymbol{R}(\omega) \hat{\boldsymbol{f}}_j = \sigma_j(\omega) \hat{\boldsymbol{u}}_j. \tag{5.8}$$

In practice, the optimal input forcings, $\hat{\boldsymbol{f}}_j$, are determined as the solutions of the eigenvalue problem

$$\boldsymbol{W}_f^{-1} \boldsymbol{H}(\omega)^* \boldsymbol{W}_u \boldsymbol{H}(\omega) \hat{\boldsymbol{f}}_j = \sigma_j^2 \hat{\boldsymbol{f}}_j, \tag{5.9}$$

where $\boldsymbol{W}_f^{-1} \boldsymbol{H}(\omega)^* \boldsymbol{W}_u \boldsymbol{H}(\omega)$ is Hermitian. The matrix inversion of $\left(\mathrm{i}\omega \boldsymbol{P}\boldsymbol{P}^T - \boldsymbol{L}\right)$ is solved using LU-factorization [254].

The RA-based wavemaker,

$$\zeta_{\mathrm{RA}}(x_1, x_2) = \frac{\|\hat{\boldsymbol{u}}_1(x_1, x_2)\| \, \|\hat{\boldsymbol{f}}_1(x_1, x_2)\|}{|\hat{\boldsymbol{u}}_1^* \boldsymbol{W}_u \hat{\boldsymbol{f}}_1|}, \tag{5.10}$$

is defined analogous to equation (5.4). Within the framework of RA, it provides a quantitative measure of the effect of the localized feedback at any given frequency [206, 213, 257, 264].

5.3 Boundary condition treatments

5.3.1 Homogeneous Dirichlet boundary conditions

Homogeneous Dirichlet boundary conditions, $\boldsymbol{q}' = 0$, are widely employed in hydrodynamic stability analysis based on the assumption that perturbation variables either vanish at the solid wall or in the far field. To approximate spatial derivatives for a node near such a boundary, we follow the Kansa method [131] and compute the RBF-FD weights using the local stencil consisting of both the interior nodes, $\{\boldsymbol{x}^{(i)}\}_{j=1}^{n^{(i)}}$, and the boundary nodes, $\{\boldsymbol{x}^{(b)}\}_{j=1}^{n^{(b)}}$. Letting $g(\boldsymbol{x}_j^{(b)}) = 0$, equation (3.4) becomes

$$\mathscr{D}g(\boldsymbol{x}_0) = \sum_{j=1}^{n^{(i)}} w_j^{(i)} g(\boldsymbol{x}_j^{(i)}) + \sum_{j=1}^{n^{(b)}} w_j^{(b)} g(\boldsymbol{x}_j^{(b)}) = \sum_{j=1}^{n^{(i)}} w_j^{(i)} g(\boldsymbol{x}_j^{(i)}), \tag{5.11}$$

and only the weights for the interior nodes will be used in the computation.

5.3.2 Boundary-normal derivatives

Neumann conditions, inflow/outflow conditions, or the enforcement of continuity necessitate the evaluation of boundary-normal derivatives and require special treatment for scattered nodes that are not structured near boundaries. Using ghost nodes requires additional, generally non-physical, conditions for their evaluation. To avoid using ghost nodes and their associated computational overhead and implementation complexity, we propose the use of specialized stencils with boundary-normal alignment. To accurately approximate derivatives in the boundary-normal direction, we propose an elliptical stencil with its major axis perpendicular to the

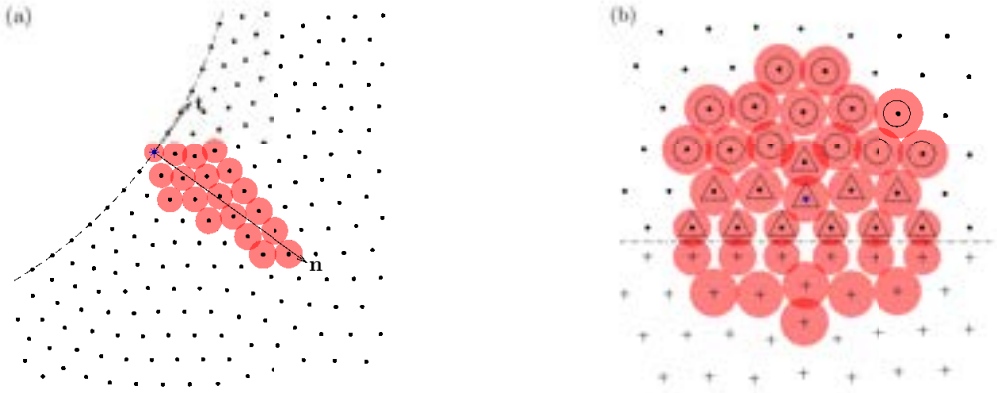

Figure 5.1. RBF stencils (red-shaded circles) for a given node (blue star): (a) boundary-normal derivatives; (b) interior node near the symmetric centerline (dot-dashed). The latter stencil includes the interior nodes ($\{\boldsymbol{x}^{\bullet}\}_{j=1}^{n^{\bullet}}$, dot) and image ghost nodes ($\{\boldsymbol{x}^{+}\}_{j=1}^{n^{+}}$, '+'). The counterparts of the image nodes, $\{\boldsymbol{x}^{\Delta}\}_{j=1}^{n^{+}}$, and the remaining nodes, $\{\boldsymbol{x}_j^{\circ}\}_{j=1}^{n^{\bullet}-n^{+}}$, are shown as triangles and circles, respectively. The area of each red-shaded circle represents the corresponding local radial control volume, $\mathrm{d}V_i$.

boundary. The elliptical form is achieved by utilizing a weighted Euclidean distance metric

$$\tilde{r} = \sqrt{a^2+b^2}\sqrt{\frac{((\boldsymbol{x}-\boldsymbol{x}_0)\cdot\boldsymbol{n})^2}{a^2}+\frac{((\boldsymbol{x}-\boldsymbol{x}_0)\cdot\boldsymbol{t})^2}{b^2}}, \tag{5.12}$$

where $\boldsymbol{n}$ and $\boldsymbol{t}$ are the normal and tangential directions, respectively, and a and b denote the corresponding scaling factors. An eccentricity of $\frac{\sqrt{a^2-b^2}}{a} = \frac{2\sqrt{6}}{5}$ is used in the computation. We use the $q = 2$ polynomial augmentation for the boundary-tangential direction and a higher-order of accuracy of $q = 4$ for the boundary-normal direction. An illustrative example is shown in figure 5.1(a). This new strategy circumvents the need to increase the local stencil near domain boundaries to prevent the Runge phenomenon, as demonstrated in [21, 23]. Without this special treatment, a significantly larger stencil size will be needed to attain stable solutions.

5.3.3 Symmetric and anti-symmetric boundary conditions

Exploiting physical and geometrical symmetries in flow problems leads to drastic computational savings. For example, a problem with simple reflectional symmetry will reduce the

size of the linearized stability and resolvent operators to 25% of that in the full problem. This is particularly important for the direct solutions of eigen- and singular-value problems, for which memory is the bottleneck. For axisymmetric problems, like the jet problem at hand, the saving is even more severe; the problem is reduced, without loss of generality, from 3D to 2D. To address pole singularities that arise in these coordinates and symmetric or anti-symmetric boundary conditions, we propose a generalization of the pole treatment method by Mohseni & Colonius [181] for scattered nodes. We introduce a set of ghost nodes, denoted as $\mathscr{X}^+$, which are symmetric to the interior nodes, $\mathscr{X}^\bullet$, with respect to the centerline. For each interior node, we divide its local stencil into two disjoint sets such that $\{\boldsymbol{x}\}_{j=1}^{n} = \{\boldsymbol{x}_j^\bullet\}_{j=1}^{n^\bullet} \cup \{\boldsymbol{x}_j^+\}_{j=1}^{n^+}$, where $\boldsymbol{x}^\bullet \in \mathscr{X}^\bullet$ and $\boldsymbol{x}^+ \in \mathscr{X}^+$, respectively, and $n = n^\bullet + n^+$. Additionally, we define $\{\boldsymbol{x}_j^\Delta\}_{j=1}^{n^+} \in \{\boldsymbol{x}_j^\bullet\}_{j=1}^{n^\bullet}$ as the counterparts of the image nodes, and $\{\boldsymbol{x}_j^\circ\}_{j=1}^{n^\bullet - n^+} = \{\boldsymbol{x}_j^\bullet\}_{j=1}^{n^\bullet} \setminus \{\boldsymbol{x}_j^\Delta\}_{j=1}^{n^+}$ represents the remaining nodes within the interior nodes, Refer to figure 5.1(b) for detailed symbol explanations. The function values at the image nodes are determined by their corresponding counterparts, given by

$$g(\boldsymbol{x}_j^+) = \eta g(\boldsymbol{x}_j^\Delta), \tag{5.13}$$

where η depends on the type of boundary conditions being imposed. Specifically, we use $\eta = 1$ for symmetric boundary conditions and $\eta = -1$ for anti-symmetric boundary conditions. The RBF-FD weights in equation (3.4) can be written as

$$\mathscr{D}g(\boldsymbol{x}_0) = \sum_{j=1}^{n^\bullet} w_j^\bullet g(\boldsymbol{x}_j^\bullet) + \sum_{j=1}^{n^+} w_j^+ g(\boldsymbol{x}_j^+) = \sum_{j=1}^{n^\bullet - n^+} w_j^\circ g(\boldsymbol{x}_j^\circ) + \sum_{j=1}^{n^+} \left(\eta w_j^+ + w_j^\Delta\right) g(\boldsymbol{x}_j^\Delta). \tag{5.14}$$

This treatment allows us to approximate derivatives solely based on the function values at the interior nodes, effectively handling pole singularities and addressing the challenges associated with scattered nodes.

Table 5.1. Overview of datasets and analyses. The columns from left to right indicate the flow description, Reynolds number, Mach number, flow type, base state, analysis type, and section number. The zero-pressure-gradient (ZPG) Blasius solution is used for analyzing the boundary layer. Analyses include linear stability (LST) and resolvent analyses (RA), along with wavemaker (WM).

Flow	Re	M	Flow type	Base state	Analysis	Sec.
Cylinder wake (§4)	$47-180$	-	2D laminar	$\overline{u},\overline{v}$	LST/RA/WM	§5.4.1
Boundary layer (ZPG)	6×10^5	-	2D laminar	$u_{\mathrm{ZPG}},v_{\mathrm{ZPG}}$	RA/WM	§5.4.2
Jet [33]	$\approx10^6$	0.9	3D turbulent	$\overline{\rho},\overline{u}_x,\overline{u}_r,\overline{u}_\theta,\overline{T}$	RA/WM	§5.4.3

5.4 Applications

We demonstrate the mesh-free RBF-FD-based hydrodynamic stability framework outlined in §5.1 and §5.2 using three representative examples: canonical steady and unsteady cylinder wakes, a self-similar non-parallel steady laminar boundary-layer flow, and the turbulent mean of a transonic jet, as summarized in table 5.1. These three examples are benchmark problems for open flows and are appropriate for validating mesh-free hydrodynamic stability. Same as in §4, we employ `DistMesh` [199] to efficiently generate scattered nodes with localized refinement in regions of interest. We highlight that the local connection information is not used in the computation.

5.4.1 Cylinder wake

We first consider the incompressible cylinder flow at diameter-based Reynolds numbers, $\mathrm{Re}=\frac{U_\infty D}{\nu}$, ranging from 47 to 180 and investigate the mean-flow stability within the two-dimensional laminar regime. The occurrence of the periodic von Kármán vortex shedding in the cylinder wake beyond the critical Reynolds number of $\mathrm{Re_c}\simeq47$ is a well-known phenomenon, owing to a Hopf bifurcation that results in flow instability, see, e.g., [24, 287]. Beyond the limit of $\mathrm{Re}\simeq188$, the cylinder flow becomes three-dimensional [16, 297].

Classical LST analysis of the cylinder base flow ought to predict the onset of unsteadiness [114, 306] but fails to capture the vortex-shedding frequency beyond Re_c [15, 253]. Previous

studies by Hammond & Redekopp [97] and Pier [203] show that LST analysis around the cylinder mean flow accurately identifies the vortex-shedding frequency compared to experimental measurements. Barkley [15] supported these findings and showed that the cylinder mean flow is marginally stable in the 2D regime. Sipp & Lebedev [253] subsequently provided theoretical underpinning by conducting a weakly nonlinear analysis and establishing criteria for utilizing mean flows in LST analysis. The vortex-shedding dynamics beyond the critical Reynolds number were later investigated using a self-consistent model [166, 167] and RA [120, 264] based on the mean flow stability. We here conduct both LST and resolvent analyses of the cylinder wake mean flow.

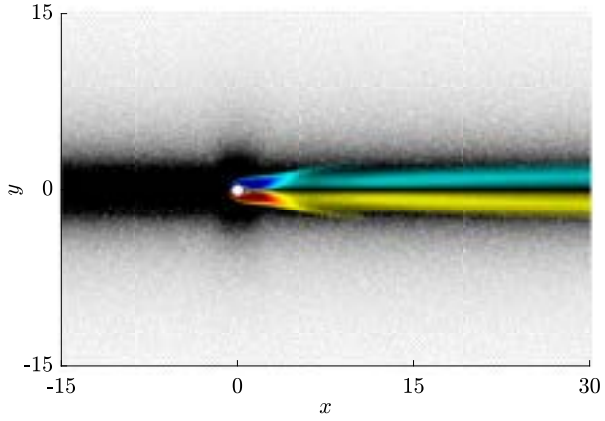

Figure 5.2. Computational grid for cylinder flows with $N = 118225$ nodes, colored using the mean vorticity, $\overline{\boldsymbol{\omega}} = \boldsymbol{D}_x\overline{\boldsymbol{v}} - \boldsymbol{D}_y\overline{\boldsymbol{u}}$, at $\mathrm{Re} = 100$.

We define the the computational domain Ω as the exterior of the cylinder $r \geq D/2 = 0.5$ and within the rectangle $-15 \leq x \leq 30$, $-15 \leq y \leq 15$. The computational domain is discretized using $N = 118225$ scattered nodes. Local grid refinement is employed near the cylinder with a characteristic distance of $\Delta r = 0.03$ and around the wake centerline with $\Delta r = 0.04$ to better resolve the flow structures. The unsteady cylinder flow is simulated using the PHS+poly RBF-FD version of the fractional-step, staggered-grid incompressible Navier-Stokes solver previously described in §4. The mean-flow profiles are obtained as the time average of flow over 20 vortex-shedding cycles. Figure 5.2 shows the mean vorticity at $\mathrm{Re} = 100$ and the computational

grid. Homogeneous boundary conditions, $u' = v' = 0$, are prescribed at the inlet and the cylinder surface. Symmetric boundary conditions with $v' = \partial u'/\partial y = 0$ are applied at the transverse boundaries. A stress-free outflow condition, $-p'\boldsymbol{n} + \frac{1}{\mathrm{Re}}\nabla \boldsymbol{u}' \cdot \boldsymbol{n} = 0$, where $\boldsymbol{n} = [1,0]^T$ is the outflow direction, is enforced at the outflow.

The local wavemaker sensitivity in equation (5.4) and the resolvent gain in equation (2.12) and are both quantified in terms of the perturbed kinetic energy. To this end, we define the integration matrices

$$\boldsymbol{W}_u = \boldsymbol{W}_f \equiv \begin{bmatrix} \mathbf{1} & \mathbf{0} \\ \mathbf{0} & \mathbf{1} \end{bmatrix} \otimes \mathrm{diag}(\mathrm{d}V_1, \mathrm{d}V_2, \cdots, \mathrm{d}V_N) \tag{5.15}$$

in equation (2.13) to approximate the integral within the computational domain, where $\otimes$ denotes the Kronecker product. Here, $\mathrm{d}V_i = \xi\pi(\Delta r_i)^2$ is the local radial control volume for each grid. The constant ξ ensures consistency with the total control volume and is defined by letting $\sum_{i=1}^{N} \mathrm{d}V_i = \xi\pi\sum_{i=1}^{N}(\Delta r_i)^2 = \int_\Omega 1\mathrm{d}\boldsymbol{x}$. Refer to figure 5.1 for practical illustrations.

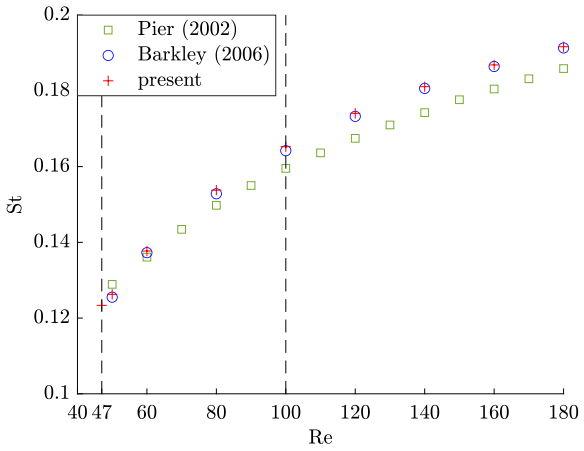

Figure 5.3. Vortex shedding frequency predicted by the leading eigenvalue of the mean-flow stability problem as a function of Reynolds number. The frequency is given as the non-dimensional Strouhal number $\mathrm{St} = \lambda_i/2\pi$. Shown for comparison are results from Pier [203] (green square) and Barkley [15] (blue circle). Two representative Reynolds numbers for the following analysis, $\mathrm{Re}_c \approx 47$ and $\mathrm{Re} = 100$, are highlighted as dashed lines.

Figure 5.3 shows the Strouhal number, $\mathrm{St} = \lambda_i/2\pi$, associated with the leading eigenval-

ues at varying Reynolds numbers. Starting from the critical Reynolds number of $\mathrm{Re}_c \approx 47$, the frequency-Reynolds number dependence exhibits the typical features of a Hopf bifurcation. Our results are in good agreement with Barkley [15], and similarly, deviate no more than 3% from those rep (see also figure 5.4

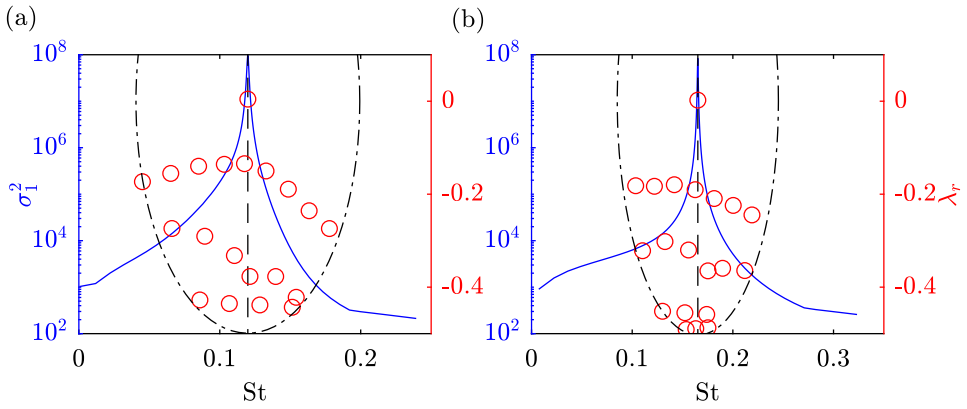

Figure 5.4. Resolvent singular values (blue curve) and stability eigenvalue (red circle) spectra for $\mathrm{Re} = 47$ (a) and $\mathrm{Re} = 100$ (b). The 20 eigenvalues closest to $\lambda_c = 0 + 0.753\mathrm{i}$ or $\mathrm{St}_c = 0.1199$ and $\lambda = 0 + 1.038\mathrm{i}$ or $\mathrm{St} = 0.1652$ (dashed lines) were found within the regions outlined by the black dot-dashed lines using the shift-and-invert Arnoldi algorithm for $\mathrm{Re} = 47$ and 100, respectively.

We next conduct a comparative study of LST and RA at two representative Reynolds numbers, the critical Reynolds number of $\mathrm{Re} = 47$ and $\mathrm{Re} = 100$, as an example of the unsteady regime. Figure 5.4 shows the resulting resolvent singular value and stability eigenvalue spectra. At $\mathrm{Re} = \mathrm{Re}_c$, both the peak of the resolvent gain and the leading eigenvalue identify the same frequency, $\mathrm{St}_c = 0.1199$, as the vortex shedding frequency. This value is in good agreement with the results of the LST analysis around the base flow, see, e.g., Giannetti & Luchini [91] ($\mathrm{St}_c \simeq 0.118$ for $\mathrm{Re}_c \simeq 46.7$), Marquet, Sipp, & Jacquin [169] ($\mathrm{St}_c \simeq 0.116$ for $\mathrm{Re}_c \simeq 46.8$), and Sipp & Lebedev [253] ($\mathrm{St}_c \simeq 0.118$ for $\mathrm{Re}_c \simeq 46.6$). Similarly, the resolvent singular value spectrum at $\mathrm{Re} = 100$ in panel 5.4(b) displays a clear peak at the vortex shedding frequency, which is now at $\mathrm{St} = 0.1652$, and again coinciding with the least stable LST eigenvalue. This result matches closely with the findings of earlier Strouhal-Reynolds number relationship [71,

119, 166, 204, 207] and RA [120, 264] studies.

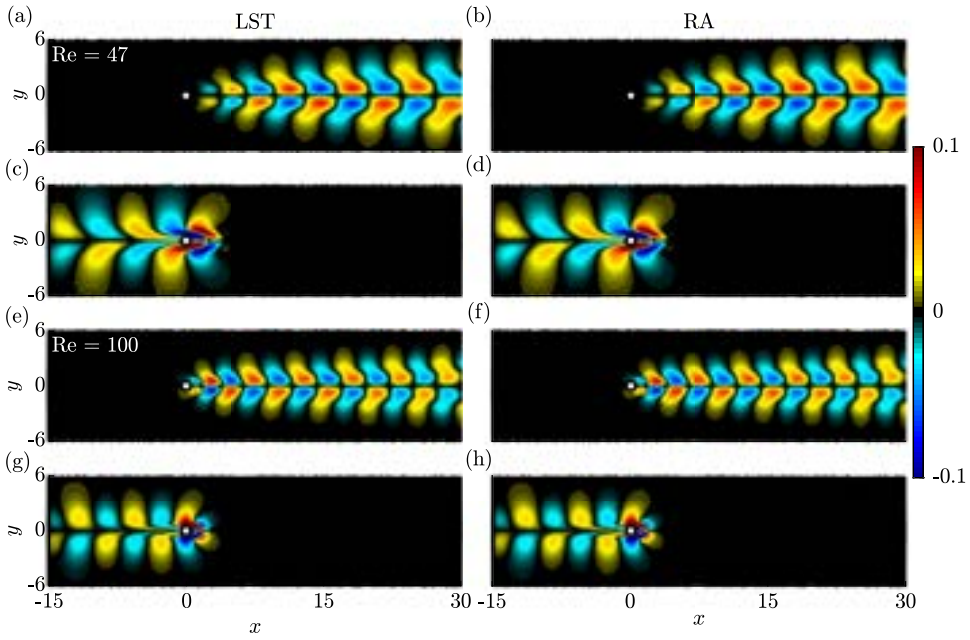

Figure 5.5. Leading modes for $\mathrm{Re} = 47$ at $\mathrm{St} = 0.1199$ (a-d) and $\mathrm{Re} = 100$ at $\mathrm{St} = 0.1652$ (e-h): (a,e) LST modes; (b,f) response modes; (c,g) adjoint modes; (d,h) forcing modes.

Figure 5.5 shows the leading LST and RA modes for the cylinder mean flow at $\mathrm{Re} = \mathrm{Re}_c$ and $\mathrm{Re} = 100$. The leading LST and optimal response modes, along with their corresponding adjoint and forcing modes, are near-identical at both Reynolds numbers. The resemblance observed between the LST and resolvent response modes is to be anticipated, as the singular value of the resolvent attains its peak at the vortex-shedding frequency [25, 264], thus exhibiting the characteristic vortex-shedding structure. This implies that the optimal forcing leverages the global instability mode to achieve maximum gain. Differing from the optimal response and LST modes, the optimal forcing and adjoint modes are active far upstream of the cylinder but peak downstream in close vicinity to the cylinder. This hallmark of convective instability was similarly observed in previous works [120, 169, 264].

We finally investigate the wavemaker ζ_{LST}, defined in equation (5.4), in figure 5.6 to quantify the sensitivity of spatially localized feedback. Wavemakers obtained from LST and RA look similar for both Reynolds numbers and reach their maxima in two symmetrically positioned

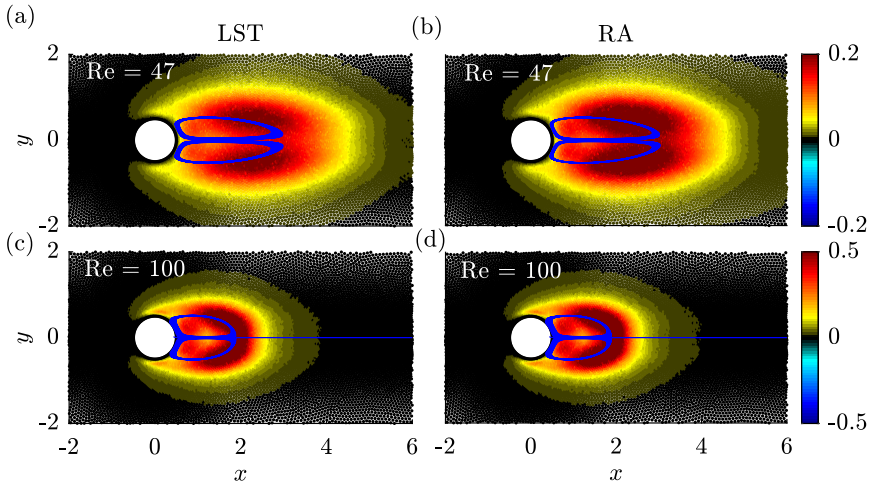

Figure 5.6. Wavemakers ζ_{LST} for mean flow at (a) $\mathrm{Re} = 47$ and (c) $\mathrm{Re} = 100$. Respective results for ζ_{RA} are shown in (b) and (d). The blue curve represents the mean flow streamlines.

lobes located across the separation bubble. This result signifies the promising applicability of RA-based wavemakers in accurately identifying the region where the flow instability mechanisms happen. The wavemaker patterns at the critical Reynolds number shown in panels 5.6 (a,c) compare well to those previously reported by Giannetti & Luchini [91] and Marquet, Sipp, & Jacquin [169]. The shrinking of wavemaker region at $\mathrm{Re} = 100$ in panels 5.6 (b,d) closely matches with the findings in Meliga, Boujo, & Gallaire [175] and Symon *et al.* [264].

5.4.2 Blasius boundary layer

We now examine the incompressible two-dimensional non-normal flat-plate boundary layer, a classic example of convectively unstable flows characterized by the amplification of disturbances during downstream advection. The convective instability of boundary-layer flows has been extensively studied through 1D LST analysis over the past century, e.g., [122, 161, 162, 209, 259]. Above the critical displacement-thickness Reynolds number of $\mathrm{Re}_{\delta,c} \approx 520$, the Tollmien–Schlichting (TS) waves are known to arise as unstable eigenmodes of the Orr-Sommerfeld equation [42]. While these locally unstable waves are damped in 2D LST [1, 4, 11, 65], investigations into the non-normality of the linearized Navier-Stokes equations for open flows have revealed an alternative pathway for disturbance amplification [50, 168, 255].

To analyze the non-modal behavior of boundary-layer flows, input-output analysis has been conducted to determine the optimal harmonic forcing that results in the largest asymptotic response [2, 12, 13, 184, 231, 254].

Following the setup by Sipp & Marquet [254], we compute the resolvent gain in the restricted domain $\Omega_{\mathrm{RA}} = [x, y/\delta] \in [0.02, 1] \times [0, 22.52]$ within the computational domain $\Omega = [x, y/\delta] \in [0.02, 1.27] \times [0, 22.52]$ such that the forcing optimizes the ratio between the restricted kinetic energy, $\iint_{\Omega_{\mathrm{RA}}} \left(|\hat{u}|^2 + |\hat{v}|^2\right) \mathrm{d}x\mathrm{d}y$, and the integral of forcing, $\iint_{\Omega} \left(|\hat{f}_u|^2 + |\hat{f}_v|^2\right) \mathrm{d}x\mathrm{d}y$. The zero-pressure-gradient (ZPG) asymptotic Blasius solution, characterized by a local Reynolds number of $\mathrm{Re}_x = \frac{U_\infty x}{\nu} = 6 \times 10^5$ or $\mathrm{Re}_\delta = \frac{U_\infty \delta(x)}{\nu} = 1332$ at the end of the restricted domain Ω_{RA}, is used as the base flow to investigate the flow instabilities, where $\delta(x) = 1.72\sqrt{x/\mathrm{Re}_x}$ is the displacement thickness. The leading edge ($x < 0.02$) is removed to avoid the singularity of the self-similar solution. Hereafter, we use the notations $\mathrm{Re} = \mathrm{Re}_{x=1}$ and $\delta = \delta(x = 1)$ for simplicity. Conversely, $x = 1$ in figures 5.8, 5.9, and 5.11 corresponds to $\mathrm{Re} = 6 \times 10^5$. All quantities and coordinates presented are dimensionless.

The computational domain Ω is discretized using $N = 726143$ scattered nodes, corresponding to 2.2×10^6 degrees of freedom. In comparison, Sipp & Marquet [254] employ 13.7×10^6 degrees of freedom. The characteristic distances of the grid are $\Delta r = 0.069\delta$ near the flat plate ($y/\delta < 4$), $\Delta r = 0.077\delta$ near the inlet ($x < 0.025$), and average at 0.081δ over the whole domain. At the inlet and the flat plate, we prescribe $u' = v' = 0$. A symmetric boundary condition with $v' = \partial u'/\partial y = 0$ is applied at the far-field ($y/\delta = 22.52$). A stress-free outflow condition is enforced at the outflow. The weight matrix $\boldsymbol{W}_u$ is defined in equation (5.15), but with zero weights in the region $\Omega \setminus \Omega_{\mathrm{RA}}$.

We first examine the leading resolvent singular value as a function of the normalized frequency, $F = 10^6 \cdot \omega/\mathrm{Re}$, in figure 5.7. Overall, our results agree well with those reported by Sipp & Marquet [254]. The slight deviation of the peak and the resolvent gains beyond the peak ($F \gtrsim 88$) are most likely attributed to differences in the base flows, that is, the ZPG self-similar Blasius solution in the present study and the fully non-parallel numerical data of Sipp & Marquet

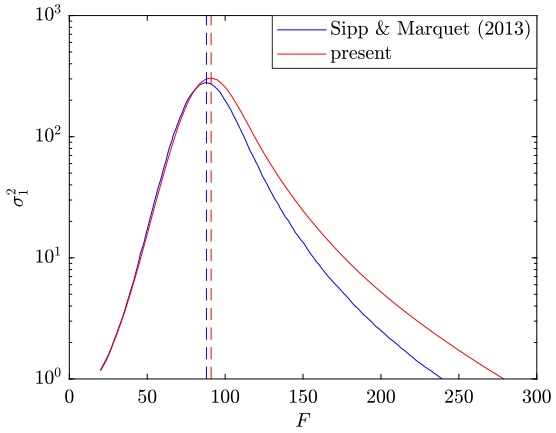

Figure 5.7. Resolvent gains (solid lines) and peak frequencies (dashed lines) for the flat-plate boundary layer and $\mathrm{Re} = 6 \cdot 10^5$.

[254] that includes the leading edge. The discrepancy at higher frequencies is potentially also related to the truncation of the leading edge, where the asymptotic Blasius solution becomes singular.

Figure 5.8 shows the optimal and suboptimal forcings and corresponding responses at $F = 100$. The optimal response exhibits clear Tollmien–Schlichting (TS) wavepackets in the downstream region, while the upstream tilted structures in the optimal forcing highlight the active role of the Orr mechanism in extracting energy from the mean shear via the Reynolds stress [42]. The clear spatial separation between leading resolvent forcing and response modes indicates the stream-wise non-normality of the system [50, 169, 255]. The suboptimal forcing and response are similar to the leading modes except for two local maxima. This modulation confirms the orthogonality in their respective inner products. Qualitative comparisons with previous studies by [1, 31, 184, 254] verify the capability of the present framework in identifying the convective instability of the boundary-layer flow.

As a quantitative assessment of the flow structures, we examine the energy density functions,

$$d_f(x) = \int_0^{y_{\max}} \left(|\hat{f}_u|^2 + |\hat{f}_v|^2\right) \mathrm{d}y, \qquad \text{and} \qquad d_u(x) = \int_0^{y_{\max}} \left(|\hat{u}|^2 + |\hat{v}|^2\right) \mathrm{d}y, \tag{5.16}$$

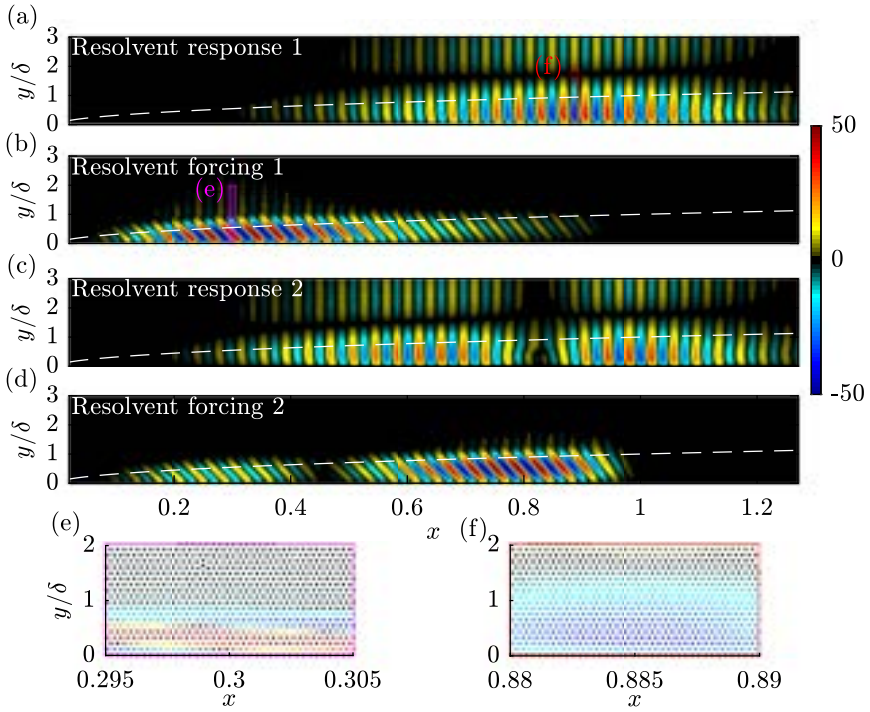

Figure 5.8. Optimal and suboptimal resolvent forcings (b,d) and corresponding responses (a,c) for the flat-plate boundary layer at $F = 10^6 \cdot \omega/\mathrm{Re} = 100$. The normalized stream-wise velocity components have been interpolated onto a stretched Cartesian mesh for visualization. Panels (e) and (f) show the local regions of the optimal forcing (magenta box) and corresponding response modes (red box) with the largest magnitudes, respectively, on the scattered nodes used for the computation. The Blasius displacement thickness, $\delta(x)$, is highlighted as the white dashed line.

in figure 5.9 for the modes shown in figure 5.8. Our results are almost identical to Sipp & Marquet [254] The spatial distribution of the optimal forcing unambiguously identifies the location of the upstream neutral point (branch I) from a local stability analysis at $x = 0.3$ and the corresponding response is localized at $x = 0.89$, which is in close proximity to the downstream neutral point (branch II).

Figure 5.10 shows the energy density distributions of the optimal forcing and response as a function of frequency, with the stream-wise coordinate given in terms of the local Reynolds number, Re_δ. The optimal forcings agree well with Sipp & Marquet [254], and their maxima effectively delineate the convectively stable/unstable boundary (branch I) obtained using local stability theory. The Orr and TS mechanisms coexist and compete while both contribute to the overall energy gain of RA. As frequency increases, the spatial support of the TS-like optimal

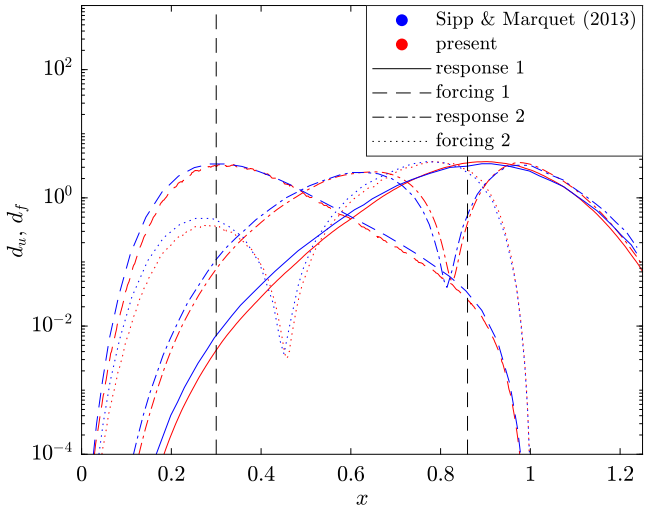

Figure 5.9. Spatial distributions of energy density for optimal (dashed) and suboptimal (dotted) forcings and corresponding responses (solid and dot-dashed, respectively) at $F = 100$. The results (red) are compared to those reported by Sipp & Marquet [254] (blue). The two vertical solid li ıl point (branch

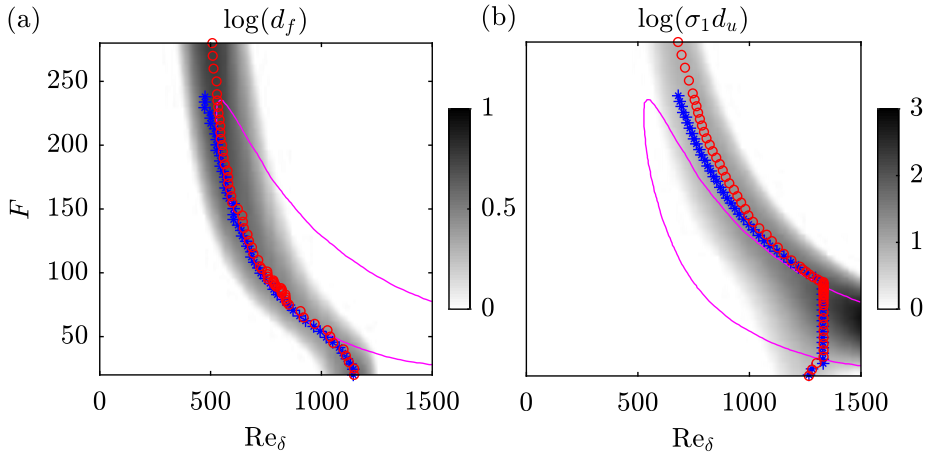

Figure 5.10. Energy density distributions for the optimal forcings (a) and responses (b) as a function of frequency. The locations of maximum energy densities are marked as red circles. The results reported by Sipp & Marquet [254] are shown as blue stars for comparison. The neutral curve obtained from a local LST analysis is shown as the magenta line.

responses decreases, suggesting that the TS mechanism is only supported in a limited region of the shear layer at high frequencies. Additionally, the energy density of the forcing shows

an increasing trend, indicating that the Orr mechanism becomes dominant at high frequencies. Similar to the deviation in the resolvent gain spectra shown in figure 5.7, we observe a slight downstream shift in the peak of optimal responses compared to the results reported by Sipp & Marquet [254] for increasing frequency ($F \gtrsim 130$).

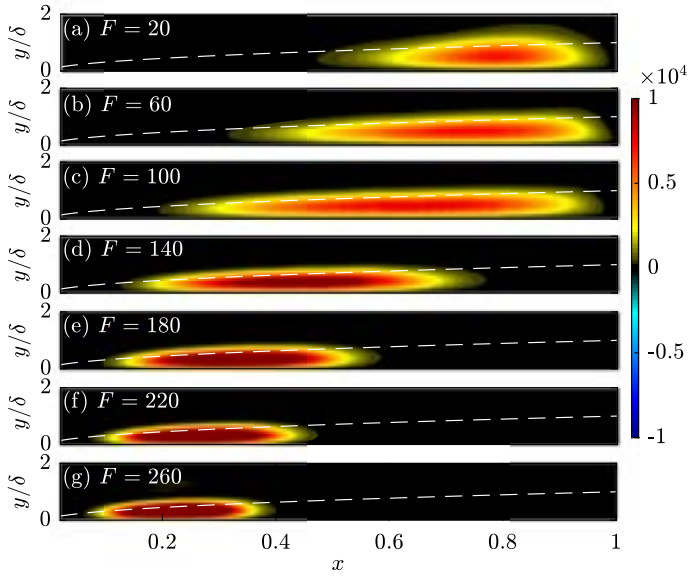

Figure 5.11. RA-based wavemaker ζ_{RA} for the flat-plate boundary layer as a function of frequency.

Finally, we show the RA-based wavemaker, defined in equation (5.10), in figure 5.11 to examine the instability mechanisms at different frequencies. The maximum magnitude of ζ_{RA} shows an increasing trend with frequency. The large magnitudes of the wavemaker are attributed to the fact that the value of the term $|\hat{\boldsymbol{u}}_1^* \boldsymbol{W}_u \hat{\boldsymbol{f}}_1|^{-1}$ is considerably greater than the value of the self-adjoint modes, which is equal to 1 [168]. This again confirms that the boundary-layer flow exhibits high non-normality. For $F \lesssim 100$ (panels 5.11 (a-c)), the RA-based wavemaker exhibits an elongated shape and is artificially restricted within the optimization domain Ω_{RA}. The wavemaker becomes more concentrated towards the upstream region for higher frequencies ($F \gtrsim 140$, panels 5.11 (d-g)). This observation suggests a transition from the TS-dominated to the Orr-dominated mechanism as the frequency increases.

5.4.3 Turbulent jet

The above two examples demonstrate the capability of the proposed numerical framework for analyzing incompressible flows within the laminar regime. We now focus on the mean flow analysis of the turbulent iso-thermal jet previously described in §2.3.4. Previous studies have demonstrated that the transonic turbulent jet under consideration displays a variety of coherent features, including the well-known Kelvin–Helmholtz instabilities of the shear layer [33], downstream non-modal Orr-type waves [202, 237], and trapped acoustic waves in the potential core [236, 273].

Owing to the rotational symmetry of the jet, we may decouple the governing equations and construct the compressible linear operator $\mathscr{L}$ in cylindrical coordinates, without loss of generality, for each azimuthal wavenumber m_θ independently. Upon linearization of the compressible Navier-St or around the azimu e general setup, inc umber of $\mathrm{Re} = 3 \times$

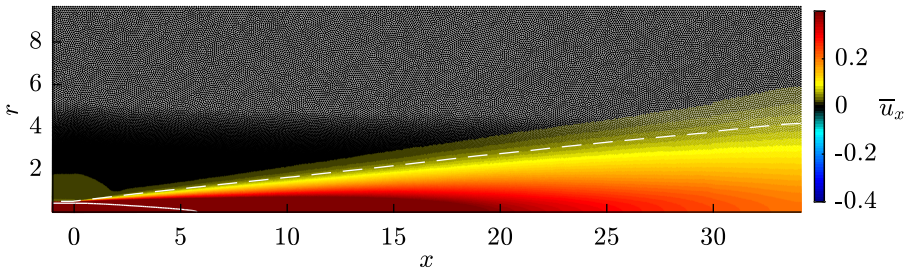

Figure 5.12. Computational grid for jet with $N = 210817 \approx 1013 \times 208$ nodes, colored using the mean streamwise velocity $\overline{u}_x$ at $\mathrm{Re} \approx 10^6$. The potential core (white solid) and the jet width (white dashed) are delineated as isolines corresponding to 99% and 5% of the jet velocity, respectively

The computational domain $\Omega = [-1, 31.01] \times [0, 9.65]$ includes the physical domain $x, r \in [0, 30] \times [0, 6]$ and the surrounding sponge regions that prevent waves from being reflected. Local refinement is used near the nozzle with $\Delta r = 0.005$ and near the jet centerline with

$\Delta r = 0.008$, resulting in $N = 210817$ scattered nodes for the construction of the RBF-FD-based global Jacobian $\boldsymbol{L}$, see figure 5.12. A structured mesh with a comparable number of $N = 185250$ was used in Schmidt *et al.* [237].

The resolvent gain is quantified in terms of the compressible energy norm defined in equation (2.27) through the weight matrices

$$\boldsymbol{W}_q = \boldsymbol{W}_f \equiv \mathrm{diag}\left(\frac{\overline{T}}{\gamma\overline{\rho}M^2}, \overline{\rho}, \overline{\rho}, \overline{\rho}, \frac{\overline{\rho}}{\gamma(\gamma-1)\overline{T}M^2}\right) \otimes \mathrm{diag}(2\pi r_1 \mathrm{d}V_1, 2\pi r_2 \mathrm{d}V_2, \cdots, 2\pi r_N \mathrm{d}V_N). \tag{5.17}$$

For compressible flows, the discrete weighted resolvent operator takes the form of

$$\boldsymbol{R}(\omega) = \boldsymbol{W}_q^{\frac{1}{2}} \boldsymbol{C} (\mathrm{i}\omega \boldsymbol{I} - \boldsymbol{L})^{-1} \boldsymbol{B} \boldsymbol{W}_f^{-\frac{1}{2}}, \tag{5.18}$$

where the input and output matrices, $\boldsymbol{B}$ and $\boldsymbol{C}$, are used to are used to focus the analysis exclusively on the physical domain. As a first demonstration, we conduct the mesh-free RA for the symmetric component of the jet with $m_\theta = 0$ in the following.

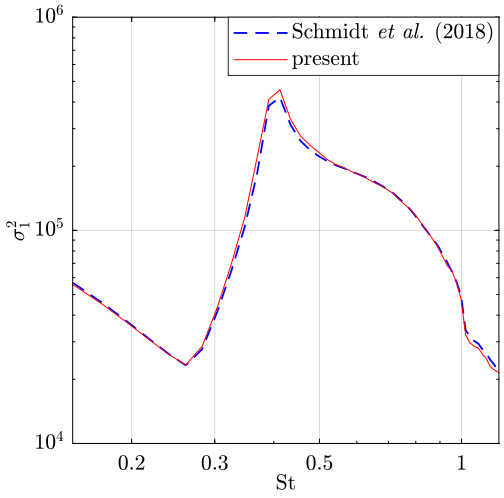

Figure 5.13. Leading resolvent singular value spectra for the transonic jet and $m_\theta = 0$. Results reported by [237] are shown as comparisons (blue dashed).

Figure 5.13 compares the leading resolvent singular value spectra to those reported by

Schmidt *et al.* [237], obtained using a 4th-order finite difference [172] and a tenth-order filter for discretization. Very good agreement is observed within the frequency range $0.15 \lesssim \mathrm{St} \lesssim 1.2$, with only a minor deviation at the peak value. This specific frequency range has been previously identified as the regime where different physical mechanisms are active in turbulent jets, see, e.g., [88, 201, 236, 237, 262, 270, 273].

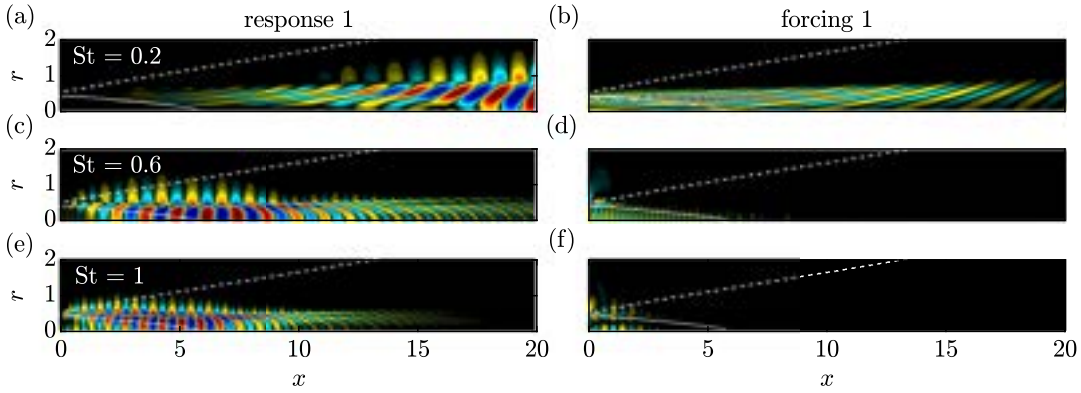

Figure 5.14. Streamwise velocity component of the optimal response (a,c,e) and corresponding forcing modes (b,d,f) at three representative frequencies: (a-b) $\mathrm{St} = 0.2$; (c-d) $\mathrm{St} = 0.6$; (e-f) $\mathrm{St} = 1$. The modes are interpolated onto a stretched Cartesian mesh with contours corresponding to $\pm 0.6 \| \cdot \|_\infty$ for visualization. The potential core and the jet width, shown in figure 5.12, are visualized for comparisons.

To verify that large-scale coherent structures in the turbulent jet are accurately captured, we investigate the leading resolvent modes at three representative frequencies, as shown in figure 5.14. At $\mathrm{St} = 0.2$, the optimal response exhibits a clear downstream ($x \gtrsim 10$) Orr-type wavepacket. The elongated structures tilted against the mean shear in the corresponding forcing are a clear indicator of the Orr mechanism associated with the optimal non-modal spatial growth [237, 269, 270]. Similar flow structures have been reported in [88, 154, 202]. For higher frequencies ($\mathrm{St} \gtrsim 0.6$), the optimal response take the form of compact Kelvin–Helmholtz (KH) wavepackets localized upstream in the initial shear layer region of the jet ($x \lesssim 10$), which can be identified as the modal KH-type shear-layer instability of the turbulent mean flow [95, 121, 262]. The corresponding forcing distributions near the lip line ($r \simeq 0.5$) remain indicative of the Orr mechanism, but this time with the KH instability [88, 118, 206, 239, 270]. Within the potential

core, the optimal response exhibits duct modes at St = 0.6 and trapped acoustic waves at St = 1. The presence of the latter is a general feature of resonance mechanisms between propagating waves associated with the isothermal and transonic jet, as previously described in [236, 273]. Notably, comparable patterns can be observed in the corresponding forcings, indicating the nearly self-adjoint nature of the trapped instability mechanism. We confirmed the modal shapes are almost identical to those obtained using the numerical scheme outlined in Schmidt *et al.* [237] (not shov

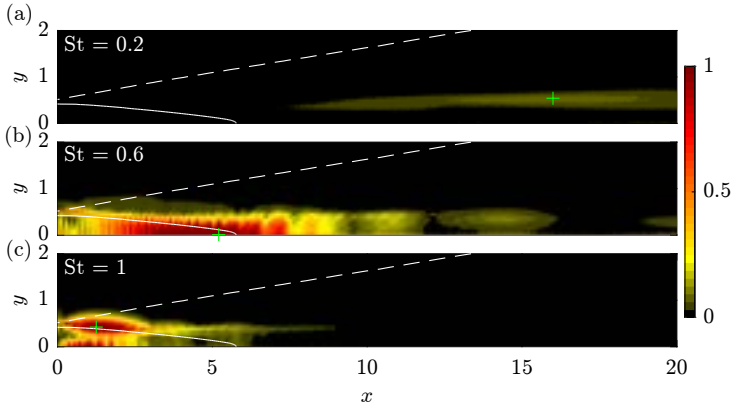

Figure 5.15. RA-based wavemaker ζ_{RA} for: (a) St = 0.2; (b) St = 0.6; (c) St = 1. The region with the strongest feedback is marked as green '+'.

Figure 5.15 shows how the RA-based wavemaker, ζ_{RA}, unveils different physical mechanisms that are active in the turbulent jet. Most notably, the wavemaker region and its overall peak move upstream as the frequency increases from St = 0.2 to 1. At St = 0.2, the optimal forcing and response modes are spatially separated (see panels 5.14(a,b)), resulting in a very weak wavemaker signature in the downstream self-similar region. This result is anticipated, as the responses at low frequencies are purely triggered by the Orr mechanism without being associated with a single global mode or a local feedback mechanism that leads to the creation of waves in a localized region. This is indicative of a non-modal convective instability. At St = 0.6, the wavemaker peaks at the centerline at $x \simeq 5$. This is the end of the potential core, where upstream traveling acoustic modes are generated, also known as duct modes, as previously described by Towne *et al.* [273]. Parallel-flow models accurately predict the occurrence of duct

modes, but the wavemaker potentially reveals the location where duct modes originate, which is not predicted by the theory. The wavemaker at $\mathrm{St} = 1$ peaks within the shear layer, which is associated with the KH instability, but it also exhibits a comparable magnitude at the upstream region of the potential core, which identifies the resonance mechanisms that trigger trapped acoustic modes [236, 273]. That is, the wavemaker analysis confirms the phase-linking between downstream KH waves and upstream traveling waves at $\mathrm{St} = 1$. Note that this is not the case for $\mathrm{St} = 0.6$, where the wavemaker is solely associated with the duct modes.

Chapter 5, in full, has been submitted for publication of the material as it may appear in Journal of Computational Physics 2024, Chu, Tianyi; Schmidt, Oliver T., Elsevier, 2024. The dissertation author was the primary investigator and author of this paper.

Chapter 6

A stochastic SPOD-Galerkin model for broadband turbulent flows

The complex and chaotic dynamics, coupled with a wide range of length and time scales, remain an open challenge for the reduced-order modeling of turbulent flows. Despite the knowledge of the Navier-Stokes equations and accurate high-fidelity methods to solve them, real-time prediction of turbulent flows is out of reach due to their immense computational cost. Reduced-order models (ROMs) have become a prevalent approach in fluid mechanics to reduce complexity by separating temporal dynamics that are governed by simplified equations, such as ordinary differentiation equations (ODEs), from a modal basis of spatial fields, as described in §2. Practical applications of ROMs for turbulent flows include real-time simulations [39, 44, 126], flow control [38, 135, 150, 220, 255, 305], and uncertainty quantification (UQ) [163, 227, 228].

6.1 Galerkin projection-based model order reduction

Among the most successful models in fluid dynamics are POD-Galerkin models that leverage the orthogonality of POD modes to obtain coupled ODEs that govern the temporal evolution of the POD expansion coefficients. Holmes *et al.* [105] and Rowley & Dawson [220] summarized and illustrated this approach. POD-Galerkin models have been successfully applied to model the wall region of incompressible turbulent boundary layers by Aubry *et al.* [8] and later, with a focus on low wave number phenomena of turbulence generation, by Holmes *et al.*

[106]. Noack *et al.* [188] proposed a hierarchy of POD-Galerkin models for viscous cylinder wakes and introduced a shift mode that accounts for the mean field correction. For compressible flows, POD-Galerkin modeling is significantly complicated by the additional energy equation and the occurrence of triple products of the state variables, which may be defined in either primitive or conservative form. It was observed by Rempfer [211] that POD-Galerkin models of general compressible flows exhibit nonphysical instability. There are several previous attempts to overcome these difficulties for moderate Reynolds number flows. In pioneering works by Rowley [217, 218], the authors implemented POD-Galerkin models for compressible cavity flows for control purposes. Later, Rowley *et al.* [219] applied simplified Navier-Stokes equations to obtain a quadratic POD-Galerkin ROM that is valid for isentropic, cold flows at moderate Mach numbers. For linearized compressible flows, Barone *et al.* [17] devised an inner symmetry product that yields stable models. Expanding on this work, Kalashnikova & Barone [127, 128] proposed stability-preserving model reduction techniques for non-linear systems. All of the work discussed so far is based on standard space-only POD modes. Recently, the use of SPOD modes as the modal basis has been explored owing to their statistical optimality and space-time coherence properties. Cong [53] and Towne [272] leveraged the space-time orthogonality of SPOD by implementing the Galerkin projection in the frequency domain. We here propose a predictive ROM that accurately reproduces the second-order flow statistics based on the oblique projection of the linearized Navier-Stokes operator onto SPOD modes.

We recall the Reynolds decomposition of the turbulent flow state,

$$\boldsymbol{q}(t) = \overline{\boldsymbol{q}} + \boldsymbol{q}'(t), \tag{6.1}$$

and discretize the linearized compressible Navier-Stokes equations (2.7) to obtain

$$\frac{\mathrm{d}}{\mathrm{d}t}\boldsymbol{q}' = \boldsymbol{L}\boldsymbol{q}' + \boldsymbol{f}. \tag{6.2}$$

We here consider $\boldsymbol{f}$ to account for the unresolved nonlinear interactions and stochastic fluctuations. This idea is inspired by the operator-based flow models, such as the stochastic structural stability theory (S3T) system by Farrell & Ioannou [68, 69], and the mean-flow based RA [111, 173]. Start from the control theoretical perspective or system identification, similar LTI formulations have also been carried out for turbulent systems, see, e.g., [36, 38, 164, 165, 220, 228].

We choose as the basis of the Galerkin ROM the first M SPOD modes (at all N_f frequencies),

$$\boldsymbol{V} = \left[\underbrace{\begin{array}{ccc} | & & | \\ \psi_{\omega_1}^{(1)} & \cdots & \psi_{\omega_1}^{(M)} \\ | & & | \end{array}}_{\omega_1} \quad \underbrace{\begin{array}{ccc} | & & | \\ \psi_{\omega_2}^{(1)} & \cdots & \psi_{\omega_2}^{(M)} \\ | & & | \end{array}}_{\omega_2} \quad \cdots \quad \underbrace{\begin{array}{ccc} | & & | \\ \psi_{\omega_{N_f}}^{(1)} & \cdots & \psi_{\omega_{N_f}}^{(M)} \\ | & & | \end{array}}_{\omega_{N_f}}\right]. \tag{6.3}$$

Here, $\psi_{\omega_k}^{(i)}$ are the ith SPOD modes of frequency ω_k and energy $\lambda_{\omega_k}^{(i)}$. The jth column of $\boldsymbol{V}$ is the $(j-\lfloor j/M \rfloor M)$th SPOD mode at the frequency $\tilde{\omega}_j = \omega_{\lceil j/M \rceil}$. This rank-$M \times N_f$ (assuming all ψ are linearly independent) SPOD basis contains

$$E_M = \frac{\sum_{i=1}^{M}\sum_{k=1}^{N_f}\lambda_{\omega_k}^{(i)}}{\sum_{i=1}^{N_b}\sum_{k=1}^{N_f}\lambda_{\omega_k}^{(i)}} \cdot 100\% \tag{6.4}$$

of the total energy density. Within the subspace $\mathscr{S}$ spanned by the columns of $\boldsymbol{V}$, the vector $\breve{\boldsymbol{q}}(t)$ that best approximates $\boldsymbol{q}'(t)$ in terms of $\|\cdot\|_E$ is found from the oblique projection

$$\breve{\boldsymbol{q}}(t) = \boldsymbol{P}\boldsymbol{q}'(t), \quad \text{where} \tag{6.5}$$

$$\boldsymbol{P} = \boldsymbol{V}\left(\boldsymbol{V}^*\boldsymbol{W}\boldsymbol{V}\right)^{-1}\boldsymbol{V}^*\boldsymbol{W} \tag{6.6}$$

is the oblique projection matrix for non-singular $\boldsymbol{V}^*\boldsymbol{W}\boldsymbol{V}$. Here, the notation $\breve{(\cdot)}$ represents the quantity that is directly obtained from data without any modeling. Alternatively, we may directly

express $\check{\boldsymbol{q}}(t)$ as a linear combination

$$\check{\boldsymbol{q}}(t) = \sum_{i=1}^{M} \sum_{k=1}^{N_f} a_k^{(i)}(t)\, \psi_{\omega_k}^{(i)} = \boldsymbol{V}\boldsymbol{a}(t) \tag{6.7}$$

of the modes $\psi_{\omega_k}^{(i)}$ by defining

$$\check{\boldsymbol{a}}(t) \equiv (\boldsymbol{V}^*\boldsymbol{W}\boldsymbol{V})^{-1}\boldsymbol{V}^*\boldsymbol{W}\boldsymbol{q}'(t) \tag{6.8}$$

as the vector of temporal expansion coefficients $a_k^{(i)}(t)$. The error vector between the true state and its approximation at any given time is defined as

$$\check{\boldsymbol{e}}(t) \equiv \boldsymbol{q}'(t) - \check{\boldsymbol{q}}(t) = (\boldsymbol{I} - \boldsymbol{P})\,\boldsymbol{q}'(t). \tag{6.9}$$

In the following, we will omit the explicit time dependence of $\boldsymbol{q}'$ and $\boldsymbol{a}$ for brevity.

Different from standard Galerkin ROMs, we next model linear dynamics and use the forcing as the compensation for the linearization under the linear time-invariant (LTI) assumption. First, we obtain the forcing

$$\check{\boldsymbol{f}} = \frac{\mathrm{d}}{\mathrm{d}t}\boldsymbol{q}' - \boldsymbol{L}\boldsymbol{q}' \tag{6.10}$$

as the offset between the linear approximation and the true state. This procedure guarantees that the forcing is consistent with the discretization. The resulting Galerkin ROM of the LTI system

$$\frac{\mathrm{d}}{\mathrm{d}t}\boldsymbol{a} = (\boldsymbol{V}^*\boldsymbol{W}\boldsymbol{V})^{-1}\boldsymbol{V}^*\boldsymbol{W}\left(\boldsymbol{L}\boldsymbol{q}' + \boldsymbol{f}\right) = \boldsymbol{L}_{\mathrm{Gal}}\boldsymbol{a} + \boldsymbol{b} \tag{6.11}$$

governs the evolution of the forced state. Both the state and the forcing are expressed in terms of their expansion coefficients, $\boldsymbol{a}$ and $\boldsymbol{b}$, respectively. In equation (6.11),

$$\boldsymbol{L}_{\mathrm{Gal}} = (\boldsymbol{V}^*\boldsymbol{W}\boldsymbol{V})^{-1}\boldsymbol{V}^*\boldsymbol{W}\boldsymbol{L}\boldsymbol{V} \tag{6.12}$$

is the system dynamics matrix, and

$$\check{\boldsymbol{b}} \equiv (\boldsymbol{V}^*\boldsymbol{W}\boldsymbol{V})^{-1}\boldsymbol{V}^*\boldsymbol{W}\boldsymbol{f} = \frac{\mathrm{d}}{\mathrm{d}t}\check{\boldsymbol{a}} - \boldsymbol{L}_{\mathrm{Gal}}\check{\boldsymbol{a}} \tag{6.13}$$

the vector of expansion coefficients of the forcing field $\boldsymbol{f}$. Equation (6.11) is an m-dimensional first-order differential equation. If a particular trajectory, for example starting from $\boldsymbol{q}'(0)$ is of interest, the corresponding initial condition can be found as $\boldsymbol{a}(0) = (\boldsymbol{V}^*\boldsymbol{W}\boldsymbol{V})^{-1}\boldsymbol{V}^*\boldsymbol{W}\boldsymbol{q}'(0)$. If $\boldsymbol{a}$ is statistically stationary, then

$$\overline{\check{\boldsymbol{b}}} = \frac{\mathrm{d}}{\mathrm{d}t}\overline{\check{\boldsymbol{a}}} - \boldsymbol{L}_{\mathrm{Gal}}\overline{\check{\boldsymbol{a}}} = 0 \tag{6.14}$$

implies that $\boldsymbol{b}$ has zero mean. This property is important in the context of inverse stochastic models, described next.

6.2 Inverse stochastic models

6.2.1 Linear inverse model (LIM)

Inverse stochastic models are data-driven models that do not require knowledge of the linear operator $\boldsymbol{L}_{\mathrm{Gal}}$. Instead, they approximate its action in the training phase of the model via a least squares approximation and model the stochasticity of the original process as additive noise. The simplest version is the linear inverse model (LIM),

$$\frac{\mathrm{d}}{\mathrm{d}t}\boldsymbol{a} = \widetilde{\boldsymbol{T}}\boldsymbol{a} + \boldsymbol{w}, \tag{6.15}$$

proposed by Penland [196, 197]. It assumes a deterministic linear operator that is forced by white noise, $\boldsymbol{w}$. The operator itself is approximated from the data in a least squares sense as

$$\widetilde{\boldsymbol{T}} = \arg\min_{\widetilde{\boldsymbol{T}}} \sum_{j=1}^{N} \left(\left\| \frac{\mathrm{d}}{\mathrm{d}t}\check{\boldsymbol{a}}[j] - \widetilde{\boldsymbol{T}}\check{\boldsymbol{a}}[j] \right\|^2 \right). \tag{6.16}$$

Note that knowledge of $\boldsymbol{L}_{\text{Gal}}$ is not required for this procedure. The underlying assumption of the LIM is that the residue of the linear regression,

$$\check{\boldsymbol{r}} = \frac{\mathrm{d}}{\mathrm{d}t}\check{\boldsymbol{a}} - \widetilde{\boldsymbol{T}}\check{\boldsymbol{a}}, \tag{6.17}$$

can be approximated as white noise. If the governing linear operator $\boldsymbol{L}_{\text{Gal}}$ is known, we may express $\widetilde{\boldsymbol{T}}$ as the sum of two matrices,

$$\widetilde{\boldsymbol{T}} = \boldsymbol{L}_{\text{Gal}} + \boldsymbol{T}. \tag{6.18}$$

Combining equations (6.11), (6.15) and (6.18) yields the relation

$$\boldsymbol{b} = \boldsymbol{T}\boldsymbol{a} + \boldsymbol{w} \tag{6.19}$$

between the forcing coefficients, $\boldsymbol{b}$, and the model coefficients, $\boldsymbol{a}$ in terms of $\boldsymbol{T}$. If the feedback matrix $\boldsymbol{T}$ is known, a random realization of the forcing coefficients can be generated to drive the stochastic model. Observe that realizations of $\boldsymbol{b}$ are generated from white noise forcing. This implies that $\boldsymbol{T}$ accounts for the correlations between the state and forcing.

6.2.2 Linear multi-level regression (MLR) models

The LIM discussed above assumes that the residue in the model's definition, equation (6.17), is white in time. However, there is no guarantee that the white-noise assumption holds for any given nonlinear process. To address this problem, Kondrashov *et al.* [139] and Kravtsov *et al.* [143] introduced the so-called linear multi-level regression (MLR) model. The idea behind the MLR model is to inflate the original model by a hierarchy of additional levels. Each level describes the dynamics of the residue of the previous level and is found by linear regression. Closure of the model is archived once the white-noise assumption holds. Denoting by $\boldsymbol{r}_1$ the first-order residue, i.e., the residue of the original model obtained using equation (6.17), the

first-level model takes the form $\frac{\mathrm{d}}{\mathrm{d}t}\boldsymbol{a} = \widetilde{\boldsymbol{T}}\boldsymbol{a} + \boldsymbol{r}_1$. The second-level system is then obtained by inflating the state vector by the first-order residue, $[\begin{smallmatrix}\boldsymbol{a}\\ \boldsymbol{r}_1\end{smallmatrix}]$, and so on. Assuming that the first $(L-1)$ residues are differentiable, the linear MRL model takes the form

$$\begin{aligned}
\text{Level 1:} \quad & \frac{\mathrm{d}}{\mathrm{d}t}\boldsymbol{a} &&= \widetilde{\boldsymbol{T}}\boldsymbol{a} + \boldsymbol{r}_1, \\
\text{Level 2:} \quad & \frac{\mathrm{d}}{\mathrm{d}t}\boldsymbol{r}_1 &&= \boldsymbol{M}_1 \begin{bmatrix} \boldsymbol{a} \\ \boldsymbol{r}_1 \end{bmatrix} + \boldsymbol{r}_2, \\
& \vdots \\
\text{Level } L\text{:} \quad & \frac{\mathrm{d}}{\mathrm{d}t}\boldsymbol{r}_L &&= \boldsymbol{M}_L \begin{bmatrix} \boldsymbol{a} \\ \boldsymbol{r}_1 \\ \vdots \\ \boldsymbol{r}_L \end{bmatrix} + \boldsymbol{w}.
\end{aligned} \tag{6.20}$$

Here, $\boldsymbol{M}_l$ is the system matrix of size $MN_f \times (l+1)MN_f$, and $\boldsymbol{r}_l$ the l-th level residue. Alternatively, equation (6.20) can be written in the matrix form as

$$\frac{\mathrm{d}}{\mathrm{d}t}\begin{bmatrix} \boldsymbol{a} \\ \boldsymbol{r}_1 \\ \vdots \\ \boldsymbol{r}_{L-1} \\ \boldsymbol{r}_L \end{bmatrix} = \begin{bmatrix} \widetilde{\boldsymbol{T}} & \boldsymbol{I} & \boldsymbol{0} & \cdots & \boldsymbol{0} \\ -\boldsymbol{M}_1- & & \boldsymbol{I} & \ddots & \vdots \\ \ddots & & \ddots & & \boldsymbol{0} \\ \multicolumn{4}{c}{\boldsymbol{M}_{L-1}} & \boldsymbol{I} \\ \multicolumn{4}{c}{\boldsymbol{M}_L} & \end{bmatrix} \begin{bmatrix} \boldsymbol{a} \\ \boldsymbol{r}_1 \\ \vdots \\ \boldsymbol{r}_{L-1} \\ \boldsymbol{r}_L \end{bmatrix} + \begin{bmatrix} \boldsymbol{0} \\ \vdots \\ \vdots \\ \boldsymbol{0} \\ \boldsymbol{w} \end{bmatrix}. \tag{6.21}$$

Equation (6.20) reduces to the classical LIM if $\boldsymbol{r}_1$ is white-in-time to start with.

6.3 The stochastic two-level SPOD-Galerkin model

The underlying idea of the proposed approach is to model a statistically stationary flow as the superposition of large-scale coherent structures that evolve on the mean flow under

the influence of stochasticity. This idea is reflected in the well-known triple-decomposition introduced by Hussain & Reynolds [110]. We choose SPOD modes as the modal basis as they optimally represent the second-order space-time statistics of the stationary flow field. The triple-decomposition further requires the 'background turbulence' to be stochastic in nature. To accomplish this goal, we employ a multi-level linear regression model, as introduced in §6.2.2. In the following, we will demonstrate that the Galerkin-projection approach shown in §6.1 is particularly well-suited for this purpose as it requires only one additional level for closure.

6.3.1 Two-level SPOD-Galerkin model

Using an infinite-dimensional linear operator to describe the nonlinear dynamics is the core concept of Koopman theory. Following this idea, EDMD [295] augments the standard DMD with additional nonlinear observables to obtain a finite-dimensional approximation of the Koopman operator. Following this, we inflate our model with additional levels to incorporate the linear evolution of nonlinear terms with the model. To obtain the most compact representation of the dynamics, it is desirable to truncate the multi-level model, equation (6.20), at the lowest possible level. Our natural starting point is therefore the two-level model

$$\text{Level 1:} \quad \frac{\mathrm{d}}{\mathrm{d}t}\boldsymbol{a} = \boldsymbol{L}_{\mathrm{Gal}}\boldsymbol{a} + \boldsymbol{b}, \tag{6.22}$$

$$\text{Level 2:} \quad \frac{\mathrm{d}}{\mathrm{d}t}\boldsymbol{b} = \boldsymbol{M}\boldsymbol{y} + \boldsymbol{r}, \qquad \text{where} \qquad \boldsymbol{y} \equiv \begin{bmatrix} \boldsymbol{a} \\ \boldsymbol{b} \end{bmatrix}. \tag{6.23}$$

Motivated by the goal of creating a physics-based model that relies on regression for closure only, we deviate from the standard linear inverse modeling approach and retain the physics-based operator $\boldsymbol{L}_{\mathrm{Gal}}$ at first level. Consistent with equation (6.11), the residue at first level is identified as the forcing vector $\boldsymbol{b}$, obtained from equation (6.13). Following the standard linear inverse

modeling paradigm, we seek closure at the second level by solving the least squares problem

$$\boldsymbol{M} = \arg\min_{\boldsymbol{M}} \sum_{j=1}^{N} \left(\left\| \frac{\mathrm{d}}{\mathrm{d}t} \check{\boldsymbol{b}}[j] - \boldsymbol{M} \check{\boldsymbol{y}}[j] \right\|^2 \right) \tag{6.24}$$

to obtain $\boldsymbol{M}$. This least squares problem is formally equivalent to a linear system problem

$$\frac{\mathrm{d}}{\mathrm{d}t} \check{\boldsymbol{B}} = \boldsymbol{M} \check{\boldsymbol{Y}}, \tag{6.25}$$

where $\check{\boldsymbol{Y}} = [\check{\boldsymbol{y}}[j], \check{\boldsymbol{y}}[2], \cdots, \check{\boldsymbol{y}}[N]]$ and $\check{\boldsymbol{B}} = \left[\check{\boldsymbol{b}}[1], \check{\boldsymbol{b}}[2], \cdots, \check{\boldsymbol{b}}[N] \right]$ are the matrices of extended vectors and forcing vectors, respectively. The solution of equation (6.25) is

$$\boldsymbol{M} = \left(\frac{\mathrm{d}}{\mathrm{d}t} \check{\boldsymbol{B}} \right) \check{\boldsymbol{Y}}^{+}, \tag{6.26}$$

where $\check{\boldsymbol{Y}}^{+}$ denotes the pseudo-inverse of the (possibly singular) extended state matrix. Once $\boldsymbol{M}$ is known, we can obtain the second-level residue $\check{\boldsymbol{r}}$ from equation (6.23) as

$$\check{\boldsymbol{r}} = \frac{\mathrm{d}}{\mathrm{d}t} \check{\boldsymbol{b}} - \boldsymbol{M} \check{\boldsymbol{y}}. \tag{6.27}$$

Form equation (6.14), we may deduce that the second-level residue $\check{\boldsymbol{r}}$ has zero mean,

$$\overline{\check{\boldsymbol{r}}} = \overline{\frac{\mathrm{d}}{\mathrm{d}t} \check{\boldsymbol{b}}} - \boldsymbol{M} \overline{\check{\boldsymbol{y}}} = 0.$$

The residue $\check{\boldsymbol{r}}$ will be approximated as white noise that can be correlated in the subspace, described next. Once $\boldsymbol{M}$ and $\boldsymbol{r}$ are determined, the final two-level model is assembled as

$$\frac{\mathrm{d}}{\mathrm{d}t} \boldsymbol{y} = \underbrace{\begin{bmatrix} \boldsymbol{L}_{\mathrm{Gal}} & \boldsymbol{I} \\ -\boldsymbol{M}- & \end{bmatrix}}_{\boldsymbol{L}_{\text{2-lvl}}} \boldsymbol{y} + \begin{bmatrix} \boldsymbol{0} \\ \boldsymbol{r} \end{bmatrix}. \tag{6.28}$$

in the form of equation (6.21). Equation (6.28) is a forced first-order linear time-invariant system for the extended state vector. The final system dynamic matrix $\boldsymbol{L}_{\text{2-lvl}}$ contains both the operator governing the linear evolution of large-scale coherent structures—represented by the basis vectors—about the mean flow, $\boldsymbol{L}_{\text{Gal}}$, and correlation information between the state and the forcing that is learned from the data in $\boldsymbol{M}$. In particular, the left square matrix $\boldsymbol{M}_{ab}$ and the right square matrix $\boldsymbol{M}_{bb}$ that constitute

$$\boldsymbol{M} = \begin{bmatrix} \boldsymbol{M}_{ab} & \boldsymbol{M}_{bb} \end{bmatrix} \tag{6.29}$$

contain correlations between the expansion coefficients and the forcing, and the correlation between the forcing components, respectively. If the residual is computed from the data by means of equation (6.27), the proposed model, equation (6.28), accurately reproduces the original flow field over all times. The remaining task is to find a suitable model for the residue $\check{\boldsymbol{r}}$.

Residue modelling

In particular, we seek a stochastic forcing model $\boldsymbol{r}$ that has the same second-order statistics as the residue $\check{\boldsymbol{r}}$. The autocorrelation function that describes the second-order statistics of the residue $\check{\boldsymbol{r}}$ at zero time-lag is readily obtained from the data as $\boldsymbol{R}_{\boldsymbol{rr}} = \overline{\check{\boldsymbol{r}}\check{\boldsymbol{r}}^*}$. Assuming that the residue $\check{\boldsymbol{r}}$ is normally distributed in time with

$$\check{\boldsymbol{r}}\Delta t \sim \mathcal{N}(0, \boldsymbol{R}_{\boldsymbol{rr}} \cdot (\Delta t)^2), \tag{6.30}$$

we may randomly generate $\boldsymbol{r}$ from Gaussian white noise $\boldsymbol{w} \sim \mathcal{N}(0, \boldsymbol{I})$ as

$$\boldsymbol{r} = \boldsymbol{G}\boldsymbol{w}, \tag{6.31}$$

where $\boldsymbol{G}$ is the unknown input distribution matrix. The role of $\boldsymbol{G}$ in our model is to color randomly generated white noise with the statistics of the residual. *Vice versa*, $\boldsymbol{G}^{-1}$ can be

interpreted as a whitening filter [284]. Gaussian white noise can be generated, by sampling from a Wiener process $\boldsymbol{\xi}$, as

$$\boldsymbol{w} \equiv \frac{\mathrm{d}\boldsymbol{\xi}}{\mathrm{d}t} = \lim_{\Delta t \to 0} \frac{\boldsymbol{\xi}(t+\Delta t) - \boldsymbol{\xi}(t)}{\Delta t}. \tag{6.32}$$

For any time increment Δt, $\Delta\boldsymbol{\xi}$ is normally distributed with zero mean and covariance matrix $\boldsymbol{I}\Delta t$. We may now express equation (6.31) in terms of $\Delta\boldsymbol{\xi}$ as

$$\boldsymbol{r}\Delta t = \boldsymbol{G}\Delta\boldsymbol{\xi}, \tag{6.33}$$

where

$$\boldsymbol{G}\Delta\boldsymbol{\xi} \sim \mathscr{N}(0, \boldsymbol{G}\boldsymbol{G}^*\Delta t) \tag{6.34}$$

follows the properties of the Wiener process. Comparing equations (6.34) and (6.30) allows us to relate the unknown matrix, $\boldsymbol{G}$, to the known covariance matrix of the residue, $\boldsymbol{R}_{\boldsymbol{rr}}$, as

$$\boldsymbol{R}_{\boldsymbol{rr}}\Delta t = \boldsymbol{G}\boldsymbol{G}^*. \tag{6.35}$$

Based on the form of equation (6.35), we obtain $\boldsymbol{G}$ from the Cholesky decomposition of $\boldsymbol{R}_{\boldsymbol{rr}}\Delta t$. Owing to this procedure of computation, $\boldsymbol{G}^{-1}$ may be referred to as a Cholesky whitening filter.

6.3.2 Stochastic two-level SPOD-Galerkin model

Closure of the model is achieved by introducing the stochastic forcing model $\boldsymbol{r}$ into equation (6.28). The resulting stochastic two-level SPOD-Galerkin model takes the form of the

stochastic differential equation

$$\mathrm{d}\boldsymbol{y} = \boldsymbol{L}_{\text{2-lvl}}\boldsymbol{y}\,\mathrm{d}t + \int_t^{t+\mathrm{d}t} \widetilde{\boldsymbol{w}}\,\mathrm{d}t, \text{ where } \quad \widetilde{\boldsymbol{w}} \equiv \begin{bmatrix} \boldsymbol{0} \\ \boldsymbol{G}\boldsymbol{w} \end{bmatrix} \tag{6.36}$$

is the process noise. Equation (6.36) is a stochastic differential equation (SDE) that can be solved numerically by approximating the time derivative using a forward difference as

$$\boldsymbol{y}[j+1] = \boldsymbol{T}\boldsymbol{y}[j] + \Delta\widetilde{\boldsymbol{\xi}}[j], \tag{6.37}$$

where j is the time index, Δt the time step, and

$$\boldsymbol{T} = \boldsymbol{I} + \boldsymbol{L}_{\text{2-lvl}}\Delta t \quad \text{and} \quad \Delta\widetilde{\boldsymbol{\xi}} \equiv \begin{bmatrix} \boldsymbol{0} \\ \boldsymbol{G}\Delta\boldsymbol{\xi} \end{bmatrix} \tag{6.38}$$

are the state transition matrix and the process noise, respectively. By construction, the process noise $\Delta\widetilde{\boldsymbol{\xi}}$ is a zero-mean Gaussian random sequence with covariance matrix

$$\widetilde{\boldsymbol{R}}_{\boldsymbol{rr}} \equiv \overline{\Delta\widetilde{\boldsymbol{\xi}}\Delta\widetilde{\boldsymbol{\xi}}^*} = \begin{bmatrix} \boldsymbol{0} & \boldsymbol{0} \\ \boldsymbol{0} & \boldsymbol{R}_{\boldsymbol{rr}}\Delta t \end{bmatrix}. \tag{6.39}$$

This completes the model. The discrete-in-time algorithm is outlined in the following.

6.3.3 Algorithm: stochastic two-level SPOD-Galerkin

Algorithm Stochastic two-level SPOD-Galerkin model

Input: Fluctuating data matrix $\boldsymbol{Q}' = [\boldsymbol{q}[1] - \overline{\boldsymbol{q}}, \boldsymbol{q}[2] - \overline{\boldsymbol{q}}, \cdots, \boldsymbol{q}[N] - \overline{\boldsymbol{q}}]$ consisting N snapshots, discretized linearized Navier-Stokes operator $\boldsymbol{L}$, time step Δt.

Output: Matrices $\boldsymbol{L}_{\text{2-lvl}}$ and $\boldsymbol{G}$ of the stochastic two-level SPOD-Galerkin model $\frac{\mathrm{d}}{\mathrm{d}t}\boldsymbol{y} = \boldsymbol{L}_{\text{2-lvl}}\boldsymbol{y} +$

$\widetilde{\boldsymbol{w}}$, where $\widetilde{\boldsymbol{w}} = \begin{bmatrix} \boldsymbol{0} \\ \boldsymbol{G}\boldsymbol{w} \end{bmatrix}$.

1. Compute the SPOD of $\boldsymbol{Q}'$ and store the SPOD modes in the column (basis) matrix $\boldsymbol{V}$.

2. Determine the expansion coefficients and the Galerkin system dynamics matrix as

$$\boldsymbol{A} = (\boldsymbol{V}^*\boldsymbol{W}\boldsymbol{V})^{-1}\boldsymbol{V}^*\boldsymbol{W}\boldsymbol{Q}' \quad \text{and} \quad \boldsymbol{L}_{\text{Gal}} = (\boldsymbol{V}^*\boldsymbol{W}\boldsymbol{V})^{-1}\boldsymbol{V}^*\boldsymbol{W}\boldsymbol{L}\boldsymbol{V},$$

   respectively.

3. Following the equation (6.13), calculate the forcing coefficients as

$$\boldsymbol{B} = \frac{\boldsymbol{A}_2^N - \boldsymbol{A}_1^{N-1}}{\Delta t} - \boldsymbol{L}_{\text{Gal}}\boldsymbol{A}_1^{N-1}.$$

   where $\boldsymbol{A}_2^N = [\boldsymbol{a}[2], \boldsymbol{a}[3], \cdots, \boldsymbol{a}[N]]$ and $\boldsymbol{A}_1^{N-1} = [\boldsymbol{a}[1], \boldsymbol{a}[2], \cdots, \boldsymbol{a}[N-1]]$.

4. Let $\boldsymbol{Y} \leftarrow \begin{bmatrix} \boldsymbol{A}_1^{N-1} \\ \boldsymbol{B} \end{bmatrix}$. Solving the linear system problem in the equation (6.26) yields

$$\boldsymbol{M} = \frac{\boldsymbol{B}_2^{N-1} - \boldsymbol{B}_1^{N-2}}{\Delta t}\boldsymbol{Y}^* \left(\boldsymbol{Y}\boldsymbol{Y}^*\right)^{-1}.$$

5. Assemble the matrices to obtain

$$\boldsymbol{L}_{2\text{–lvl}} \leftarrow \begin{bmatrix} \boldsymbol{L}_{\text{Gal}} & \boldsymbol{I} \\ -\boldsymbol{M}- \end{bmatrix}.$$

   .

6. Calculate the linear regression residue as

$$\boldsymbol{R} = \frac{\boldsymbol{B}_2^{N-1} - \boldsymbol{B}_1^{N-2}}{\Delta t} - \boldsymbol{M}\boldsymbol{Y}_1^{N-2}.$$

7. Determine the matrix $\boldsymbol{G}$ by solving the Cholesky decomposition

$$\boldsymbol{G}\boldsymbol{G}^* = \frac{\Delta t}{N-2}\boldsymbol{R}\boldsymbol{R}^*.$$

The resulting stochastic two-level SPOD-Galerkin model is propagated in time as

$$\boldsymbol{y}[j+1] = [\boldsymbol{I} + \boldsymbol{L}_{2\text{-lvl}}\Delta t]\,\boldsymbol{y}[j] + \begin{bmatrix} \boldsymbol{0} \\ \boldsymbol{G}\sqrt{\Delta t}\boldsymbol{w} \end{bmatrix},$$

where j is the time index, see equations (6.36)-(6.38). The zero mean, unit variance Gaussian white noise $\boldsymbol{w}$ which drives the system is obtained from a random number generator.

6.3.4 Uncertainty quantification and spectral analysis

Next, we leverage the resemblance of equation (6.37) to first-order vector autoregression (VAR) processes to conduct an uncertainty quantification analysis of the model. Following Stengel [260], we analyze the propagation of the uncertainty in terms of the expected value of the extended state vector, $\langle \boldsymbol{y}[j] \rangle$, where $\langle \cdot \rangle$ denotes the average over a large number of realizations of $\Delta\widetilde{\boldsymbol{\xi}}[j]$. Since the forcing has zero-mean, the equation

$$\langle \boldsymbol{y}[j] \rangle = \langle \boldsymbol{T}\boldsymbol{y}[j] + \Delta\widetilde{\boldsymbol{\xi}}[j-1] \rangle = \boldsymbol{T}\langle \boldsymbol{y}[j-1] \rangle \tag{6.40}$$

shows that $\boldsymbol{T}$ functions as the propagator of the expected value of the state. If $\boldsymbol{T}$ is stable with $\max\{|\lambda(\boldsymbol{T})|\} < 1$, then the average of $\boldsymbol{y}[j]$ at large time, denoted by $\lim_{j\to\infty}\langle \boldsymbol{y}[j] \rangle$, is zero. Denoting by

$$\boldsymbol{y}'[j] = \boldsymbol{y}[j] - \langle \boldsymbol{y}[j] \rangle \tag{6.41}$$

the fluctuation of the state, we may compute the auto-covariance matrix $\boldsymbol{P}^{(j)}$ of the state as

$$\begin{aligned} \boldsymbol{P}[j] &= \left\langle \boldsymbol{y}'[j]\boldsymbol{y}'^{*}[j] \right\rangle \\ &= \boldsymbol{T}\boldsymbol{P}[j-1]\boldsymbol{T}^{*} + \widetilde{\boldsymbol{R}}_{\boldsymbol{rr}}. \end{aligned} \tag{6.42}$$

Equation (6.42) is the propagation equation for auto-covariance of the state, which is readily obtained by combining equations (6.37), (6.40), and (6.41). Here, we made use of the fact that the fluctuating state is uncorrelated to the process noise, that is, $\langle \boldsymbol{y}'[j-1]\Delta\widetilde{\boldsymbol{\xi}}^{*}[j-1] \rangle = 0$. The reason is that the stochastic component of $\boldsymbol{y}'[j-1]$ is computed from the evaluation of the stochastic process at the previous time instant, $\Delta\widetilde{\boldsymbol{\xi}}^{*}[j-2]$, see equation (6.37).

If the true state $\boldsymbol{y}[1]$ is used as the initial condition, then $\boldsymbol{P}[0] = 0$ from equation 6.42, and it can be shown that the matrix sequence $\{\boldsymbol{P}[j]\}$ converges to the true covariance

$$\boldsymbol{P} = \lim_{j\to\infty} \boldsymbol{P}[j] = \sum_{n=0}^{\infty} \boldsymbol{T}^{n} \widetilde{\boldsymbol{R}}_{\boldsymbol{rr}} \left(\boldsymbol{T}^{*}\right)^{n}, \tag{6.43}$$

which solves the discrete-time Lyapunov equation

$$\boldsymbol{T}\boldsymbol{P}\boldsymbol{T}^{*} - \boldsymbol{P} + \widetilde{\boldsymbol{R}}_{\boldsymbol{rr}} = 0. \tag{6.44}$$

Since $\widetilde{\boldsymbol{R}}_{\boldsymbol{rr}}$ is hermitian and positive-definite by construction, the existence and uniqueness of the solution $\boldsymbol{P}$ are guaranteed by the Lyapunov theorem if $\boldsymbol{T}$ is stable. Since the process noise $\Delta\widetilde{\boldsymbol{\xi}}[j]$ is Gaussian, the distribution of the realizations of the state, $\boldsymbol{y}$, is also Gaussian for the LTI system at hand. Therefore, the 95% confidence interval of $\boldsymbol{y}$ at t_j can be determined as

$$\mathrm{CI} = \left(\langle \boldsymbol{y}[j] \rangle - 2\sqrt{\mathrm{diag}(\boldsymbol{P}_j)},\ \langle \boldsymbol{y}[j] \rangle + 2\sqrt{\mathrm{diag}(\boldsymbol{P}_j)} \right). \tag{6.45}$$

In the limit of large times with $j \to \infty$, this interval converges to the bounded interval $\left(-2\sqrt{\mathrm{diag}(\boldsymbol{P})}, 2\sqrt{\mathrm{diag}(\boldsymbol{P})}\right)$. Under the assumption that the realizations generated by the

discrete SDE, equation (6.37), are weakly stationary with zero mean and covariance matrix $\boldsymbol{P}$, the time-lagged autocorrelation function can be determined analytically as

$$\boldsymbol{R}_{\boldsymbol{yy}}(n) \equiv \langle \boldsymbol{y}[j]\boldsymbol{y}^*[j+n] \rangle = \boldsymbol{P}\,(\boldsymbol{T}^*)^{|n|}\,. \tag{6.46}$$

By way of the Wiener-Khinchin theorem, the analytical expression for the spectral density function

$$\begin{aligned} \boldsymbol{S}_{\boldsymbol{yy}}(\omega) &= \frac{1}{\sqrt{2\pi}} \sum_{n=-\infty}^{\infty} \boldsymbol{R}_{\boldsymbol{yy}}(n) \mathrm{e}^{-\mathrm{i}\omega n} \\ &= \frac{1}{\sqrt{2\pi}} \boldsymbol{P} \left[\left(\boldsymbol{I} - \mathrm{e}^{-\mathrm{i}\omega} \boldsymbol{T}^* \right)^{-1} + \left(\boldsymbol{I} - \mathrm{e}^{\mathrm{i}\omega} \boldsymbol{T}^* \right)^{-1} - \boldsymbol{I} \right]. \end{aligned} \tag{6.47}$$

is found by means of the discrete-time Fourier transform. The diagonal of $\boldsymbol{S}_{\boldsymbol{yy}}(\omega)$ then contains the power spectral density of $\boldsymbol{y}$.

6.4 Example of a turbulent jet

We consider the same turbulent jet previously described in §2.3.4 as an example of a statistically stationary flow. We construct a stochastic two-level SPOD-Galerkin model for the symmetric component of the jet with $m_\theta = 0$. The same spectral parameters in §2.3.4 are used.

6.4.1 Subspace modeling

Figure 6.1 shows the SPOD expansion coefficients, $\check{\boldsymbol{a}}_i(t)$, obtained from the oblique projection defined in equation (6.8) for the three modes shown in figure 2.3(a-c). Results are shown for the rank 1×129 basis, that is, the basis consisting exclusively of the leading SPOD modes (one mode per frequency). Note again that each SPOD mode is, by construction, associated with a single frequency. To confirm that the oblique projection truthfully represents this property, we compute the periodograms (right column) to reveal the frequency content of the expansion coefficients. It is observed that the PSD indeed peaks at the respective SPOD frequencies. This confirms that the SPOD modes in fact predominantly represent the spectral

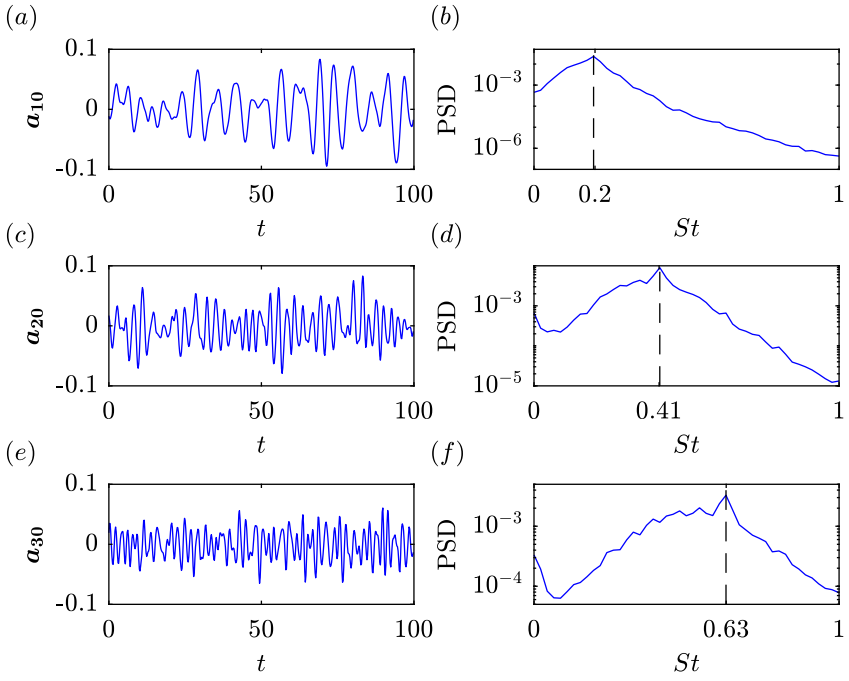

Figure 6.1. SPOD expansion coefficients $\boldsymbol{a}_i(t)$ for the three representative modes shown in figure 2.3(a-c) as part of the rank 1×129 basis: $(a-b)$ $St = 0.2$; $(c-d)$ $St = 0.41$; $(e-f)$ $St = 0.63$. Time trace over 100 time units (left), and PSD (right). The frequency of the SPOD modes are marked by dashed lines in the spectra.

content they optimally account for by construction. Even though the model does technically not depend on this property, we note that this observation can be interpreted as an *a posteriori* justification for the use of the oblique projection introduced in equation (6.8), and therefore also of the use of SPOD modes as a modal basis in the time domain.

Figure 6.2 (a) compares the compressible energy norm, $\|\boldsymbol{q}(\boldsymbol{x},t)\|_E$, of the full LES data, $\check{\boldsymbol{q}}_{\text{full}}$, to the energy of the partial reconstructions for modal bases. It can be observed that all reconstructions follow the dynamics of $\check{\boldsymbol{q}}_{\text{full}}$. The approximately constant offset between the energy of $\check{\boldsymbol{q}}_{\text{full}}$ and the low-rank approximations is similarly reflected in the retained SPOD energy. In particular, $\check{\boldsymbol{q}}_{1\times129}$, $\check{\boldsymbol{q}}_{2\times129}$, $\check{\boldsymbol{q}}_{3\times129}$, $\check{\boldsymbol{q}}_{10\times129}$ account for 13%, 21%, 27%, and 52% of the total energy, respectively. Figure 6.2(b) shows that the offset between the low-rank approximation and the true state is almost constant. This implies that the error stems, almost exclusively, from the energy contained in scales that are not important from a dynamics perspective.

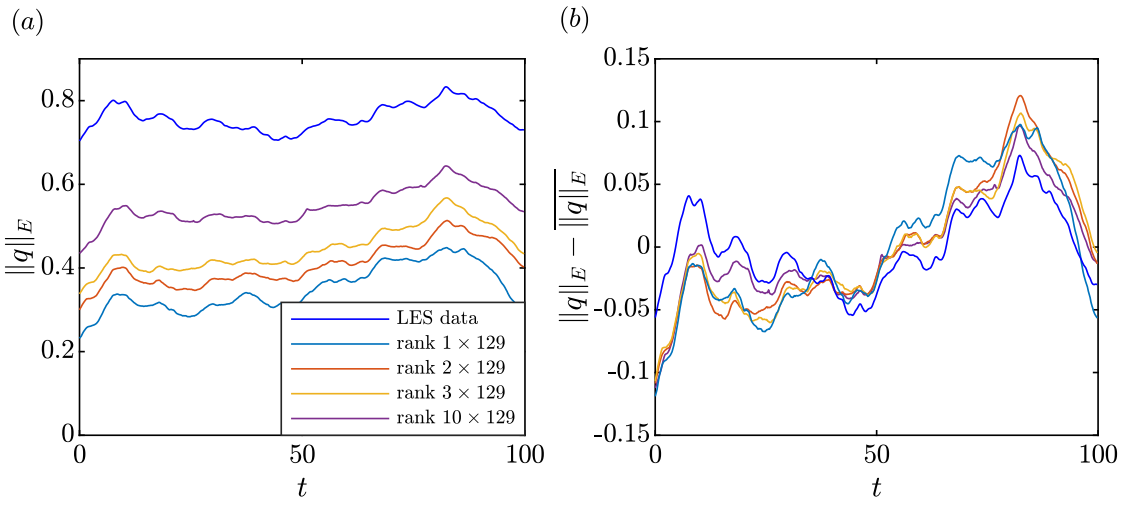

Figure 6.2. Compressible energy norm in (a), and deviation from the mean energy in (b). The LES data and the low-rank approximations with 13%, 21%, 27%, 52% energy are reported. Part (b) emphasises that the dynamics (deviation from the mean) are well captured even by the lowest-rank approximation.

In figure 6.3, the stability of the naive Galerkin ROM of the LTI system, equation (6.12), and the two-level model, equation (6.28), is addressed in terms of the eigenvalue spectra of the corresponding operators, $\boldsymbol{L}_{\text{Gal}}$ and $\boldsymbol{L}_{\text{2-lvl}}$, respectively. The dashed blue line in the spectra corresponds to the disc of radius $\frac{1}{\Delta t}$, centered about $-\frac{1}{\Delta t}$. It demarcates the region of stability; eigenvalues inside the circle are associated with temporal decay, whereas eigenvalues on the outside are associated with exponential amplification. Clearly, the simple Galerkin ROM is unstable, whereas the two-level model is stable. Furthermore, the eigenvalues of the 2-level model are mostly confined to the upper half of the stability region. This behaviour is explained by the symmetry of the SPOD spectrum and the restriction of the modal basis to non-redundant positive frequency content. Figure 6.3(d-f) shows that the eigenvalues of $\boldsymbol{L}_{\text{2-lvl}}$ remain confined to a specific area within the region of stability when the model rank is increased. These results demonstrate that the transition matrices $\boldsymbol{H}$ computed using equation (6.38) are stable, that is, $\max\{|\lambda(\boldsymbol{H})|\} < 1$. Hence, when there is no stochastic input to the SDE, equation (6.37), the extended state vector $\boldsymbol{y}$ vanishes as $t \to \infty$ as its expected value is zero. In accordance with the

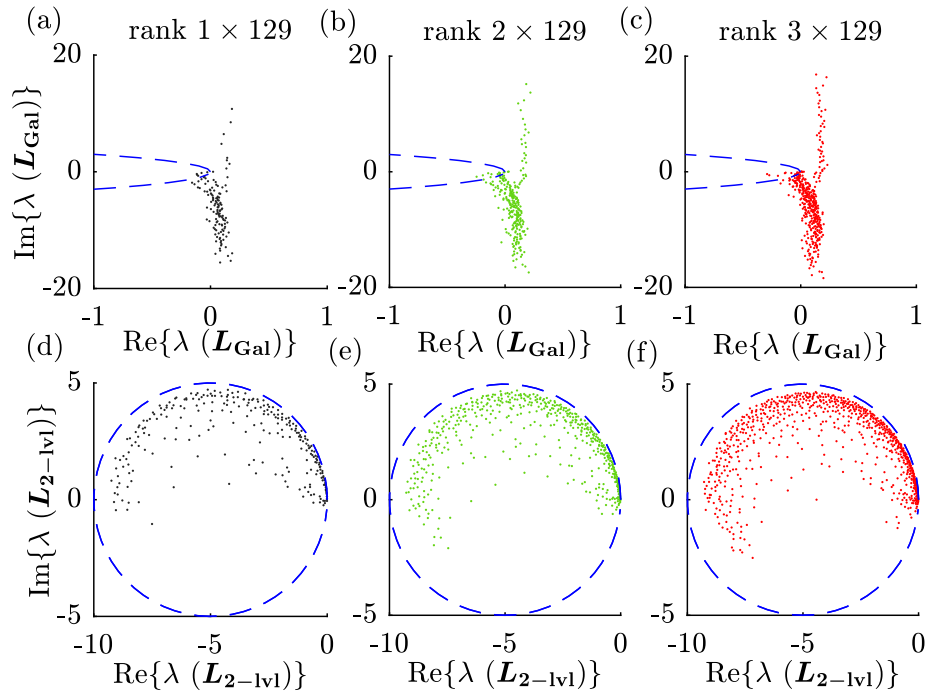

Figure 6.3. Eigenvalues of the standard SPOD-Galerkin ROM, $\lambda(\boldsymbol{L}_{\text{Gal}})$, and the proposed two-level model, $\lambda(\boldsymbol{L}_{2\text{-lvl}})$: (a,d) rank 1×129 (black); (b,e) 2×129 (green); (c,f) 3×129 (red). The blue dashed circle represents the stability region. The eigenvalues outside of the unit disc in (a-c) indicate that Galerkin projection yields an unstable model. On the contrary, the two-level model in (d-f) is stable.

modeling philosophy, appropriate forcing input is necessary to sustain the turbulent flow.

As the turbulence closure relies on linear regression, it has to be shown that $\boldsymbol{L}_{2\text{-lvl}}$ converges as more data is used for its construction. Consider the sequence of matrices, $\{\boldsymbol{L}_{2\text{-lvl}}^{(n)}\}$, where n is the number of snapshots used in the linear regression, equation (6.25). We define a normalized norm of these the matrix sequence, $\|\cdot\|_D$, as

$$\|\boldsymbol{L}_{2\text{-lvl}}\|_D \equiv \frac{\|\boldsymbol{L}_{2\text{-lvl}}^{(n)} - \boldsymbol{L}_{2\text{-lvl}}^{(N)}\|_F}{\|\boldsymbol{L}_{2\text{-lvl}}^{(N)}\|_F}, \tag{6.48}$$

where $\|\cdot\|_F$ denotes the Frobenius norm, and N is the total number of available snapshots. The norm $\|\cdot\|_D$ measures the normalized distance between the matrices constructed with n and N snapshots. The convergence of $\boldsymbol{L}_{2\text{-lvl}}$ as more and more data is added is apparent from figure 6.4.

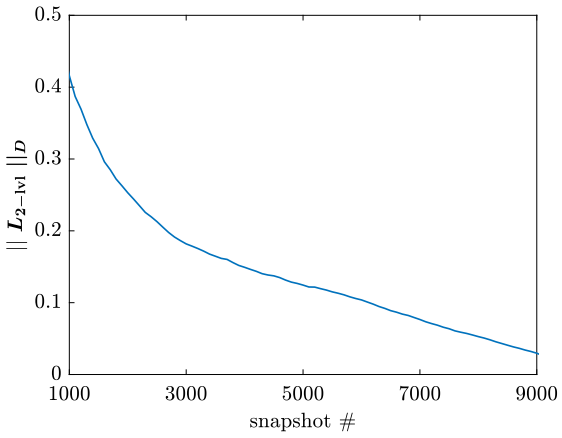

Figure 6.4. Convergence of the matrix sequence $\{\boldsymbol{L}_{\text{2-lvl}}^{(n)}\}$.

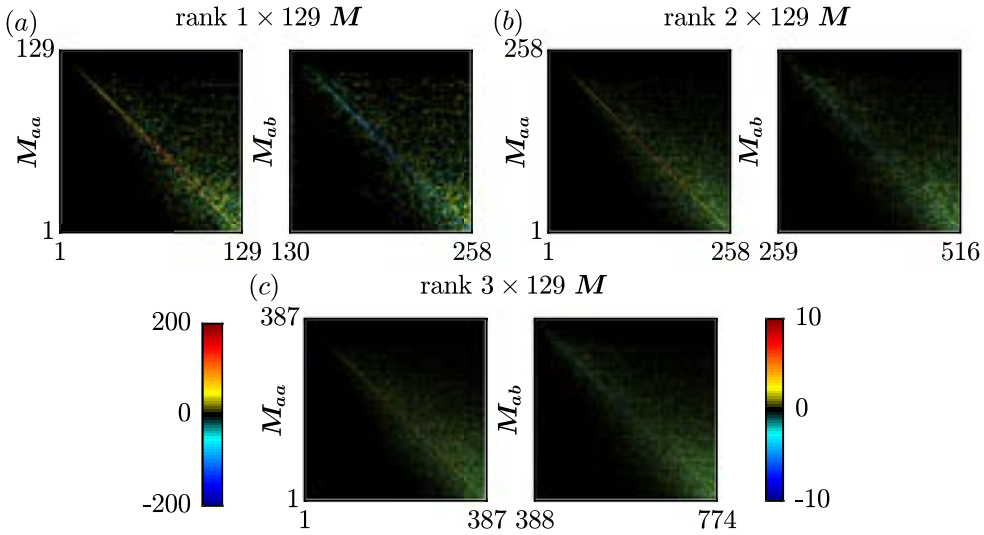

Figure 6.5. Matrices $\boldsymbol{M}_{ab}$ (left column) and $\boldsymbol{M}_{bb}$ (right column), computed from the least-squares problem (6.25) for models of different rank: (*a*) rank 1×129; (*b*) rank 2×129; (*c*) rank 3×129.

Figure 6.5 compares the left, $\boldsymbol{M}_{ab}$ (left column), and the right, $\boldsymbol{M}_{bb}$ (right column), square matrices that together form $\boldsymbol{M}$, as defined in equation (6.29), for modal basis of three different sizes. The matrix $\boldsymbol{M}_{ab}$ represents the cross–correlation information between the expansion and the forcing coefficients. Compared to the off-diagonal entries, a notable positive correlation is observed on the diagonal of the matrix $\boldsymbol{M}_{ab}$. This suggests that the correlation between the expansion and the forcing coefficients at the same frequencies dominate. The matrix $\boldsymbol{M}_{bb}$ shows the cross-correlation between the forcing coefficients. This matrix, too, is diagonally-dominant; however, the autocorrelation of the forcing is negative. In the following discussion of figure 6.6 below, we will show that this procedure of computing $\boldsymbol{M}$ leads to an almost flat residue spectrum.

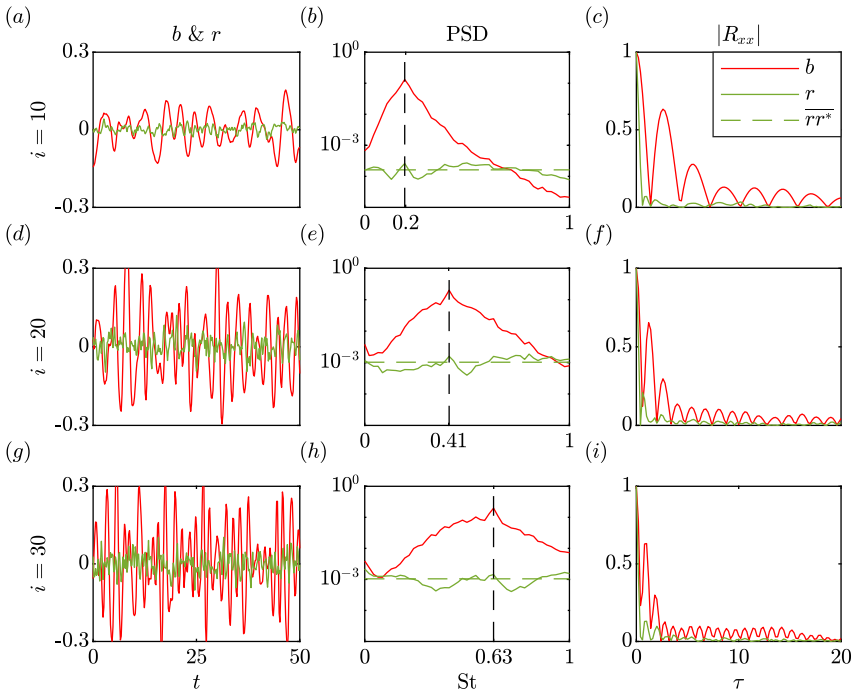

Figure 6.6. Time traces (left column), spectra (middle column) and autocorrelation estimates (right column) of the rank 1×129 forcing coefficients, $\boldsymbol{b}$ (red), and residue, $\boldsymbol{r}$ (green), at three representative frequencies: $(a-c)$ $i = 10$, or $St = 0.2$; $(d-f)$ $i = 20$, or $St = 0.41$; $(g-i)$ $i = 30$, or $St = 0.63$. In (b,e,h), vertical dashed lines indicate the SPOD mode frequencies and horizontal dashed green lines the mean PSD of the residue. The absolute values of the normalized autocorrelation is shown in (c,f,i).

Following the steps outlined in §6.3.1, we proceed with the modeling of the second-level

residue. Recall that the proposed model closure hinges on the assumption that the highest-level residue can be modeled as random noise. This assumption is tested in figure 6.6, which examines the temporal evolution and the spectra of the forcing coefficients, $\boldsymbol{b}(t)$, and the residue, $\boldsymbol{r}(t)$. The rank 1×129 case is shown as an example. It is observed that the residue is of significantly lower amplitude than the forcing. Similar to the trend observed for the SPOD expansion coefficient in figure 6.1, the PSD of the forcing coefficients, shown in the right column, attains its maximum value at the corresponding mode frequency. For the frequencies at hand, a separation of at least two orders of magnitude between the maximum and minimum values of the PSD is found. The PSD of the residue, on the contrary, is significantly flatter. To further quantify the white noise assumption, figure 6.6(c,f,i) show the corresponding (normalized) autocorrelations calculated as $R_{xx}(\tau) = \langle x(t)x(t+\tau)\rangle$, where the ensemble average $\langle\cdot\rangle$ is taken over the same blocks for the SPOD, see §2.3.4. The autocorrelations of the residue decay rapidly, whereas the forcing coefficients are correlated over 20 or more time units. This suggests that the residue can be modeled as white-in-time. Both the spectral flatness and the rapid drop of the autocorrelation motivate the truncation of the multi-level stochastic model at the second level.

To further motivate the proposed model truncation at the second level, we next examine the probability distributions of the rank 1×129 coefficients $\boldsymbol{a}$ and $\boldsymbol{b}$, and the corresponding residue $\boldsymbol{r}$ in figure 6.7. As desired, the probability distributions of residue are nearly Gaussian, which is clearly not the case for the mode and forcing coefficients. In accordance with the observations made in the context of figure 6.6, this suggests that $\boldsymbol{r}$ may be modeled with components that are mutually correlated, but that are white-in-time. In the model, the correlation between the components of the residue is accounted for by the matrix $\boldsymbol{G}$ (see equation (6.35)) that filters the white-in-time input $\boldsymbol{w}$ to generate the process noise $\widetilde{\boldsymbol{w}}$ that drives the final model.

6.4.2 Model performance

Consistent with the equation (6.37), we use the forward Euler method to march the SDE, equation (6.36), forward in time. The time step of the original data, $\Delta t = 0.2$, is used to guarantee

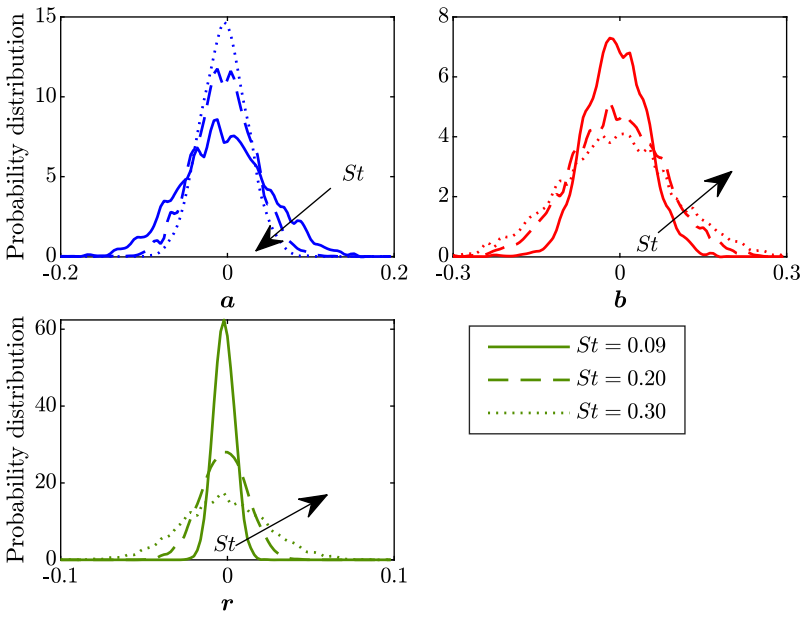

Figure 6.7. The probability distribution of rank 1×129 state coefficients $\boldsymbol{a}$ (blue), forcing coefficients $\boldsymbol{b}$ (red) and the residue $\boldsymbol{r}$ (green) at different frequencies: $St = 0.09$ (solid), $St = 0.20$, (dashed), $St = 0.30$ (dotted).

consistency with the modeling of the forcing and the residue. The initial condition for the model is within the training set, resulting in the flow field hindcast for the turbulent jet.

Figure 6.8 shows the comparison between the rank 1×129 approximation, $\breve{\boldsymbol{a}}_{1\times129}$, and a single realization of the rank 1×129 model, $\boldsymbol{a}_{1\times129}$, as well as their power spectra at different frequencies. Starting from an initial condition taken from the data, this example of a realization of the stochastic model follows the initial transient dynamics of the data for approximately 3 time units. To demonstrate that the model accurately captures the known trajectory, we run the model without stochastic forcing and the true residue as the input $\boldsymbol{r}$. It can be seen that the model output (red dots) and the LES trajectory (black line) are indistinguishable. A more rigorous approach to quantify the predictability of the model is the use of the analytical 95% confidence interval defined by equation (6.45), and Monte Carlo simulation. For the latter, 10^4 realizations of the stochastic model, all starting from the same initial condition, were computed. It can be seen that the envelope of uncertainty closely follows the reference in the vicinity of $t = 0$. As

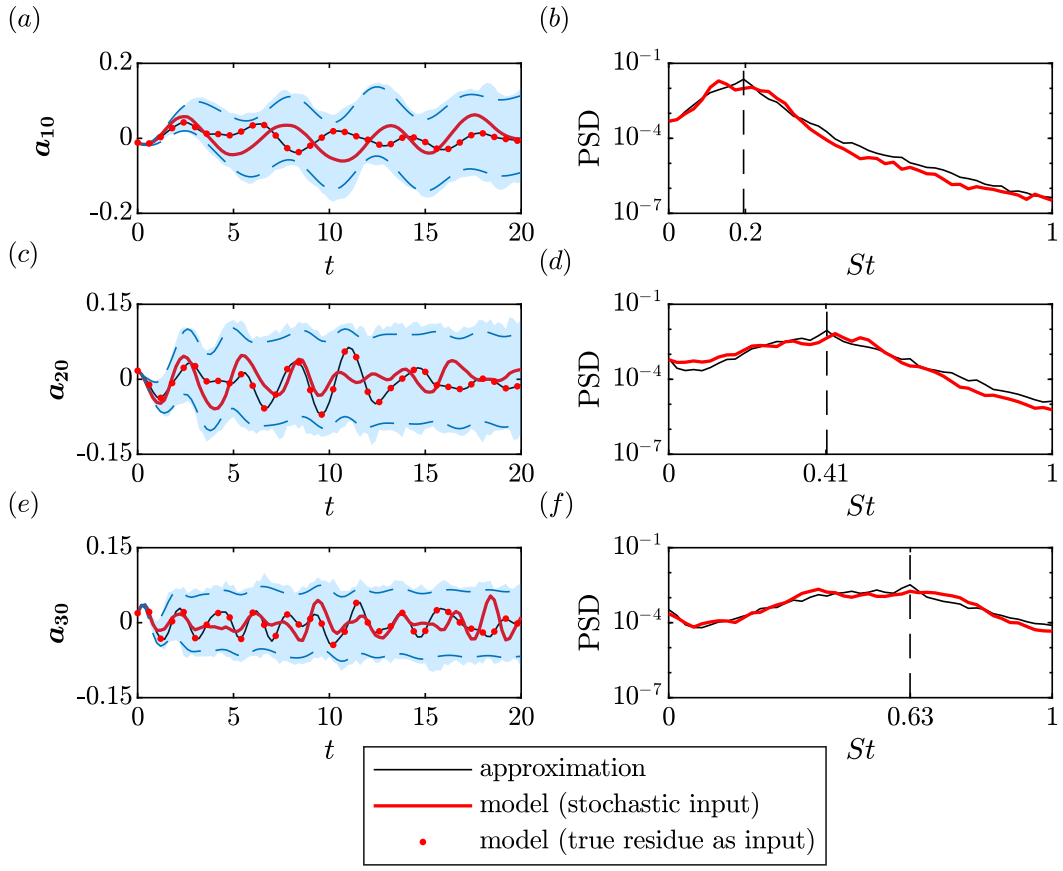

Figure 6.8. Time series and spectra for the rank 1×129 approximation (black line, representing the original data) and a single realization of the rank 1×129 model (red line) for three representative frequencies: (a,b) $St = 0.2$; (c,d) $St = 0.41$; (e,f) $St = 0.63$. Red dots show the model output when the true residue taken from the data is used as input. It is indistinguishable from the data. Blue dashed lines mark the analytic 95% confidence interval. The blue shaded area outlines a Monte Carlo envelope based on 10^4 realizations of the stochastic model, for comparison.

theoretically predicted in the context of equation (6.45), the region of uncertainty stays bounded for larger times, implying that the model is stable. A good agreement is also found between the power spectra of the coefficients of $\boldsymbol{a}_{1\times129}$ and $\check{\boldsymbol{a}}_{1\times129}$. This observation confirms that the model preserves the direct correspondence between modes and frequencies inherent to SPOD.

Figure 6.9 shows, analogously to figure 6.8(b,d,f), the power spectra of $\boldsymbol{a}_{1\times129}$ and $\check{\boldsymbol{a}}_{10\times129}$ at different frequencies. For all frequencies, the power spectra of the rank 10×129 approximation and model follow the order of the SPOD eigenvalues. As for the rank 1×129

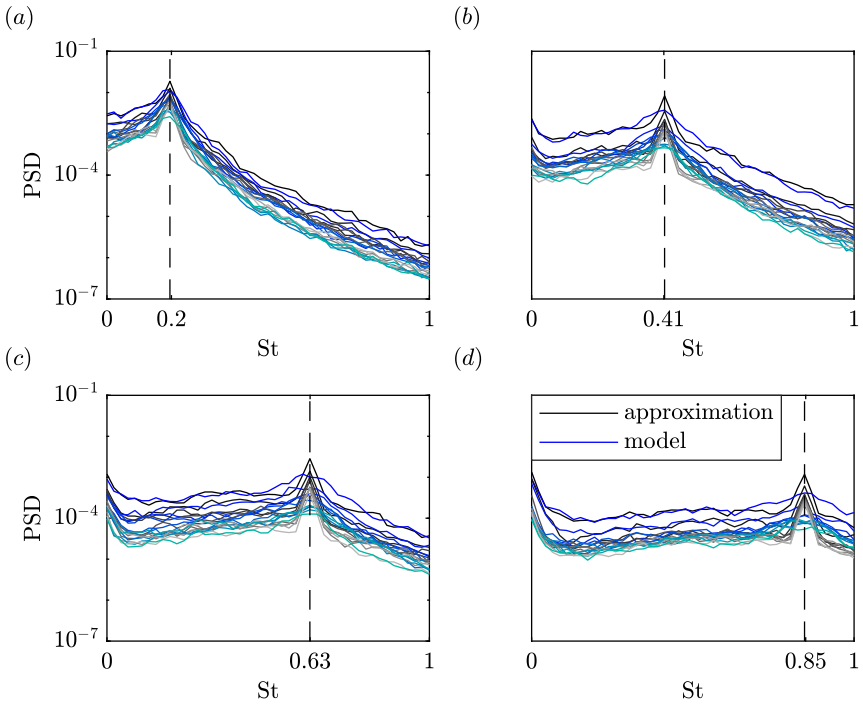

Figure 6.9. The power spectra of the first three state coefficients $\boldsymbol{a}_i$ of rank 10×129 approximation (black) and model (blue) at four representative frequencies: (a) $St = 0.2$; (b) $St = 0.41$; (c) $St = 0.63$; (d) $St = 0.85$.

model, a favourable agreement between approximation and model is observed. In summary, figures 6.8 and 6.9 demonstrate that both the dynamics and statistics of the state coefficients $\check{\boldsymbol{a}}$ are well described by two-level models of different fidelity. More results for the rank 2×129 and 3×129 models are provided in appendix B.1.

Having found that the spectral content of individual projection coefficients is represented well by the model, we now focus on the entire fluctuating flow field $\boldsymbol{q}'$. Figure 6.10 compares the compressible energy norm of $\check{\boldsymbol{a}}_{\text{full}}$, $\check{\boldsymbol{q}}_{10\times129}$, and a single realization of $\boldsymbol{q}_{10\times129}$. Also indicated in gray is the region of uncertainty obtained from 2500 Monte Carlo realizations of the model that start from the same initial condition. Two shifted axes are used to account for the constant offset between the oblique projection and model, on one hand, and the full data, on the other hand (see discussion of figure 6.2). A favorable agreement of the general dynamics is observed between $\check{\boldsymbol{q}}_{10\times129}$ and $\boldsymbol{q}_{10\times129}$. Starting from the initial condition of the data, the random realization

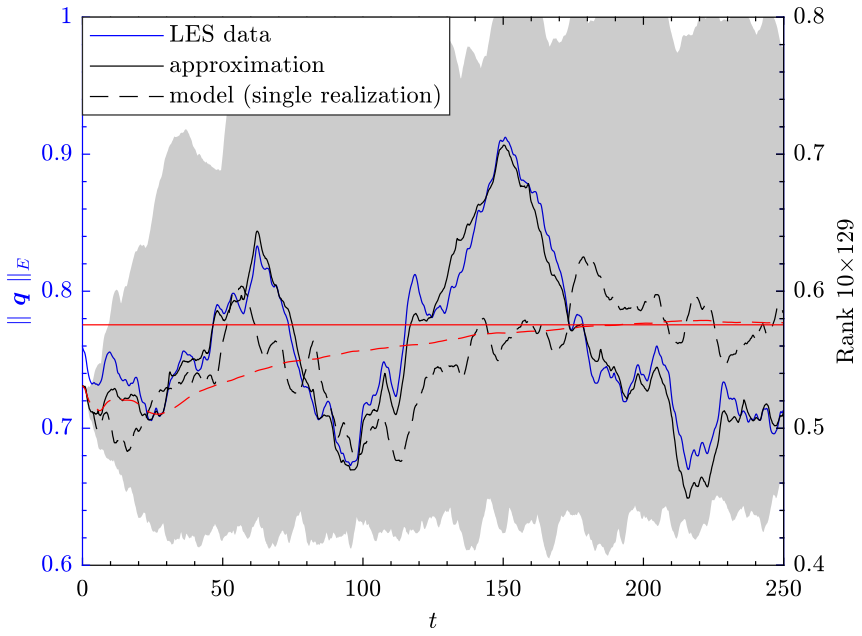

Figure 6.10. Comparison between the compressible energy norms of LES data (blue), rank 10×129 approximation (black), and a single realization of the stochastic model (black dashed). The shaded area is a Monte Carlo envelope based on 2500 model evaluations. The ensemble average of Monte Carlo simulations (red dashed) and the long-time mean of rank 10×129 approximation (red solid) are shown for comparison.

shown here (first Monte Carlo sample) follows the general trend of the data for, arguably, up to 100 time units. The model uncertainty region show that significantly larger variations are of course possible, but that the model stays bounded within an expected range. As desired, the ensemble average of the Monte Carlo simulations converges to the long-time mean of reduced-rank approximation.

After establishing that the approach yields a good model of the flow dynamics in terms of energy, we next compare the original, approximated and modeled flow fields. As examples, figure 6.11 compares the instantaneous pressure fields at $t = 5$ for rank 1×129 and rank 10×129. The same realization of the stochastic $\boldsymbol{q}_{10\times129}$ as in figure 6.10 above (dashed line) is shown. From figure 6.10, we expect that the model closely follows the approximation (and therefore the data) at this short time after its initialization. This can be clearly seen for both the rank 1×129 and rank 10×129 approximations and models in figure 6.11(b,c) and 6.11(d,e), respectively. As

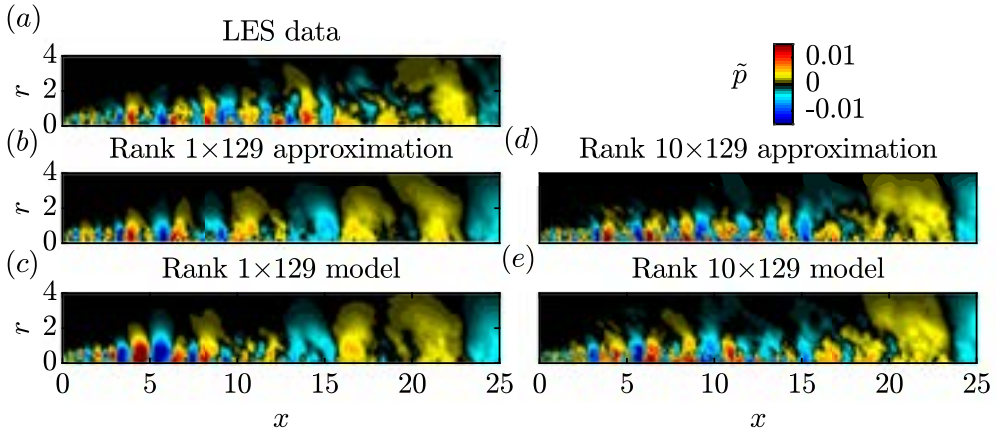

Figure 6.11. Comparison between pressure fields of the LES data, its low-rank approximations, and random realizations of the two-level model at $t = 5$: (a) LES data; (b,c) rank 1×129 and model; (d,e) rank 10×129 and model. The pressure is normalized by its root mean square for comparability (see discussion of figure 6.2).

expected, the higher-rank approximation and model yield a more detailed picture of the flow. But even for rank 1×129, many of the eminent features of the LES data are accurately captured. Due to the stochastic nature of the problem, this similarity fades for larger times. Instead, the stochastic model will yield a unique flow trajectory that can be interpreted as surrogate data that accurately reproduces the second-order statistics and dynamics of the input data.

The temporal evolution of the pressure field is investigated in terms of x-t diagrams at $r = 0.5$ (along the lipline) in figure 6.12. The convective nature of the flow field becomes apparent from the diagonal pattern corresponding to the advection of the wavepackets previously seen in figure 6.11. The original LES data shown in figure 6.12(a) is compared to its low-rank approximations (middle) and the model output (right). It can be seen that $\boldsymbol{q}_{1\times129}$ in figure 6.12(c) exhibits dynamics that are highly reminiscent of $\check{\boldsymbol{q}}_{1\times129}$ and $\check{\boldsymbol{q}}_{\text{full}}$. Similar observations are made for $\check{\boldsymbol{q}}_{10\times129}$ and $\boldsymbol{q}_{10\times129}$ in figure 6.12(d) and (e), respectively. We note that the vertical stripes in figure 6.12(d) stem from spatial aliasing, which occurs for subdominant modes at high frequencies. We emphasize that this issue is linked to the discretization of the data set, which was interpolated from the unstructured LES grid to a cylindrical grid for post-processing. The phenomenon is, however, accurately reproduced by the model in figure 6.12(e).

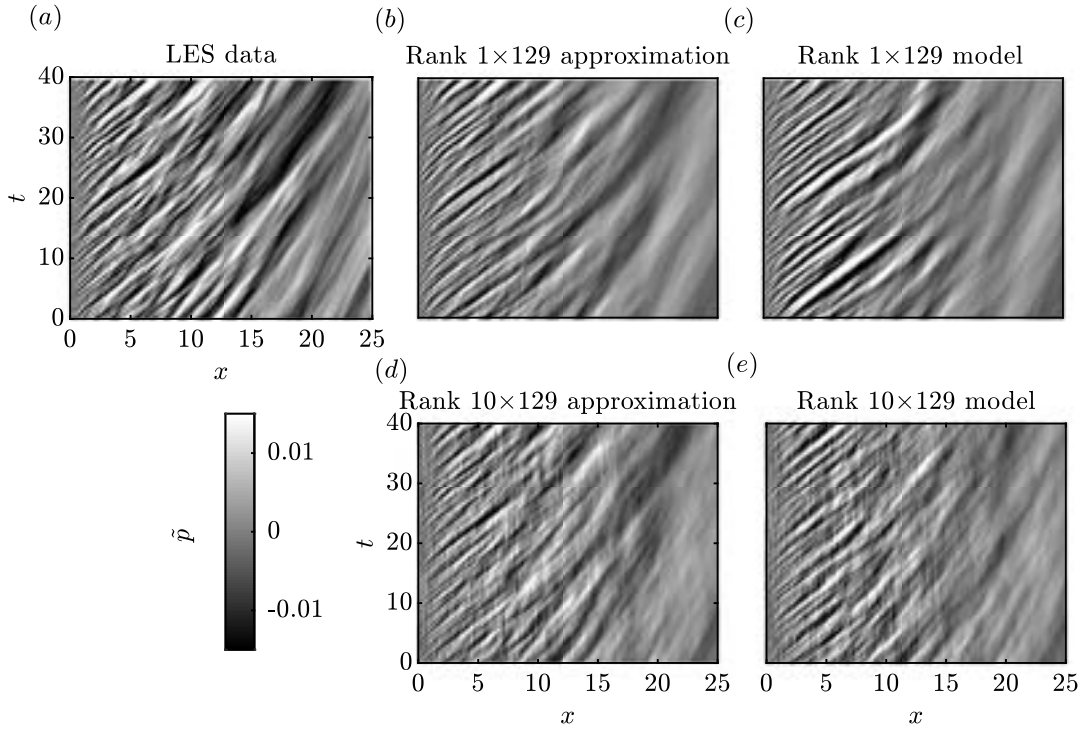

Figure 6.12. Comparison between LES data (a), rank 1×129 and model (b-c), rank 1×129 and model (d-e) of normalized pressure component at $r = 0.5$ for different time.

After establishing that the model reproduces a surrogate flow field that is qualitatively very similar to the original data, we now focus on the flow statistics. An obvious choice is to use the SPOD for this purpose as well. In figure 6.13, we hence compare the SPOD eigenvalue spectra of LES data to both the rank 1×129 and 10×129 approximations and models, respectively. For clarity, only the leading two eigenvalues are shown for $\breve{\boldsymbol{q}}_{\text{full}}$, and the leading 3 eigenvalues for $\breve{\boldsymbol{q}}_{10\times129}$ and $\boldsymbol{q}_{10\times129}$. It can be seen that both models accurately reproduce the eigenvalue spectra of the LES data for all but the lowest frequencies. $\boldsymbol{q}_{10\times129}$ accurately follows $\breve{\boldsymbol{q}}_{10\times129}$ at frequencies with $St > 0.2$, but somewhat under-predicts the $\breve{\boldsymbol{q}}_{10\times129}$ at lower frequencies. For $\boldsymbol{q}_{1\times129}$, we observe an overall very good fit between approximation and model for the leading mode. In accordance with the conjectures drawn from figure 6.12, we conclude that $\boldsymbol{q}_{1\times129}$ produces an accurate surrogate flow field, both qualitatively and statistically.

Chapter 6, in full, is a reprint of the material as it appear in Theoretical and Computational

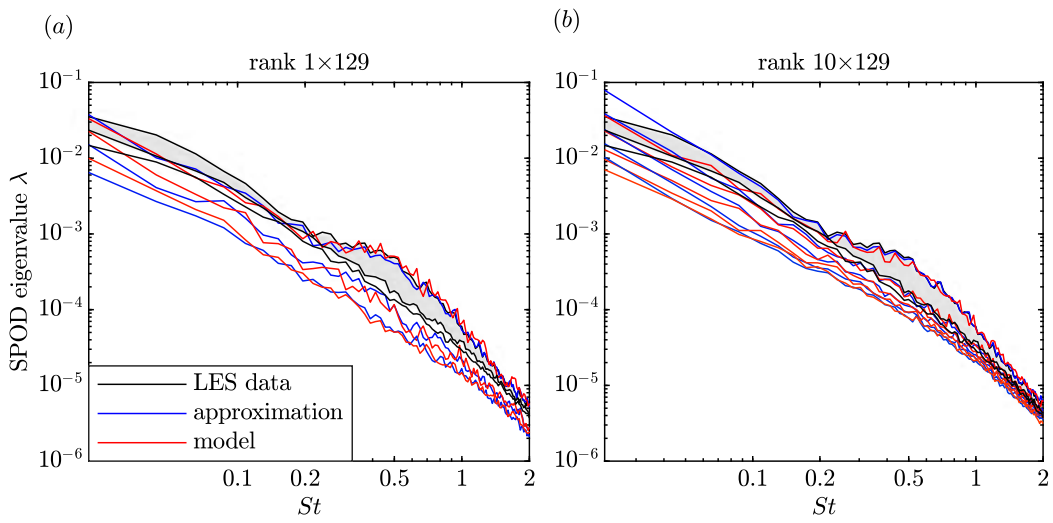

Figure 6.13. Comparison of SPOD eigenvalue spectra of the LES data (black), low-rank approximations (blue) and 2–level models (red): (a) rank 1×129; (b) rank 10×129. The leading two eigenvalues are shown for the LES data (with shaded area between them), and the leading three eigenvalues for the approximations and models, respectively.

Fluid Dynamics 2021, Chu, Tianyi; Schmidt, Oliver T., Springer, 2021. The dissertation author was the primary investigator and author of this paper.

Chapter 7

A convolutional Koopman model for turbulent dynamics

Operator-based ROMs require knowledge of the governing equations. Therefore, they are challenged when the physical description of the system dynamics is difficult to formulate, as is true in examples including climate science and physiology. As an alternative, data-driven modeling techniques have become increasingly popular for analyzing and controlling high-dimensional dynamical systems such as turbulence based on the rise of high-fidelity data collection, see, e.g., [38, 144, 62, 176]. Analogous to the operator-based ROM in equation (6.11), we aim to leverage the properties of SPOD described in §2.3.4 to model turbulent flows as an LTI system,

$$\frac{\mathrm{d}}{\mathrm{d}t}\boldsymbol{a} = \boldsymbol{K}\boldsymbol{a} + \boldsymbol{b}, \tag{7.1}$$

in a purely data-driven manner. The Koopman/DMD perspective introduced in §2.3.2 provides a straightforward data-driven way of modeling nonlinear dynamical systems by performing the linear dynamic regression of the observable sequence, $\boldsymbol{\phi}[i]$. The art of the Koopman operator lies in selecting the right observables, and it can embed the state dynamics into a low-dimensional manifold [40]. The arguably most straightforward way to reduce dimensionality is to use the amplitudes of spatial modes obtained via projection as linear observables. When the spatial

modes, $\boldsymbol{\psi}_j$, are orthogonal, the projection reduces to the inner product

$$\phi_j(\boldsymbol{q}) = \left\langle \boldsymbol{\psi}_j, \boldsymbol{q} - \overline{\boldsymbol{q}} \right\rangle = \left\langle \boldsymbol{\psi}_j, \boldsymbol{q}' \right\rangle, \tag{7.2}$$

where the inner product is defined in equation (2.17). We leverage the cheap-to-compute property of the inner product to obtain observables without requiring orthogonality of the spatial modes. We later demonstrate in §7.2 that SPOD offers the optimal modal basis for Fourier convolution. The linear observable vector $\boldsymbol{\phi}$, however, may be overly constrained for adequately describing the complex dynamics encountered in fluids or other nonlinear systems. We then explore the application of time-delay embedding as a means to capture the nonlinear dynamics.

7.1 Time-delay embedding

Time-delay embedding has been incorporated with Koopman theory to represent chaotic systems as linear dynamic models, such as the Hankel-DMD model [5], the HODMD model [147], and the HAVOK model [36]. These approaches obtain time-delay observables by performing the SVD of a large Hankel matrix. Alternatively, we may define a general time-delay observable vector $\boldsymbol{a} \in \mathbb{C}^{N_k}$ as a linear combination of previous and future observables, $\boldsymbol{\phi}$, with

$$\boldsymbol{a}[i] \equiv \sum_{h=1-N_f}^{N_f} \mathscr{C}_h(\boldsymbol{\phi}[i+h]), \tag{7.3}$$

where the linear maps, $\mathscr{C}_h : \mathbb{C}^{N_k} \to \mathbb{C}^{N_k}$, assign weights for different instants. The linearity of the Koopman operator $\mathscr{K}$ yields

$$\begin{aligned} \boldsymbol{a}[i+1] = \sum_{h=1-N_f}^{N_f} \mathscr{C}_h(\boldsymbol{\phi}[i+h+1]) &= \sum_{h=1-N_f}^{N_f} \mathscr{C}_h(\mathscr{K}\boldsymbol{\phi}[i+h]) \\ &= \mathscr{K}\left(\sum_{h=1-N_f}^{N_f} \mathscr{C}_h(\boldsymbol{\phi}[i+h]) \right) = \mathscr{K}\boldsymbol{a}[i], \end{aligned} \tag{7.4}$$

which gives

$$\boldsymbol{a}[i+1] = \mathscr{K}\boldsymbol{a}[i]. \tag{7.5}$$

This implies that $\boldsymbol{a}$ spans a Koopman-invariant subspace, that is, the same Koopman operator $\mathscr{K}$ governs the evolution of both the observables, $\boldsymbol{\phi}$, and the corresponding time-delay observables, $\boldsymbol{a}$. Equation (7.4) also exhibits an inherent equivalence to HODMD. By comparing the second and the third terms and shifting the time index with N_f, $\boldsymbol{\phi}[i+1]$ can be cast into a linear combination of the previous $2N_f$ states, that is,

$$\begin{aligned}\boldsymbol{\phi}[i+1] = \quad & \underbrace{\mathscr{C}_{N_f}^{-1}\left(\mathscr{K}\circ\mathscr{C}_{N_f} - \mathscr{C}_{N_f-1}\right)}_{\mathscr{R}_{2N_f}}\boldsymbol{\phi}[i] + \underbrace{\mathscr{C}_{N_f}^{-1}\left(\mathscr{K}\circ\mathscr{C}_{N_f-1} - \mathscr{C}_{N_f-2}\right)}_{\mathscr{R}_{2N_f-1}}\boldsymbol{\phi}[i-1] + \cdots \\ & + \underbrace{\mathscr{C}_{N_f}^{-1}\left(\mathscr{K}\circ\mathscr{C}_{2-N_f} - \mathscr{C}_{1-N_f}\right)}_{\mathscr{R}_2}\boldsymbol{\phi}[i-2N_f+2] + \underbrace{\mathscr{C}_{N_f}^{-1}\left(\mathscr{K}\circ\mathscr{C}_{1-N_f}\right)}_{\mathscr{R}_1}\boldsymbol{\phi}[i-2N_f+1],\end{aligned} \tag{7.6}$$

where $\mathscr{C}^{-1}$ represents the inverse operator of $\mathscr{C}$. Here, the linear operators $\mathscr{R}_1, \cdots, \mathscr{R}_{2N_f}$ are constructed as linear combinations of the Koopman operator $\mathscr{K}$ and linear maps $\mathscr{C}$. Their finite-dimensional representations recover the formalisation of HODMD.

We use equation (7.3) to specialize the construction of the time-delay coordinates as a convolution process by assigning the linear maps as

$$\mathscr{C}_h(\boldsymbol{\phi}) \equiv \begin{bmatrix} c_{h,1}\phi_1 & c_{h,2}\phi_2 & \cdots & c_{h,N_k}\phi_{N_k} \end{bmatrix}^T, \tag{7.7}$$

where the $c_{h,1}, \cdots, c_{h,N_k}$ are nonzero convolutional weights. Together with equation (7.4), we formalize the idea of using a Koopman operator to evolve the convolutional coordinates. This idea has been previously explored by Kamb *et al.* [129]. Most notably, as mentioned before, the Koopman operator remains invariant under the convolution. Hankel singular vectors are particularly well-suited for convolution bases as they converge to Legendre polynomials in the

limit of short delays [92] and to a Fourier basis in the limit of long delays [30]. The natural choice for the convolution basis for a statistically stationary process is the Fourier basis. We avoid the construction of a Hankel matrix altogether by considering the Fourier convolution,

$$a_j(t) \equiv \int_{-T_0}^{T_0} \phi_j(t+\tau) \mathrm{e}^{-\mathrm{i}\tilde{\omega}_j \tau} w(\tau)\, \mathrm{d}\tau. \tag{7.8}$$

to obtain the convolutional coordinates, a_j, that describe the temporal dynamics of individual frequency components. Here, $\tilde{\omega}_j \in \{\omega_l\}_{l=1}^{2N_f}$ is the associated frequency. The Fourier series, $\{\mathrm{e}^{-\mathrm{i}\omega_l \tau}\}_{l=1}^{2N_f}$, are orthonormal on the time interval $[-T_0, T_0]$. In practice, a window function $w(\tau)$ is included to minimize spectral leakage. The discrete form of equation (7.8) on the time interval $(-N_f\Delta t, N_f\Delta t]$ can be written as

$$a_j[i] = \sum_{h=1-N_f}^{N_f} c_{h,j} \phi_j[i+h] \tag{7.9}$$

by defining the convolutional weights as

$$c_{h,j} \equiv \mathrm{e}^{-\mathrm{i}\tilde{\omega}_j h\Delta t} w[h\Delta t]\Delta t. \tag{7.10}$$

Equation (7.9) is a continuously discrete convolution sum for the observable ϕ. Instead of explicitly computing the convolutional weights, we use the fast Fourier transform (FFT) to perform the discrete convolution. In the following, we demonstrate that SPOD provides the optimal modal basis for the Fourier convolution.

7.2 Optimal convolutional coordinates from SPOD

The first step to finding the modal basis vector is to obtain the span of the Fourier basis. We decompose the fluctuating state into its temporal discrete Fourier modes, $\hat{(\cdot)}$, on the time

interval $(-N_f\Delta t, N_f\Delta t]$ as

$$\boldsymbol{q}'(t) = \frac{1}{2N_f\Delta t}\sum_{l=1}^{2N_f}\hat{\boldsymbol{q}}(\omega_l)\mathrm{e}^{\mathrm{i}\omega_l t}, \tag{7.11}$$

where $\omega_l = l\pi/(N_f\Delta t)$ is the angular frequency. Inserting equation (7.2) into equation (7.11) yields the jth observable

$$\phi_j(\boldsymbol{q}) = \frac{1}{2N_f\Delta t}\sum_{l=1}^{2N_f}\left\langle \boldsymbol{\psi}_j, \hat{\boldsymbol{q}}(\omega_l)\right\rangle_x \mathrm{e}^{\mathrm{i}\omega_l t}. \tag{7.12}$$

Substituting this expression for the observable in equation (7.9) and using the definition of the convolutional weights, $c_{h,j}$, from equation (7.10) leads to

$$\begin{aligned}
a_j[i] &= \sum_{h=1-N_f}^{N_f} c_{h,j}\left(\frac{1}{2N_f\Delta t}\sum_{l=1}^{2N_f}\left\langle \boldsymbol{\psi}_j, \hat{\boldsymbol{q}}(\omega_l)\right\rangle_x \mathrm{e}^{\mathrm{i}\omega_l(i+h)\Delta t}\right)\\
&= \frac{1}{2N_f\Delta t}\sum_{l=1}^{2N_f}\left\langle \boldsymbol{\psi}_j, \hat{\boldsymbol{q}}(\omega_l)\right\rangle_x \left(\sum_{h=1-N_f}^{N_f} c_{h,j}\,\mathrm{e}^{\mathrm{i}\omega_l(i+h)\Delta t}\right)\\
&= \frac{1}{2N_f\Delta t}\sum_{l=1}^{2N_f}\left\langle \boldsymbol{\psi}_j, \hat{\boldsymbol{q}}(\omega_l)\right\rangle_x \left(\Delta t\,\mathrm{e}^{\mathrm{i}\omega_l(i\Delta t)}\sum_{h=1-N_f}^{N_f}\mathrm{e}^{\mathrm{i}(\omega_l-\tilde{\omega}_j)h\Delta t}w[h\Delta t]\right)\\
&= \sum_{l=1}^{2N_f}\left\langle \boldsymbol{\psi}_j, \hat{\boldsymbol{q}}(\omega_l)\right\rangle_x \mathrm{e}^{\mathrm{i}\omega_l(i\Delta t)}\delta(\omega_l-\tilde{\omega}_j)\\
&= \left\langle \boldsymbol{\psi}_j, \hat{\boldsymbol{q}}(\tilde{\omega}_j)\right\rangle_x \mathrm{e}^{\mathrm{i}\tilde{\omega}_j(i\Delta t)},
\end{aligned} \tag{7.13}$$

where $\delta(\cdot)$ represents the Dirac delta function. The magnitude of a_j only depends on the inner product of the jth basis vector, $\boldsymbol{\psi}_j$, and the Fourier mode associated with frequency $\tilde{\omega}_j$, $\hat{\boldsymbol{q}}(\tilde{\omega}_j)$. With modes that have unit energy, $\|\boldsymbol{\psi}_j\|_x = 1$, we seek the convolutional coordinates that optimally represent the flow field at each given frequency, $\tilde{\omega}_j$. This objective is formalized by maximizing the quantity

$$\begin{aligned}\lambda_j = \mathrm{E}\{a_j a_j^*\} &= \mathrm{E}\{\left(\left\langle \boldsymbol{\psi}_j, \hat{\boldsymbol{q}}(\tilde{\omega}_j)\right\rangle_x \mathrm{e}^{\mathrm{i}\tilde{\omega}_j(i\Delta t)}\right)\left(\left\langle \boldsymbol{\psi}_j, \hat{\boldsymbol{q}}(\tilde{\omega}_j)\right\rangle_x \mathrm{e}^{\mathrm{i}\tilde{\omega}_j(i\Delta t)}\right)^*\} \\ &= \mathrm{E}\{\left\langle \boldsymbol{\psi}_j, \hat{\boldsymbol{q}}(\tilde{\omega}_j)\right\rangle_x \left\langle \hat{\boldsymbol{q}}(\tilde{\omega}_j), \boldsymbol{\psi}_j\right\rangle_x\} \\ &= \mathrm{E}\{\left\langle \boldsymbol{\psi}_j, \hat{\boldsymbol{q}}(\tilde{\omega}_j)\hat{\boldsymbol{q}}(\tilde{\omega}_j)^* \boldsymbol{W}\boldsymbol{\psi}_j\right\rangle_x\} \\ &= \left\langle \boldsymbol{\psi}_j, \boldsymbol{S}_j \boldsymbol{W}\boldsymbol{\psi}_j\right\rangle_x, \end{aligned} \tag{7.14}$$

where $\boldsymbol{S}_j = \mathrm{E}\{\hat{\boldsymbol{q}}(\tilde{\omega}_j)\hat{\boldsymbol{q}}(\tilde{\omega}_j)^*\}$ is the cross-spectral density matrix. Equation (7.14) represents a generalized Rayleigh quotient, and its maximum values can be found from the eigenvalue problem

$$\boldsymbol{S}_j \boldsymbol{W}\boldsymbol{\psi}_j^{(\alpha)} = \lambda_j^{(\alpha)}\boldsymbol{\psi}_j^{(\alpha)}. \tag{7.15}$$

This is the same eigenvalue problem previously introduced in equation (2.25). The corresponding eigenvectors, $\boldsymbol{\psi}_j^{(\alpha)}$, are therefore SPOD modes. Even though the SPOD modes across different frequencies are not orthogonal in the spatial inner product, $\langle\cdot,\cdot\rangle_x$, the convolution in equation (7.13) reinstates the space-time orthogonality, $\int_{-T_0}^{T_0}\left\langle \boldsymbol{\psi}_j^{(\alpha)}\mathrm{e}^{\mathrm{i}\tilde{\omega}_j t}, \boldsymbol{\psi}_k^{(\beta)}\mathrm{e}^{\mathrm{i}\tilde{\omega}_k t}\right\rangle_x \mathrm{d}t = 2T_0\delta(\alpha-\beta)\delta(\tilde{\omega}_j-\tilde{\omega}_k)$, thereby preserving the direct correspondence between modes and frequencies inherent to SPOD. The optimality we require for the convolutional Koopman model hence naturally recovers SPOD modes as the adequate basis.

To represent the dynamics at all scales of turbulence, we choose a modal basis that includes all $2N_f$ frequency components. At each frequency, we pick the leading M modes to retain the largest amount of energy. The resulting basis takes the form of the rank $M \times 2N_f$ SPOD basis, $\boldsymbol{V}$, as introduced in equation (6.3). Inserting equation (7.12) into the Fourier convolution (7.9) recovers the convolutional integral used by Nekkanti & Schmidt [186] to compute discrete time-continuous SPOD expansion coefficients. This also implies that the convolutional coordinates, $\boldsymbol{a}$, facilitate the optimal low-reconstruction of the flow field in the

space-time sense, $\int_{-T_0}^{T_0} \langle \boldsymbol{q}_1, \boldsymbol{q}_2 \rangle_x \, \mathrm{d}t$. For a given time index i and a given time-lag $h \in [1-N_f, N_f]$, the flow field can be reconstructed as

$$\boldsymbol{q}'[i;h] \approx \frac{1}{2N_f \Delta t w(h\Delta t)} \sum_{j=1}^{2MN_f} \left(a_j[i+h] \boldsymbol{\psi}_j \right) \mathrm{e}^{\mathrm{i}\tilde{\omega}_j (N_f - h)\Delta t}. \tag{7.16}$$

As the window-weighted average leads to better reconstruction [186], we consider the time window $[h_-, h_+] \subset [1-N_f, N_f]$ such that

$$\begin{aligned} \boldsymbol{q}'[i] \approx \mathrm{E}_{h\in[h_-,h_+]}\{\boldsymbol{q}'[i;h]\} &= \frac{1}{2N_f \Delta t \sum_{h=h_-}^{h_+} w(h\Delta t)} \sum_{h=h_-}^{h_+} \sum_{j=1}^{2MN_f} \left(a_j[i+h] \boldsymbol{\psi}_j \right) \mathrm{e}^{\mathrm{i}\tilde{\omega}_j (N_f - h)\Delta t} \\ &= \sum_{j=1}^{2MN_f} \underbrace{\left(\frac{\sum_{h=h_-}^{h_+} \left(a_j[i+h] \right) \mathrm{e}^{\mathrm{i}\tilde{\omega}_j (N_f - h)\Delta t}}{2N_f \Delta t \sum_{h=h_-}^{h_+} w(h\Delta t)} \right)}_{\tilde{a}_j[i]} \boldsymbol{\psi}_j, \end{aligned} \tag{7.17}$$

which can be written in a compact form as

$$\boldsymbol{q}'[i] \approx \boldsymbol{V} \tilde{\boldsymbol{a}}[i]. \tag{7.18}$$

Here, $\tilde{a}_j$ constitutes the jth component of $\tilde{\boldsymbol{a}}$. Given the convolutional coordinates a_j, equation (7.17) offers a particularly economical way for the reconstruction of flow data, as both the weighting and Fourier inversion are performed on the coordinates, not on the flow data.

7.3 Forced LTI system

The use of convolutional coordinates implicitly embeds nonlinearity into the Koopman operator, $\mathscr{K}$. For fully turbulent flows, it is unrealistic to expect a truncated linear operator, $\boldsymbol{K}$, to govern the dynamics of all temporal scales. We hence suggest augmenting the linear Koopman model in equation (7.5) with an exogenous time-invariant forcing, $\boldsymbol{b}$, to account for the remaining nonlinear interactions and background turbulence. The resulting evolution model for the discrete

time-continuous convolutional coordinates can be written as a continuous-time LTI system,

$$\frac{\mathrm{d}}{\mathrm{d}t}\boldsymbol{a} = \boldsymbol{K}\boldsymbol{a} + \boldsymbol{b}. \tag{7.19}$$

Here, $\boldsymbol{K} \in \mathbb{C}^{N_k \times N_k}$ is a finite-dimensional approximation of the continuous-time version of the Koopman operator. In the absence of $\boldsymbol{b}$, the matrix $\boldsymbol{K}$ can be learned from the raw data, $\breve{(\cdot)}$, by solving the least-squares problem with L_2 regularization [104],

$$\boldsymbol{K} = \arg\min_{\boldsymbol{K}} \frac{1}{2}\left(\sum_{i=1}^{N-1}\left\|\frac{\mathrm{d}}{\mathrm{d}t}\breve{\boldsymbol{a}}[i+1] - \boldsymbol{K}\breve{\boldsymbol{a}}[i]\right\|^2 + \gamma_1\|\boldsymbol{K}\|^2\right), \tag{7.20}$$

where γ_1 is the ridge parameter. L_2 regularization is particularly well-suited for enhancing model stability when the training data is noisy, which is true for turbulent flows. Instead of considering $\boldsymbol{b}$ as merely stochastic, we treat $\boldsymbol{b}$ as an independent dynamical variable that models the residual nonlinear dynamics. Our approach is next discussed in §7.4.

7.4 The stochastic low-dimensional inflated convolutional Koopman (SLICK) model

In §6, we proposed a two-level framework for modeling the nonlinear forcing of a SPOD-Galerkin ROM, which drives the oblique projection-based expansion coefficients in time via the reduced-order linearized Navier-Stokes operator. Here, we follow the idea of using a linear operator to describe the inflated nonlinear state to construct a purely data-driven ROM for SPOD-convolutional coordinates. Analogous to equation (6.28), we inflate the forced LTI system in equation (7.1) to incorporate the dynamics of $\boldsymbol{b}$ within the model, such that

$$\frac{\mathrm{d}}{\mathrm{d}t}\underbrace{\begin{bmatrix}\boldsymbol{a}\\ \boldsymbol{b}\end{bmatrix}}_{\boldsymbol{y}} = \underbrace{\begin{bmatrix}\boldsymbol{K} & \boldsymbol{I}\\ \boldsymbol{M}_{ab} & \boldsymbol{M}_{bb}\end{bmatrix}}_{\boldsymbol{K}_y}\begin{bmatrix}\boldsymbol{a}\\ \boldsymbol{b}\end{bmatrix} + \underbrace{\begin{bmatrix}\boldsymbol{0}\\ \boldsymbol{G}\boldsymbol{w}\end{bmatrix}}_{\widetilde{\boldsymbol{w}}}. \tag{7.21}$$

Here, the matrix $\boldsymbol{K}_y$ is the EDMD operator within the time-delay framework that governs the linear dynamics of the compound convolutional coordinates, $\boldsymbol{y}$. It consists of $\boldsymbol{K}$, which drives the motion of the most energetic coherent structures, along with the linear deterministic correlation between the forcing and the compound state, modeled as $\boldsymbol{M}_{ab}$ and $\boldsymbol{M}_{bb}$. The white noise input, $\boldsymbol{w}$, is colored by a dewhitening filter, $\boldsymbol{G}$, as a stochastic source to facilitate turbulence closure while preserving the same second-order flow statistics. Without the need for the linearized Navier-Stokes operator, the stochastic low-dimensional inflated convolutional Koopman (SLICK) model in equation (7.21) establishes a purely data-driven ROM based on Koopman theory. With an initial condition and the stochastic input, the SLICK model can be solved numerically analogous to equation (6.37) as

$$\boldsymbol{y}[i+1] = \underbrace{(\boldsymbol{I} + \boldsymbol{K}_y \Delta t)}_{\boldsymbol{T}} \boldsymbol{y}[i] + \begin{bmatrix} \boldsymbol{0} \\ \boldsymbol{G}\Delta\boldsymbol{\xi} \end{bmatrix}, \tag{7.22}$$

where $\Delta\boldsymbol{\xi}$ is an independent Gaussian increment of a Wiener process with zero mean and covariance matrix $\boldsymbol{I}\Delta t$.

To incorporate $\boldsymbol{b}$ within the model, we follow the inverse modeling paradigm [139, 143, 196, 197] by using the offset between the linearized dynamics and the true data sequence,

$$\check{\boldsymbol{b}} = \frac{\mathrm{d}}{\mathrm{d}t}\check{\boldsymbol{a}} - \boldsymbol{K}\check{\boldsymbol{a}}, \tag{7.23a}$$

to inform the model in the training phase via linear regression. The still-existing nonlinear dynamics within $\boldsymbol{b}$ are modeled by matrices $\boldsymbol{M}_{ab}$ and $\boldsymbol{M}_{bb}$, whose constructions are generally the same as in the operator-based model introduced in §6. One minor discrepancy is that we here include an L2 regularization when determining the matrix $\boldsymbol{M}$, such that

$$\boldsymbol{M} = \arg\min_{\boldsymbol{M}} \sum_{i=1}^{N} \left(\left\| \frac{\mathrm{d}}{\mathrm{d}t}\check{\boldsymbol{b}}[i] - \boldsymbol{M}\check{\boldsymbol{y}}[i] \right\|^2 + \gamma_2 \|\boldsymbol{M}\|^2 \right), \tag{7.24}$$

where γ_2 is the ridge parameter. This helps circumvent the overdetermining issue from the training set. With regularization, we have to update the dewhitening filter $\boldsymbol{G}$ to ensure that the second-order statistics are accurately reproduced by the model. As shown in equation (6.44), the auto-covariance matrix of $\boldsymbol{y}[i]$ converges to the solution of a discrete-time Lyapunov equation

$$\boldsymbol{T}\boldsymbol{P}\boldsymbol{T}^* - \boldsymbol{P} + \begin{bmatrix} \boldsymbol{0} & \boldsymbol{0} \\ \boldsymbol{0} & \boldsymbol{G}\boldsymbol{G}^*\Delta t \end{bmatrix} = 0 \tag{7.25}$$

if $\boldsymbol{T}$ is stable. To ensure that the model reproduces the second-order flow statistics, we determine the matrix $\boldsymbol{G}$ using the auto-covariance matrices of the training data,

$$\check{\boldsymbol{P}}_1 = \mathrm{E}\{(\check{\boldsymbol{y}}\check{\boldsymbol{y}}^*)\,|_{i=1}^{N-1}\} \quad \text{and} \quad \check{\boldsymbol{P}}_2 = \mathrm{E}\{(\check{\boldsymbol{y}}\check{\boldsymbol{y}}^*)\,|_{i=2}^{N}\}, \tag{7.26}$$

such that

$$\boldsymbol{G}\boldsymbol{G}^* \approx \boldsymbol{H} = \frac{1}{\Delta t}\begin{bmatrix} \boldsymbol{0} & \boldsymbol{1} \end{bmatrix} \underbrace{\left(\check{\boldsymbol{P}}_2 - \boldsymbol{T}\check{\boldsymbol{P}}_1\boldsymbol{T}^*\right)}_{\check{\boldsymbol{H}}} \begin{bmatrix} \boldsymbol{0} \\ \boldsymbol{1} \end{bmatrix}. \tag{7.27}$$

Here, the ergodicity hypothesis is applied, assuming that the long-term statistics are the same as ensemble statistics. The matrix $\boldsymbol{H}$ is hermitian but not guaranteed positive semi-definite. To address this, we perform an eigenvalue decomposition of $\boldsymbol{H}$,

$$\boldsymbol{H} = \boldsymbol{V}_H\boldsymbol{D}_H\boldsymbol{V}_H^*. \tag{7.28}$$

We then adjust its negative eigenvalues to a small positive value $0 < \varepsilon \ll 1$, and rescale the positive ones to maintain the trace of $\boldsymbol{H}$, which can be interpreted as the total variance of the stochastic forcing. Similar approaches have been employed in other LIM studies, see, e.g.,

[197, 248]. The matrix $\boldsymbol{G}$ can then be determined as

$$\boldsymbol{G} = \boldsymbol{V}_H \tilde{\boldsymbol{D}}_H^{1/2}, \tag{7.29}$$

where $\tilde{\boldsymbol{D}}_H$ represents the updated diagnal eigenvalue matrix.

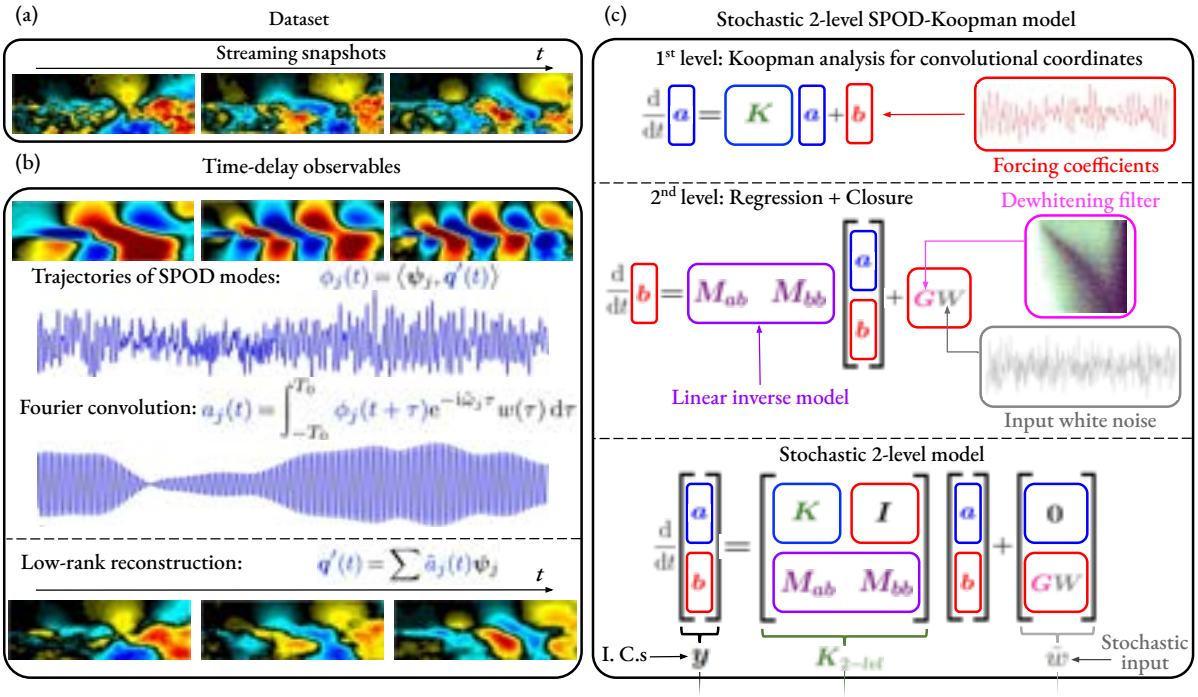

Figure 7.1. Schematic of the SLICK model for broadband turbulent flows: (a) collecting data as equally sampled snapshots; (b) performing model-order reduction and time-delay embedding using SPOD-based convolution; (c) training the SLICK model. The open cavity flow described in §7.5.3 is shown as an example.

The summary of the SLICK model is shown in figure 7.1, demonstrated using a turbulent open-cavity flow as an example. While the model encompasses complex concepts, it can be formulated by a simple discrete-in-time algorithm, as outlined in appendix C.1.

7.5 Examples

We demonstrate the SLICK model using three different examples: a numerically integrated stochastic complex Ginzburg–Landau equation (SCGL), a turbulent jet by Brès *et al.* [33],

Table 7.1. Overview of datasets. SCGL for stochastic complex Ginzburg–Landau equation, SRK4 for the fourth-order stochastic Runge-Kutta algorithm.

Flow	Method	Variables	N/N_∞	N_q	Overview
SCGL	SRK4 [133, 134]	q	20000/80000	220	Fig. 7.2
Jet	LES [33]	p	9000/10000	950×195	Fig. 7.7
Open cavity	TR-PIV [307]	u, v	14400/16000	$156 \times 55 \times 2$	Fig. 7.14

and an open cavity flow by Zhang *et al.* [307], as summarized in table 7.1. These three examples are representative of statistically stationary turbulent flows and exhibit different spectral content: the open cavity data has tonal peaks and an underlying broadband spectrum [33]; the turbulent jet data has broadband turbulence spectra [308]. The lack of physical dynamical descriptions of the latter two examples motivates data-driven modeling approaches. In the rest of this section, we assess the model in terms of initial transient dynamics, flow statistics, and uncertainty quantification. Beyond qualitative evaluation, two metrics, correlation and root-mean-square error, are employed to quantify the performance of the model. The training set comprises N consecutive snapshots out of a total of N_∞ snapshots, and it can be shifted in time. The corresponding test set begins immediately after the end of each training set. The weighted convolutional coordinates, $\tilde{\boldsymbol{a}}$, are weighted through the first half of the block in equation (7.17), i.e., $h_- = 1 - N_f$ and $h_+ = 0$. This arrangement confirms the causality of the model.

7.5.1 Stochastic complex Ginzburg–Landau equation

We first consider the SCGL equation,

$$\frac{\partial}{\partial t} q = \left(-\nu \frac{\partial}{\partial x} + \gamma \frac{\partial^2}{\partial x^2} + \mu \right) q - \xi q |q|^2 + \int_\Omega g(x,x') \eta(x') w(x') \, \mathrm{d}x', \tag{7.30}$$

which is widely used as a model to study instabilities in spatially evolving flows. Here, the parameter μ is expressed in a quadratic form as $\mu(x) = \mu_0 - C_\mu^2 + \frac{\mu_2}{2} x^2$, see, e.g., [13, 47, 54, 109, 275]. The parameter selection follows Ilak *et al.* [112]. Specifically, we choose the supercritical case with $\mu_0 = 0.41$, where the linear component of the SCGL equation is globally

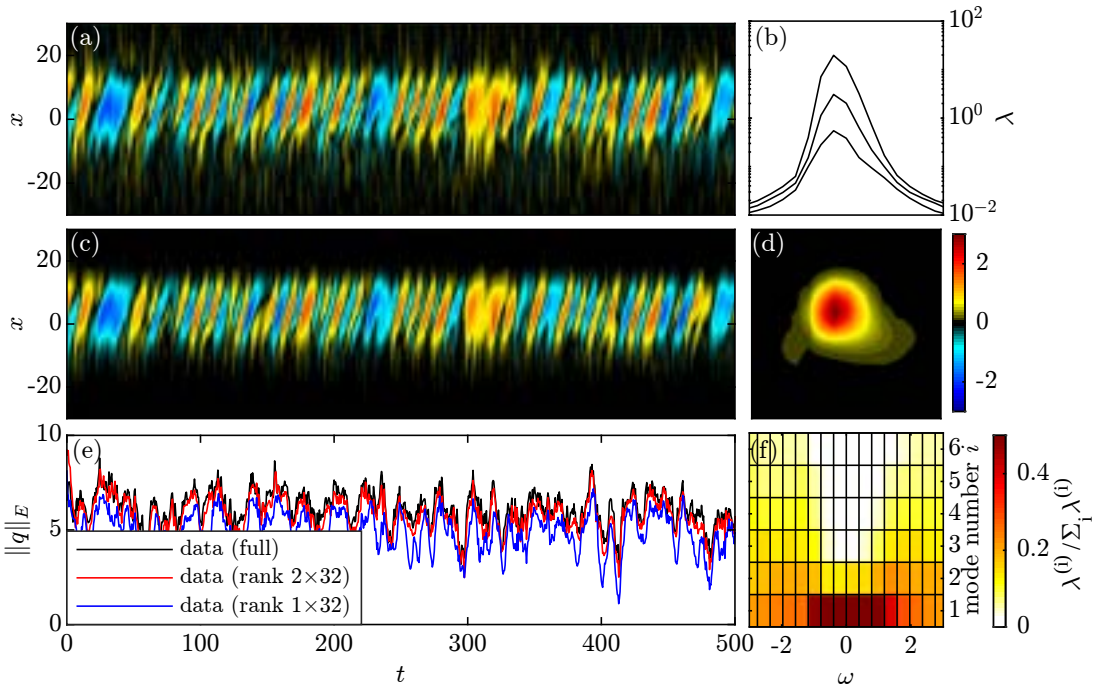

Figure 7.2. Overview of the stochastic complex Ginzburg-Landau equation. Time domain: temporal evolution for full data (a), rank 2×32 data (c), and energy (e). Frequency domain: the first three SPOD eigenvalue spectra (b), weighted leading SPOD modes $\sqrt{\overline{\|q\|}\lambda(\omega)}\psi(x;\omega)$ (d), and the percentage of energy accounted by each mode (f) as functions of frequency.

unstable [50, 107] exhibits similarities to vortex shedding in the presence of crossflow past a cylinder [108, 205]. Additionally, including a cubic nonlinearity with $\xi = 0.1$ induces a limit cycle behavior in the system. The Gaussian white noise input, $w \sim \mathcal{N}(0,1)$, has a uniformly distributed phase spanning from 0 to 2π and is spatially constrained with an exponential envelope of $\eta(x) = \exp[-(x/60)^{10}]$. The Gaussian kernel function, $g(x,x') = \frac{1}{4\sqrt{2\pi}}\exp\left[-\frac{1}{2}\left(\frac{x-x'}{4}\right)^2\right]$, is utilized to spatially correlate the white noise input to enhance statistical convergence [275]. To generate data, the computational domain, $x \in [-85, 85]$, is discretized using $N_q = 220$ uniformly distributed nodes and a 6th-order finite difference scheme [172]. The fourth-order stochastic Runge-Kutta algorithm (SRK4) by Kasdin [133, 134] is employed to numerically integrate equation (7.30) over time. Panels 7.2(a,e) show the temporal evolution of the spatial pattern and the corresponding energy, respectively.

We perform SPOD using $N = 20000$ snapshots at a time step of $\Delta t = 0.5$, a block size of

$N_f = 32$, and an overlap of 75%. Panels 7.2(b,d) show the first three SPOD eigenvalue spectra and the leading SPOD modes as a function of the angular frequency $\omega = 2\pi f$, respectively. The SPOD eigenvalue attains its peak at $\omega = -0.39$. Figure 7.2(f) presents the energy distribution among different modes, indicating that the first two modes capture most of the energy, specifically accounting for 92.5% of the total energy. As shown in panels 7.2(c,e), the data reconstruction using 2×32 modes, $\check{\boldsymbol{q}}_{2\times 32}$, demonstrates remarkable accuracy. Hereafter, we will use the first two SPOD modes to construct the ROM. No regularization is implemented in this case. The model assumptions are later verified in appendix C.2.

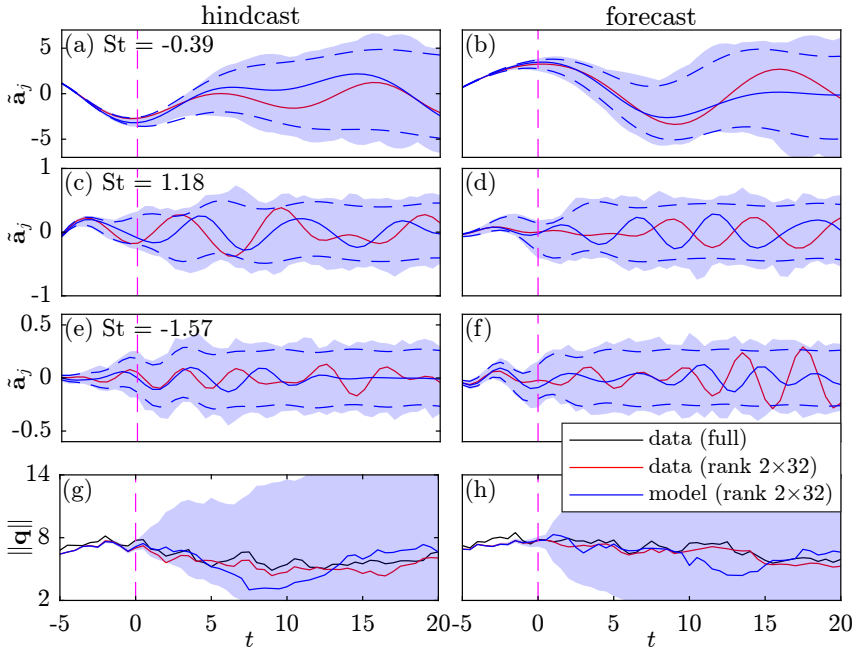

Figure 7.3. Hindcast (a,c,e,g) and forecast (b,d,f,g) for the SCGL equation through a single realization of the SLICK model (blue) in terms of the leading $\tilde{\boldsymbol{a}}$ at three representative frequencies: (a-b) St=-0.39, (c-d) St=1.18, and (e-f) St=-1.57, along with (g-h) the total energy of the state field. Shown for comparison are the full SCGL data (black) and the rank 2×32 data (red). Magenta dashed lines show the onset of prediction. Blue dashed lines mark the analytic 95% confidence interval. The shaded area is a Monte Carlo envelope based on 5000 model evaluations.

We first assess the model using one initial condition within the training set. Panels 7.3 (a,c,e,g) compares the rank 2×32 data and a single realization of the stochastic rank 2×32 model for the hindcast. Starting from the onset of prediction ($t = 0$), this example of realization follows the initial transient dynamics of the data for approximately 3 time units. Model UQ

is performed through the utilization of both the analytical 95% confidence interval and 5000 Monte Carlo simulations, showing that larger variations are possible in later time periods, but the model is bounded within an expected range. Notably, the envelope of the uncertainty for total energy only tends to expand when the prediction starts. Next, we evaluate the model using a single initial condition from the test set to make forecasts, as shown in panels 7.3 (b,d,f,h). The overall trend closely resembles those obtained in the hindcast, indicating that the dataset is well-conver

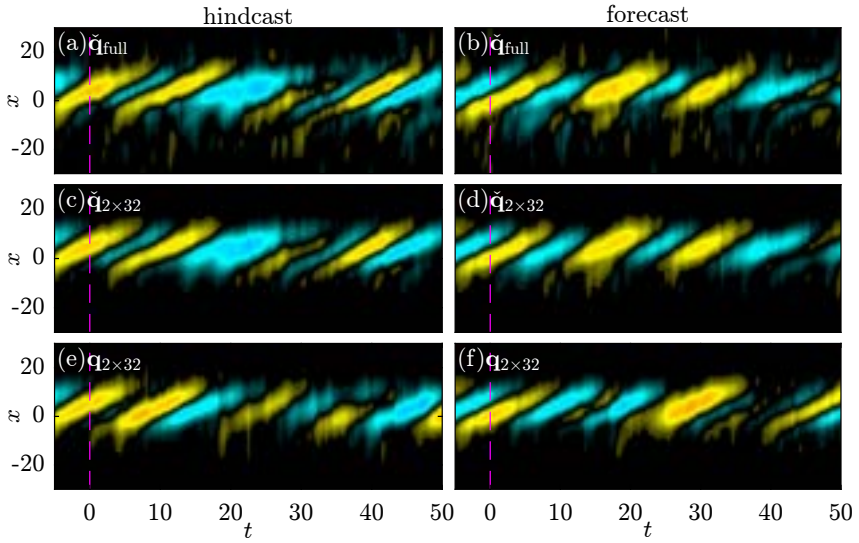

Figure 7.4. Spatial-temporal evolution of the full data (a-b), the rank 2×32 data (c-d) and the rank 2×32 model (e-f) for hindcast (a,c,e) and forecast (b,d,f).

Next, we compare the spatial-temporal evolution of the full data, the rank 2×32 data, and the model for both hindcast and forecast in figure 7.4. The overall dynamics are, arguably, qualitatively well-predicted up to $t = 10$ for both cases. At later times, the large-scale structures are still well-predicted for hindcast. While the phase may exhibit subsequent deviations, the model continues to predict the occurrence of large-scale structures in forecasts.

For qualitative assessment of the model across various initial conditions and independent

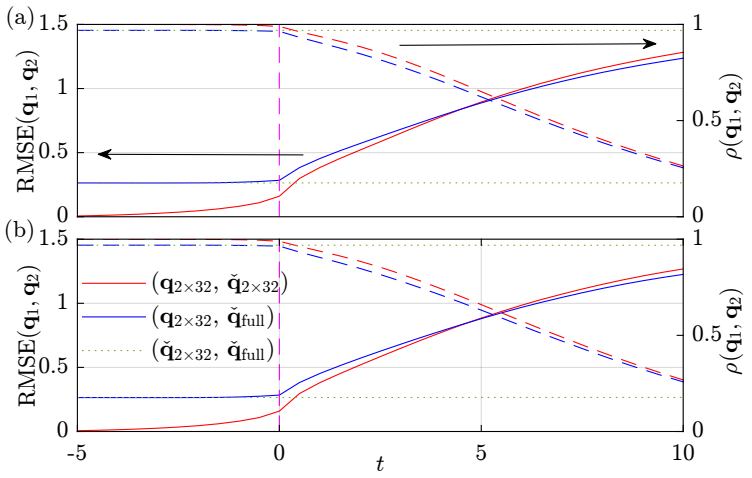

Figure 7.5. Normalized RMSE (left) and correlation (right) for hindcast (a) and forecast (b). 2000 initial conditions are used to run the model, with each initial condition undergoing 200 Monte Carlo simulations. Shaded areas of the same color show the largest variance (overlapping regions appear purple). Results between $\check{\boldsymbol{q}}_{2\times32}$ and $\check{\boldsymbol{q}}_{\text{full}}$ are shown as comparisons (green-dotted).

stochastic inputs, we consider two different metrics: the Pearson correlation coefficient

$$\rho(\boldsymbol{q}_1, \boldsymbol{q}_2) = \frac{\mathrm{E}\{(\boldsymbol{q}_1 - \mathrm{E}\{\boldsymbol{q}_1\})^* \boldsymbol{W} (\boldsymbol{q}_2 - \mathrm{E}\{\boldsymbol{q}_2\})\}}{\sqrt{\mathrm{E}\{\|\boldsymbol{q}_1 - \mathrm{E}\{\boldsymbol{q}_1\}\|^2\}\mathrm{E}\{\|\boldsymbol{q}_2 - \mathrm{E}\{\boldsymbol{q}_2\}\|^2\}}}, \tag{7.31}$$

and the normalized root-mean-square error (RMSE)

$$\mathrm{RMSE}(\boldsymbol{q}_1, \boldsymbol{q}_2) = \sqrt{\mathrm{E}\Big\{\frac{\|\boldsymbol{q}_1 - \boldsymbol{q}_2\|^2}{\|\boldsymbol{q}_2\|^2}\Big\}}. \tag{7.32}$$

Figure 7.5 shows the normalized RMSE and correlation for 2000 initial conditions, with each undergoing 200 Monte Carlo simulations. The overall results for hindcast and forecast are comparable. The model exhibits a slight deviation from the low-rank data at $t = 0$, yet it demonstrates a nearly identical difference compared to the full data. At $t \simeq 6$, the normalized RMSEs are nearly 1, and the correlation coefficients are around 0.5 compared to both the low-rank and full data. This indicates a prediction of fair accuracy along with a moderate positive correlation. We can thus regard the prediction horizon of the model as approximately $t \lesssim 6$.

Having confirmed that the model successfully reproduces a surrogate flow field exhibiting

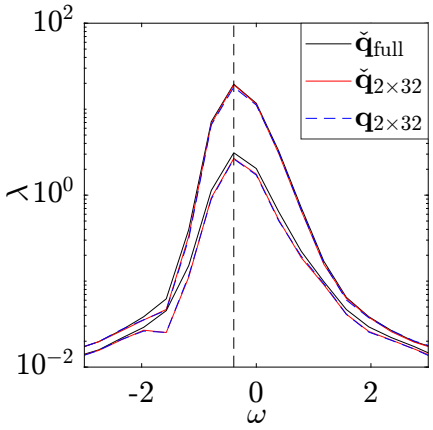

Figure 7.6. Comparison of SPOD eigenvalue spectra of the full data (black), rank 2×32 data (red) and rank 2×32 model (blue).

both qualitative and quantitative similarities to the data, our attention now shifts to the flow statistics. A natural choice is also to employ SPOD for this purpose. Figure 7.6 compares the leading two SPOD eigenvalues of $\check{\boldsymbol{q}}_{\text{full}}$, $\check{\boldsymbol{q}}_{2\times32}$, and $\boldsymbol{q}_{2\times32}$. It can be observed that the SPOD eigenvalue spectra for $\boldsymbol{q}_{2\times32}$ and $\check{\boldsymbol{q}}_{2\times32}$ are indistinguishable, both of which closely resemble those of $\check{\boldsymbol{q}}_{\text{full}}$. The aforementioned results validate that the rank 2×32 model accurately performs hindcast and forecast tasks qualitatively, quantitatively, and statistically.

7.5.2 A turbulent jet

We next consider the LES data of a turbulent jet described in §2.3.4. The SPOD-based Galerkin model in §6 requires the knowledge of the linearized Navier-Stokes operator and all primitive variables. In this work, we only take the pressure field as the representation of the flow state to assess the proposed data-driven model. The weighted pressure 2-norm is used to quantify the flow energy. Figure 7.7 provides a comprehensive overview of the turbulent jet in both temporal and frequency domains. Here, SPOD is performed using a block size of $2N_f = 128$, and an overlap of 75% for the best practice of the model. Panel 7.7(g) shows the frequency-time diagram and reveals intermittent events. As an example, the instant marked as blue dashed lines in panels 7.7(g,h) highlights a high-energy event that corresponds to low-frequency downstream wavepackets, see panel 7.7(a). This supports the motivation for incorporating an exogenous

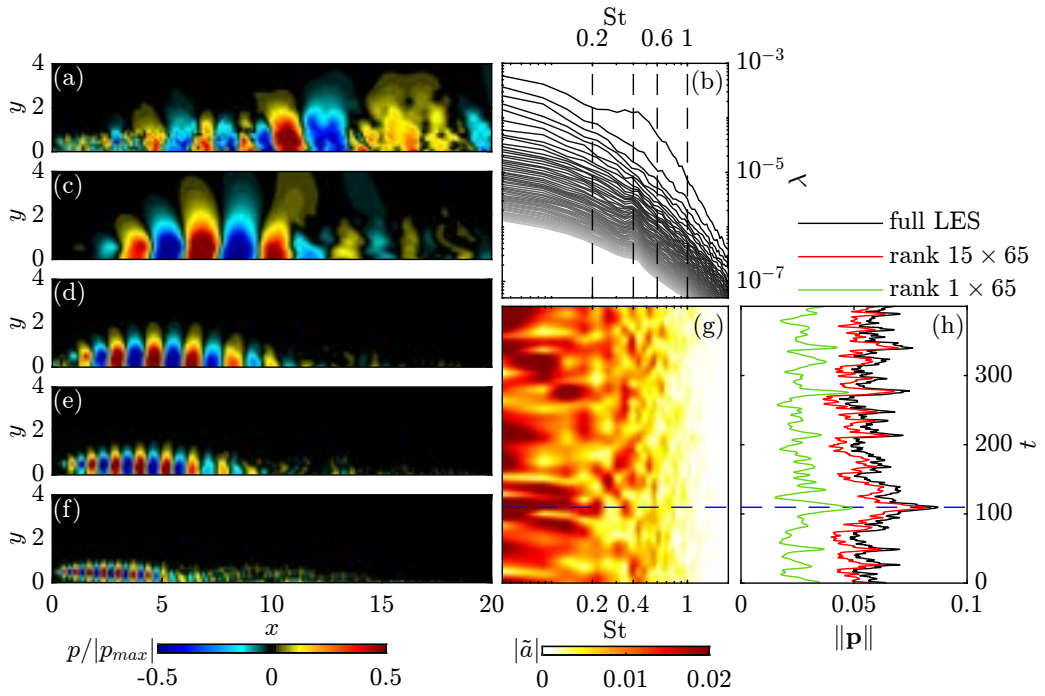

Figure 7.7. Overview of the turbulent jet: (a) instantaneous pressure field (marked as blue dashed lines in (g,h)); (b) SPOD eigenvalue spectra; Leading SPOD modes at 4 representative frequencies (black dashed): (c) St= 0.2; (d) St= 0.4; (e) St= 0.6; (f) St= 1; (g) frequency-time diagram in terms of $|\tilde{a}|$; (h) time traces of the weighted pressure 2-norm.

forcing term in the equation (7.19) to trigger these events. In the following, we construct the model for the jet using the first 15 modes of all 65 non-negative frequency components that contain 83.6% of the energy. As shown in panel 7.7(h), the rank 15×65 data, $\check{\boldsymbol{p}}_{15\times65}$, provides a promising reconstruction that accurately captures the dynamics of the full LES data, $\check{\boldsymbol{p}}_{\text{full}}$. The training set comprises $N = 9000$ consecutive snapshots. The L2 regularizations are performed with $\gamma_1/\mathrm{E}\{\|\boldsymbol{a}\|^2\} = 10^{-3}$ and $\gamma_2/\mathrm{E}\{\|\boldsymbol{y}\|^2\} = 10^{-4}$ for best practices.

Similar to figure 7.3, we compare the rank 15×65 data and a single realization of the rank 15×65 model in figure 7.8. A favorable agreement is observed between the low-rank data and the model for hindcast. Commencing from the onset of prediction ($t = 0$), the envelope of the uncertainty region closely follows the general trend of the data, arguably, up to $t = 15$. Results for the forecast are shown in panels 7.8 (b,d,f,h). Unlike the case for the SCGL equation, the model exhibits deviations from the reference at an earlier time ($t \simeq 5$) compared to the hindcast, yet it

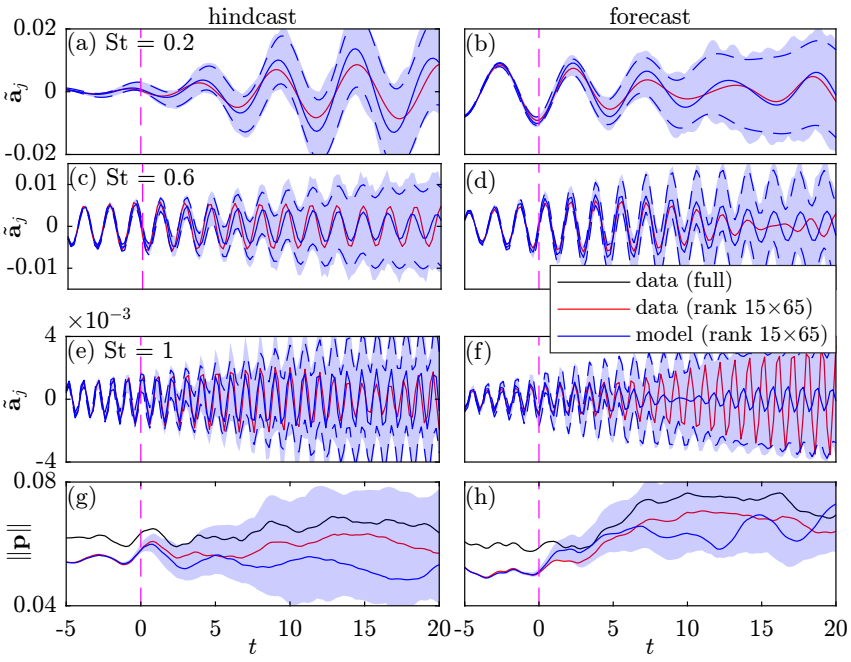

Figure 7.8. Hindcast (a,c,e,g) and forecast (b,d,f,h) for the turbulent jet through a single realization of the SLICK model (blue) in terms of the leading $\tilde{\boldsymbol{a}}$ at three representative frequencies: (a-b) St=0.2, (c-d) St=0.6, and (e-f) St=1, along with (g-h) the total energy of the pressure field. Shown for comparison are the full LES data (black) and the rank 15×65 data (red). Magenta dashed lines show the onset of prediction. Blue dashed lines mark the analytic 95% confidence interval. The shaded area is a Monte Carlo envelope based on 3000 model evaluations.

continues to predict the initial and overall dynamics effectively. This suggests that the model has not achieved complete convergence with the utilization of 9000 snapshots for a turbulent jet, and incorporating additional snapshots could contribute to enhancing its performance.

To examine the contributions of these convolutional coordinates to the surrogate flow field, we compare the instantaneous pressure fields from $t = 0$ to $t = 5$ for the full LES data, the rank 15×65 data, and the model. Figure 7.9 shows the results for hindcast. It can be observed that the model closely resembles the low-rank data (and therefore the full data) up to $t \simeq 2$, and even at $t = 5$, it accurately captures many prominent features of the pressure field. Due to the stochastic nature of the problem and the convective nature of the jet, the similarity of the upstream patterns fades more quickly. Instead, the stochastic model will yield a surrogate flow field that accurately reproduces the second-order statistics of the jet.

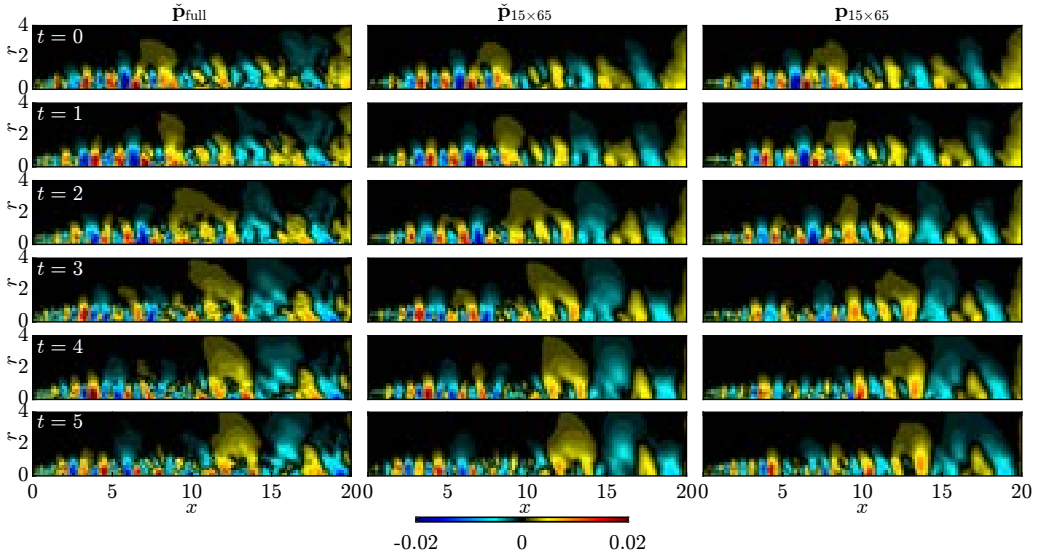

Figure 7.9. Pressure field hindcast for the turbulent jet at different leading times: (left) the full LES data; (middle) the rank 15×65 data; (right) a random realization of the SLICK model.

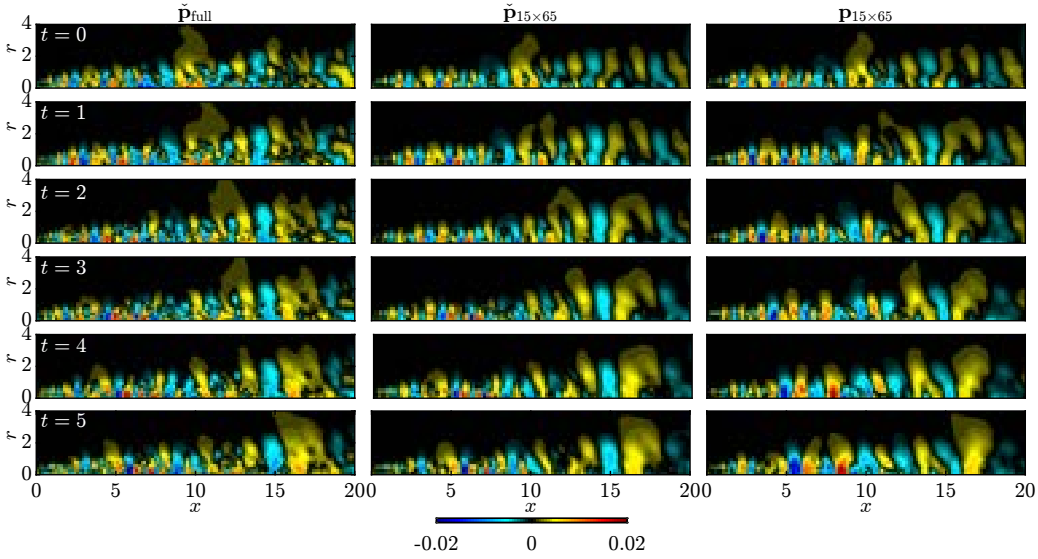

Figure 7.10. Same as figure 7.9 but for forecast.

We next show the results for forecast in figure 7.10. The model deviates from the data at an earlier time around $t \simeq 3$. Given the challenge in real-time prediction for turbulent flows with a high Reynolds number, this result is expected. At larger times, the SLICK model exhibits significant discrepancy from the data, yet the second-order statistics remain.

To examine the continuous spatial-temporal evolution of the flow field, we show the

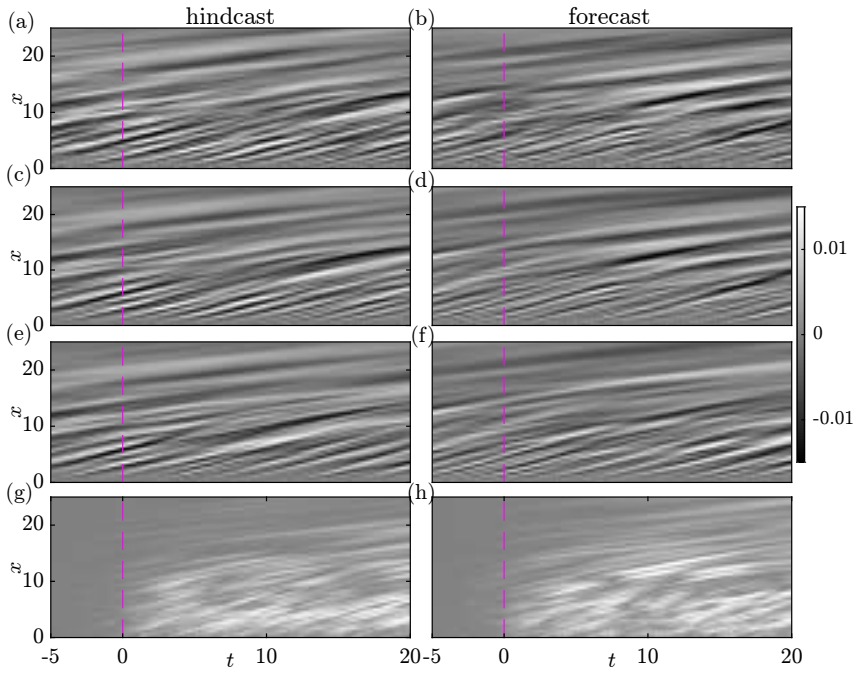

Figure 7.11. Comparisons between the full LES data $\check{\boldsymbol{p}}_{\text{full}}$ (a,b), the rank 15×65 data $\check{\boldsymbol{p}}_{15\times65}$ (c,d), the model $\boldsymbol{p}_{15\times65}$ (e-f), and the absolute error between $\check{\boldsymbol{p}}_{15\times65}$ and $\boldsymbol{p}_{15\times65}$ (g-h) for hindcast (a,c,e,g) and forecast (b,d,f,h) at $r = 0.5$ for different times.

x-t diagrams at $r = 0.5$ (along the lip line) for both hindcast and forecast in figure 7.11. The convective characteristics of the flow field manifest through the diagonal pattern associated with the propagation of the wavepackets previously seen in figures 7.9 and 7.10. The model demonstrates general dynamics that closely resemble those of $\check{\boldsymbol{p}}_{15\times65}$ and $\check{\boldsymbol{p}}_{\text{full}}$ for both hindcast and forecast. More specifically, the model accurately predicts the initial transient dynamics up to $t \simeq 5$ for the hindcast and around $t \simeq 3$ for the forecast. As shown in panels 7.11(g,h), the discrepancy between the model and the low-rank data is predominantly evident at the inlet before propagating downstream. Again, this originates from the convective nature of the jet.

Figure 7.12 shows the normalized RMSE and correlation for the hindcast and forecast of the jet. Unlike the case for SCGL in figure 7.5, the overall results for the hindcast outperform those for the forecast, which can also be qualitatively observed in figures 7.9-7.11. The correlation coefficients are around 0.5 at $t \simeq 5$ for the hindcast and $t \simeq 3$ for the forecast, quantitatively confirming the corresponding prediction horizons for each case.

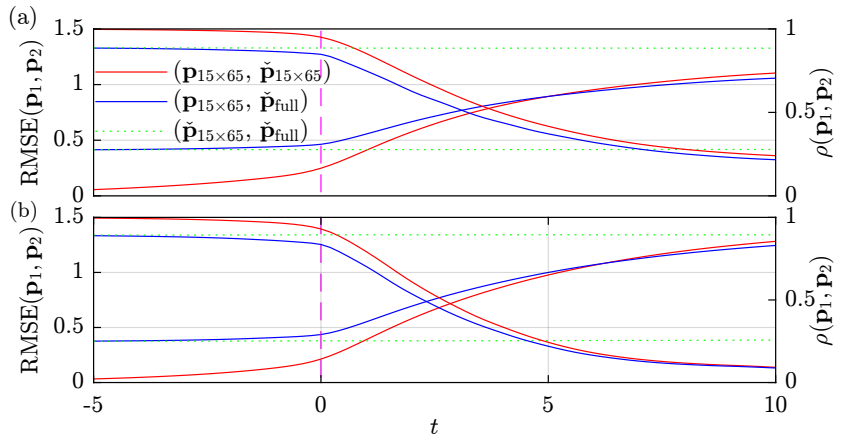

Figure 7.12. Normalized RMSE (left) and correlation (right) for the hindcast (a) and forecast (b) of the jet. 500 initial conditions are used to run the model, with each undergoing 50 Monte Carlo simulations. Results between $\check{\boldsymbol{p}}_{15\times65}$ and $\check{\boldsymbol{p}}_{\text{full}}$ are shown as comparisons (green-dotted).

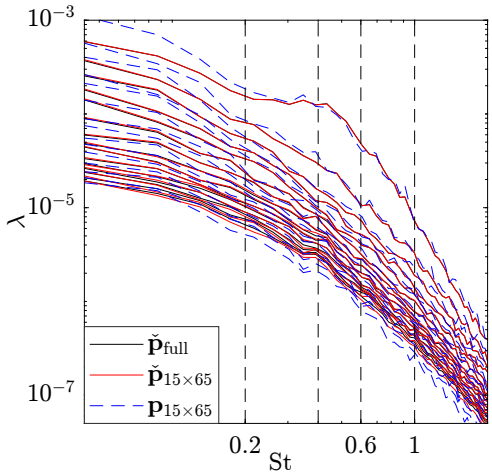

Figure 7.13. Comparison of SPOD eigenvalue spectra of the LES data (black), the rank 15×65 data (red), and model (blue).

Finally, we validate that the model accurately reproduces the second-order statistics of the high-Reynolds number turbulent jet. Figure 7.13 compares the SPOD eigenvalue spectra of the surrogate flow field produced by the model with those of both the full LES and low-rank data. Except for minor deviations at low frequencies, the model closely matches the eigenvalue spectra of the LES data, especially in the frequency range $0.2 \lesssim \text{St} \lesssim 1.2$, where different physical mechanisms are active in turbulent jets [88, 201, 236, 237, 262, 270, 273]. This suggests that the surrogate flow field conveys relevant physical interpretations.

7.5.3 An open cavity flow

Finally, we consider the experimental data of a high-Reynolds number flow over an open cavity obtained from time-resolved particle image velocimetry (TR-PIV) measurements. The measurement noise is present in this dataset. The center plane of the open cavity has a length-to-depth ratio of $L/D = 6$ and a width-to-depth ratio of $W/D = 3.85$. The Reynolds number based on the cavity depth is $\mathrm{Re} = \rho U_\infty D/\mu \approx 3.3 \times 10^5$, and the Mach number is $M = U_\infty/c_\infty = 0.6$. The value of c_∞ represents the far-field speed of sound. Data collection utilized a sampling rate of 16 kHz. For further details, refer to Zhang *et al.*[307, 308]. We non-dimensionalize the spatial coordinates, the velocity components, and time units using D, U_∞, and L/U_∞, respectively. The Strouhal number is defined as $\mathrm{St} = fL/U_\infty$. The flow state is represented as the compound velocity field, $q = [u, v]^T$. The flow energy is quantified using the turbulent kinetic energy, $\mathrm{TKE} = \frac{1}{2}\int_\Omega \left((u')^2 + (v')^2\right) \mathrm{d}\boldsymbol{x}$.

A comprehensive overview of the open cavity flow is provided in figure 7.14, encompassing both the temporal and frequency domains. Here, SPOD is performed using $N_\infty = 16000$ snapshots at a block size of $2N_f = 256$ and an overlap of 75%. These parameters are chosen to provide the best practice for the model performance. The resulting SPOD eigenvalue spectra in panel 7.19(b) match well with those reported by Zhang *et al.* [308] and Schmidt [233], particularly the dominant second and third Rossiter tones. These peaks are also evident in the frequency-time diagram in panel 7.19(g). The SPOD modes with higher energy do not necessarily contribute to the TKE. As an example, panels 7.19(a,g,h) show an instant that is both dominated by the low-frequency modes and corresponds to a high-energy event. The SLICK model is constructed using the first 20 modes of all 129 non-negative frequency components that contain 76.6% of the energy. As shown in panel 7.19(h), the rank 20×129 data, $\check{\boldsymbol{q}}_{20\times129}$, provides a promising reconstruction that accurately captures the dynamics of the full PIV data, $\check{\boldsymbol{q}}_{\mathrm{full}}$. The training set comprises $N = 14400$ consecutive snapshots. The same ridge parameters in §7.5.2 ,$\gamma_1/\mathrm{E}\{\|\boldsymbol{a}\|^2\} = 10^{-3}$ and $\gamma_2/\mathrm{E}\{\|\boldsymbol{y}\|^2\} = 10^{-4}$, are used for L2 regularization.

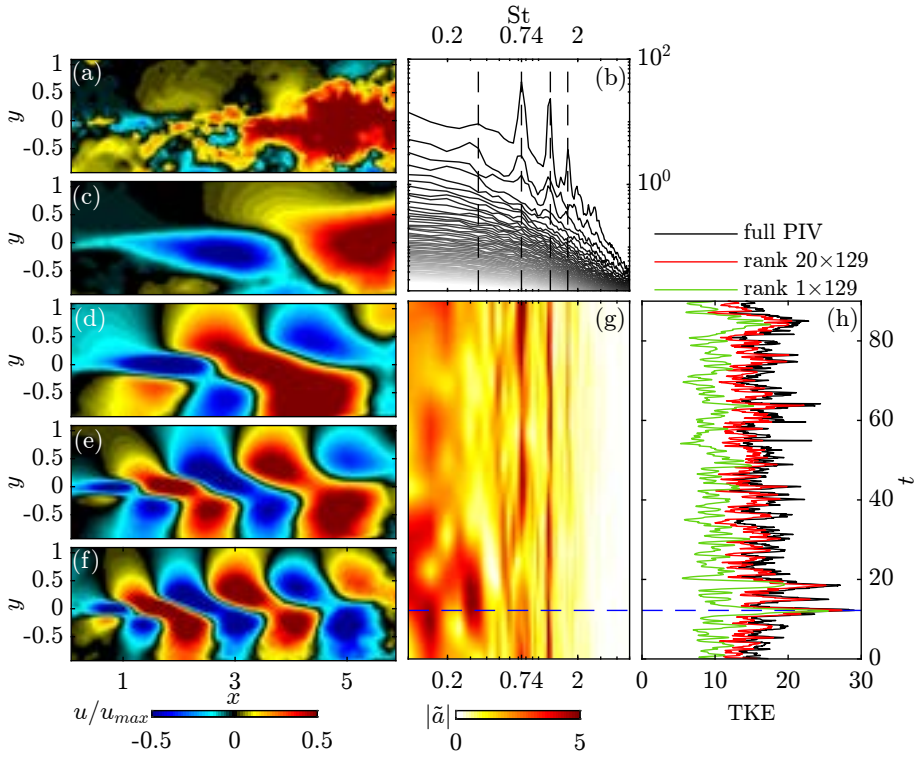

Figure 7.14. Overview of the open cavity flow: (a) instantaneous streamwise velocity (marked as blue dashed lines in (g,h)); (b) SPOD eigenvalue spectra; leading SPOD modes at the first 4 Rossiter frequencies (black dashed): (c) St= 0.34; (d) St= 0.74; (e) St= 1.23; (f) St= 1.67; (g) frequency-time diagram; (h) time traces of TKE.

Figure 7.15 compares the trajectories of the rank 20×129 data and model for both the hindcast and forecast. The two shown realizations demonstrate favorable agreements with the low-rank data. Compared to the SCGL and jet cases (see figures 7.3 and 7.8), the model exhibits much larger uncertainty bounds in the total energy at $t = 0$. This is attributed to the presence of measurement noise, gaps, and artifacts stemming from the PIV measurements within the dataset, leading to increased uncertainty in inferring the dynamical system from the data.

Figure 7.16 compares the instantaneous velocity fields from $t = 0$ to $t = 1.19$ for $\check{\boldsymbol{u}}_{\text{full}}$, $\check{\boldsymbol{u}}_{20\times129}$, and $\boldsymbol{u}_{20\times129}$ for both the hindcast and forecast. For the hindcast, it can be observed that the model closely resembles the data up to half of the flow-through time, $t \simeq 0.48$. Even after unit flow-through time at $t = 1.19$, the model qualitatively captures many prominent features of the streamwise velocity field. As expected, the similarity between the model and the low-rank

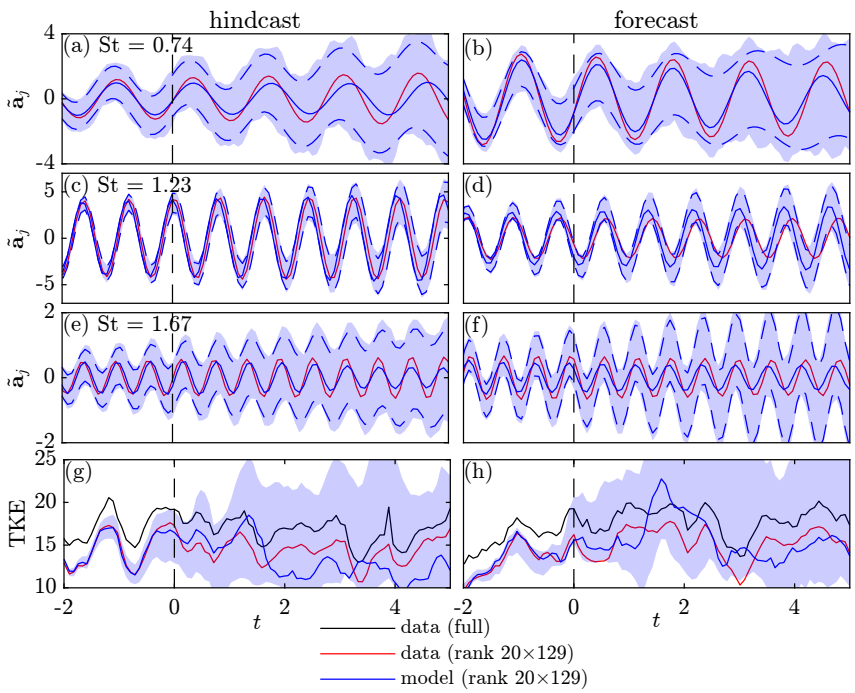

Figure 7.15. Hindcast (a,c,e,g) and forecast (b,d,f,h) for the open cavity flow through a single realization of the stochastic model (blue) in terms of $\tilde{\boldsymbol{a}}$ at three peak Rossiter frequencies: (a-b) St=0.74, (c-d) St=1.23, and (e-f) St=1.67, along with (g-h) the total TKE. Shown for comparison are the full PIV data (black) and the rank 20×129 data (red). Blue dashed lines mark the analytic 95% confidence interval. The shaded area is a Monte Carlo envelope based on 3000 model evaluations.

data diminishes more rapidly for the forecast. The prediction horizon ends at approximately one-quarter of the flow-through time, $t \simeq 0.24$. After that, the surrogate flow field will emulate the second-order statistics rather than the dynamic behavior of the open cavity flow.

Similar to figure 7.11, we show the x-t diagrams at $y = 0$ for both the hindcast and forecast for the open cavity flow in figure 7.17. The model closely resembles the general convective behavior of the flow field. Consistent with 7.16, the model for the hindcast has a longer prediction horizon than the forecast. Unlike the case of the jet, the discrepancy between $\check{\boldsymbol{u}}_{20\times129}$ and $\boldsymbol{u}_{20\times129}$ does not originate from the inlet, where the velocity profile is nearly uniform, but rather from the middle part of the cavity, where the recirculation region is located.

Figure 7.18 shows the error analysis of the SLICK model. Compared to figures 7.5 and 7.12, the overall model performance undergoes degradation as a consequence of measurement

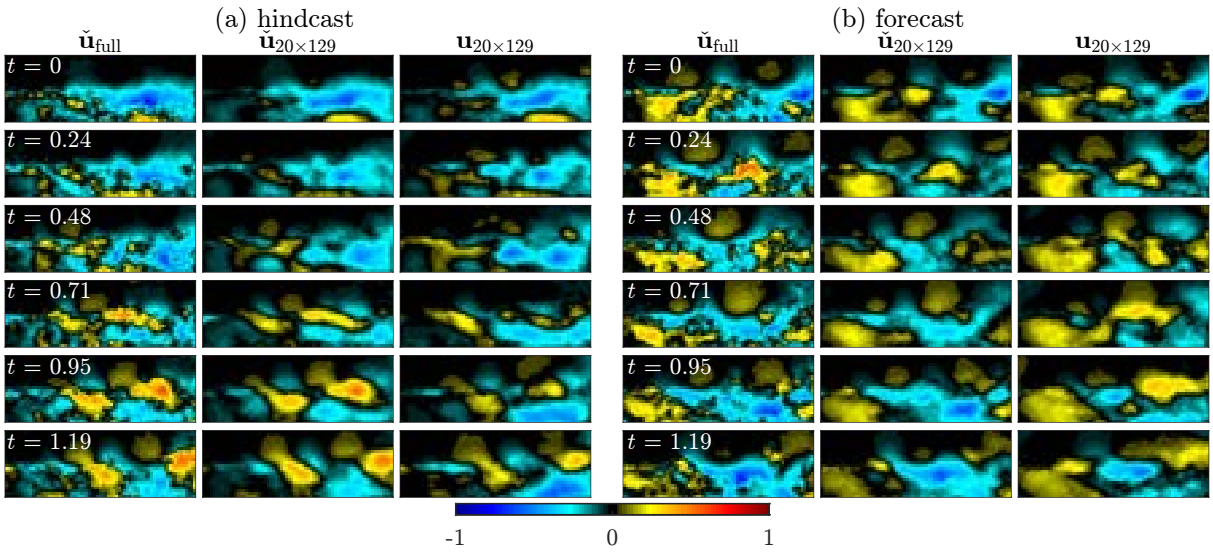

Figure 7.16. Streamwise velocity field hindcast (a) and forecast (b) for the open cavity flow within the domain $x, y \in [0, 6] \times [-1, 1]$ at different leading times.

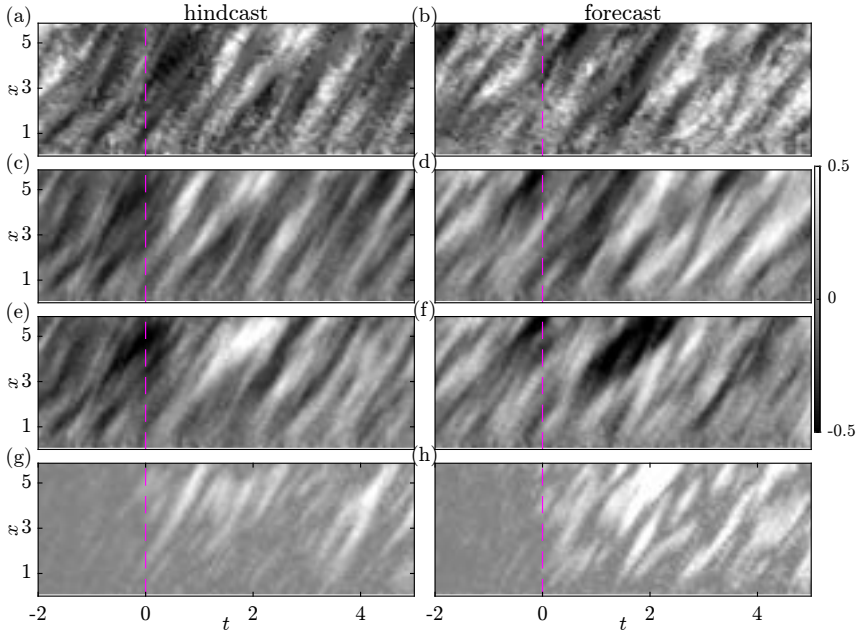

Figure 7.17. Comparisons between the full PIV data $\check{\boldsymbol{u}}_{\text{full}}$ (a,b), the rank 20×129 data $\check{\boldsymbol{u}}_{20\times129}$ (c,d), the model $\boldsymbol{u}_{20\times129}$ (e-f) and the absolute error between $\check{\boldsymbol{u}}_{20\times129}$ and $\boldsymbol{u}_{20\times129}$ (g-h) for the hindcast (a,c,e,g) and the forecast (b,d,f,h) at $y = 0$ for different times.

noise and gaps within the data. These challenges are intrinsic to PIV measurements, rendering the modeling of PIV data a complex endeavor. Despite this, our model yields qualitatively accurate predictions ($\rho \gtrsim 0.5$) for hindcasting at $t \simeq 1$ and forecasting at $t \simeq 0.25$.

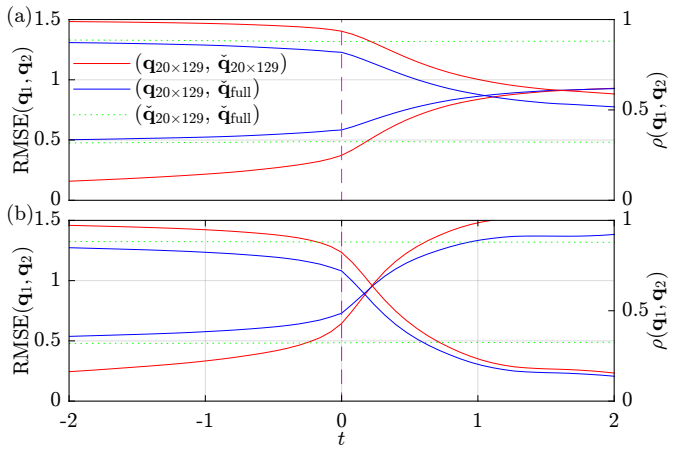

Figure 7.18. Normalized RMSE (left) and correlation (right) for hindcast (a) and forecast (b) of the open cavity flow. 300 initial conditions are used to run the model, with each undergoing 50 Monte Carlo simulations. Results between $\check{\boldsymbol{q}}_{20\times129}$ and $\check{\boldsymbol{q}}_{\text{full}}$ are shown as comparisons (green-dotted).

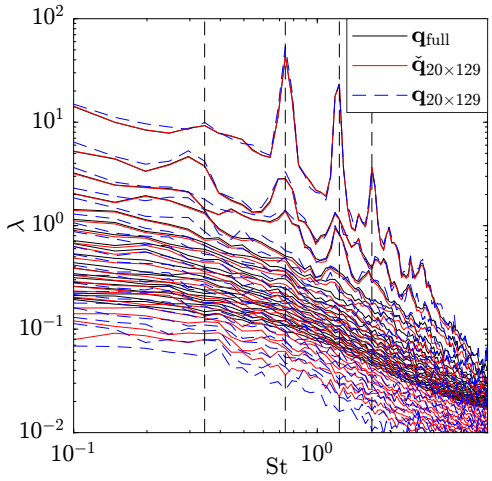

Figure 7.19. Comparison of SPOD eigenvalue spectra of the full PIV data (black), the rank 20×129 data (red), and model (blue).

Figure 7.19 compares the SPOD eigenvalue spectra of $\boldsymbol{q}_{20\times129}$ with those of both $\check{\boldsymbol{q}}_{20\times129}$ and $\check{\boldsymbol{q}}_{\text{full}}$. The model closely matches the eigenvalue spectra of the data, particularly at the peak Rossiter frequencies, therefore preserving the second-order statistics of the flow field. In accordance with the conjectures drawn above, we conclude that the SLICK model can effectively generate accurate surrogate flow fields for the PIV data in both qualitative and statistical aspects.

Chapter 7, in full, is currently being prepared for submission for publication of the

material. The dissertation author was the primary investigator and author of this paper.

Chapter 8

Equations of motion for weakly compressible point vortices

In the incompressible argument, point vortices have no internal structures, but for the compressible case, we will need to consider the flow in the vortex cores on scales of $O(M)$ smaller than the distance between vortices. In addition, at large distances of $O(M^{-1})$ from the vortical region, as pointed out by Leppington [153], the Rayleigh–Jansen expansion will become disordered, indicating the presence of a wavelike far field. This feature was already present in previous work on sound generation by vortical flows in aeroacoustics using Matched Asymptotic Expansions (MAE; see [55, 191] for an overview).

The Rayleigh–Jansen expansion is an expansion in small Mach number. Before writing it down in § 8.1, we consider the momentum equation in complex form, as in Llewellyn Smith [157], taken over the small circle with radius e. We take $e \gg M$, as we are interested in the momentum balance over circles that are asymptotically small with respect to the region between vortices but much larger than the vortex cores, i.e. e is an intermediate variable in the terminology of MAE. This means that one can use either the core solution or the vortex solution when evaluating the right-hand side of (1.4), since the terms on the right-hand side are all contour integrals evaluated at radius e. The left-hand side, however, is a surface integral that must be calculated in the inner variable. To leading order in M, we have $\hat{\Phi} = \kappa\theta$ where $\kappa = \Gamma/(2\pi)$ is

the scaled circulation and θ is the polar angle, so that in vectorial form, the momentum is

$$\oint \int_{s_v}^{e/M} \hat{\rho}(M^{-1}\hat{\nabla}\Phi)M^2 s\,\mathrm{d}s\,\mathrm{d}\theta \approx M^2 \oint \int_{s_v}^{e/M} \left[1-(\gamma-1)\frac{\kappa^2}{2s^2}\right]^{1/(\gamma-1)} \left[\frac{\kappa}{Ms}\boldsymbol{t}+\boldsymbol{U}\right] s\,\mathrm{d}s\,\mathrm{d}\theta, \tag{8.1}$$

where $\boldsymbol{t}$ is the unit vector tangential to the circle. The lower limit s_v is the smallest value of s for which the pressure and density in (1.7–1.8) are positive, and is obtained from the condition $2{s_v}^2 = (\gamma-1)\kappa^2$. We see that the term in $\boldsymbol{t}$ cancels by symmetry. In complex form, we then obtain

$$P = \pi\overline{W}\left[e^2 + \kappa^2 M^2 \log M - \kappa^2 M^2 \log e + M^2 C + O\left(\frac{M^4}{e^2}\right)\right], \tag{8.2}$$

for $e \gg M$, where

$$C = 2\int_{s_v}^{\infty} \left\{\left[1-(\gamma-1)\frac{\kappa^2}{2s^2}\right]^{\beta} - 1 + \frac{\kappa^2}{2s^2}\right\} s\,\mathrm{d}s - {s_v}^2 + \kappa^2 \log s_v \tag{8.3}$$

$$= 2\beta[\psi(\beta) - \psi(1) - 1] + 2 - {s_v}^2 + \kappa^2 \log s_v, \tag{8.4}$$

where $\psi(z)$ is the digamma function and we write $\beta = (\gamma-1)^{-1}$ for brevity. We see that (8.2) contains a term of $O(M^2 \log M)$ if the flow is unsteady. This means that such a term must exist in appropriate time-derivatives of the Rayleigh–Jansen expansion, either as a term in the expansion or as a result of slow time variation.

Terms in the Rayleigh–Jansen expansion will evolve on slow time scales to allow the position of vortices to change. Figure 8.1 illustrates the different regions of the flow and gives some notation.

8.1 Derivation of the equation of motion for a vortex

8.1.1 Rayleigh–Jansen expansion of the global solution in the vortical region and time dependence

Motivated by the discussion above, we consider a modified version of the Rayleigh–

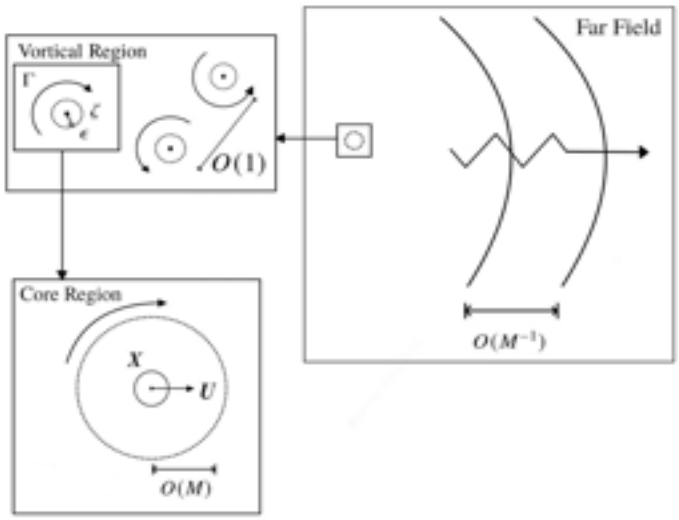

Figure 8.1. Schematic illustrating the different regions of the flow.

Jansen expansion in the form

$$\phi(t,z,\bar{z}) = \phi_0(t,z) + M^2 \log M \phi_1(t,z) + M^2 \phi_2(t,z,\bar{z}) + \cdots, \tag{8.5}$$

where the arguments of the two first terms reflect the fact that they correspond to incompressible flow in the vortical region, since from (1.6) we have $\nabla^2\phi_0 = \nabla^2\phi_1 = 0$. The governing equation for ϕ_2,

$$\nabla^2\phi_2 = \frac{\partial^2\phi_0}{\partial t^2} + 2\frac{\partial\phi_0}{\partial x_i}\frac{\partial^2\phi_0}{\partial x_i \partial t} + \frac{\partial\phi_0}{\partial x_i}\frac{\partial\phi_0}{\partial x_j}\frac{\partial^2\phi_0}{\partial x_i \partial x_j}, \tag{8.6}$$

does not contain γ.

Define a complex potential $F_0 = \phi_0 + \mathrm{i}\psi_0$, since the flow at leading order is incompressible and irrotational. Similarly there is a complex potential $F_1 = \phi_1 + \mathrm{i}\psi_1$. These potentials are harmonic functions that decay far from the vortex. Since F_0 has logarithmic singularities, F_1 cannot have singularities of higher order, while logarithmic singularities in F_1 are disallowed by requiring the vorticity to be entirely at $O(1)$. Hence, as an analytic function bounded at infinity with no singularities, F_1 is a constant that can be taken to be 0 without loss of generality.

This means that the Rayleigh–Jansen expansion does not have a term at $O(M^2 \log M)$. The term entering the matching from (8.2) must come from taking the $O(M^2 \log M)$ time dependence into account appropriately, as is done in (8.10) below. Using $\phi_0 = (F_0 + \overline{F_0})/2$, (8.6) becomes

$$\nabla^2 \phi_2 = 2\frac{\partial^2 F_2}{\partial z \partial \overline{z}} + c.c. = \frac{1}{2}(F_{0tt} + 2F_{0z}\overline{F_{0zt}} + F_{0zz}\overline{F_{0z}^2} + c.c.), \tag{8.7}$$

where $c.c.$ stands for complex conjugate and we have defined a function $F_2(t, z, \overline{z})$ such that $\phi_2 = (F_2 + \overline{F}_2)/2$. Note that, because the flow at $O(M^2)$ is no longer incompressible, there is no streamfunction corresponding to ϕ_2, so we call F_2 a potential but not a complex potential. Only the real part of F_2 matters, and the complex velocity $w_2 = u_2 - \mathrm{i}v_2$ is given by $w_2 = \partial_z(F_2 + \overline{F}_2)$. We can integrate (8.7) and obtain a particular solution for ϕ_2 as the real part of

$$F_2(z, \overline{z}) = \frac{1}{4}(z - Z_0)\overline{J(z)} + \frac{1}{2}F_{0t}(z)\overline{F_0(z)} + \frac{1}{4}w_0(z)\overline{I(z)} + G(z), \tag{8.8}$$

where Z_0 is a time-dependent centre of vorticity that can be picked to simplify the analysis for specific cases. The functions $I(z)$ and $J(z)$ are defined globally by

$$I(z) = \int_{z_I}^{z} w_0^2 \, \mathrm{d}z, \qquad J(z) = \int_{z_J}^{z} F_{0tt} \, \mathrm{d}z. \tag{8.9}$$

The integration limits z_I and z_J will also be picked depending on the global nature of the flow. The full $O(M^2)$ potential (8.8) is composed of an inhomogeneous part and a homogeneous part, $G(z)$, which is made up of homogeneous solutions of the Poisson equation (8.6), i.e. solutions of Laplace's equation that can be written as functions of z. They are used to enforce single-valuedness of the velocity field, appropriate behaviour near the vortices and boundary conditions.

It turns out that the location of the vortex is not uniquely defined when it is expanded in Mach number. We can remove this ambiguity by requiring that the location not be expanded in Mach number (this is reminiscent of slaving principles as in Warn *et al.* [292]). However, we need to allow the position to evolve in time at higher order in M to allow matching of the

terms in (8.2). This leads to the use of multiple time scales. Given the form of (8.2), we consider all variables to be functions of $t_0 = t$, $t_1 = tM^2 \log M$ and $t_2 = tM^2$ (and possibly further time scales). We define

$$\frac{\mathrm{d}}{\mathrm{d}t} = \frac{\partial}{\partial t_0} + M^2 \log M \frac{\partial}{\partial t_1} + M^2 \frac{\partial}{\partial t_2} + o(M^2), \tag{8.10}$$

Hence $\mathrm{d}\overline{\zeta}/\mathrm{d}t = W = W_0 + M^2 \log M W_1 + M^2 W_2 + o(M^2)$, so that $W_0 = \overline{\zeta}_{,0}$, $W_1 = \overline{\zeta}_{,1}$, $W_2 = \overline{\zeta}_{,2}$, where we write $\zeta_{,i} = \partial\zeta/\partial t_i$. We can now write pressure and density using the full time dependence by expanding (1.7–1.8) written in complex notation:

$$p_0 = -\frac{1}{2}(|w_0|^2 + F_{0,0} + \overline{F}_{0,0}), \tag{8.11}$$

$$p_1 = -\frac{1}{2}(F_{0,1} + \overline{F}_{0,1}), \tag{8.12}$$

$$p_2 = -\frac{1}{2}(F_{0,2} + \overline{F}_{0,2}) + \frac{1}{8}(|w_0|^2 + F_{0,0} + \overline{F}_{0,0})^2 - \frac{1}{2}(w_0\overline{w}_2 + \overline{w}_0 w_2 + F_{2,0} + \overline{F}_{2,0}), \tag{8.13}$$

$$\rho_2 = -\frac{1}{2}(|w_0|^2 + F_{0,0} + \overline{F}_{0,0}). \tag{8.14}$$

There is a dynamically irrelevant component $p_{-2} = (\gamma M^2)^{-1}$ that can be ignored, while $\rho_0 = 1$.

8.1.2 Local solution for the $O(M^2)$ potential

We now consider the solution near the vortex located at $z = \zeta$. The following expansions provide the terms needed to compute the equations of motion, writing $\varepsilon = z - \zeta$ and $e = |\varepsilon|$:

$$F_0 = -\mathrm{i}\kappa \log\varepsilon + f_0 + f_1\varepsilon + \frac{1}{2}f_2\varepsilon^2 + \frac{1}{3}f_3\varepsilon^3 + o(e^3), \tag{8.15}$$

$$F_{0,0} = \frac{\mathrm{i}\kappa\zeta_{,0}}{\varepsilon} + f_{0,0} - f_1\zeta_{,0} + (f_{1,0} - f_2\zeta_{,0})\varepsilon + o(e), \tag{8.16}$$

$$F_{0,00} = \mathrm{i}\kappa\left[\frac{\zeta_{,00}}{\varepsilon} + \frac{\zeta_{,0}^2}{\varepsilon^2}\right] + f_{0,00} - (f_1\zeta_{,0})_{,0} - (f_{1,0} - f_2\zeta_{,0})\zeta_{,0} + o(1), \tag{8.17}$$

$$J = \mathrm{i}\kappa\left[\zeta_{,00}\log\varepsilon - \frac{\zeta_{,0}^2}{\varepsilon}\right] + J_0 + [f_{0,00} - (f_1\zeta_{,0})_{,0} - (f_{1,0} - f_2\zeta_{,0})\zeta_{,0}]\varepsilon + o(e), \tag{8.18}$$

$$w_0 = -\frac{\mathrm{i}\kappa}{\varepsilon} + f_1 + f_2\varepsilon + f_3\varepsilon^2 + o(e^2), \tag{8.19}$$

$$I = \frac{\kappa^2}{\varepsilon} - 2\mathrm{i}\kappa f_1 \log\varepsilon + I_0 + (-2\mathrm{i}\kappa f_2 + f_1^2)\varepsilon + (-\mathrm{i}\kappa f_3 + f_1 f_2)\varepsilon^2 + o(e^2). \tag{8.20}$$

We have expressed the coefficients of F_0 in the above form for later convenience. The coefficients f_0, f_1, ... depend on time in general. While the coefficient f_0 appears to have no dynamical meaning, it is different from one vortex to another and hence is kept.

The first step is to ensure that the velocity field obtained from F_2 in (8.8) is single-valued. While F_0 has a multi-valued logarithmic term near ζ, the resulting complex velocity, w_0, is single-valued. However, F_2 contains logarithmic terms of the form $\log\overline{\varepsilon}$ multiplied by functions of z. The resulting velocity is not single-valued, but becomes single-valued when adding a homogeneous solution with the same z-dependence multiplied by $\log\varepsilon$. This corresponds to including the following contribution in $G(z)$:

$$l(z)\log(z-\zeta) = \left[\frac{1}{4}(z-Z_0)(-\mathrm{i}\kappa\overline{\zeta}_{,00}) + \frac{1}{2}F_{0,0}(z)(\mathrm{i}\kappa) + \frac{1}{4}w_0(z)(2\mathrm{i}\kappa\overline{f}_1)\right]\log\varepsilon. \tag{8.21}$$

The square bracket defines the function $l(z)$. The effect of (8.21) in the expansion of F_2 near a vortex is to replace $\log\varepsilon$ terms by $\log e^2$.

We then include two homogeneous terms in $G(z)$:

$$\frac{\mu}{z-\zeta} + \xi\log(z-\zeta), \tag{8.22}$$

which allow us to remove unacceptable singularities in F_2 near $\varepsilon = 0$. Since F_0 has logarithmic singularities, F_2 cannot have singularities of higher order, or else the expansion would be disordered near $\varepsilon = 0$. Logarithmic singularities in F_2 are removed by requiring the vorticity to be entirely at $O(1)$. Unlike Crowdy & Krishnamurthy [58] we do not require a term in ε^{-2}.

Finally, the local expansion of $G(z)$ also contains terms from expanding the counterparts of the terms inside the square bracket in (8.8) due to other vortices and to other homogeneous contributions to $G(z)$. From the forms of $F_{0,0}$ and of $I(z)$, the former lead to terms of $O(\varepsilon^{-1})$ as well as analytic terms. The latter are denoted by $K(z)$. The result is a contribution $g_{-1}\varepsilon^{-1} + g_0 + g_1\varepsilon + O(e^2)$ near the vortex. (These contributions are calculated explicitly for the two-vortex

case in § 8.2.)

We can now write down the expansion for F_2 needed to remove singular terms:

$$F_2 = -\frac{\mathrm{i}\kappa^3}{4|\varepsilon|^2} + \frac{\kappa^2 \log e^2}{4\varepsilon}(-2\zeta_{,0} + 2\overline{f}_1) + \frac{1}{4\varepsilon}(2\mathrm{i}\kappa\overline{f}_0\zeta_{,0} - \mathrm{i}\kappa\overline{I_0} + 4\mu + 4g_{-1}) + \frac{\kappa^2}{4\overline{\varepsilon}}f_1 + \frac{\mathrm{i}\kappa}{4\overline{\varepsilon}}(\zeta - Z_0)\overline{\zeta_{,0}^2}$$
$$+ \frac{1}{4}[2\mathrm{i}\kappa(f_{0,0} - f_1\zeta_{,0}) + 2\mathrm{i}\kappa|f_1|^2 - \mathrm{i}\kappa(\zeta - Z_0)\overline{\zeta}_{,00}]\log e^2 + \xi\log\varepsilon + O(1). \tag{8.23}$$

The term in ε^{-2} is purely imaginary and hence can be ignored, while the term in $\varepsilon^{-1}\log e^2$ cancels from the $O(1)$ result, which will be rederived in the current framework and notation below. Since F_2 only enters the solution via its real part, removing the singular terms in its real part leads to the following conditions:

$$2\mathrm{i}\kappa\overline{f}_0\zeta_{,0} - \mathrm{i}\kappa(\overline{\zeta - Z_0})\zeta_{,0}^2 - \mathrm{i}\kappa\overline{I}_0 + 4\mu + \kappa^2\overline{f}_1 + 4g_{-1} = 0, \tag{8.24}$$

$$2\mathrm{i}\kappa(f_{0,0} - f_1\zeta_{,0}) - 2\mathrm{i}\kappa(\overline{f}_{0,0} - \overline{f}_1\overline{\zeta}_{,0}) + 4\xi - \mathrm{i}\kappa(\zeta - Z_0)\overline{\zeta}_{,00} + \mathrm{i}\kappa(\overline{\zeta - Z_0})\zeta_{,00} = 0. \tag{8.25}$$

8.1.3 Conservation of momentum

We now return to the conservation of momentum, viewing it as a matching problem for an expansion in M, with e serving as the independent variable. We define Q as the left-hand side of (1.4) and express it as an expansion in the inner variable, s, and define q as the right-hand side and express it as an expansion in the vortex variable, e. We expand the time-derivative of (8.2) in the inner variable, using $W = W_0 + M^2\log M W_1 + M^2 W_2 + \cdots$ and $\mathrm{d}/\mathrm{d}t = \partial_{,0} + M^2\log M\partial_{,1} + M^2\partial_{,2} + \cdots$, giving

$$Q = \pi[\overline{W}_{0,0} + M^2\log M(\overline{W}_{0,1} + \overline{W}_{1,0}) + M^2(\overline{W}_{0,2} + \overline{W}_{2,0}) + o(M^2)]$$
$$\times [M^2 s^2 - \kappa^2 M^2\log s + M^2 C + O(M^2 s^{-2}))] + O(M^2), \tag{8.26}$$

where the final $O(M^2)$ term includes an as yet unknown dependence on s. In anticipation of using Van Dyke's rule (e.g. [102]), we employ the notation $Q^{(n,.)}$ to denote the n-term truncation

of the function Q and $Q^{(n,m)}$ to denote its subsequent truncation to m terms when rewritten in the outer variable. Then $Q_0 = Q^{(0,.)} = 0$ since there are no $O(1)$ terms in (8.26). Expanding the right-hand side of (1.4) leads to the exact result

$$\begin{aligned} q_0 &= \mathrm{i}\oint_{\mathscr{C}} p_0\,\mathrm{d}z - \frac{\mathrm{i}}{2}\oint_{\mathscr{C}} \overline{w}_0[(\overline{w}_0 - \overline{W}_0)\,\mathrm{d}\overline{z} - (w_0 - W_0)\,\mathrm{d}z] \\ &= \pi\mathrm{i}\kappa[\overline{W}_0 - 2\overline{f}_1 + \zeta_{,0}] + \pi[\overline{f}_{1,0} - \overline{f}_2(\overline{\zeta}_{,0} - W_0)]e^2. \end{aligned} \tag{8.27}$$

The $(0,0)$ term in Van Dyke's rule is $Q^{(0,0)} = q^{(0,0)}$, so that

$$0 = \pi\mathrm{i}\kappa[\overline{W}_0 - 2\overline{f}_1 + \zeta_{,0}]. \tag{8.28}$$

Using $\zeta_{,0} = \overline{W}_0$ leads to

$$\overline{\zeta}_{,0} = W_0 = f_1, \tag{8.29}$$

i.e. the incompressible result expressed in the current notation.

We should now group the $O(M^2\log M)$ and $O(M^2)$ terms together to continue with Van Dyke's rule. We should also compute $Q^{(2,.)}$. We shall avoid doing this, and instead carry out the matching informally. This approach works, but to be safe we will revisit the formal matching in appendix §D.1. In the vortex region, the right-hand side of (1.4) gives the $O(M^2\log M)$ contribution

$$q_1 = \mathrm{i}\oint_{\mathscr{C}} p_1\,\mathrm{d}z - \frac{\mathrm{i}}{2}\oint_{\mathscr{C}} \overline{w}_0[-\overline{W}_1\,\mathrm{d}\overline{z} + W_1\,\mathrm{d}z] = \pi\mathrm{i}\kappa[\overline{W}_1 + \zeta_{,1}] + \pi[\overline{f}_{1,1} - \overline{f}_2(\overline{\zeta}_{,1} - W_1)]e^2. \tag{8.30}$$

These two terms correspond to the terms

$$\pi M^2\log M[\overline{W}_{0,0} + (\overline{W}_{0,1} + \overline{W}_{1,0})e^2] \tag{8.31}$$

in (8.26). The constant term gives the evolution equation on the timescale t_1 as

$$\zeta_{,1} = -\frac{\mathrm{i}\kappa}{2}\overline{W}_{0,0} = -\frac{\mathrm{i}\kappa}{2}\zeta_{,00}. \tag{8.32}$$

At this point, the terms at $O(e^2)$ do not match. This is because the matching requires further terms in Q, as discussed appendix §D.1.

The $O(M^2)$ contribution is

$$\begin{aligned} q_2 =& \mathrm{i}\oint_{\mathscr{C}} p_2\,\mathrm{d}z - \frac{\mathrm{i}}{2}\oint_{\mathscr{C}} \rho_2\overline{w}_0[(W_0-\overline{W}_0)\,\mathrm{d}\overline{z} - (w_0-W_0)\,\mathrm{d}z] \\ &- \frac{\mathrm{i}}{2}\oint_{\mathscr{C}} \overline{w}_2[(\overline{w}_0-\overline{W}_0)\,\mathrm{d}\overline{z} - (w_0-W_0)\,\mathrm{d}z] - \frac{\mathrm{i}}{2}\oint_{\mathscr{C}} \overline{w}_0[(\overline{w}_2-\overline{W}_2)\,\mathrm{d}\overline{z} - (w_2-W_2)\,\mathrm{d}z]. \end{aligned} \tag{8.33}$$

To obtain this, we need to consider further terms in the local expansion of F_2. Using the conditions (8.24–8.25), we find

$$F_2 \mathrel{\mathring{=}} A + B\frac{\varepsilon}{\overline{\varepsilon}} + D\varepsilon\log e^2 + H\varepsilon + L\frac{\varepsilon^2}{\overline{\varepsilon}} + o(e), \tag{8.34}$$

where the relation $\mathrel{\mathring{=}}$ means that the equality ignores purely imaginary terms. The coefficients needed are

$$D = \frac{\mathrm{i}\kappa}{4}[-\overline{\zeta}_{,00} + 2(f_{1,0} - f_2\zeta_{,0}) + 2\overline{f}_1 f_2] = \frac{\mathrm{i}\kappa}{4}f_{1,0}, \tag{8.35}$$

$$\begin{aligned} H =& \frac{1}{4}[\overline{J}_0 + 2\overline{f}_0(f_{1,0} - f_2\zeta_{,0}) + f_2\overline{I}_0 + 2f_1(\overline{f}_{0,0} - \overline{f}_1\overline{\zeta}_{,0}) + \overline{f}_1(-2\mathrm{i}\kappa f_2 + f_1^2)] \\ &+ \frac{1}{4}(\overline{\zeta} - \overline{Z_0})[f_{0,00} - (f_1\zeta_{,0})_{,0} - (f_{1,0} - f_2\zeta_{,0})\zeta_{,0}] + g_1. \end{aligned} \tag{8.36}$$

The expansion (8.34) leads to

$$w_2 = \frac{B}{\overline{\varepsilon}} - \overline{B}\frac{\overline{\varepsilon}}{\varepsilon^2} + D(\log e^2 + 1) + \overline{D}\frac{\overline{\varepsilon}}{\varepsilon} + H + 2L\frac{\varepsilon}{\overline{\varepsilon}} - \overline{L}\frac{\varepsilon^2}{\overline{\varepsilon}^2} + o(1), \tag{8.37}$$

$$F_{2,0} \mathrel{\mathring{=}} B\left(\overline{\zeta}_{,0}\frac{\varepsilon}{\overline{\varepsilon}^2} - \frac{\zeta_{,0}}{\overline{\varepsilon}}\right) + o(e^{-1}). \tag{8.38}$$

Substituting into (8.33) and computing the integrals leads to extensive cancellation, yielding

$$q_2 = -\frac{\pi}{2}\kappa^2\overline{f}_{1,0} + \pi \mathrm{i}\kappa\zeta_{,2} + \pi \mathrm{i}\kappa\overline{W}_2 - 2\pi \mathrm{i}\kappa\overline{H} - 2\pi \mathrm{i}\kappa\overline{D}(1+\log e^2) + o(1). \tag{8.39}$$

We see from (8.26) that the $\log e$ term in q_2 cancels the $\log e$ term at $\mathrm{O}(M^2)$ in Q. Recalling that $\zeta_{,2} = \overline{W}_2$ gives the equation for the slow evolution of ζ as

$$\zeta_{,2} = -\frac{\mathrm{i}\overline{W}_{0,0}}{2\kappa}C - \frac{\mathrm{i}\kappa}{4}\overline{f}_{1,0} + \overline{D} + \overline{H} = -\frac{\mathrm{i}\kappa}{2}\overline{f}_{1,0}\left(1 + \frac{C}{\kappa^2}\right) + \overline{H}. \tag{8.40}$$

It is useful to check the behaviour of a single point vortex. The incompressible complex potential is $F_0 = -\mathrm{i}\kappa\log(z-\zeta)$. The point vortex does not move at $O(1)$. Hence $\zeta_{,1} = 0$ and

$$F_2 = \frac{1}{4}w_0\overline{I(z)} + G(z) = \frac{1}{4}\left(-\frac{\mathrm{i}\kappa}{z-\zeta}\right)\left[\frac{\kappa^2}{\overline{z}-\overline{\zeta}} - \frac{\kappa^2}{\overline{z}_I - \overline{\zeta}}\right] + \frac{\mu}{z-\zeta}. \tag{8.41}$$

The arbitrariness of z_I is irrelevant, as it is cancelled by μ_1 when removing the simple pole in F_2. The leading-order term is purely imaginary so that it can be ignored. Hence the $O(M^2)$ velocity of a single point vanishes, a necessary feature for this model.

8.1.4 Global solution

The results above are applicable near every vortex, because neither the vortex circulation nor the vortex location has a preferred value. We can now assemble a global solution that is valid everywhere in the vortical region. The $O(M^2)$ potential is given by the sum of the inhomogeneous part (8.8) and of a homogeneous part. The homogeneous part takes the form

$$G(z) = \sum_m \left(\frac{\mu_m}{z-\zeta_m} + [\xi_m + l_m(z)]\log(z-\zeta_m)\right) + K(z) \tag{8.42}$$

and includes contributions from each vortex of the form (8.21) and (8.22), while $K(z)$ includes possible further terms (e.g. to satisfy boundary conditions or to set the circulation around objects

in the flow). We now consider the expansion near vortex n of the sum in (8.42) omitting term n, writing the rest of the sum as $g_{-1}\varepsilon_n^{-1} + g_0 + g_1\varepsilon_n + O(e_n^2)$, with $\varepsilon_n = z - \zeta_n$ and $e_n = |\varepsilon_n|$. The calculations above show that g_0 is not needed. We find, for vortex n,

$$g_{-1} = \frac{1}{2}\kappa_n \sum_m{}' \kappa_m \left(\overline{f_1^{(m)}} - \zeta_{n,0} \right) \log \zeta_{mn} = \frac{1}{2}\kappa_n \sum_m{}' \kappa_m \left(\zeta_{m,0} - \zeta_{n,0} \right) \log \zeta_{mn}, \tag{8.43}$$

$$g_1 = \sum_m{}' \left(-\frac{\mu_m}{\zeta_{mn}^2} + \frac{\xi_m + l_0^{(mn)}}{\zeta_{mn}} + l_1^{(mn)} \log \zeta_{mn} \right) + K'(\zeta_n), \tag{8.44}$$

where $\zeta_{mn} = \zeta_n - \zeta_m$ and the prime in the summation indicates that term n is omitted (the derivation is given in appendix §D.2).

8.2 Two vortices in the plane

We consider the simplest situation consisting of two point vortices in the infinite plane. In cases such as this, there are no other contributions to the potential F_0 beyond the vortices, which means that $K(z) = 0$ in (8.42). While some simple geometries can also be solved using the method of images and could hence be considered as consisting of a finite number of vortices, the dynamics of the actual and image vortices are different: the latter are not physical so that their motion is set by boundary conditions rather than matching.

Results for the leading-order potential, complex velocity, I and J are equally simple for N vortices; we will take N=2 after presenting general results. We have

$$F_0 = \sum_{n=1}^{N} \frac{\Gamma_n}{2\pi \mathrm{i}} \log(z - \zeta_n), \qquad w_0 = \sum_{n=1}^{N} \frac{\Gamma_n}{2\pi \mathrm{i}} \frac{1}{z - \zeta_n}. \tag{8.45}$$

The decay properties of $w(z)$ for large $|z|$ mean that we can take $z_I = \infty$. It is known that the incompressible two- and three-vortex cases are integrable. The system has four real conserved quantities, two of which combine to give the complex vortex momentum $\sum_{n=1}^{N} \Gamma_n \zeta_n$. Conservation of this quantity means that integral $J(z)$ is convergent at infinity, so that we can take $z_J = 0$.

To calculate the integrals I and J, we use the primitives

$$\int^z \sum_m \left[-\frac{\mathrm{i}\kappa_m}{z-\zeta_m} \right]^2 \mathrm{d}z = \sum_m \frac{\kappa_m^2}{z-\zeta_m} + {\sum_{m,n}}' \frac{\kappa_m \kappa_n}{\zeta_{nm}} \log \frac{z-\zeta_n}{z-\zeta_m} \tag{8.46}$$

and

$$\int^z \sum_m \mathrm{i}\kappa_m \left[\frac{\zeta_{m,00}}{z-\zeta_m} + \frac{\zeta_{m,0}^2}{(z-\zeta_m)^2} \right] \mathrm{d}z = \sum_m \mathrm{i}\kappa_m \left[\zeta_{m,00} \log(z-\zeta_m) - \frac{\zeta_{m,0}^2}{z-\zeta_m} \right], \tag{8.47}$$

where the primed sums indicate $m \neq n$.

For the two-vortex case, the total circulation is $\Gamma_\infty = \Gamma_1 + \Gamma_2$, so there are two different cases, corresponding to $\Gamma_\infty = 0$ and $\Gamma_\infty \neq 0$. In the latter case, the conservation laws show that the vortices must stay in a bounded area of the plane. The former case corresponds to a co-propagating dipole pair in the incompressible limit. Expressions for f_0, f_1, J_0 and g_{-1} for the two vortices are given in appendix §D.3. The relation (8.25) gives $\xi_1 = \xi_2 = 0$ if Z_0 is taken to be on the line joining ζ_1 and ζ_2, although the final result for the motion of the vortices is independent of Z_0.

In the co-propagating case, we can take $\kappa = \kappa_1 = -\kappa_2$. Then ζ_{21} and $|\zeta_1|^2 - |\zeta_2|^2$ are independent of t_0. Without loss of generality, we take the positions of the vortices at $t = 0$ to be $\pm \mathrm{i}a_0$ with a_0 real, yielding

$$\zeta_1 = \mathrm{i}a + \frac{\kappa t}{2a}, \qquad \zeta_2 = -\mathrm{i}a + \frac{\kappa t}{2a}, \tag{8.48}$$

with $a = a(t_1, t_2)$ and $a(0,0) = a_0$. Since $\zeta_{1,00} = \zeta_{2,00} = 0$, we find from (8.32) that ζ_1 and ζ_2 do not depend on t_1, so that $a = a(t_2)$. Since $f_{1,0} = 0$, $D = 0$, and since $(\zeta_1 - \zeta_2)_{,0} = 0$, we have $g_{-1} = 0$. Calculations (see appendix §D.3) lead to $H_1 = 0$, with the Z_0 terms cancelling. Substituting into (8.40), along with $f_{1,0} = 0$, means that ζ does not change with t_2. Hence we recover the result of Leppington [153] and Crowdy & Krishnamurthy [58]: the translation speed of the co-propagating vortex pair does not change at $O(M^2)$. The current procedure is of course

lengthier than that needed to obtain this result in a co-moving frame in which the pair is at rest, but we can now address the fundamentally unsteady co-rotating pair.

For the co-rotating case, $\kappa = \kappa_1 = \kappa_2$, so that $\zeta_1 + \zeta_2$ is independent of t_0. Without loss of generality, we take the positions of the vortices at $t = 0$ to be $\pm a_0$ with a_0 real, yielding

$$\zeta_1 = a\mathrm{e}^{\mathrm{i}\varphi}, \qquad \zeta_2 = -a\mathrm{e}^{\mathrm{i}\varphi} \tag{8.49}$$

with $\varphi = \theta + \kappa t/(2a^2) = \theta + \omega t$. Here a and θ are functions of t_1 and t_2 with $a(0,0) = a_0$ and $\theta(0,0) = 0$. Since $\zeta_{1,00} = -\omega^2\zeta_1$, we find from (8.32) that

$$a_{,1} = 0, \qquad \theta_{,1} = \omega_1 = \frac{\kappa\omega^2}{2} = \frac{\kappa^3}{8a^4}. \tag{8.50}$$

The radius is only a function of t_2, while the rotation rate varies with t_1. Since the $\theta_{,1}$ term has the same sign as the $\mathrm{O}(1)$ rotation rate, it leads to a slowing down of the rotational motion when multiplied by $M^2 \log M$, which is negative since $0 < M^2 \ll 1$. Fairly extensive algebra (see appendix §D.3) gives

$$H_1 = -\frac{\mathrm{i}\kappa^3}{16a^3}\mathrm{e}^{-\mathrm{i}\varphi}\left(1 - \log 4a^2\right) \tag{8.51}$$

and

$$\zeta_{1,2} = -\frac{\mathrm{i}\kappa}{2}\overline{f}^{(1)}_{1,0}\left(1 + \frac{C}{\kappa^2}\right) + \overline{H}_1 = \frac{\mathrm{i}\kappa^3}{8a^3}\mathrm{e}^{\mathrm{i}\varphi}\left(1 + \frac{C}{\kappa^2}\right) + \overline{H}_1 = \frac{\mathrm{i}\kappa^3}{8a^4}\zeta\left(\frac{3}{2} + \frac{C}{\kappa^2} - \log 2a\right). \tag{8.52}$$

Here, the constant C is given in (8.4). Once again there is a correction to the rotation speed:

$$\theta_{,2} = \omega_2 = \frac{\kappa^3}{8a^4}\left(\frac{3}{2} + \frac{C}{\kappa^2} - \log 2a\right). \tag{8.53}$$

In dimensional form, we can combine the frequencies to obtain

$$\omega^* = \frac{\kappa_*}{2a_*}\left[1+\frac{\kappa_*^2}{4c_0^2a_*^2}\left(-\log\left(\frac{2a^*\Gamma}{c_0L^2}\right)+\frac{3}{2}+\frac{C\Gamma^2}{\kappa_*^2}\right)\right], \tag{8.54}$$

where stars represent dimensional quantities. The circulation scale is $\Gamma = LV$. There is no unique choice of scalings, but the simplest choice is probably $\Gamma = 2\kappa_*$ and $L = 2a_*$, so that Γ is the total circulation divided by 2π and L is the distance between vortices. Then

$$\omega^* = \frac{\kappa_*}{2a_*}\left[1+\frac{\kappa_*^2}{4c_0^2a_*^2}\left(-\log\left(\frac{\kappa_*}{c_0a_*}\right)+\frac{3}{2}+4C\right)\right]. \tag{8.55}$$

For the general two-vortex case, the vortices rotate about their centre of vorticity at $O(1)$. Write $\zeta_1 = a\mathrm{e}^{\mathrm{i}\varphi}$ and $\zeta_2 = -b\mathrm{e}^{\mathrm{i}\varphi}$ with $a\kappa_1 = b\kappa_2$ so that the centre of vorticity is at the origin with $Z_0 = 0$. Then

$$\omega = \frac{\kappa_1}{b(a+b)} = \frac{\kappa_2}{a(a+b)}. \tag{8.56}$$

The $O(M^2\log M)$ equations become

$$\zeta_{1,1} = -\zeta_{2,1} = \frac{\mathrm{i}\kappa_1\kappa_2\omega}{2\overline{\zeta}_{21}}. \tag{8.57}$$

The velocities of the vortices are the same, but their angular velocities differ, so that as they move their trajectories will no longer be circles. The centre of the vorticity $\zeta_c = (\kappa_1\zeta_1+\kappa_2\zeta_2)/(\kappa_1+\kappa_2)$ moves slowly with the $O(M^2\log M)$ velocity

$$\zeta_{c,1} = \frac{\mathrm{i}\kappa_1\kappa_2(\kappa_1-\kappa_2)\omega}{2\overline{\zeta}_{21}(\kappa_1+\kappa_2)}. \tag{8.58}$$

The $O(M^2)$ motion is

$$\zeta_{1,2} = \frac{\mathrm{i}\kappa_1\kappa_2(\kappa_1+\kappa_2)}{4|\zeta_{21}|^2\overline{\zeta}_{21}}\left(3+\frac{2C_1}{\kappa_1^2}-\log|\zeta_{21}|^2\right),\ \zeta_{2,2} = \frac{\mathrm{i}\kappa_1\kappa_2(\kappa_1+\kappa_2)}{4|\zeta_{12}|^2\overline{\zeta}_{12}}\left(3+\frac{2C_2}{\kappa_2^2}-\log|\zeta_{12}|^2\right). \tag{8.59}$$

This slow motion can be decomposed into rotation about a slowly moving centre with the $O(M^2)$ correction

$$\zeta_{c,2} = \frac{\mathrm{i}\kappa_1\kappa_2(\kappa_1-\kappa_2)}{4|\zeta_{21}|^2\overline{\zeta}_{21}}\left(3+\frac{2(C_1\kappa_2-C_2\kappa_1)}{\kappa_1\kappa_2(\kappa_1-\kappa_2)}-\log|\zeta_{21}|^2\right). \tag{8.60}$$

This shows that the relative equilibrium of the co-rotating vortices evolves slowly in time due to the weak compressibility effects, although in the symmetric case, it is only the rotation rate that changes.

8.3 Point vortex inside a circle

We now introduce a boundary into the fluid domain. The simplest case is to take a single point vortex either inside a circle of radius R. The $O(1)$ potential takes a simple form, using the method of images. The boundary condition at $O(M^2)$ now requires explicit consideration. The case of the vortex inside a circle does not have a far field, while the vortex outside the circle has a degree of freedom associated with the circulation bound to the circle. We restrict ourselves here to the case of motion inside a circle

The $O(1)$ potential is

$$F_0 = -\mathrm{i}\kappa\log(z-\zeta)+\mathrm{i}\kappa\log(z-\zeta_i). \tag{8.61}$$

The image vortex at $\zeta_i = R^2/\overline{\zeta}$ ensures that the no-flow boundary condition at $|z|=R$ is satisfied. The point vortex moves in a circle with radius a with angular velocity $\omega = \kappa/(R^2-a^2)$. The same calculation as in § 8.2 gives $\theta_{,1} = \kappa\omega^2/2$.

Moving to $O(M^2)$, it is easiest to take the lower limit in J to be the origin. The velocity needs to be bounded and single-valued need inside the circle. Outside the circle, this is not required, but any branch cuts will need to avoid the circle. This is always possible by taking the branch cut radially to infinity. Because the flow at $O(M^2)$ is not incompressible, we need to use

the velocity in the boundary condition on the circle, which we write as

$$\text{Re } zw_2(z) = 0 \quad \text{on } z\bar{z} = R^2. \tag{8.62}$$

Given the inhomogeneous portion of F_2, we will need to satisfy the boundary condition (8.62) as well as require the solution to be single-valued inside the circle with appropriate behaviour near ζ. The potential F_2 can be written

$$F_2(z) = l(z)\log\overline{\varepsilon} + l_i'(z)\log\overline{\varepsilon}_i + \frac{1}{4}(z - Z_0)\overline{\tilde{J}(z)} + \frac{1}{4}w_0(z)\overline{\tilde{I}(z)} + G(z). \tag{8.63}$$

We now enforce single-valuedness near $z = \zeta$. Previously we added the terms $l(z)\log\varepsilon$ and $l_i(z)\log\varepsilon_i$ to F_2. These do not satisfy the boundary condition. Instead, since ζ_i is not in the physical domain, we do not enforce single-valuedness there. Hence we add to F_2 the terms $l(z)\log\varepsilon$ and $m_i(z)\log\varepsilon_i$, then pick the function $m_i(z)$ to satisfy the boundary condition. We hence have the following logarithmic terms in w_2:

$$l'(z)\log e^2 + l_i'(z)\log\overline{\varepsilon}_i + m_i'(z)\log\varepsilon_i. \tag{8.64}$$

A simple extension to the Milne-Thomson circle theorem shows that if $f(z)$ is a function of z, then

$$f(z) - \frac{R^2}{z^2}\bar{f}(R^2/z) \tag{8.65}$$

satisfies the boundary condition (8.62). Similarly we find that both of the expressions

$$f(z)\overline{g(z)} - f(z)\bar{g}(R^2/z), \qquad f(z)\overline{g(z)} - \frac{R^2}{z^2}\overline{f}(R^2/z)g(z) \tag{8.66}$$

satisfy (8.62). Using these results (see appendix §D.4), we obtain a logarithmic contribution that is single-valued at ζ, has no singularity at ζ and satisfies the boundary condition.

We satisfy the boundary condition by adding terms that do not introduce a singularity at ζ. We have to remove the singularity introduced in the full expression for w_2 at the origin by the above process. This takes the form $\lambda z^{-2} + \nu z^{-1}$. We remove the singularity by adding

$$-\frac{\lambda}{z^2} + \frac{\overline{\lambda}}{R^2} - \frac{\nu}{z}. \tag{8.67}$$

The second term ensures that the boundary condition is satisfied for the extra $-\lambda z^{-2}$ term. The $-\nu z^{-1}$ term that has been added satisfies the boundary condition if ν is imaginary. One cannot add a term to remove it, as it corresponds to a volume source (or sink) at the origin. Such a term cannot be present. Verifying that the real part of ν vanishes is a useful check on the calculations. Finally we need to remove the singularity at ζ by adding terms that satisfy the boundary condition, namely

$$\frac{\xi}{\varepsilon} + \frac{\overline{\xi}\zeta_i}{z\varepsilon_i} - \frac{\mu}{\varepsilon^2} + \frac{\overline{\mu}\zeta_i^2}{R^2\varepsilon_i^2}. \tag{8.68}$$

This seems to introduce another pole at the origin, but in fact $\xi = 0$ as will be verified.

The details of the lengthy calculation are presented in appendix §D.4. The final, deceptively simple, result is

$$D + H = \frac{\mathrm{i}\kappa^3 a \mathrm{e}^{-\mathrm{i}\varphi}}{4(R^2 - a^2)^2} \left[\log \frac{(R^2 - a^2)^3}{R^4} + \frac{R^4}{a^4} \log \frac{R^2}{R^2 - a^2} + 1 \right]. \tag{8.69}$$

We see that the vortex continues to move in circles, and it is just the angular velocity that changes.

We can adapt the above calculation to a vortex outside a circle. Now the behaviour of logarithmic terms near infinity needs to be examined, and one needs to examine possible non-decaying analytic growing terms near infinity. When the fluid region is outside the circle, there is a freedom in choosing the circulation around the circle. We leave this calculation for future work.

Chapter 8, in part, is a reprint of the material as it appears in Philosophical Transactions of the Royal Society A 2022. Llewellyn Smith, Stefan G.; Chu, Tianyi; Hu Zinan, The Royal

Society, 2022. The dissertation author was one of the primary investigators and authors of this paper.

Chapter 9

Summary

This study explores three fundamental aspects of fluid dynamics, focusing on analytical investigation, computational methodologies, and reduced-order modeling for vortical and turbulent flows. We examine diverse flow scenarios, encompassing different Mach numbers, ranging from incompressible to compressible, and different Reynolds numbers, spanning from laminar to turbulent. These flows serve as illustrative exemplars to systematically investigate and explore the physics of fluid dynamics from varied perspectives.

In the first part, we delve into the dynamics of point vortices under the assumption of a small Mach number. Employing a modified Rayleigh–Jansen expansion and the method of Matched Asymptotic Expansions, our analytical study unveils the modification of point vortices' motion over long time scales. In the second part, we explore the use of PHS+poly RBF-FD discretizations to establish a mesh-free framework for both flow simulations and hydrodynamic stability analysis. We conduct a systematic parameter study to identify a set of parameters ensuring stability while balancing accuracy and computational efficiency within this framework. In the third part, we introduce two model order-reduction techniques: the operator-based Galerkin projection and the data-driven time-delay Koopman approach, both based on SPOD modes. The result models accurately capture the initial transient dynamics and reproduce the second-order statistics of broadband turbulent flows. In summary, the amalgamation of these three parts not only enhances our comprehension of flow physics but also propels our exploration into new

perspectives. This holistic approach facilitates further potential advancements in our scientific understanding of flow physics.

Appendix A

Navier-Stoke solver

A.1 Modified wavenumber diagrams for $q = 4$

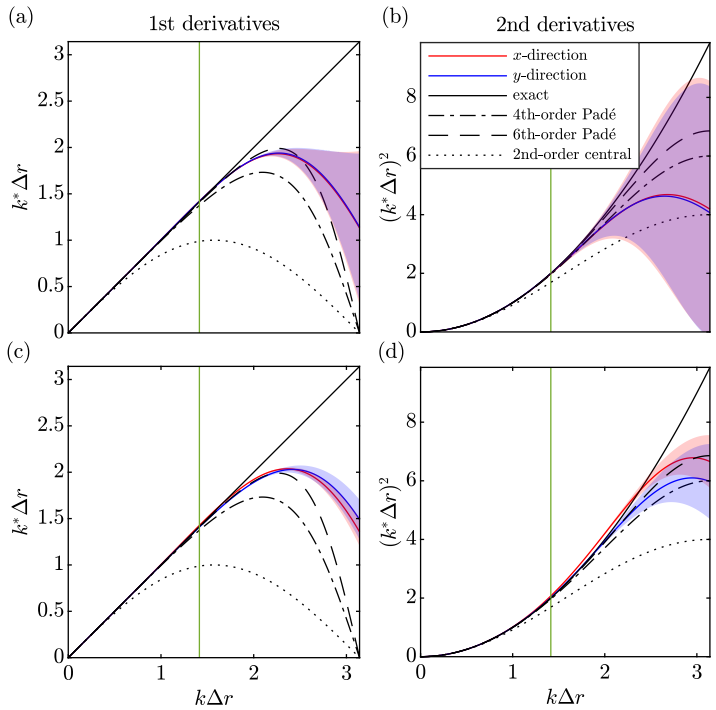

Figure A.1. Modified wavenumber diagrams for $(n,m,q) = (28,7,4)$: (a,b) same as figure 3.5 for $\boldsymbol{D}^{(V,V)}$; (c,d): same as figure 3.9 for $\boldsymbol{D}^{(P,P)}$.

Panels A.1(a,b) show the modified wavenumber diagrams for the differentiation matrices $\boldsymbol{D}^{(V,V)}$ obtained using the combination $(n,m,q) = (28,7,4)$. The results are visually indistinguishable from those in figure 3.5, indicating that increasing the polynomial degree, q, beyond

3 does not improve the accuracy for a fixed RBF stencil size, here $n = 28$. The corresponding diagram for the $(P,P)-$grid is shown in panels A.1(c,d). In the same way as for the $(V,V)-$grid, the modified wavenumber curves in figures 3.9 and A.1(c,d) are nearly identical.

A.2 Relative errors for V-to-P and P-to-V grid derivatives

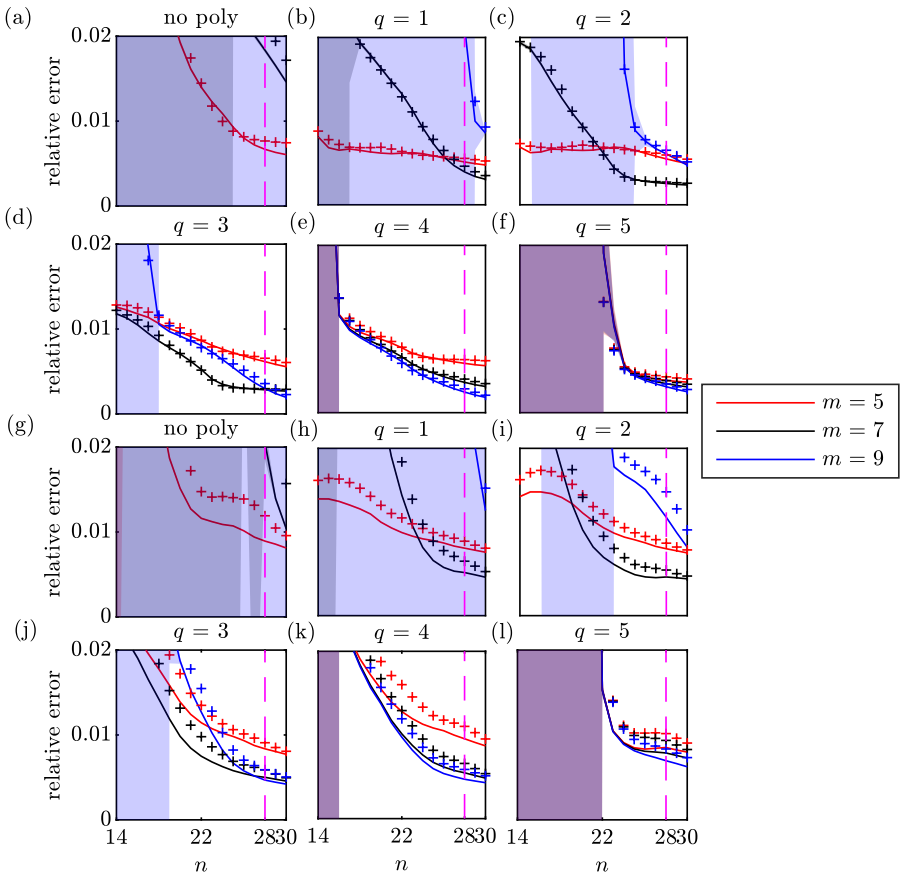

Figure A.2. Relative errors for staggered nodes: (a-f) same as figure 3.3 for $\boldsymbol{D}_x^{(V,P)}$; (g-l) same as figure 3.3 for $\boldsymbol{D}_x^{(P,V)}$. The results for the y-derivatives are shown as '+'.

The staggered node layout introduced in §4.1 requires differentiation matrices that operate between the V- and P-grids (see equations (4.4) and (4.7) of the fractional step algorithm). Panels A.2(a-f) show the relative errors for the differentiation matrix $\boldsymbol{D}^{(V,P)}$, which operates on the (V,P)-grid shown in figure 3.2(c) for varying n, m and q. Similar trends as for the collocated (V,V)- and (P,P)-grids are found. For the same reasons discussed in §3.4, and for consistency

with the differentiation operators on the collocated grids, we proceed with the same parameter combination of $(n,m,q) = (28,7,3)$. The same parameter study is repeated for the differentiation operator $\boldsymbol{D}^{(P,V)}$ in panels A.2(g-l) with a comparable outcome and the same conclusion.

A.3

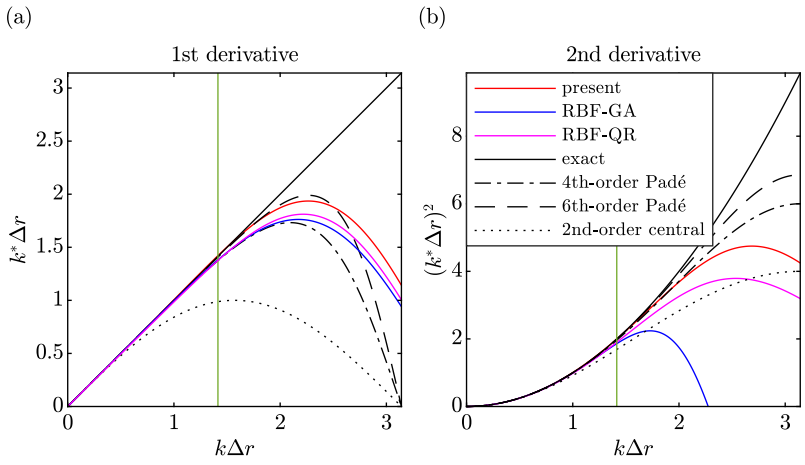

Figure A.3. Comparison with RBF-QR and RBF-GA on the (V,V)-grid with $n = 28$: modified wavenumber diagrams for the (a) first derivative; (b) second derivative. The recommended maximum modified wavenumber of $k\Delta r = \sqrt{2}$ is shown in green.

Figure A.3 compares the accuracy of different RBF-FD methods for a fixed stencil size of $n = 28$. The comparison is conducted on the (V,V)-grid, on which both the first and second derivatives are required. The accuracy and numerical stability of the RBF-QR and RBF-GA methods depend on their shape parameters. The corresponding values of $\varepsilon_{\text{QR}} = 2.5$ and $\varepsilon_{\text{GA}} = ...$ are taken from the standard references by [82] and [28], respectively. It can be seen that all three RBF-FD variants perform very well up to our recommended maximum modified wavenumber of $k\Delta r = \sqrt{2}$ for both the first and second derivatives. For fewer points per wavelength, that is $k\Delta r \gtrsim \sqrt{2}$, the proposed PHS+poly variant with $(n,m,q) = (28,7,3)$ stays closer to the spectral limit, in particular for the second derivative. With the caveat that the shape parameters of the RBF-QR and RBF-GA variants are not optimized for this specific node distribution, the results show that the proposed PHS+poly discretization is highly competitive. An advantage of

PHS+poly, arguably, is that the optimization of its integer parameters, m and q as demonstrated in §3, for a fixed stencil size is more straight forward than finding the optimal value of a continuous shape parameter.

A.4 Time stepping accuracy

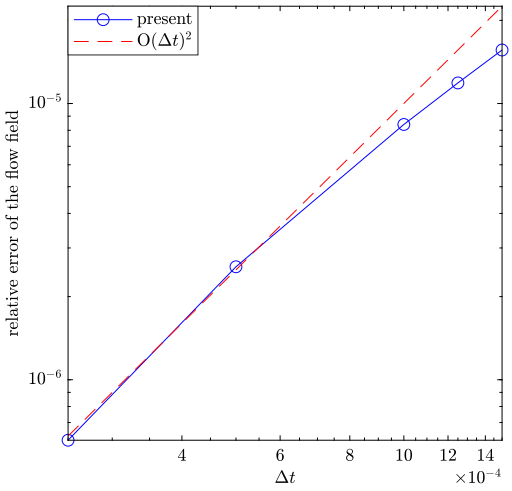

Figure A.4. Relative error of the flow field at different time steps.

Figure A.4 shows the relative error of the flow field simulated using different time steps. As a test case, we use the lid-driven cavity flow at Re = 1000 and compute the error for the steady-state solution, see §4.2.1. The close match between the theoretical curve and the simulation error for small Δt confirms that the algorithm possesses an order of accuracy of $O(\Delta t)^2$. This is consistent with the numerical scheme described in §4.1.

Appendix B

SPOD-Galerkin model

B.1 Stochastic SPOD-Galerkin two-level model for rank 2×129 and rank 3×129 cases

This appendix reports the additional results for the rank 2×129 and rank 3×129 cases. Figure B.1(a-d) show the comparison between the power spectra of the state coefficients $\boldsymbol{a}_i$ and the rank 2×129 expansion coefficients at different frequencies. Figure B.1(e-h) report the corresponding results for the rank 3×129 case. Good agreements between the approximations and models are observed in both cases. The corresponding SPOD eigenvalue spectra shown in figure B.1(i-j) show that both models accurately reproduce the eigenvalue spectra of the LES data for a wide range of frequencies. From these observations and the favourable results obtained for the 1×129 baseline model, as previously reported in figures 6.8 and 6.13, it concluded that subdominant SPOD modes are not required in the modal expansion.

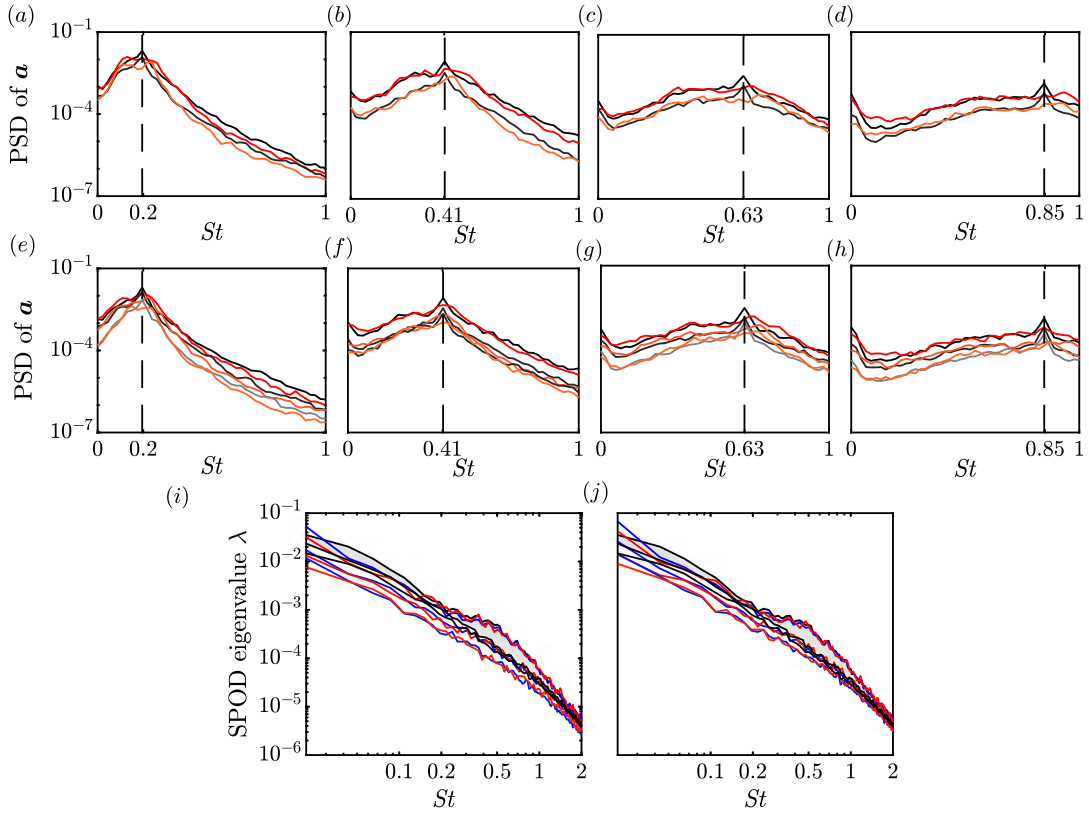

Figure B.1. Power spectra of the state coefficients $\boldsymbol{a}_i$ of low-rank approximations (red) and 2–level models (black) of rank 2×129 (first row) and rank 3×129 (second row) at four representative frequencies: (a,e) $St = 0.2$; (b,f) $St = 0.41$; (c,g) $St = 0.63$; (d,h) $St = 0.85$. Comparison of SPOD eigenvalue spectra of the LES data (black), low-rank approximations (blue) and 2–level models (red): (i) rank 2×129; (j) rank 3×129. Compare figures 6.8, 6.10 and 6.13.

Appendix C

Stochastic low-dimensional inflated convolutional Koopman (SLICK) model

C.1 Algorithm

Input: Fluctuating data matrix $\boldsymbol{Q}' = \begin{bmatrix} | & | & & | \\ \boldsymbol{q}[1]-\overline{\boldsymbol{q}} & \boldsymbol{q}[2]-\overline{\boldsymbol{q}} & \cdots & \boldsymbol{q}[N]-\overline{\boldsymbol{q}} \\ | & | & & | \end{bmatrix}$ consisting N snapshots, time step Δt, weight matrix $\boldsymbol{W}$, windowing function w.

Output: SPOD convolutional coordinates $\boldsymbol{a}$, matrices of the SLICK model $\boldsymbol{y}[j+1] = \boldsymbol{T}\boldsymbol{y}[j] + \begin{bmatrix} \boldsymbol{0} \\ \boldsymbol{G}\sqrt{\Delta t}\boldsymbol{w} \end{bmatrix}$, and surrogate flow field.

Phase 1 – Koopman analysis of the low-dimensional convolutional coordinates

1. Compute the SPOD of $\boldsymbol{Q}'$ and store the first M SPOD modes (at all N_f frequencies) in the column matrix $\boldsymbol{V}$.

2. Segment the data matrix and determine the ith observable block as

$$\boldsymbol{\Phi}[i] = \begin{bmatrix} | & & | \\ \boldsymbol{\phi}[i] & \cdots & \boldsymbol{\phi}[i+2N_f-1] \\ | & & | \end{bmatrix} = \overline{\boldsymbol{V}}^*\overline{\boldsymbol{W}} \begin{bmatrix} | & & | \\ \boldsymbol{q}'[i] & \cdots & \boldsymbol{q}'[i+2N_f-1] \\ | & & | \end{bmatrix}.$$

Calculate and store the DFT using a windowed fast Fourier transform

$$\hat{\boldsymbol{\Phi}}[i] = \mathrm{FFT}\left(\boldsymbol{\Phi}[i]\right) = \begin{pmatrix} — & \hat{\boldsymbol{\phi}}_1[i] & — \\ & \vdots & \\ — & \hat{\boldsymbol{\phi}}_{N_k}[i] & — \end{pmatrix}.$$

3. For each block, determine the expansion coefficient vector with a time shift $N_f - 1$ as

$$\boldsymbol{a}[i+N_f-1] = \begin{bmatrix} \left(\hat{\boldsymbol{\phi}}_1\right)_{l_1}[i] \\ \vdots \\ \left(\hat{\boldsymbol{\phi}}_{N_k}\right)_{l_{N_k}}[i] \end{bmatrix},$$

where the index $l_j = \lceil \frac{j}{M} \rceil$ denotes the element associated with the frequency ω_j in $\hat{\boldsymbol{\phi}}$.

4. Determine the discrete modified Koopman operator as

$$\boldsymbol{K} = \frac{\boldsymbol{A}_2 - \boldsymbol{A}_1}{\Delta t} \boldsymbol{A}_1^* \left(\boldsymbol{A}_1 \boldsymbol{A}_1^* + \gamma_1 \boldsymbol{I}\right)^{-1},$$

where

$$\boldsymbol{A} = \begin{bmatrix} | & & | \\ \boldsymbol{a}[N_f] & \cdots & \boldsymbol{a}[N-N_f] \\ | & & | \end{bmatrix},$$

and the subscripts, $(\cdot)_1$ and $(\cdot)_2$, represent the submatrices by excluding the last and the first columns, respectively.

Phase 2 – Stochastic inflated model

1. Store the remaining residue,

$$\boldsymbol{B} = \frac{\boldsymbol{A}_2 - \boldsymbol{A}_1}{\Delta t} - \boldsymbol{K}\boldsymbol{A}_1,$$

as a data matrix of the forcing coefficients.

2. Let $\boldsymbol{Y} \leftarrow \begin{bmatrix} \boldsymbol{A} \\ \boldsymbol{B} \end{bmatrix}$. Solving the linear system problem in the equation (6.26) yields

$$\boldsymbol{M} = \frac{\boldsymbol{B}_2 - \boldsymbol{B}_1}{\Delta t} \boldsymbol{Y}_1^* \left(\boldsymbol{Y}_1 \boldsymbol{Y}_1^* + \gamma_2 \boldsymbol{I}\right)^{-1}.$$

3. Assemble the matrices to obtain

$$\boldsymbol{T} \leftarrow \boldsymbol{I} + \begin{bmatrix} \boldsymbol{K_a} & \boldsymbol{I} \\ -\boldsymbol{M}- \end{bmatrix} \Delta t.$$

4. Compute

$$\boldsymbol{H} = \frac{\begin{bmatrix} \boldsymbol{0} & \boldsymbol{1} \end{bmatrix} \left(\boldsymbol{Y}_2 \boldsymbol{Y}_2^* - \boldsymbol{T}\boldsymbol{Y}_1 \boldsymbol{Y}_1^* \boldsymbol{T}^*\right) \begin{bmatrix} \boldsymbol{0} \\ \boldsymbol{1} \end{bmatrix}}{(N - N_f - 2)\Delta t}$$

and its eigenvalue decomposition

$$\boldsymbol{H} = \boldsymbol{V}_H \boldsymbol{D}_H \boldsymbol{V}_H^*.$$

5. Set the negative eigenvalues in $\boldsymbol{D}_H$ to 10^{-15} and rescale the rest positive eigenvalues such

that $\mathrm{tr}(\boldsymbol{D}_H) = \mathrm{tr}(\tilde{\boldsymbol{D}}_H)$. Determine the matrix $\boldsymbol{G}$ as

$$\boldsymbol{G} = \boldsymbol{V}_H \tilde{\boldsymbol{D}}_H^{1/2}.$$

The resulting SLICK model is propagated in time as

$$\boldsymbol{y}[j+1] = \boldsymbol{T}\boldsymbol{y}[j] + \begin{bmatrix} \boldsymbol{0} \\ \boldsymbol{G}\sqrt{\Delta t}\boldsymbol{w} \end{bmatrix}.$$

The zero mean, unit variance Gaussian white noise $\boldsymbol{w}$, which drives the system, is obtained from a random number generator.

Phase 3 – Flow field reconstruction

1. Collect $\boldsymbol{a}$ from data or model.

2. For each instant i, perform the inversion of SPOD-based convolution in the subspace as

$$\tilde{\boldsymbol{a}}[i] = \frac{\sum_{h=h_-}^{h_+} \left(a_j[i+h]\right) \mathrm{e}^{-\mathrm{i}\tilde{\omega}_j(h\Delta t)}}{2N_f \Delta t \sum_{h=h_-}^{h_+} w(h\Delta t)}.$$

3. Reconstruct the flow field at each time step i as

$$\boldsymbol{q}'[i] = \boldsymbol{V}\tilde{\boldsymbol{a}}[i],$$

C.2 Convergence and assumption validation

Figure C.1 shows the real parts of the leading SPOD observables ϕ_j, defined in equation (7.2), and the convolutional coordinates $\boldsymbol{a}$, defined in equation (7.8), at three representative frequencies. In contrast to $\boldsymbol{\phi}$, $\boldsymbol{a}$ are discrete-continuous in time but can effectively capture the intermittent nature of the system states. Furthermore, it is noteworthy that the PSD of $\boldsymbol{a}$

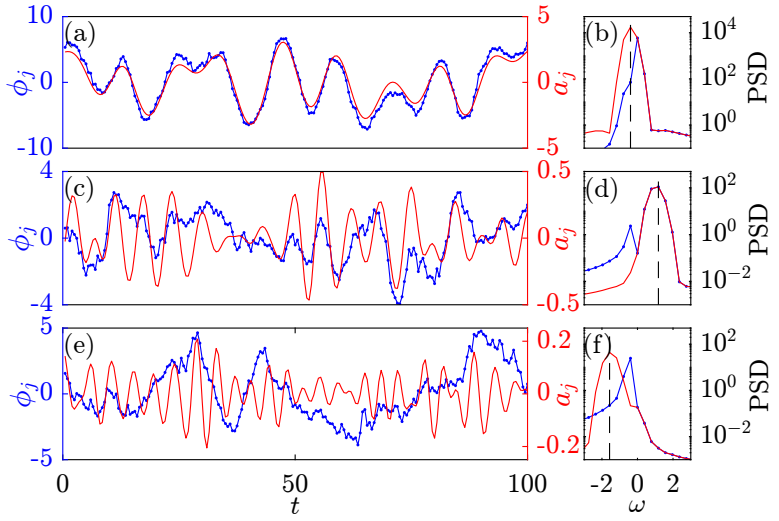

Figure C.1. Time traces (a,c,e) and spectra (b,d,f) of the leading SPOD observables $\boldsymbol{\phi}$ (blue) and convolutional coordinates $\boldsymbol{a}$ (red) at three representative frequencies: (a-c) $\omega = -0.39$; (d-f) $\omega = 1.18$; (g-i) $\omega = -1.57$.

peaks at the respective SPOD frequencies, showing that the convolution process preserves the orthogonality property and mode-frequency correspondence inherent in the SPOD.

Next, we investigate the convergence of the modified Koopman operator as the amount of data used for its construction increases. We introduce a matrix norm, $\|\cdot\|_D$, as

$$\|\boldsymbol{K}\|_D \equiv \frac{\|\boldsymbol{K}^{(N)} - \boldsymbol{K}^{(N_\infty)}\|_F}{\|\boldsymbol{K}^{(N_\infty)}\|_F}, \tag{C.1a}$$

which measures the normalized distance between the matrices constructed with N and N_∞ snapshots. Here, $\|\cdot\|_F$ denotes the Frobenius norm, and N_∞ is the total number of available snapshots.

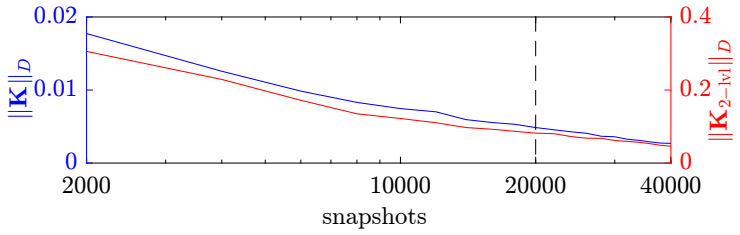

Figure C.2. Convergence of the modified Koopman operators $\boldsymbol{K}$ (blue) and $\boldsymbol{K}_y$ (red).

Figure C.2 shows the convergence of $\boldsymbol{K}$ and $\boldsymbol{K}_{\text{2-lvl}}$, defined in equations (7.20) and (6.28), respectively, as the total number of snapshots N_∞ is set to 80000. As the amount of snapshots increases, both matrices demonstrate nearly algebraic convergence. The stability of $\boldsymbol{K}_{\text{2-lvl}}$ is verified in figure C.5. In the following, the training set is defined as a dataset comprising $N = 20000$ snapshots, where the normalized norm values for the matrices are found to be $\|\boldsymbol{K}\|_D = 0.0$[illegible] test set.

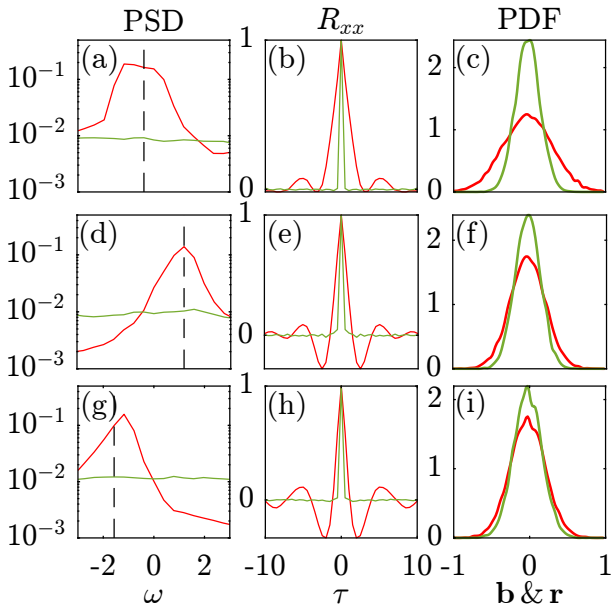

Figure C.3. Spectra (left column), autocorrelation estimates (middle column) and the probability distribution (right column) of the rank 2×32 forcing coefficients, $\boldsymbol{b}$ (red), and residue, $\boldsymbol{r}$ (green), at three representative frequencies: (a-c) $\omega = -0.39$; (d-f) $\omega = 1.18$; (g-i) $\omega = -1.57$.

Subsequently, we proceed to validate the underlying assumption of the model, which posits that the residue can be modeled as Gaussian random noise. To accomplish this, we examine the spectra, (normalized) autocorrelations $R_{xx}(\tau) = \langle x(t)x(t+\tau)\rangle$, and probability distributions of both the forcing coefficients, $\check{\boldsymbol{b}}(t)$ and the residue, $\check{\boldsymbol{r}}(t)$ in figure C.3. As in panels C.3(a,d,f), it is evident that the PSD of the residue remains nearly constant across frequencies, whereas the PSD of the forcing coefficients peaks near the corresponding mode frequency. Panels C.3(b,e,h) show that the autocorrelations of the residue exhibit a rapid decay, while the forcing coefficients display correlations that persist for 10 or more time units. The combined evidence of spectral

flatness and the rapid drop of the autocorrelation supports the proposition that the residue can be adequately modeled as white-in-time. We finally examine the probability distributions of $\check{\boldsymbol{b}}$ and $\check{\boldsymbol{r}}$ in panels C.3(e,f,i). Notably, the probability distributions of residue at different frequencies are nearly Gaussian. This confirms that $\check{\boldsymbol{r}}$ can be modeled using mutually correlated but white-in-time components.

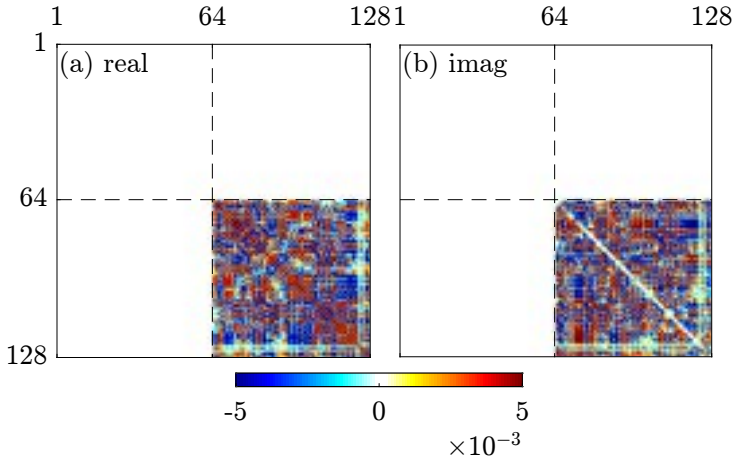

Figure C.4. Matrix $\check{\boldsymbol{H}}$: (a) real part; (b) imaginary part.

Figure C.4 shows the matrix $\check{\boldsymbol{H}}$ defined in equation (7.27). Notably, both its real and imaginary components are primarily active in the bottom-right quadrant. This observation confirms the viability of truncating $\check{\boldsymbol{H}}$ to solely retain this quadrant. The matrix $\boldsymbol{G}$ is then calculated using equations (7.28-6.35) to correlate the white-in-time input $\boldsymbol{w}$ for different frequencies, generating the process noise $\widetilde{\boldsymbol{w}}$ that drives the final model.

C.3 Eigenvalues of $\boldsymbol{K}_y$

Figure C.5 shows the eigenvalues of the inflated Koopman operator $\boldsymbol{K}_y$ defined in equation (6.28) for all the cases under consideration. It can be observed that all the eigenvalues stay within the stability region. With L2 regularization, part of the eigenvalues associated with higher frequencies are pushed away from the unit circle. This prevents the overfitting of these high-frequency noise-like signals from the data.

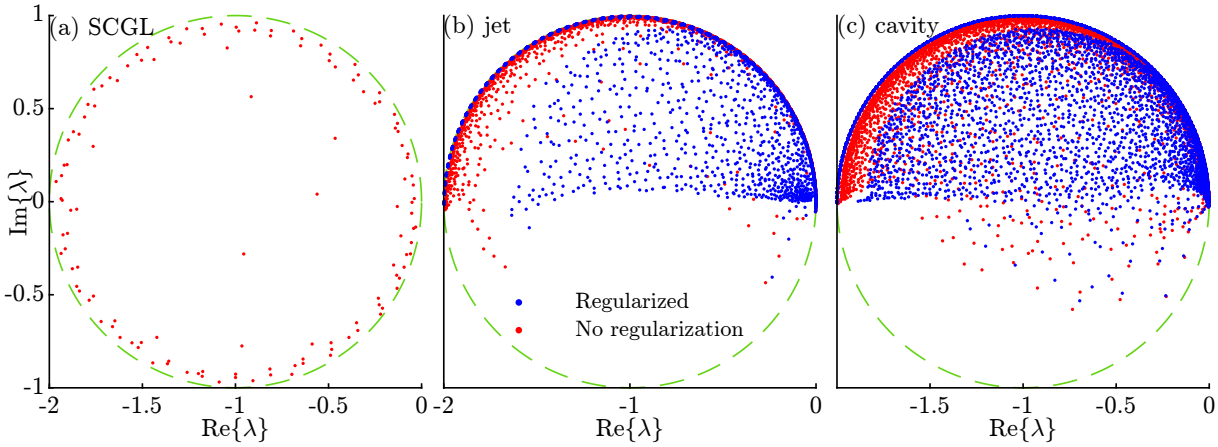

Figure C.5. Eigenvalues of the two-level system dynamic matrix $\boldsymbol{K}_y$ for different datasets: (a) SCGL; (b) jet; (c) open cavity flow. The green dashed circle represents the stability region.

Appendix D

Compressible point vortices

D.1 Inner region and formal matching

D.1.1 Velocity potential

In the steady case, BNEEY [18], Leppington [153] and Crowdy & Krishnamurthy [58] were able to obtain the solution without carrying out a formal matching procedure, by requiring certain growth conditions on the potential near the vortices. In the unsteady case here, we used the $O(1)$ solution in the core region to obtain equations of motion for the point vortices, but did not compute further terms in the inner region. We now carry out the formal matching procedure to verify that the approach in the main body of the paper is correct. We follow the analyses of BNEEY [18] and Leppington [153] closely (and no longer cite these references in this section), with the extensions required.

We expand the velocity potential $\hat{\Phi}$ near the vortex at $z=\zeta$ as $\hat{\Phi} = \Phi_{c0} + \kappa\theta + \Delta(M)\kappa\Phi_1 + \cdots$, where Φ_{c0} is a constant with no dynamical significance and $\Delta(M)$ is a gauge function to be determined. The leading-order term satisfies the expansion and we obtain the following equation for Φ_1:

$$\left(1-\frac{2(\gamma-1)}{2s^2}\right)\frac{\partial^2\Phi_1}{\partial s^2}+\left(1-\frac{2(\gamma-3)}{2s^2}\right)\frac{1}{s}\frac{\partial\Phi_1}{\partial s}+\left(1-\frac{2(\gamma+1)}{2s^2}\right)\frac{1}{s^2}\frac{\partial^2\Phi_1}{\partial\theta^2}=0. \qquad \text{(D.1)}$$

This is the same equation as for the steady case. Terms associated with the travelling reference

frame appear at higher order.

We now match the velocity potential ϕ to the vortex region, which will fix $\Delta(M)$. Rewriting the outer potential in terms of the inner variable, we have, from (8.20),

$$F^{(0,.)} = -\mathrm{i}\kappa \log Ms\mathrm{e}^{\mathrm{i}\theta} + f_0 + f_1 Ms\mathrm{e}^{\mathrm{i}\theta} + \frac{1}{2} f_2 M^2 s^2 \mathrm{e}^{2\mathrm{i}\theta} + O(M^3 s^3). \tag{D.2}$$

In the notation of Matched Asymptotic Expansions, we can write

$$\phi^{(0,0)} = \kappa\theta + \mathrm{Re}\ \ f_0. \tag{D.3}$$

In the inner region, we find

$$\Phi^{(0,.)} = g + \Phi_{c0} + \kappa\theta, \tag{D.4}$$

in which contributions from $\boldsymbol{U}$ do not appear. Van Dyke's rule, $\phi^{(0,0)} = \Phi^{(0,0)}$, gives

$$\kappa\theta + \mathrm{Re}\, f_0 = \Phi_{c0} + \kappa\theta + g, \tag{D.5}$$

which is identically satisfied for the $\kappa\theta$ term and relates the dynamically irrelevant constants f_0, Φ_{c0} and g. Since $F_1 = 0$,

$$\phi^{(1,1)} = \phi^{(0,0)} + Ms\mathrm{Re}\, f_1 \mathrm{e}^{\mathrm{i}\theta}. \tag{D.6}$$

Examining (D.1) shows that its solutions for $s \gg 1$ look like $s^{\pm m}\mathrm{e}^{\pm \mathrm{i}m\theta}$ for integer m; essentially they are tending to harmonic functions. We denote the solution that grows in s as $\chi_m(s)\mathrm{e}^{\mathrm{i}\theta}$. For large m, we have

$$\chi_1(s) = s + O(s^{-1}\log s), \tag{D.7}$$

$$\chi_2(s) = s^2 + \frac{5}{2} + O(s^{-2}\log s), \tag{D.8}$$

These are the only modes that we need. From (D.6) we see that we need the mode-1 solution of

the form $A_1\chi_1(s)e^{i\theta}+c.c.$ in the matching. Hence the next equation in Van Dyke's hierarchy, $\phi^{(1,1)}=\Phi^{(1,1)}$, gives

$$Ms\mathrm{Re}\, f_1 e^{i\theta}=\boldsymbol{U}_0\cdot\hat{\boldsymbol{x}}+\Phi_{c1}\mathrm{Re}\,[A_1 s e^{i\theta}+c.c.]. \tag{D.9}$$

This is satisfied with $\Phi_{c1}=A_1=0$, because $f_1=W_0$ from (8.29), the leading-order result for point vortices. Physically, the velocity of the vortex core matches motion of the fluid as one tends to the core. Hence the solution in the core region vanishes at $O(M)$.

The use of a moving reference frame has removed the $O(M)$ term, along with a multitude of higher-order terms that it would have forced. Note that $\Phi_1=s^{-1}e^{i\theta}$ is an exact solution of (D.1). However it matches to terms in the vortex region that are singular. These are not consistent with point vortex solutions. (There is a clash of notation here: the superscripts in this section do not match the subscripts used previously. The superscripts indicate orders of truncation, grouping logarithmic terms with purely algebraic ones, while the subscripts used previously explicitly distinguish between $M^2\log M$ and M^2.)

The conclusion is that $\Delta=M^2$. Continuing,

$$\phi^{(2,2)}=\phi^{(1,1)}+\frac{1}{2}M^2s^2\mathrm{Re}\, f_2e^{2i\theta}+M^2\mathrm{Re}\,[A+Be^{2i\theta}]. \tag{D.10}$$

Crucially, the new terms that require matching do not include a linear term in s. The $O(M^2)$ solution in the core region can be written as $\Phi_2=\Phi_{c,2}+A_2\chi_2(s)e^{2i\theta}+c.c.$, with $\chi_2(s)=s^2+5/2+O(s^{-2}\log s)$ for large s, using the fact that (D.1) is linear. Hence

$$\Phi^{(2,2)}=\Phi^{(1,1)}+M^2\Phi_{c2}+\left[A_2\left(\varepsilon^2+\frac{5}{2}M^2\right)e^{2i\theta}+c.c.\right]. \tag{D.11}$$

Note that the core-region terms with $\boldsymbol{U}_1$ and $\boldsymbol{U}_2$ first appear in $\Phi^{(3,.)}$. Equating (D.10) and (D.11) leads to equations for A_2 and Φ_{c2}.

To reach the terms at $O(M^3\log M)$ and $O(M^3)$ that were mentioned in § 8.18.1.3, we

discuss one more order. From (1.6), we see that the solutions in the vortex region at these orders are harmonic functions. By the same argument as used for F_1, they must vanish. Hence we have

$$\phi^{(3,3)} = \phi^{(2,2)} + \frac{1}{3}M^3 s^3 \mathrm{Re}\, f_3 \mathrm{e}^{3\mathrm{i}\theta} + M^3 \mathrm{Re}\,[2DMs\log s\mathrm{e}^{\mathrm{i}\theta} + Hs\mathrm{e}^{\mathrm{i}\theta} + Ls\mathrm{e}^{3\mathrm{i}\theta}]. \tag{D.12}$$

The solution in the core region is more involved. We note that

$$\Phi^{(2,3)} = \Phi^{(2,2)} + [M^2 \log M \boldsymbol{U}_1 + M^2 \boldsymbol{U}_2]\cdot\hat{\boldsymbol{x}}. \tag{D.13}$$

We see that, to be able to match to (D.12), we need terms in $\hat{\Phi}$ at $O(M^3\log M)$ and $\mathrm{O}(M^3)$. Using (1.10), we find that the former satisfies (D.1), while the equation for the latter has a forcing term on the right-hand side given by $U_{0j}\partial\hat{\Phi}_0/\partial s_j$. We do not carry out the full matching at this order, because it is not needed.

D.1.2 Conservation of momentum

We can now formalize the matching argument of § 8.1 to verify the equations of motion rigorously. We have the information we need for q:

$$\begin{aligned} q^{(2,2)} =& M^2\log M[\pi\mathrm{i}\kappa[\overline{W}_1 + \zeta_{,1}] + \pi\overline{f}_{1,1}e^2] \\ &+ M^2\left[-\frac{\pi}{2}\kappa^2\overline{f}_{1,0} + \pi\mathrm{i}\kappa\zeta_{,2} + \pi\mathrm{i}\kappa\overline{W}_2 - 2\pi\mathrm{i}\kappa\overline{H} - 2\pi\mathrm{i}\kappa\overline{D}(1+\log e^2)\right]. \end{aligned} \tag{D.14}$$

where we have used the result $Q^{(0.0)} = q^{(0,0)} = 0$ established earlier as well as the identity $\overline{\zeta}_{,1} = W_1$. For the inner region, we return to (8.1) using the full expansion:

$$P = M^2 \oint \int_{s_v}^{s} [\hat{\rho}_0 + O(M^2)]\left[\boldsymbol{U} + \frac{\kappa}{Ms'}\boldsymbol{t} + O(M)\right] s'\,\mathrm{d}s'\,\mathrm{d}\theta. \tag{D.15}$$

Since we need $Q^{(2,.)}$ and the time derivatives cannot reduce the powers of M, we see that we have enough terms. We obtain

$$Q^{(2,2)} = \pi\overline{W}_{0,0}e^2 + \pi\overline{W}_{0,0}(\kappa^2 M^2 \log M - \kappa^2 M^2 \log e + M^2 C), \tag{D.16}$$

We see that Van Dyke's rule, $Q^{(2,2)} = q^{(2,2)}$, corresponds to the result obtained before, on comparing (D.14) and (D.16). Hence the approach of § 8.1.3 gave the correct answer.

D.2 Details of the global solution

To obtain (8.44), we expand the function

$$l_m(z) = \frac{1}{4}(z - Z_0)(-\mathrm{i}\kappa_m \overline{\zeta}^{(m)}_{,00}) + \frac{1}{2}F_{0,0}(\mathrm{i}\kappa_m) + \frac{1}{4}w_0(2\mathrm{i}\kappa_m \overline{f}^{(m)}_1) \tag{D.17}$$

near vortex n and obtain

$$\begin{aligned} l_m(z) =& \frac{1}{4}(\zeta - Z_0 + \varepsilon)_n(-\mathrm{i}\kappa_m \overline{\zeta}^{(m)}_{,00}) + \frac{1}{2}\left[\frac{\mathrm{i}\kappa\zeta_{,0}}{\varepsilon} + f_{0,0} - f_1\zeta_{,0} + (f_{1,0} - f_2\zeta_{,0})\varepsilon\right]^{(n)}(\mathrm{i}\kappa_m) \\ &+ \frac{1}{4}\left[-\frac{\mathrm{i}\kappa}{\varepsilon} + f_1 + f_2\varepsilon\right]^{(n)}(2\mathrm{i}\kappa_m \overline{f}^{(m)}_1) + O(e_n^2) \qquad \text{(D.18)} \\ =& l^{(mn)}_{-1}\varepsilon_n^{-1} + l^{(mn)}_0 + l^{(mn)}_1\varepsilon_n + O(e_n^2). \qquad \text{(D.19)} \end{aligned}$$

The coefficients are given by

$$l^{(mn)}_{-1} = \frac{1}{2}\kappa_n\kappa_m(\overline{f}^{(m)}_1 - \zeta_{n,0}), \tag{D.20}$$

$$l^{(mn)}_0 = \frac{1}{4}(\zeta_n - Z_0)(-\mathrm{i}\kappa_m \overline{\zeta}^{(m)}_{,00}) + \frac{1}{2}(f_{0,0} - f_1\zeta_{,0})^{(n)}(\mathrm{i}\kappa_m) + \frac{1}{2}f_1^{(n)}(\mathrm{i}\kappa_m \overline{f}^{(m)}_1), \tag{D.21}$$

$$l^{(mn)}_1 = \frac{1}{4}(-\mathrm{i}\kappa_m \overline{\zeta}^{(m)}_{,00}) + \frac{1}{2}(f_{1,0} - f_2\zeta_{,0})^{(n)}(\mathrm{i}\kappa_m) + \frac{1}{2}f_2^{(n)}(\mathrm{i}\kappa_m \overline{f}^{(m)}_1). \tag{D.22}$$

D.3 Two vortices in the plane

The integrals I and J become

$$I(z) = \int_\infty^z \left[-\frac{\mathrm{i}\kappa_1}{z-\zeta_1} - \frac{\mathrm{i}\kappa_2}{z-\zeta_2} \right]^2 \mathrm{d}z = \frac{\kappa_1^2}{z-\zeta_1} + \frac{\kappa_2^2}{z-\zeta_2} + \frac{2\kappa_1\kappa_2}{\zeta_{12}} \log \frac{z-\zeta_1}{z-\zeta_2}, \tag{D.23}$$

$$J(z) = \int_\infty^z F_{0,00}\, \mathrm{d}z = \mathrm{i}\kappa_1 \zeta_{1,00} \log(z-\zeta_1) + \mathrm{i}\kappa_2 \zeta_{2,00} \log(z-\zeta_2) - \frac{\mathrm{i}\kappa_1 \zeta_{1,0}^2}{z-\zeta_1} - \frac{\mathrm{i}\kappa_2 \zeta_{2,0}^2}{z-\zeta_2}. \tag{D.24}$$

Using superscripts to indicate the vortex for which terms are being calculated, we expand the potentials and integrals about the locations of the two vortices to give

$$f_0^{(1)} = -\mathrm{i}\kappa_2 \log \zeta_{21}, \quad f_1^{(1)} = -\frac{\mathrm{i}\kappa_2}{\zeta_{21}}, \quad f_2^{(1)} = \frac{\mathrm{i}\kappa_2}{\zeta_{21}^2}, \quad I_0^{(1)} = \frac{\kappa_2^2}{\zeta_{21}} + \frac{2\kappa_1\kappa_2}{\zeta_{21}} \log \zeta_{21}, \tag{D.25}$$

$$f_0^{(2)} = -\mathrm{i}\kappa_1 \log \zeta_{12}, \quad f_1^{(2)} = -\frac{\mathrm{i}\kappa_1}{\zeta_{12}}, \quad f_2^{(2)} = \frac{\mathrm{i}\kappa_1}{\zeta_{12}^2}, \quad I_0^{(2)} = \frac{\kappa_1^2}{\zeta_{12}} + \frac{2\kappa_1\kappa_2}{\zeta_{12}} \log \zeta_{12}, \tag{D.26}$$

and

$$J_0^{(1)} = \mathrm{i}\kappa_2 \zeta_{2,00} \log \zeta_{21} - \frac{\mathrm{i}\kappa_2 \zeta_{2,0}^2}{\zeta_{21}}, \quad J_0^{(2)} = \mathrm{i}\kappa_1 \zeta_{1,00} \log \zeta_{12} - \frac{\mathrm{i}\kappa_1 \zeta_{1,0}^2}{\zeta_{12}}. \tag{D.27}$$

In addition

$$g_{-1}^{(2)} = \frac{1}{2}\kappa_1\kappa_2(\zeta_1-\zeta_2)_{,0} \log \zeta_{12} = \frac{i\kappa_1\kappa_2(\kappa_1+\kappa_2)}{2\overline{\zeta}_{21}} \log \zeta_{12}. \tag{D.28}$$

This leads to $H_1 = 0$.

For the co-propagating case, we find

$$l_0^{(21)} = \frac{1}{2}(-f_1^{(1)}\zeta_{,0}^{(1)})(\mathrm{i}\kappa_2) + \frac{1}{2}f_1^{(1)}(\mathrm{i}\kappa_2\overline{f}_1^{(2)}) = \frac{1}{2}(\mathrm{i}\kappa_2)f_1^{(1)}(-\zeta_{,0}^{(1)} + \overline{f}_1^{(2)}) = 0, \tag{D.29}$$

and by symmetry $l_0^{(12)} = 0$. A similar argument shows that $l_1^{(21)} = l_1^{(12)} = 0$. The remaining

constraint (8.24) becomes

$$\mu_2 = \frac{\mathrm{i}\kappa^3}{2\overline{\zeta}_{21}} + \frac{\mathrm{i}\kappa^3}{4\overline{\zeta}_{12}^2}(\overline{\zeta}_2 - \overline{Z}_0^{(2)}) = -\frac{\kappa^3}{4a} - \frac{\mathrm{i}\kappa^3}{16a^2}(\overline{\zeta}_2 - \overline{Z}_0^{(2)}), \tag{D.30}$$

For the co-rotating case, we can compute the terms required in the t_2-equation. The centre of vorticity remains at the origin, so we take $Z_0 = 0$. We have

$$f_0^{(1)} = -\mathrm{i}\kappa \log(2a\mathrm{e}^{\mathrm{i}\varphi}), \qquad f_1^{(1)} = -\frac{\mathrm{i}\kappa}{2a}\mathrm{e}^{-\mathrm{i}\varphi}, \qquad f_2^{(1)} = \frac{\mathrm{i}\kappa}{4a^2}\mathrm{e}^{-2\mathrm{i}\varphi}. \tag{D.31}$$

Then

$$f_{0,0}^{(1)} = \frac{\kappa^2}{2a^2}, \qquad f_{1,0}^{(1)} = -\frac{\kappa^2}{4a^3}\mathrm{e}^{-\mathrm{i}\varphi}, \qquad D_1 = -\frac{\mathrm{i}\kappa^3}{16a^3}\mathrm{e}^{-\mathrm{i}\varphi}, \qquad g_{-1}^{(1)} = -\frac{\mathrm{i}\kappa^3}{2a}\mathrm{e}^{\mathrm{i}\varphi}\log(2a\mathrm{e}^{\mathrm{i}\varphi}) \tag{D.32}$$

and

$$\mu_2 = -\frac{\mathrm{i}\kappa^3}{16a}\mathrm{e}^{\mathrm{i}\varphi}\left(8\log 4a^2 - 1\right), \qquad l_0^{(21)} = -\frac{\mathrm{i}\kappa^3}{16a^2}, \qquad l_1^{(21)} = -\frac{\mathrm{i}\kappa^3}{16a^3}\mathrm{e}^{-\mathrm{i}\varphi}. \tag{D.33}$$

This gives

$$H_1 = -\frac{\mathrm{i}\kappa^3}{16a^3}\mathrm{e}^{-\mathrm{i}\varphi}\left(1 - \log 4a^2\right) \tag{D.34}$$

and

$$\zeta_{1,2} = -\frac{\mathrm{i}\kappa}{2}\overline{f}_{1,0}^{(1)}\left(1 + \frac{C}{\kappa^2}\right) + \overline{H}_1 = \frac{\mathrm{i}\kappa^3}{8a^3}\mathrm{e}^{\mathrm{i}\varphi}\left(1 + \frac{C}{\kappa^2}\right) + \overline{H}_1 = \frac{\mathrm{i}\kappa^3}{8a^4}\zeta\left(\frac{3}{2} + \frac{C}{\kappa^2} - \log 2a\right). \tag{D.35}$$

Once again there is a correction to the rotation speed:

$$\theta_{,2} = \frac{\kappa^3}{8a^4}\left(\frac{3}{2} + \frac{C}{\kappa^2} - \log 2a\right). \tag{D.36}$$

For the general two-vortex case, we have

$$\mu_2 = \frac{\mathrm{i}\kappa_1\kappa_2(\kappa_1-\kappa_2)}{4\overline{\zeta}_{12}} - \frac{\mathrm{i}\kappa_1^2\kappa_2}{4\overline{\zeta}_{12}^2}\overline{\zeta_2 - Z_0} - \frac{\mathrm{i}\kappa_1\kappa_2(\kappa_1+\kappa_2)}{2\overline{\zeta}_{21}}\log|\zeta_{12}|^2, \tag{D.37}$$

$$l_0^{(21)} = -\frac{\mathrm{i}\kappa_1\kappa_2(\kappa_1+\kappa_2)}{4\zeta_{21}^2\overline{\zeta}_{21}}(\zeta_1 - Z_0), \tag{D.38}$$

$$l_1^{(21)} = -\frac{\mathrm{i}\kappa_1\kappa_2(\kappa_1+\kappa_2)}{4\zeta_{21}^2\overline{\zeta}_{21}}, \tag{D.39}$$

and $\xi_2 = 0$ if Z_0 is aligned between the two vortices. This gives

$$\begin{aligned} g_1 =& \frac{\mathrm{i}\kappa_1\kappa_2(\kappa_1-\kappa_2)}{4\zeta_{21}^2\overline{\zeta}_{21}} + \frac{\mathrm{i}\kappa_1^2\kappa_2}{4\zeta_{21}^2\overline{\zeta}_{21}^2}\overline{\zeta_2 - Z_0} + \frac{\mathrm{i}\kappa_1\kappa_2(\kappa_1+\kappa_2)}{2\zeta_{21}^2\overline{\zeta}_{21}}\log|\zeta_{21}|^2 \\ & - \frac{\mathrm{i}\kappa_1\kappa_2(\kappa_1+\kappa_2)}{4\zeta_{21}^3\overline{\zeta}_{21}}(\zeta_1 - Z_0) - \frac{\mathrm{i}\kappa_1\kappa_2(\kappa_1+\kappa_2)}{4\zeta_{21}^2\overline{\zeta}_{21}}\log\zeta_{21}. \end{aligned} \tag{D.40}$$

The term H_1 can then be obtained as

$$H_1 = \frac{\mathrm{i}\kappa_1\kappa_2}{4|\zeta_{21}|^2}\left(\frac{\kappa_1(\overline{\zeta}_2 - \overline{Z_0}) + \kappa_2(\overline{\zeta}_1 - \overline{Z_0})}{|\zeta_{21}|^2} - \frac{(\kappa_1+\kappa_2)}{\zeta_{21}^2}(\zeta_1 - Z_0) - \frac{\kappa_2}{\zeta_{21}}\right) + \frac{\mathrm{i}\kappa_1\kappa_2(\kappa_1+\kappa_2)}{4\zeta_{21}^2\overline{\zeta}_{21}}\log|\zeta_{21}|^2. \tag{D.41}$$

Selecting Z_0 appropriately gives

$$H_1 = \frac{\mathrm{i}\kappa_1\kappa_2(\kappa_1+\kappa_2)}{4|\zeta_{21}|^2\zeta_{21}}\left(-1 + \log|\zeta_{21}|^2\right). \tag{D.42}$$

We then obtain (8.59).

D.4 Point Vortex inside a circle

The functions $\tilde{J}(z)$ and $\tilde{I}(z)$ retain the non-logarithmic terms:

$$\tilde{J}(z) = -\frac{\mathrm{i}\kappa\zeta_{,0}^2}{\varepsilon} + \frac{\mathrm{i}\kappa\zeta_{i,0}^2}{\varepsilon_i} + J_0, \qquad \tilde{I}(z) = \frac{\kappa^2}{\varepsilon} + \frac{\kappa^2}{\varepsilon_i}. \tag{D.43}$$

We have

$$l(z) = \frac{1}{4}(z - Z_0)(-\mathrm{i}\kappa\overline{\zeta}_{,00}) + \frac{\kappa^2}{2\varepsilon_i}(\zeta_{i,0} - \overline{f}_1), \tag{D.44}$$

$$l_i(z) = \frac{1}{4}(z - Z_0)(\mathrm{i}\kappa\overline{\zeta}_{i,00}) - \frac{\kappa^2}{2\varepsilon_i}(\zeta_{i,0} - \overline{f}_1^{(i)}) \tag{D.45}$$

since $\zeta_{,0} = \overline{f}_1 = \overline{f}_1^i$, so the only singularities are of $l(z)$ and $l_i(z)$ are at ζ_i and ∞. Note that

$$l(z) + l_i(z) = -\frac{\mathrm{i}\kappa}{4}(z - Z_0)[\overline{\zeta}_{,00} - \overline{\zeta}_{i,00}]. \tag{D.46}$$

Then the velocity w_2 can be written

$$\begin{aligned} w_2 =& l'(z)\log\overline{\varepsilon} + \overline{\frac{l(z)}{\varepsilon}} + l_i'(z)\log\overline{\varepsilon}_i + \overline{\frac{l_i(z)}{\varepsilon_i}} + \frac{1}{4}\overline{\tilde{J}(z)} + \frac{1}{4}(\overline{z} - \overline{Z}_0)\tilde{J}'(z) \\ &+ \frac{1}{4}w_0'(z)\overline{\tilde{I}(z)} + \frac{1}{4}\overline{w_0(z)}\tilde{I}'(z) + G'(z). \end{aligned} \tag{D.47}$$

Given the inhomogeneous portion of F_2, we will need to satisfy the boundary condition (8.62) as well as require the solution to be single-valued inside the circle with appropriate behaviour near ζ. The potential F_2 can be written

$$F_2(z) = l(z)\log\overline{\varepsilon} + l_i'(z)\log\overline{\varepsilon}_i + \frac{1}{4}(z - Z_0)\overline{\tilde{J}(z)} + \frac{1}{4}w_0(z)\overline{\tilde{I}(z)} + G(z). \tag{D.48}$$

We now enforce single-valuedness near $z = \zeta$. Previously we added the terms $l(z)\log\varepsilon$ and $l_i(z)\log\varepsilon_i$ to F_2. These do not satisfy the boundary condition. Instead, since ζ_i is not in the physical domain, we do not enforce single-valuedness there. Hence we add to F_2 the terms $l(z)\log\varepsilon$ and $m_i(z)\log\varepsilon_i$, then pick the function $m_i(z)$ to satisfy the boundary condition. We hence have the following logarithmic terms in w_2:

$$l'(z)\log e^2 + l_i'(z)\log\overline{\varepsilon}_i + m_i'(z)\log\varepsilon_i. \tag{D.49}$$

A simple extension to the Milne-Thomson circle theorem shows that if $f(z)$ is a function of z, then

$$f(z) - \frac{R^2}{z^2}\bar{f}(R^2/z) \tag{D.50}$$

satisfies the boundary condition (8.62). Similarly we find that both of the expressions

$$f(z)\overline{g(z)} - f(z)\bar{g}(R^2/z), \qquad f(z)\overline{g(z)} - \frac{R^2}{z^2}\overline{f}(R^2/z)g(z) \tag{D.51}$$

satisfy (8.62).

We now add to (D.49)

$$-l'(z)\log\left(\frac{R^2}{z} - \overline{\zeta}\right) - l'(z)\log\varepsilon - l_i'(z)\log\left(\frac{R^2}{z} - \frac{R^2}{\zeta}\right) - \frac{R^2}{z^2}\bar{m}'(R^2/z)\log\left(\frac{R^2}{z} - \frac{R^2}{\zeta}\right). \tag{D.52}$$

Noting that

$$\log\left(\frac{R^2}{z} - \overline{\zeta}\right) = \log\frac{(-\overline{\zeta}\varepsilon_i)}{z}, \qquad \log\left(\frac{R^2}{z} - \frac{R^2}{\zeta}\right) = \log\frac{(-R^2\varepsilon)}{\zeta z}, \tag{D.53}$$

we see that (D.52) has logarithmic singularities at ε and at the origin. These can be simultaneously removed by requiring

$$\bar{m}_i(z) = l(R^2/z) + l_i(R^2/z) = -\frac{\mathrm{i}\kappa}{4}\left(\frac{R^2}{z} - Z_0\right)[\overline{\zeta}_{,00} - \overline{\zeta}_{i,00}]. \tag{D.54}$$

The expression (D.52) reduces to

$$-l'(z)\log\left(\frac{a^2\varepsilon_i}{R^2}\right), \tag{D.55}$$

which is single-valued in the fluid domain. The term $m'(z)\log\varepsilon_i$ has a double pole at the origin

from (D.54). This can be removed by adding the following expression

$$-m_i'(z)\log(-\zeta_i)+\frac{R^2}{z^2}\bar{m}_i'(R^2/z)\log(-\zeta_i)=-m_i'(z)\log(-\zeta_i)-[l'(z)+l_i'(z)]\log(-\overline{\zeta}_i). \tag{D.56}$$

The sum of (D.49), (D.55) and (D.56) is single-valued at ζ, has no singularity at ζ and satisfies the boundary condition.

We now consider the non-logarithmic terms in w_2. These can be written as

$$\begin{aligned}
&\frac{\overline{l(z)}+l(z)}{\varepsilon}+\frac{\overline{l_i(z)}+m_i(z)}{\varepsilon_i}+\frac{1}{4}\overline{\tilde{J}(z)}+\frac{1}{4}(\overline{z}-\overline{Z}_0)\tilde{J}'(z)+\frac{1}{4}w_0'(z)\overline{\tilde{I}(z)}+\frac{1}{4}\overline{w_0(z)}\tilde{I}'(z) &\text{(D.57)}\\
=&\frac{1}{\varepsilon}\left[\frac{1}{4}(\overline{z}-\overline{Z}_0)(\mathrm{i}\kappa\zeta_{,00})+\frac{\kappa^2}{2\overline{\varepsilon}_i}(\overline{\zeta}_{i,0}-f_1)+\frac{1}{4}(z-Z_0)(-\mathrm{i}\kappa\overline{\zeta}_{,00})+\frac{\kappa^2}{2\varepsilon_i}(\zeta_{i,0}-\overline{f}_1)\right]\\
&+\frac{1}{\varepsilon_i}\left[\frac{1}{4}(\overline{z}-\overline{Z}_0)(-\mathrm{i}\kappa\zeta_{i,00})-\frac{\kappa^2}{2\overline{\varepsilon}_i}(\overline{\zeta}_{i,0}-f_1^{(i)})+\frac{\mathrm{i}\kappa}{4}\left(\frac{R^2}{z}-\overline{Z}_0\right)(\zeta_{,00}-\zeta_{i,00})\right]\\
&+\frac{1}{4}\left[\frac{\mathrm{i}\kappa\overline{\zeta}_{,0}^2}{\overline{\varepsilon}}-\frac{\mathrm{i}\kappa\overline{\zeta}_{i,0}^2}{\overline{\varepsilon}_i}+\overline{J}_0+\frac{2\mathrm{i}\kappa^3}{\varepsilon^2\overline{\varepsilon}_i}-\frac{2\mathrm{i}\kappa^3}{\varepsilon_i^2\overline{\varepsilon}}\right]+\frac{1}{4}(\overline{z}-\overline{Z}_0)\left[\frac{\mathrm{i}\kappa\zeta_{,0}^2}{\varepsilon^2}-\frac{\mathrm{i}\kappa\zeta_{i,0}^2}{\varepsilon_i^2}\right]. &\text{(D.58)}
\end{aligned}$$

We satisfy the boundary condition by adding terms that do not introduce a singularity at ζ. The following tables list in their first row terms in (D.58) and in their second rows the terms to add to satisfy the boundary condition. First, from (D.50) or just from removing the term,

$$\begin{array}{cccccccc}
\alpha & \dfrac{\alpha}{\varepsilon} & \dfrac{\alpha}{\varepsilon_i} & \dfrac{\alpha z}{\varepsilon} & \dfrac{\alpha}{\varepsilon^2} & \dfrac{\alpha}{\varepsilon_i^2} & \dfrac{\alpha}{z\varepsilon_i}\\
-\alpha & \dfrac{\overline{\alpha}\zeta_i}{z\varepsilon_i} & -\dfrac{\alpha}{\varepsilon_i} & \dfrac{\overline{\alpha}R^2\zeta_i}{z^2\varepsilon_i} & -\dfrac{\overline{\alpha}\zeta_i^2}{R^2\varepsilon_i^2} & -\dfrac{\alpha}{\varepsilon_i^2} & -\dfrac{\alpha}{z\varepsilon_i}.
\end{array} \tag{D.59}$$

(Note that these choices are not unique. For example one could take $-\overline{\alpha}R^2/z^2$ for the first case. Uniqueness will come later when the singularities at the origin and at ζ are taken into account.)

Then, from (D.51),

$$\begin{array}{cccccccccc} \dfrac{\alpha}{\overline{\varepsilon}} & \dfrac{\alpha}{\overline{\varepsilon}_i} & \dfrac{\alpha\overline{z}}{\varepsilon} & \dfrac{\alpha\overline{z}}{\varepsilon^2} & \dfrac{\alpha\overline{z}}{\varepsilon_i} & \dfrac{\alpha\overline{z}}{\varepsilon_i^2} & \dfrac{\alpha}{\varepsilon\overline{\varepsilon}_i} & \dfrac{\alpha}{\varepsilon^2\overline{\varepsilon}_i} & \dfrac{\alpha}{\varepsilon_i^2\overline{\varepsilon}} \\ \dfrac{\alpha\zeta_i z}{R^2\varepsilon_i} & -\dfrac{\overline{\alpha}R^2}{z^2\varepsilon_i} & \dfrac{\overline{\alpha}\zeta_i}{\varepsilon_i} & -\dfrac{\overline{\alpha}\zeta_i^2 z}{R^2\varepsilon_i^2} & -\dfrac{\alpha R^2}{z\varepsilon_i} & -\dfrac{\alpha R^2}{z\varepsilon_i^2} & \dfrac{\overline{\alpha}\zeta_i}{z\varepsilon_i^2} & -\dfrac{\overline{\alpha}\zeta_i^2}{R^2\varepsilon_i^3} & \dfrac{\alpha z\zeta_i}{R^2\varepsilon_i^3}. \end{array} \tag{D.60}$$

The remaining terms are lengthier:

$$\begin{aligned} \frac{\alpha}{\varepsilon\varepsilon_i}: \quad & \text{add} \quad \frac{\overline{\alpha}\zeta_i}{(\overline{\zeta}-\overline{\zeta}_i)z\varepsilon_i}+\frac{\alpha}{(\zeta-\zeta_i)\varepsilon_i} \\ \frac{\alpha}{\varepsilon_i\overline{\varepsilon}_i}: \quad & \text{add} \quad \frac{\alpha z\zeta}{R^2\varepsilon_i\varepsilon}-\frac{\alpha\zeta^2}{R^2(\zeta-\zeta_i)\varepsilon}-\frac{\overline{\alpha}\overline{\zeta}}{z(\overline{\zeta}-\overline{\zeta}_i)\varepsilon_i}. \end{aligned} \tag{D.61}$$

Every term in (D.58) takes one of the above forms.

We have to remove the singularity introduced in the full expression for w_2 at the origin by the above process. This takes the form $\lambda z^{-2}+\nu z^{-1}$. We remove the singularity by adding

$$-\frac{\lambda}{z^2}+\frac{\overline{\lambda}}{R^2}-\frac{\nu}{z}. \tag{D.62}$$

The second term ensures that the boundary condition is satisfied for the extra $-\lambda z^{-2}$ term. The $-\nu z^{-1}$ term that has been added satisfies the boundary condition if ν is imaginary. One cannot add a term to remove it, as it corresponds to a volume source (or sink) at the origin. Such a term cannot be present. Verifying that the real part of ν vanishes is a useful check on the calculations. Finally we need to remove the singularity at ζ by adding terms that satisfy the boundary condition, namely

$$\frac{\xi}{\varepsilon}+\frac{\overline{\xi}\zeta_i}{z\varepsilon_i}-\frac{\mu}{\varepsilon^2}+\frac{\overline{\mu}\zeta_i^2}{R^2\varepsilon_i^2}. \tag{D.63}$$

This seems to introduce another pole at the origin, unless $\xi=0$, which will need to be checked.

We now give the details of the calculation, starting by setting $Z_0 = 0$. Writing down the form for w_2 that satisfies the boundary conditions gives

$$
\begin{aligned}
w_2 = &\left[\frac{1}{4}(-\mathrm{i}\kappa\overline{\zeta}_{,00}) - \frac{\kappa^2}{2\varepsilon_i^2}(\zeta_{i,0} - \overline{f}_1)\right]\log\frac{R^2e^2}{a^2\varepsilon_i} \\
&+ \left[\frac{1}{4}(\mathrm{i}\kappa\overline{\zeta}_{i,00}) + \frac{\kappa^2}{2\varepsilon_i^2}(\zeta_{i,0} - \overline{f}_1)\right]\log\overline{\varepsilon}_i - \frac{\mathrm{i}\kappa}{4}\frac{R^2}{z^2}(\zeta_{,00} - \zeta_{i,00})\log\left(-\frac{\varepsilon_i}{\zeta_i}\right) \\
&+ \frac{\mathrm{i}\kappa}{4}(\overline{\zeta}_{,00} - \overline{\zeta}_{i,00})\log(-\overline{\zeta}_i) \\
&+ \frac{1}{\varepsilon}\left[\frac{1}{4}\overline{z}(\mathrm{i}\kappa\zeta_{,00}) + \frac{\kappa^2}{2\overline{\varepsilon}_i}(\overline{\zeta}_{i,0} - f_1) + \frac{1}{4}z(-\mathrm{i}\kappa\overline{\zeta}_{,00}) + \frac{\kappa^2}{2\varepsilon_i}(\zeta_{i,0} - \overline{f}_1)\right] \\
&+ \frac{1}{\varepsilon_i}\left[\frac{1}{4}\overline{z}(-\mathrm{i}\kappa\zeta_{i,00}) - \frac{\kappa^2}{2\overline{\varepsilon}_i}(\overline{\zeta}_{i,0} - f_1^{(i)})\right] \\
&+ \frac{1}{4}\left[\frac{\mathrm{i}\kappa\overline{\zeta}_{,0}^2}{\overline{\varepsilon}} - \frac{\mathrm{i}\kappa\overline{\zeta}_{i,0}^2}{\overline{\varepsilon}_i} + \frac{2\mathrm{i}\kappa^3}{\varepsilon^2\overline{\varepsilon}_i} - \frac{2\mathrm{i}\kappa^3}{\varepsilon_i^2\overline{\varepsilon}}\right] \\
&+ \frac{1}{4}\overline{z}\left(\frac{\mathrm{i}\kappa\zeta_{,0}^2}{\varepsilon^2} - \frac{\mathrm{i}\kappa\zeta_{i,0}^2}{\varepsilon_i^2}\right) \\
&+ \frac{\mathrm{i}\kappa\zeta_{,00}R^2\zeta_i}{4z^2\varepsilon_i} + \frac{\mathrm{i}\kappa\overline{\zeta}_{,0}^2\zeta_i z}{4R^2\varepsilon_i} - \frac{\mathrm{i}\kappa\zeta_{i,0}^2R^2}{4z^2\varepsilon_i} - \frac{\mathrm{i}\kappa\overline{\zeta}_{,00}\zeta_i}{4\varepsilon_i} + \frac{\mathrm{i}\kappa\overline{\zeta}_{,0}^2\zeta_i^2 z}{4R^2\varepsilon_i^2} \\
&+ \frac{\mathrm{i}\kappa\zeta_{i,00}R^2}{4z\varepsilon_i} + \frac{\mathrm{i}\kappa\zeta_{i,0}^2R^2}{4z\varepsilon_i^2} + \frac{\kappa^2(\zeta_{i,0} - \overline{f}_1)\zeta_i}{2z\varepsilon_i^2} + \frac{\mathrm{i}\kappa^3\zeta_i^2}{2R^2\varepsilon_i^3} - \frac{\mathrm{i}\kappa^3 z\zeta_i}{2R^2\varepsilon_i^3} \\
&+ \frac{\kappa^2(\overline{\zeta}_{i,0} - f_1)\zeta_i}{2(\overline{\zeta} - \overline{\zeta}_i)z\varepsilon_i} + \frac{\kappa^2(\zeta_{i,0} - \overline{f}_1)}{2(\zeta - \zeta_i)\varepsilon_i} + \frac{\alpha z\zeta}{R^2\varepsilon_i\varepsilon} - \frac{\alpha\zeta^2}{R^2(\zeta - \zeta_i)\varepsilon} - \frac{\overline{\alpha}\overline{\zeta}}{z(\overline{\zeta} - \overline{\zeta}_i)\varepsilon_i} \\
&- \frac{\lambda}{z^2} + \frac{\overline{\lambda}}{R^2} - \frac{\nu}{z} - \frac{\mu}{\varepsilon^2} + \frac{\overline{\mu}\zeta_i^2}{R^2\varepsilon_i^2},
\end{aligned}
\tag{D.64}
$$

where $\alpha = -\kappa^2(\overline{\zeta}_{i,0} - f_1)/2$. Expanding about the origin gives

$$
\lambda = -\frac{\mathrm{i}\kappa\zeta_{,00}R^2}{4} + \frac{\mathrm{i}\kappa\zeta_{i,0}^2R^2}{4\zeta_i}, \tag{D.65}
$$

$$
\begin{aligned}
\nu = &\frac{\mathrm{i}\kappa R^2}{4\zeta_i}(\zeta_{,00} - \zeta_{i,00}) - \frac{\mathrm{i}\kappa\zeta_{,00}R^2}{2\zeta_i} + \frac{\mathrm{i}\kappa\zeta_{i,0}^2R^2}{2\zeta_i^2} \\
&+ \frac{\kappa^2(\zeta_{i,0} - \overline{f}_1)}{2\zeta_i} - \frac{\kappa^2(\overline{\zeta}_{i,0} - f_1)}{2(\overline{\zeta} - \overline{\zeta}_i)} - \frac{\kappa^2(\zeta_{i,0} - \overline{f}_1)\overline{\zeta}}{2(\overline{\zeta} - \overline{\zeta}_i)\zeta_i}.
\end{aligned}
\tag{D.66}
$$

The first of these relations gives λ. In the second, we see that every term in ν is pure imaginary, since ζ_i, $\zeta_{i,00}$, $-\mathrm{i}\zeta_{,0} = -\mathrm{i}\overline{f}_1$ and $-\mathrm{i}\zeta_{i,0}$ have the same argument. Hence the term in z^{-1} satisfies the boundary condition. The ε^{-2} and ε^{-1} terms near $z = \zeta$ give

$$\mu = \frac{\mathrm{i}\kappa\zeta_{,0}^2\overline{\zeta}}{4} + \frac{\mathrm{i}\kappa^3}{2(\overline{\zeta} - \overline{\zeta}_i)} \tag{D.67}$$

and $\xi = 0$.

Finally we calculate the constant term in (8.37). We obtain

$$\begin{aligned}
w_2 = &\left[\frac{1}{4}(-\mathrm{i}\kappa\overline{\zeta}_{,00}) - \frac{\kappa^2}{2\delta_i^2}(\zeta_{i,0} - \overline{f}_1)\right]\log\frac{R^2}{a^2\delta_i} \\
&+ \left[\frac{1}{4}(\mathrm{i}\kappa\overline{\zeta}_{i,00}) + \frac{\kappa^2}{2\delta_i^2}(\zeta_{i,0} - \overline{f}_1)\right]\log\overline{\delta}_i - \frac{\mathrm{i}\kappa}{4}\frac{R^2}{\zeta^2}(\zeta_{,00} - \zeta_{i,00})\log\left(-\frac{\delta_i}{\zeta_i}\right) \\
&+ \frac{\mathrm{i}\kappa}{4}(\overline{\zeta}_{,00} - \overline{\zeta}_{i,00})\log(-\overline{\zeta}_i) \\
&+ \frac{1}{\delta_i}\left[\frac{1}{4}\overline{\zeta}(-\mathrm{i}\kappa\zeta_{i,00}) - \frac{\kappa^2}{2\overline{\delta}_i}(\overline{\zeta}_{i,0} - f_1^{(i)})\right] + \frac{1}{4}\left[-\frac{\mathrm{i}\kappa\overline{\zeta}_{i,0}^2}{\overline{\delta}_i}\right] + \frac{1}{4}\overline{\zeta}\left(-\frac{\mathrm{i}\kappa\zeta_{i,0}^2}{\delta_i^2}\right) \\
&+ \frac{\mathrm{i}\kappa\zeta_{,00}R^2\zeta_i}{4\zeta^2\delta_i} + \frac{\mathrm{i}\kappa\overline{\zeta}_{,0}^2\zeta_i\zeta}{4R^2\delta_i} - \frac{\mathrm{i}\kappa\zeta_{i,0}^2R^2}{4\zeta^2\delta_i} - \frac{\mathrm{i}\kappa\overline{\zeta}_{,00}\zeta_i}{4\delta_i} + \frac{\mathrm{i}\kappa\overline{\zeta}_{,0}^2\zeta_i^2\zeta}{4R^2\delta_i^2} \\
&+ \frac{\mathrm{i}\kappa\zeta_{i,00}R^2}{4\zeta\delta_i} + \frac{\mathrm{i}\kappa\zeta_{i,0}^2R^2}{4\zeta\delta_i^2} + \frac{\kappa^2(\zeta_{i,0} - \overline{f}_1)\zeta_i}{2\zeta\delta_i^2} + \frac{\mathrm{i}\kappa^3\zeta_i^2}{2R^2\delta_i^3} - \frac{\mathrm{i}\kappa^3\zeta\zeta_i}{2R^2\delta_i^3} \\
&+ \frac{\kappa^2(\overline{\zeta}_{i,0} - f_1)\zeta_i}{2(\overline{\zeta} - \overline{\zeta}_i)\zeta\delta_i} + \frac{\kappa^2(\zeta_{i,0} - \overline{f}_1)}{2(\zeta - \zeta_i)\delta_i} + \frac{\kappa^2(\zeta_{i,0} - \overline{f}_1)\overline{\zeta}}{2\zeta(\overline{\zeta} - \overline{\zeta}_i)\delta_i} - \frac{\lambda}{\zeta^2} + \frac{\overline{\lambda}}{R^2} - \frac{\nu}{\zeta} + \frac{\overline{\mu}\zeta_i^2}{R^2\delta_i^2},
\end{aligned} \tag{D.68}$$

where $\delta_i = \zeta - \zeta_i$. After lengthy algebra we obtain

$$D + H = \frac{\mathrm{i}\kappa^3 a\mathrm{e}^{-\mathrm{i}\varphi}}{4(R^2 - a^2)^2}\left[\log\frac{(R^2 - a^2)^3}{R^4} + \frac{R^4}{a^4}\log\frac{R^2}{R^2 - a^2} + 1\right]. \tag{D.69}$$

Bibliography

[1] E. Åkervik, U. Ehrenstein, F. Gallaire, and D. S. Henningson. Global two-dimensional stability measures of the flat plate boundary-layer flow. *Eur. J. Mech. B-Fluids.*, 27(5):501–513, 2008.

[2] F. Alizard, S. Cherubini, and J.-C. Robinet. Sensitivity and optimal forcing response in separated boundary layer flows. *Phys. Fluids*, 21(6), 2009.

[3] F. Alizard, T. Gibis, B. Selent, U. Rist, and C. Wenzel. Stochastic receptivity of laminar compressible boundary layers: An input-output analysis. *Phys. Rev. Fluids.*, 7(7):073902, 2022.

[4] F. Alizard and J.-C. Robinet. Spatially convective global modes in a boundary layer. *Phys. Fluids*, 19(11), 2007.

[5] H. Arbabi and I. Mezić. Ergodic theory, dynamic mode decomposition, and computation of spectral properties of the koopman operator. *SIAM Journal on Applied Dynamical Systems*, 16(4):2096–2126, 2017.

[6] H. Arbabi and T. Sapsis. Generative stochastic modeling of strongly nonlinear flows with non-gaussian statistics. *SIAM-ASA J. Uncertain. Quantif.*, 10(2):555–583, 2022.

[7] K. Ardalan, D. I. Meiron, and D. I. Pullin. Steady compressible vortex flows – the hollow-core vortex array. *J. Fluid Mech.*, 301:1–17, 1995.

[8] N. Aubry, P. Holmes, J. L. Lumley, and E. Stone. The dynamics of coherent structures in the wall region of a turbulent boundary layer. *J. Fluid Mech.*, 192:115–173, 1988.

[9] F. Auteri, N. Parolini, and L. Quartapelle. Numerical investigation on the stability of singular driven cavity flow. *J. Comput. Phys.*, 183(1):1–25, 2002.

[10] H. J. Bae, S. T. M. Dawson, and B. J. McKeon. Resolvent-based study of compressibility effects on supersonic turbulent boundary layers. *J. Fluid Mech.*, 883:A29, 2020.

[11] S. Bagheri, E. Åkervik, L. Brandt, and D. S. Henningson. Matrix-free methods for the stability and control of boundary layers. *AIAA J.*, 47(5):1057–1068, 2009.

[12] S. Bagheri, L. Brandt, and D. S. Henningson. Input–output analysis, model reduction and control of the flat-plate boundary layer. *J. Fluid Mech.*, 620:263–298, 2009.

[13] S. Bagheri, D. S. Henningson, J. Hoepffner, and P. J. Schmid. Input-output analysis and control design applied to a linear model of spatially developing flows. *Appl. Mech. Rev.*, 62(2), 2009.

[14] S. Bagheri, P. Schlatter, P. J. Schmid, and D. S. Henningson. Global stability of a jet in crossflow. *J. Fluid Mech.*, 624:33–44, 2009.

[15] D. Barkley. Linear analysis of the cylinder wake mean flow. *Europhys. Lett.*, 75(5):750, 2006.

[16] D. Barkley and R. D. Henderson. Three-dimensional floquet stability analysis of the wake of a circular cylinder. *J. Fluid Mech.*, 322:215–241, 1996.

[17] M. F. Barone, I. Kalashnikova, D. J. Segalman, and H. K. Thornquist. Stable galerkin reduced order models for linearized compressible flow. *J. Compt. Phys.*, 228(6):1932–1946, 2009.

[18] A. Barsony-Nagy, J. Er-El, and S. Yungster. Compressible flow past a contour and stationary vortices. *J. Fluid Mech.*, 178:367–378, 1987.

[19] N. Bartwal, S. Shahane, S. Roy, and S. P. Vanka. Application of a high order accurate meshless method to solution of heat conduction in complex geometries. *Comput. Therm. Sci.*, 14(3), 2022.

[20] V. Bayona. Comparison of moving least squares and rbf+ poly for interpolation and derivative approximation. *J. Sci. Comput.*, 81:486–512, 2019.

[21] V. Bayona. An insight into rbf-fd approximations augmented with polynomials. *Comput. Math. Appl.*, 77(9):2337–2353, 2019.

[22] V. Bayona, N. Flyer, and B. Fornberg. On the role of polynomials in rbf-fd approximations: Iii. behavior near domain boundaries. *J. Comput. Phys.*, 380:378–399, 2019.

[23] V. Bayona, N. Flyer, B. Fornberg, and G. A. Barnett. On the role of polynomials in rbf-fd approximations: Ii. numerical solution of elliptic pdes. *J. Comput. Phys.*, 332:257–273, 2017.

[24] H. Bénard. The formation of gyration centres at the back of a moving obstacle. *C. R. Acad. Sci.*, 147:839–842, 1908.

[25] S. Beneddine, D. Sipp, A. Arnault, J. Dandois, and L. Lesshafft. Conditions for validity of mean flow stability analysis. *J. Fluid Mech.*, 798:485–504, 2016.

[26] R. Betchov and A. Szewczyk. Stability of a shear layer between parallel streams. *Phys. Fluids*, 6(10):1391–1396, 1963.

[27] D. I. Blokhintsev. Acoustics of a non-homogeneous moving medium. Technical Report 1399, National Advisory Committee for Aeronautics, 1946.

[28] E. F. Bollig, N. Flyer, and G. Erlebacher. Solution to pdes using radial basis function finite-differences (rbf-fd) on multiple gpus. *J. Comput. Phys.*, 231(21):7133–7151, 2012.

[29] N. Bonne, V. Brion, E. Garnier, R. Bur, P. Molton, D. Sipp, and L. Jacquin. Analysis of the two-dimensional dynamics of a mach 1.6 shock wave/transitional boundary layer interaction using a rans based resolvent approach. *J. Fluid Mech.*, 862:1166–1202, 2019.

[30] E. Bozzo, R. Carniel, and D. Fasino. Relationship between singular spectrum analysis and fourier analysis: Theory and application to the monitoring of volcanic activity. *Comput. Math. with Appl.*, 60(3):812–820, 2010.

[31] L. Brandt, D. Sipp, J. O. Pralits, and O. Marquet. Effect of base-flow variation in noise amplifiers: the flat-plate boundary layer. *J. Fluid Mech.*, 687:503–528, 2011.

[32] M. Braza, P. Chassaing, and H. Ha Minh. Numerical study and physical analysis of the pressure and velocity fields in the near wake of a circular cylinder. *J. Fluid Mech.*, 165:79–130, 1986.

[33] G. A. Brès, P. Jordan, V. Jaunet, M. Le Rallic, A. V. G. Cavalieri, A. Towne, S. K. Lele, T. Colonius, and O. T. Schmidt. Importance of the nozzle-exit boundary-layer state in subsonic turbulent jets. *J. Fluid Mech.*, 851:83–124, 2018.

[34] C.-H. Bruneau and M. Saad. The 2d lid-driven cavity problem revisited. *Comput. & fluids*, 35(3):326–348, 2006.

[35] S. L. Brunton. Notes on koopman operator theory. 2019.

[36] S. L. Brunton, B. W. Brunton, J. L. Proctor, E. Kaiser, and J. N. Kutz. Chaos as an intermittently forced linear system. *Nat. Commun.*, 8(1):1–9, 2017.

[37] S. L. Brunton, B. W. Brunton, J. L. Proctor, and J. N. Kutz. Koopman invariant subspaces and finite linear representations of nonlinear dynamical systems for control. *PloS one*, 11(2):e0150171, 2016.

[38] S. L. Brunton and B. R. Noack. Closed-loop turbulence control: Progress and challenges. *Appl. Mech. Rev.*, 67(5), 2015.

[39] S. L. Brunton, B. R. Noack, and P. Koumoutsakos. Machine learning for fluid mechanics. *Annu. Rev. Fluid Mech.*, 52:477–508, 2020.

[40] M. Budišić, R. Mohr, and I. Mezić. Applied koopmanism. *Chaos*, 22(4):047510, 2012.

[41] B. Bugeat, J.-C. Chassaing, J.-C. Robinet, and P. Sagaut. 3d global optimal forcing and response of the supersonic boundary layer. *J. Comput. Phys.*, 398:108888, 2019.

[42] K. M. Butler and B. F. Farrell. Three-dimensional optimal perturbations in viscous shear flow. *Phys. Fluids A*, 4(8):1637–1650, 1992.

[43] D. Calhoun. A cartesian grid method for solving the two-dimensional streamfunction-vorticity equations in irregular regions. *J. Comput. Phys.*, 176(2):231–275, 2002.

[44] K. Carlberg, C. Farhat, J. Cortial, and D. Amsallem. The gnat method for nonlinear model reduction: effective implementation and application to computational fluid dynamics and turbulent flows. *J. Comput. Phys.*, 242:623–647, 2013.

[45] R. E. Carlson and T. A. Foley. The parameter r2 in multiquadric interpolation. *Comput. Math. Appl.*, 21(9):29–42, 1991.

[46] André VG Cavalieri, Daniel Rodríguez, Peter Jordan, Tim Colonius, and Yves Gervais. Wavepackets in the velocity field of turbulent jets. *J. Fluid Mech.*, 730:559–592, 2013.

[47] K. K. Chen and C. W. Rowley. H2 optimal actuator and sensor placement in the linearised complex ginzburg–landau system. *J. Fluid Mech.*, 681:241–260, 2011.

[48] K. K. Chen, J. H. Tu, and C. W. Rowley. Variants of dynamic mode decomposition: boundary condition, koopman, and fourier analyses. *J. Nonlinear Sci.*, 22:887–915, 2012.

[49] P. P. Chinchapatnam, K. Djidjeli, P. B. Nair, and M. Tan. A compact rbf-fd based meshless method for the incompressible navier—stokes equations. *Proc. IME. M-J Eng. Marit. Environ.*, 223(3):275–290, 2009.

[50] J.-M. Chomaz. Global instabilities in spatially developing flows: non-normality and nonlinearity. *Annu. Rev. Fluid Mech.*, 37:357–392, 2005.

[51] B.-T. Chu. On the energy transfer to small disturbances in fluid flow (part i). *Acta Mech.*, 1(3):215–234, 1965.

[52] T. Colonius, S. K. Lele, and P. Moin. Sound generation in a mixing layer. *J. Fluid Mech.*, 330:375–409, 1997.

[53] Lin Cong. Model order reduction in the frequency domain via spectral proper orthogonal decomposition. *Ph.D. thesis, University of Illinois at Urbana-Champaign.*, 2019.

[54] C. Cossu and J. M. Chomaz. Global measures of local convective instabilities. *Phys. Rev. Lett.*, 78(23):4387, 1997.

[55] D. G. Crighton. Basic principles of aerodynamic noise generation. *Prog. Aerospace Sci.*, 16:31–96, 1975.

[56] D. G. Crighton and M. Gaster. Stability of slowly diverging jet flow. *J. Fluid Mech.*, 77(2):397–413, 1976.

[57] D. G. Crowdy and V. S. Krishnamurthy. The effect of core size on the speed of compressible hollow vortex streets. *J. Fluid Mech.*, 836:797–827, 2018.

[58] D. G. Crowdy and Vikas S. Krishnamurthy. Speed of a von Kármán point vortex street in a weakly compressible fluid. *Phys. Rev. Fluids*, 2:114701, 2017.

[59] M. F. De Pando, D. Sipp, and P. J. Schmid. Efficient evaluation of the direct and adjoint linearized dynamics from compressible flow solvers. *J. Comput. Phys.*, 231(23):7739–7755, 2012.

[60] H. Ding, C. Shu, K. S. Yeo, and D. Xu. Simulation of incompressible viscous flows past a circular cylinder by hybrid fd scheme and meshless least square-based finite difference method. *Comput. Methods Appl. Mech. Engrg.*, 193(9-11):727–744, 2004.

[61] H. Ding, C. Shu, K. S. Yeo, and D. Xu. Numerical computation of three-dimensional incompressible viscous flows in the primitive variable form by local multiquadric differential quadrature method. *Comput. Methods Appl. Mech. Engrg.*, 195(7-8):516–533, 2006.

[62] T. Duriez, S. L. Brunton, and B. R. Noack. *Machine learning control-taming nonlinear dynamics and turbulence*, volume 116. Springer, 2017.

[63] A. Dwivedi, G. S. Sidharth, and M. R. Jovanović. Oblique transition in hypersonic double-wedge flow. *J. Fluid Mech.*, 948:A37, 2022.

[64] A. M. Edstrand, P. J. Schmid, K. Taira, and L. N. Cattafesta. A parallel stability analysis of a trailing vortex wake. *J. Fluid Mech.*, 837:858–895, 2018.

[65] U. Ehrenstein and F. Gallaire. On two-dimensional temporal modes in spatially evolving open flows: the flat-plate boundary layer. *J. Fluid Mech.*, 536:209–218, 2005.

[66] L. E. Eriksson and A. Rizzi. Computer-aided analysis of the convergence to steady state of discrete approximations to the euler equations. *J. Comput. Phys.*, 57(1):90–128, 1985.

[67] B. F. Farrell and P. J. Ioannou. Stochastic forcing of the linearized navier–stokes equations. *Phys. Fluids A*, 5(11):2600–2609, 1993.

[68] B. F. Farrell and P. J. Ioannou. Structural stability of turbulent jets. *J. Atmos. Sci.*, 60(17):2101–2118, 2003.

[69] B. F. Farrell and P. J. Ioannou. Dynamics of streamwise rolls and streaks in turbulent wall-bounded shear flow. *J. Fluid Mech.*, 708:149–196, 2012.

[70] G. E. Fasshauer and J. G. Zhang. On choosing "optimal" shape parameters for rbf approximation. *Numer. Algorithms.*, 45:345–368, 2007.

[71] U. Fey, M. König, and H. Eckelmann. A new strouhal–reynolds-number relationship for the circular cylinder in the range 47¡ re¡ 2×10^5. *Phys. Fluids*, 10(7):1547–1549, 1998.

[72] N. Flyer, G. A. Barnett, and L. J. Wicker. Enhancing finite differences with radial basis functions: experiments on the navier–stokes equations. *J. Comput. Phys.*, 316:39–62, 2016.

[73] N. Flyer and B. Fornberg. Radial basis functions: Developments and applications to planetary scale flows. *Comput. & Fluids*, 46(1):23–32, 2011.

[74] N. Flyer, B. Fornberg, V. Bayona, and G. A. Barnett. On the role of polynomials in rbf-fd approximations: I. interpolation and accuracy. *J. Comput. Phys.*, 321:21–38, 2016.

[75] N. Flyer and E. Lehto. Rotational transport on a sphere: Local node refinement with radial basis functions. *J. Comput. Phys.*, 229(6):1954–1969, 2010.

[76] N. Flyer, E. Lehto, S. Blaise, G. B. Wright, and A. St-Cyr. A guide to rbf-generated finite differences for nonlinear transport: Shallow water simulations on a sphere. *J. Comput. Phys.*, 231(11):4078–4095, 2012.

[77] N. Flyer and G. B. Wright. Transport schemes on a sphere using radial basis functions. *J. Comput. Phys.*, 226(1):1059–1084, 2007.

[78] N. Flyer and G. B. Wright. A radial basis function method for the shallow water equations on a sphere. *Proc. Math. Phys. Eng. Sci.*, 465(2106):1949–1976, 2009.

[79] B. Fornberg, T. A. Driscoll, G. Wright, and R. Charles. Observations on the behavior of radial basis function approximations near boundaries. *Comput. Math. Appl.*, 43(3-5):473–490, 2002.

[80] B. Fornberg and N. Flyer. Solving pdes with radial basis functions. *Acta Numer.*, 24:215–258, 2015.

[81] B. Fornberg, E. Larsson, and N. Flyer. Stable computations with gaussian radial basis functions. *SIAM J. Sci. Comput*, 33(2):869–892, 2011.

[82] B. Fornberg and E. Lehto. Stabilization of rbf-generated finite difference methods for convective pdes. *J. Comput. Phys.*, 230(6):2270–2285, 2011.

[83] B. Fornberg, E. Lehto, and C. Powell. Stable calculation of gaussian-based rbf-fd stencils. *Comput. Math. Appl.*, 65(4):627–637, 2013.

[84] B. Fornberg and C. Piret. A stable algorithm for flat radial basis functions on a sphere. *SIAM J. Sci. Comput.*, 30(1):60–80, 2008.

[85] B. Fornberg and G. Wright. Stable computation of multiquadric interpolants for all values of the shape parameter. *Comput. Math. Appl.*, 48(5-6):853–867, 2004.

[86] P. Frame and A. Towne. Space-time pod and the hankel matrix. *Plos One*, 18(8):e0289637, 2023.

[87] R. Franke. Scattered data interpolation: tests of some methods. *Math. Comp.*, 38(157):181–200, 1982.

[88] X. Garnaud, L. Lesshafft, P. J. Schmid, and P. Huerre. The preferred mode of incompressible jets: linear frequency response analysis. *J. Fluid Mech.*, 716:189–202, 2013.

[89] M. Gaster, E. Kit, and I. Wygnanski. Large-scale structures in a forced turbulent mixing layer. *J. Fluid Mech.*, 150:23–39, 1985.

[90] U. Ghia, K. N. Ghia, and C. T. Shin. High-re solutions for incompressible flow using the navier-stokes equations and a multigrid method. *J. Comput. Phys.*, 48(3):387–411, 1982.

[91] F. Giannetti and P. Luchini. Structural sensitivity of the first instability of the cylinder wake. *J. Fluid Mech.*, 581:167–197, 2007.

[92] J. F. Gibson, J. D. Farmer, M. Casdagli, and S. Eubank. An analytic approach to practical state space reconstruction. *Phys. D: Nonlin. Phenom.*, 57(1-2):1–30, 1992.

[93] M. N. Glauser, S. J. Leib, and W. K. George. Coherent structures in the axisymmetric turbulent jet mixing layer. In *Turbulent Shear Flows 5*, pages 134–145. Springer, 1987.

[94] S. V. Gordeyev and F. O. Thomas. Coherent structure in the turbulent planar jet. part 1. extraction of proper orthogonal decomposition eigenmodes and their self-similarity. *J. Fluid Mech.*, 414:145–194, 2000.

[95] K. Gudmundsson and T. Colonius. Instability wave models for the near-field fluctuations of turbulent jets. *J. Fluid Mech.*, 689:97–128, 2011.

[96] D. Gunderman, N. Flyer, and B. Fornberg. Transport schemes in spherical geometries using spline-based rbf-fd with polynomials. *J. Comput. Phys.*, 408:109256, 2020.

[97] D. A. Hammond and L. G. Redekopp. Global dynamics of symmetric and asymmetric wakes. *J. Fluid Mech.*, 331:231–260, 1997.

[98] R. L. Hardy. Multiquadric equations of topography and other irregular surfaces. *Math. Comp.*, 76(8):1905–1915, 1971.

[99] F. H. Harlow and J. E. Welch. Numerical calculation of time-dependent viscous incompressible flow of fluid with free surface. *Phys. Fluids.*, 8(12):2182–2189, 1965.

[100] F. Hecht. New development in freefem++. *J. Numer. Math.*, 20(3-4):251–266, 2012.

[101] S. D. Heister, J. M. McDonough, A. R. Karagozian, and D. W¿ Jenkins. The compressible vortex pair. *J. Fluid Mech.*, 220:339–354, 1990.

[102] E. J. Hinch. *Pertubation Nethods*. Cambridge Univesity Press, Cambridge, 1991.

[103] C.-M. Ho and P. Huerre. Perturbed free shear layers. *Annu. Rev. Fluid Mech.*, 16(1):365–422, 1984.

[104] A. E. Hoerl and R. W. Kennard. Ridge regression: Biased estimation for nonorthogonal problems. *Technometrics*, 12(1):55–67, 1970.

[105] P. Holmes, J. L. Lumley, and G. Berkooz. *Turbulence, coherent structures, dynamical systems and symmetry*. Cambridge university press, 1996.

[106] P. Holmes, J. L. Lumley, G. Berkooz, J. C. Mattingly, and R. W. Wittenberg. Low-dimensional models of coherent structures in turbulence. *Phys. Rep.*, 287(4):337–384, 1997.

[107] P. Huerre. Open shear flow instabilities. *Perspective in Fluid Dynamics*, pages 159–229, 2000.

[108] P. Huerre and P. A. Monkewitz. Local and global instabilities in spatially developing flows. *Annu. Rev. Fluid Mech.*, 22(1):473–537, 1990.

[109] R. E. Hunt and D. G. Crighton. Instability of flows in spatially developing media. *Proc. R. Soc. A*, 435(1893):109–128, 1991.

[110] A. K. M. F. Hussain and W. C. Reynolds. The mechanics of an organized wave in turbulent shear flow. *J. Fluid Mech.*, 41(2):241–258, 1970.

[111] Y. Hwang and C. Cossu. Amplification of coherent streaks in the turbulent couette flow: an input–output analysis at low reynolds number. *J. Fluid Mech.*, 643:333–348, 2010.

[112] M. Ilak, S. Bagheri, L. Brandt, C. W. Rowley, and D. S. Henningson. Model reduction of the nonlinear complex ginzburg–landau equation. *SIAM J. Appl. Dyn. Syst.*, 9(4):1284–1302, 2010.

[113] A. Iske. On the approximation order and numerical stability of local lagrange interpolation by polyharmonic splines, in: W. haussmann, k. jetter, m. reimer, j. stöckler (eds.). In *Modern developments in multivariate approximation, in: International Series of Numerical Mathematics, Birkh´auser, Basel.*, pages 153–165. Springer, 2003.

[114] C. P. Jackson. A finite-element study of the onset of vortex shedding in flow past variously shaped bodies. *J. Fluid Mech.*, 182:23–45, 1987.

[115] I. Jacobi and B. J. McKeon. Dynamic roughness perturbation of a turbulent boundary layer. *J. Fluid Mech.*, 688:258–296, 2011.

[116] A. Javed, K. Djidjeli, J. T. Xing, and S. J. Cox. A hybrid mesh free local rbf-cartesian fd scheme for incompressible flow around solid bodies. *Int. J. Math. Comput. Phys. Elect. Comput. Eng.*, 7:957–966, 2013.

[117] A. Javed, K. Djijdeli, and J. T. Xing. Shape adaptive rbf-fd implicit scheme for incompressible viscous navier–strokes equations. *Comput. & Fluids*, 89:38–52, 2014.

[118] J. Jeun, J. W. Nichols, and M. R. Jovanović. Input-output analysis of high-speed axisymmetric isothermal jet noise. *Phys. Fluids.*, 28(4), 2016.

[119] H. Jiang and L. Cheng. Strouhal–reynolds number relationship for flow past a circular cylinder. *J. Fluid Mech.*, 832:170–188, 2017.

[120] B. Jin, S. Symon, and S. J. Illingworth. Energy transfer mechanisms and resolvent analysis in the cylinder wake. *Phys. Rev. Fluids*, 6(2):024702, 2021.

[121] P. Jordan and T. Colonius. Wave packets and turbulent jet noise. *Annu. Rev. Fluid Mech.*, 45:173–195, 2013.

[122] R. Jordinson. The flat plate boundary layer. part 1. numerical integration of the orr—sommerfeld equation. *J. Fluid Mech.*, 43(4):801–811, 1970.

[123] R. D. Joslin, C. L. Streett, and C.-L. Chang. Spatial direct numerical simulation of boundary-layer transition mechanisms: Validation of pse theory. *Theor. Comput. Fluid Dyn.*, 4(6):271–288, 1993.

[124] M. R. Jovanović and B. Bamieh. Componentwise energy amplification in channel flows. *J. Fluid Mech.*, 534:145–183, 2005.

[125] J.-N. Juang and R. S. Pappa. An eigensystem realization algorithm for modal parameter identification and model reduction. *J. Guid. Control Dyn.*, 8(5):620–627, 1985.

[126] E. Kaiser, B. R. Noack, L. Cordier, A. Spohn, M. Segond, M. Abel, G. Daviller, J. Östh, S. Krajnović, and R. K. Niven. Cluster-based reduced-order modelling of a mixing layer. *J. Fluid Mech.*, 754:365–414, 2014.

[127] I. Kalashnikova and M.F. Barone. Stable and efficient galerkin reduced order models for non-linear fluid flow. In *6th AIAA Theoretical Fluid Mechanics Conference*, page 3110, 2011.

[128] I Kalashnikova and M.F. Barone. Efficient non-linear proper orthogonal decomposition/galerkin reduced order models with stable penalty enforcement of boundary conditions. *Int. J. Numer. Meth. Eng.*, 90(11):1337–1362, 2012.

[129] M. Kamb, E. Kaiser, S. L. Brunton, and J. N. Kutz. Time-delay observables for koopman: Theory and applications. *SIAM Journal on Applied Dynamical Systems*, 19(2):886–917, 2020.

[130] E. J. Kansa. Multiquadrics—a scattered data approximation scheme with applications to computational fluid-dynamics—i surface approximations and partial derivative estimates. *Comput. Math. Appl.*, 19(8-9):127–145, 1990.

[131] E. J. Kansa. Multiquadrics—a scattered data approximation scheme with applications to computational fluid-dynamics—ii solutions to parabolic, hyperbolic and elliptic partial differential equations. *Comput. Math. Appl.*, 19(8-9):147–161, 1990.

[132] E. J. Kansa and Y. C. Hon. Circumventing the ill-conditioning problem with multiquadric radial basis functions: applications to elliptic partial differential equations. *Comput. Math. Appl*, 39(7-8):123–137, 2000.

[133] N. J. Kasdin. Discrete simulation of colored noise and stochastic processes and 1/f/sup/spl alpha//power law noise generation. *Proc. IEEE*, 83(5):802–827, 1995.

[134] N. J. Kasdin. Runge-kutta algorithm for the numerical integration of stochastic differential equations. *J. Guid. Control Dyn.*, 18(1):114–120, 1995.

[135] J. Kim and T. R. Bewley. A linear systems approach to flow control. *Annu. Rev. Fluid Mech.*, 39:383–417, 2007.

[136] J. Kim and P. Moin. Application of a fractional-step method to incompressible navier-stokes equations. *J. Comput. Phys.*, 59(2):308–323, 1985.

[137] M. J. Kloker. A robust high-resolution split-type compact fd scheme for spatial direct numerical simulation of boundary-layer transition. *Appl. Sci. Res.*, 59:353–377, 1997.

[138] S. Klus, P. Koltai, and C. Schütte. On the numerical approximation of the perron-frobenius and koopman operator. *J. Comput. Dyn.*, 3:51 – 79, 09 2016.

[139] D. Kondrashov, S. Kravtsov, A. W. Robertson, and M. Ghil. A hierarchy of data-based enso models. *J. Clim.*, 18(21):4425–4444, 2005.

[140] B. O. Koopman. Hamiltonian systems and transformation in hilbert space. *Proc. Natl. Acad. Sci.*, 17(5):315–318, 1931.

[141] M. Korda and I. Mezić. On convergence of extended dynamic mode decomposition to the koopman operator. *Journal of Nonlinear Science*, 28(2):687–710, 2018.

[142] J. Kou, S. Le Clainche, and W. Zhang. A reduced-order model for compressible flows with buffeting condition using higher order dynamic mode decomposition with a mode selection criterion. *Phys. Fluids*, 30(1):016103, 2018.

[143] S. Kravtsov, D. Kondrashov, and M. Ghil. Multilevel regression modeling of nonlinear processes: Derivation and applications to climatic variability. *J. Clim.*, 18(21):4404–4424, 2005.

[144] J. N. Kutz, S. L. Brunton, B. W. Brunton, and J. L. Proctor. *Dynamic mode decomposition: data-driven modeling of complex systems*. SIAM, 2016.

[145] E. Larsson, E. Lehto, A. Heryudono, and B. Fornberg. Stable computation of differentiation matrices and scattered node stencils based on gaussian radial basis functions. *SIAM J. Sci. Comput.*, 35(4):A2096–A2119, 2013.

[146] S. Le Borne and W. Leinen. Guidelines for rbf-fd discretization: Numerical experiments on the interplay of a multitude of parameter choices. *J. Sci. Comput.*, 95(1):8, 2023.

[147] S. Le Clainche and J. Vega. Higher order dynamic mode decomposition. *SIAM Journal on Applied Dynamical Systems*, 16(2):882–925, 2017.

[148] S. Le Clainche and J. Vega. Higher order dynamic mode decomposition to identify and extrapolate flow patterns. *Phys. Fluids*, 29(8):084102, 2017.

[149] S. Le Clainche, J. Vega, and J. Soria. Higher order dynamic mode decomposition of noisy experimental data: The flow structure of a zero-net-mass-flux jet. *Experimental Thermal and Fluid Science*, 88:336–353, 2017.

[150] K. H. Lee, L. Cortelezzi, J. Kim, and J. Speyer. Application of reduced-order controller to turbulent flows for drag reduction. *Phys. Fluids*, 13(5):1321–1330, 2001.

[151] S. Lee, S. K. Lele, and P. Moin. Direct numerical simulation of isotropic turbulence interacting with a weak shock wave. *J. Fluid Mech.*, 251:533–562, 1993.

[152] S. K. Lele. Compact finite difference schemes with spectral-like resolution. *J. Comput. Phys.*, 103(1):16–42, 1992.

[153] F. G. Leppington. The field due to a pair of line vortices in a compressible fluid. *J. Fluid Mech.*, 559:45–55, 2006.

[154] L. Lesshafft, O. Semeraro, V. Jaunet, A. V. G. Cavalieri, and P. Jordan. Resolvent-based modeling of coherent wave packets in a turbulent jet. *Phys. Rev. Fluid*, 4(6):063901, 2019.

[155] Q. Li, F. Dietrich, E. M. Bollt, and I. G. Kevrekidis. Extended dynamic mode decomposition with dictionary learning: A data-driven adaptive spectral decomposition of the koopman operator. *Chaos: An Interdisciplinary Journal of Nonlinear Science*, 27(10):103111, 2017.

[156] C. Liu, X. Zheng, and C. H. Sung. Preconditioned multigrid methods for unsteady incompressible flows. *J. Comput. Phys.*, 139(1):35–57, 1998.

[157] S. G. Llewellyn Smith. How do singularities move in potential flow? *Physica D*, 240:1644–1651, 2011.

[158] P. Luchini and A. Bottaro. Adjoint equations in stability analysis. *Annu. Rev. Fluid Mech.*, 46:493–517, 2014.

[159] J. L. Lumley. The structure of inhomogeneous turbulent flows. *Atmospheric turbulence and radio wave propagation*, 1967.

[160] J. L. Lumley. *Stochastic tools in turbulence*. Academic Press, 1970.

[161] L. M. Mack. A numerical study of the temporal eigenvalue spectrum of the blasius boundary layer. *J. Fluid Mech.*, 73(3):497–520, 1976.

[162] L. M. Mack. Boundary-layer linear stability theory. *Agard rep.*, 709(3):1–3, 1984.

[163] A. J. Majda and N. Chen. Model error, information barriers, state estimation and prediction in complex multiscale systems. *Entropy*, 20(9):644, 2018.

[164] A. J. Majda and J. Harlim. Physics constrained nonlinear regression models for time series. *Nonlinearity*, 26(1):201, 2012.

[165] A. J. Majda and Y. Lee. Conceptual dynamical models for turbulence. *Proc. Natl Acad. Sci.*, 111(18):6548–6553, 2014.

[166] V. Mantič-Lugo, C. Arratia, and F. Gallaire. Self-consistent mean flow description of the nonlinear saturation of the vortex shedding in the cylinder wake. *Phys. Rev. Lett.*, 113(8):084501, 2014.

[167] V. Mantič-Lugo, C. Arratia, and F. Gallaire. A self-consistent model for the saturation dynamics of the vortex shedding around the mean flow in the unstable cylinder wake. *Phys. Fluids.*, 27(7), 2015.

[168] M. Marquet, O.and Lombardi, J.-M. Chomaz, D. Sipp, and L. Jacquin. Direct and adjoint global modes of a recirculation bubble: lift-up and convective non-normalities. *J. Fluid Mech.*, 622:1–21, 2009.

[169] O. Marquet, D. Sipp, and L. Jacquin. Sensitivity analysis and passive control of cylinder flow. *J. Fluid Mech.*, 615:221–252, 2008.

[170] E. Martini, D. Rodríguez, A. Towne, and A. V. G. Cavalieri. Efficient computation of global resolvent modes. *J. Fluid Mech.*, 919:A3, 2021.

[171] G. E. Mattingly and W. O. Criminale. The stability of an incompressible two-dimensional wake. *J. Fluid Mech.*, 51(2):233–272, 1972.

[172] K. Mattsson and J. Nordström. Summation by parts operators for finite difference approximations of second derivatives. *J. Comput. Phys.*, 199(2):503–540, 2004.

[173] B. J. McKeon and A. S. Sharma. A critical-layer framework for turbulent pipe flow. *J. Fluid Mech.*, 658:336–382, 2010.

[174] D. I. Meiron, D. W. Moore, and D. I. Pullin. On steady compressible flows with compact vorticity; the compressible stuart vortex. *J. Fluid Mech.*, 409:29–49, 2000.

[175] P. Meliga, E. Boujo, and F. Gallaire. A self-consistent formulation for the sensitivity analysis of finite-amplitude vortex shedding in the cylinder wake. *J. Fluid Mech.*, 800:327–357, 2016.

[176] M. Mendez, A. Ianiro, B. Noack, and S. (Eds.) Brunton. *Data-Driven Fluid Mechanics: Combining First Principles and Machine Learning*. Cambridge University Press, 2023.

[177] I. Mezić. Spectral properties of dynamical systems, model reduction and decompositions. *Nonlinear Dyn.*, 41:309–325, 2005.

[178] I. Mezić. Analysis of fluid flows via spectral properties of the koopman operator. *Annu. Rev. Fluid Mech.*, 45:357–378, 2013.

[179] R. Moarref and M. R. Jovanović. Model-based design of transverse wall oscillations for turbulent drag reduction. *J. Fluid Mech.*, 707:205–240, 2012.

[180] R. Moarref, M. R. Jovanović, J. A. Tropp, A. S. Sharma, and B. J. McKeon. A low-order decomposition of turbulent channel flow via resolvent analysis and convex optimization. *Phys. Fluids*, 26(5), 2014.

[181] K. Mohseni and T. Colonius. Numerical treatment of polar coordinate singularities. *J. Comput. Phys.*, 157(2):787–795, 2000.

[182] P. Moin. *Fundamentals of engineering numerical analysis*. Cambridge University Press, 2010.

[183] P. A. Monkewitz. Subharmonic resonance, pairing and shredding in the mixing layer. *J. Fluid Mech.*, 188:223–252, 1988.

[184] A. Monokrousos, E. Åkervik, L. Brandt, and D. S. Henningson. Global three-dimensional optimal disturbances in the blasius boundary-layer flow using time-steppers. *J. Fluid Mech.*, 650:181–214, 2010.

[185] D. W. Moore and D. I. Pullin. The compressible vortex pair. *J. Fluid Mech.*, 185:171–204, 1987.

[186] A. Nekkanti and O. T. Schmidt. Frequency–time analysis, low-rank reconstruction and denoising of turbulent flows using spod. *J. Fluid Mech.*, 926, 2021.

[187] H. Nishikawa. A flexible gradient method for unstructured-grid solvers. *Internat. J. Numer. Methods Fluids*, 93(6):2015–2021, 2021.

[188] B. R. Noack, K. Afanasiev, M. MORZYŃSKI, G. Tadmor, and F. Thiele. A hierarchy of low-dimensional models for the transient and post-transient cylinder wake. *J. Fluid Mech.*, 497:335–363, 2003.

[189] B. R. Noack and H. Eckelmann. A global stability analysis of the steady and periodic cylinder wake. *J. Fluid Mech.*, 270:297–330, 1994.

[190] K. Oberleithner, L. Rukes, and J. Soria. Mean flow stability analysis of oscillating jet experiments. *J. Fluid Mech.*, 757:1–32, 2014.

[191] F. Obermeier. The application of singular perturbation methods to aerodynamic sound generation. In C.-M. Brauner, B. Gay, and J. Mathieu, editors, *Singular Perturbations and Boundary Layer Theory*, number 594 in Lecture Notes in Mathematics, pages 400–421, Berlin, 1977. Springer.

[192] Y. Ohmichi and K. Yamada. Matrix-free triglobal adjoint stability analysis of compressible navier–stokes equations. *J. Comput. Phys.*, 437:110332, 2021.

[193] N. Park and K. Mahesh. Numerical and modeling issues in les of compressible turbulence on unstructured grids. In *Presented at AIAA Aerosp. Sci. Meet. Exhib., 45th, Reno, NV, AIAA Pap.*, page 722, 2007.

[194] S. Patankar. *Numerical heat transfer and fluid flow*. Taylor & Francis, 2018.

[195] Y.-F. Peng, Y.-H. Shiau, and R. R. Hwang. Transition in a 2-d lid-driven cavity flow. *Comput. & Fluids*, 32(3):337–352, 2003.

[196] C. Penland. Random forcing and forecasting using principal oscillation pattern analysis. *Mon. Weather Rev.*, 117(10):2165–2185, 1989.

[197] C. Penland. A stochastic model of indopacific sea surface temperature anomalies. *Phys. D*, 98(2-4):534–558, 1996.

[198] A. Peplinski, P. Schlatter, and D. S. Henningson. Global stability and optimal perturbation for a jet in cross-flow. *Eur. J. Mech. B-Fluids.*, 49:438–447, 2015.

[199] P. O. Persson. Mesh generation for implicit geometries [ph. d. thesis]. *Massachusetts Institute of Technology*, 2005.

[200] J.-L. Pfister, N. Fabbiane, and O. Marquet. Global stability and resolvent analyses of laminar boundary-layer flow interacting with viscoelastic patches. *J. Fluid Mech.*, 937:A1, 2022.

[201] E. Pickering, G. Rigas, P. A. S. Nogueira, A. V. G. Cavalieri, O. T. Schmidt, and T. Colonius. Lift-up, kelvin–helmholtz and orr mechanisms in turbulent jets. *J. Fluid Mech.*, 896:A2, 2020.

[202] E. Pickering, G. Rigas, O. T. Schmidt, D. Sipp, and T. Colonius. Optimal eddy viscosity for resolvent-based models of coherent structures in turbulent jets. *J. Fluid Mech.*, 917:A29, 2021.

[203] B. Pier. On the frequency selection of finite-amplitude vortex shedding in the cylinder wake. *J. Fluid Mech.*, 458:407–417, 2002.

[204] F. L. Ponta and H. Aref. Strouhal-reynolds number relationship for vortex streets. *Phys. Rev. Lett.*, 93(8):084501, 2004.

[205] M. Provansal, C. Mathis, and L. Boyer. Bénard-von kármán instability: transient and forced regimes. *J. Fluid Mech.*, 182:1–22, 1987.

[206] U. A. Qadri and P. J. Schmid. Effect of nonlinearities on the frequency response of a round jet. *Phys. Rev. Fluids*, 2(4):043902, 2017.

[207] S. C. Reddy and D. S. Henningson. Energy growth in viscous channel flows. *J. Fluid Mech.*, 252:209–238, 1993.

[208] S. C. Reddy, P. J. Schmid, and D. S. Henningson. Pseudospectra of the orr–sommerfeld operator. *SIAM J. Appl. Math.*, 53(1):15–47, 1993.

[209] H. L. Reed, W. S. Saric, and D. Arnal. Linear stability theory applied to boundary layers. *Annu. Rev. Fluid Mech.*, 28(1):389–428, 1996.

[210] M. A. Regan and K. Mahesh. Global linear stability analysis of jets in cross-flow. *J. Fluid Mech.*, 828:812–836, 2017.

[211] D. Rempfer. On low-dimensional galerkin models for fluid flow. *Theor. Comput. Fluid Dyn.*, 14(2):75–88, 2000.

[212] J. M. Ribeiro, C.-A. Yeh, and K. Taira. Randomized resolvent analysis. *Phys. Rev. Fluid*, 5(3):033902, 2020.

[213] J. M. Ribeiro, C.-A. Yeh, K. Zhang, and K. Taira. Wing sweep effects on laminar separated flows. *J. Fluid Mech.*, 950:A23, 2022.

[214] G. Rigas, D. Sipp, and T. Colonius. Nonlinear input/output analysis: application to boundary layer transition. *J. Fluid Mech.*, 911:A15, 2021.

[215] S. Rippa. An algorithm for selecting a good value for the parameter c in radial basis function interpolation. *Adv. Comput. Math.*, 11:193–210, 1999.

[216] K. Rosenberg and B. J. McKeon. Computing exact coherent states in channels starting from the laminar profile: A resolvent-based approach. *Phys. Rev. E*, 100(2):021101, 2019.

[217] C. W. Rowley. *Modeling, simulation, and control of cavity flow oscillations*. PhD thesis, California Institute of Technology, 2002.

[218] C. W. Rowley, T. Colonius, and R. Murray. Dynamical models for control of cavity oscillations. In *AIAA Pap.*, page 2126, 2001.

[219] C. W. Rowley, T. Colonius, and R. M. Murray. Model reduction for compressible flows using pod and galerkin projection. *Phys. D*, 189(1-2):115–129, 2004.

[220] C. W. Rowley and S. T. Dawson. Model reduction for flow analysis and control. *Annu. Rev. Fluid Mech.*, 49:387–417, 2017.

[221] C. W. Rowley, I. Mezić, S. Bagheri, P. Schlatter, and D. S. Henningson. Spectral analysis of nonlinear flows. *J. Fluid Mech.*, 641:115–127, 2009.

[222] D. Russell and Z. J. Wang. A cartesian grid method for modeling multiple moving objects in 2d incompressible viscous flow. *J. Comput. Phys.*, 191(1):177–205, 2003.

[223] P. G. Saffman. *Vortex dynamics*. Cambridge University Press, Cambridge, 1992.

[224] R. Samtaney, D. I. Pullin, and B. Kosović. Direct numerical simulation of decaying compressible turbulence and shocklet statistics. *Phys. Fluids*, 13(5):1415–1430, 2001.

[225] L. G. C. Santos, N. Manzanares-Filho, G. J. Menon, and E. Abreu. Comparing rbf-fd approximations based on stabilized gaussians and on polyharmonic splines with polynomials. *Internat. J. Numer. Methods Engrg.*, 115(4):462–500, 2018.

[226] Y. V. S. S. Sanyasiraju and G. Chandhini. Local radial basis function based gridfree scheme for unsteady incompressible viscous flows. *J. Comput. Phys.*, 227(20):8922–8948, 2008.

[227] T. P. Sapsis and A. J. Majda. Blended reduced subspace algorithms for uncertainty quantification of quadratic systems with a stable mean state. *Phys. D*, 258:61–76, 2013.

[228] T. P. Sapsis and A. J. Majda. Statistically accurate low-order models for uncertainty quantification in turbulent dynamical systems. *Proc. Natl Acad. Sci.*, 110(34):13705–13710, 2013.

[229] P. J. Schmid. Dynamic mode decomposition of numerical and experimental data. *J. Fluid Mech.*, 656:5–28, 2010.

[230] P. J. Schmid. Dynamic mode decomposition and its variants. *Annu. Rev. Fluid Mech.*, 54:2022, 2021.

[231] P. J. Schmid and D. S. Henningson. *Stability and transition in shear flows*. Springer, 2002.

[232] P. J. Schmid, D. Violato, and F. Scarano. Decomposition of time-resolved tomographic piv. *Exp. Fluids*, 52:1567–1579, 2012.

[233] O. T. Schmidt. Spectral proper orthogonal decomposition using multitaper estimates. *Theor. Comput. Fluid Dyn.*, 36(5):741–754, 2022.

[234] O. T. Schmidt and T. Colonius. Guide to spectral proper orthogonal decomposition. *AIAA J.*, 58(3):1023–1033, 2020.

[235] O. T. Schmidt and P. J. Schmid. A conditional space–time pod formalism for intermittent and rare events: example of acoustic bursts in turbulent jets. *J. Fluid Mech.*, 867:R2, 2019.

[236] O. T. Schmidt, A. Towne, T. Colonius, A. V. Cavalieri, P. Jordan, and G. A. Brès. Wavepackets and trapped acoustic modes in a turbulent jet: coherent structure eduction and global stability. *J. Fluid Mech.*, 825:1153–1181, 2017.

[237] O. T. Schmidt, A. Towne, G. Rigas, T. Colonius, and G. A. Brès. Spectral analysis of jet turbulence. *J. Fluid Mech.*, 855:953–982, 2018.

[238] O. Semeraro, G. Bellani, and F. Lundell. Analysis of time-resolved piv measurements of a confined turbulent jet using pod and koopman modes. *Exp. Fluids*, 53:1203–1220, 2012.

[239] O. Semeraro, L. Lesshafft, V. Jaunet, and P. Jordan. Modeling of coherent structures in a turbulent jet as global linear instability wavepackets: theory and experiment. *Int. J. Heat Fluid Flow.*, 62:24–32, 2016.

[240] T. K. Sengupta, M. K. Rajpoot, S. Saurabh, and V. V. S. N. Vijay. Analysis of anisotropy of numerical wave solutions by high accuracy finite difference methods. *J. Comput. Phys.*, 230(1):27–60, 2011.

[241] S. Shahane, A. Radhakrishnan, and S. P. Vanka. A high-order accurate meshless method for solution of incompressible fluid flow problems. *J. Comput. Phys.*, 445:110623, 2021.

[242] S. Shahane and S. P. Vanka. Consistency and convergence of a high order accurate meshless method for solution of incompressible fluid flows. *arXiv preprint arXiv:2202.02828*, 2022.

[243] S. Shahane and S. P. Vanka. A semi-implicit meshless method for incompressible flows in complex geometries. *J. Comput. Phys.*, 472:111715, 2023.

[244] V. Shankar. The overlapped radial basis function-finite difference (rbf-fd) method: A generalization of rbf-fd. *J. Comput. Phys.*, 342:211–228, 2017.

[245] V. Shankar and A. L. Fogelson. Hyperviscosity-based stabilization for radial basis function-finite difference (rbf-fd) discretizations of advection–diffusion equations. *J. Comput. Phys.*, 372:616–639, 2018.

[246] V. Shankar, A. Narayan, and R. M. Kirby. Rbf-loi: Augmenting radial basis functions (rbfs) with least orthogonal interpolation (loi) for solving pdes on surfaces. *J. Comput. Phys.*, 373:722–735, 2018.

[247] A. S. Sharma and B. J. McKeon. On coherent structure in wall turbulence. *J. Fluid Mech.*, 728:196–238, 2013.

[248] S.-I. Shin, P. D. Sardeshmukh, M. Newman, C. Penland, and M. A. Alexander. Impact of annual cycle on enso variability and predictability. *J. Clim.*, 34(1):171–193, 2021.

[249] C. Shu, H. Ding, and K. S. Yeo. Local radial basis function-based differential quadrature method and its application to solve two-dimensional incompressible navier–stokes equations. *Comput. Methods Appl. Mech. Engrg.*, 192(7-8):941–954, 2003.

[250] C. Shu, H. Ding, and K. S. Yeo. Computation of incompressible navier-stokes equations by local rbf-based differential quadrature method. *CMES Comput. Model. Eng. Sci.*, 7(2):195–206, 2005.

[251] G. S. Sidharth, A. Dwivedi, G. V. Candler, and J. W. Nichols. Onset of three-dimensionality in supersonic flow over a slender double wedge. *Phys. Rev. Fluids*, 3(9):093901, 2018.

[252] D. Sipp. Open-loop control of cavity oscillations with harmonic forcings. *J. Fluid Mech.*, 708:439–468, 2012.

[253] D. Sipp and A. Lebedev. Global stability of base and mean flows: a general approach and its applications to cylinder and open cavity flows. *J. Fluid Mech.*, 593:333–358, 2007.

[254] D. Sipp and O. Marquet. Characterization of noise amplifiers with global singular modes: the case of the leading-edge flat-plate boundary layer. *Theor. Comput. Fluid Dyn.*, 27:617–635, 2013.

[255] D. Sipp, O. Marquet, P. Meliga, and A. Barbagallo. Dynamics and control of global instabilities in open-flows: a linearized approach. *Appl. Mech. Rev.*, 63(3), 2010.

[256] L. Sirovich. Turbulence and the dynamics of coherent structures. i. coherent structures. *Quart. Appl. Math.*, 45(3):561–571, 1987.

[257] C. S. Skene, C.-A. Yeh, P. J. Schmid, and K. Taira. Sparsifying the resolvent forcing mode via gradient-based optimisation. *J. Fluid Mech.*, 944:A52, 2022.

[258] A. M. O. Smith. Transition, pressure gradient and stability theory. *Rep. ES 26388. Douglas Aircraft Co., El Segundo, CA.*, 1956.

[259] F. T. Smith. On the non-parallel flow stability of the blasius boundary layer. *Proc. R. Soc. London Ser. A*, 366(1724):91–109, 1979.

[260] R. Stengel. Stochastic optimal control: Theory and application. 1986.

[261] L. Su. A radial basis function (rbf)-finite difference (fd) method for the backward heat conduction problem. *Appl. Math. Comput.*, 354:232–247, 2019.

[262] T. Suzuki and T. Colonius. Instability waves in a subsonic round jet detected using a near-field phased microphone array. *J. Fluid Mech.*, 565:197–226, 2006.

[263] T. Suzuki and S. K. Lele. Shock leakage through an unsteady vortex-laden mixing layer: application to jet screech. *J. Fluid Mech.*, 490:139–167, 2003.

[264] S. Symon, K. Rosenberg, S. T. M. Dawson, and B. J. McKeon. Non-normality and classification of amplification mechanisms in stability and resolvent analysis. *Phys. Rev. Fluids*, 3(5):053902, 2018.

[265] R. Tan, A. Ooi, and R. D. Sandberg. Two dimensional analysis of hybrid spectral/finite difference schemes for linearized compressible navier–stokes equations. *J. Sci. Comput.*, 87:1–41, 2021.

[266] G. I. Taylor. Recent work on the flow of compressible fluids. *J. Lond. Math. Soc.*, 5:224–240, 1930.

[267] V. Theofilis. Global linear instability. *Annu. Rev. Fluid Mech.*, 43:319–352, 2011.

[268] G. Tiesinga, F. W. Wubs, and A. E. P. Veldman. Bifurcation analysis of incompressible flow in a driven cavity by the newton–picard method. *J. Comput. Appl. Math.*, 140(1-2):751–772, 2002.

[269] G. Tissot, F. C. Lajús Jr, A. V. G. Cavalieri, and P. Jordan. Wave packets and orr mechanism in turbulent jets. *Phys. Rev. Fluids*, 2(9):093901, 2017.

[270] G. Tissot, M. Zhang, F. C. Lajús, A. V. G. Cavalieri, and P. Jordan. Sensitivity of wavepackets in jets to nonlinear effects: the role of the critical layer. *J. Fluid Mech.*, 811:95–137, 2017.

[271] A. I. Tolstykh. On using rbf-based differencing formulas for unstructured and mixed structured-unstructured grid calculations. In *Proc. 16th IMACS World Congress.*, volume 228, pages 4606–4624. Lausanne, 2000.

[272] A. Towne. Space-time galerkin projection via spectral proper orthogonal decomposition and resolvent modes. In *AIAA Scitech 2021 Forum*, page 1676, 2021.

[273] A. Towne, A. V. Cavalieri, P. Jordan, T. Colonius, O. Schmidt, V. Jaunet, and G. A. Brès. Acoustic resonance in the potential core of subsonic jets. *J. Fluid Mech.*, 825:1113–1152, 2017.

[274] A. Towne, G. Rigas, O. Kamal, E. Pickering, and T. Colonius. Efficient global resolvent analysis via the one-way navier–stokes equations. *J. Fluid Mech.*, 948:A9, 2022.

[275] A. Towne, O. T. Schmidt, and T. Colonius. Spectral proper orthogonal decomposition and its relationship to dynamic mode decomposition and resolvent analysis. *J. Fluid Mech.*, 847:821–867, 2018.

[276] L. N. Trefethen, A. E. Trefethen, S. C. Reddy, and T. A. Driscoll. Hydrodynamic stability without eigenvalues. *Science*, 261(5121):578–584, 1993.

[277] J. H. Tu, C. W. Rowley, D. M. Luchtenburg, S. L. Brunton, and J. N. Kutz. On dynamic mode decomposition: Theory and applications. *J. Comput. Dyn.*, 1(2):391–421, 11 2014.

[278] Laurette Tuckerman and Philip Marcus. Formation of taylor vortices in spherical couette flow. In *Ninth Int'l Conf. on Numerical Methods in Fluid Dynamics.*, pages 552–556. Springer, 1985.

[279] Laurette S Tuckerman and Dwight Barkley. *Bifurcation analysis for timesteppers*. Springer, 2000.

[280] M. Tutkun and W. K. George. Lumley decomposition of turbulent boundary layer at high reynolds numbers. *Phys. Fluids*, 29(2):020707, 2017.

[281] M. Tutkun, P. B. V. Johansson, and W. K. George. Three-component vectorial proper orthogonal decomposition of axisymmetric wake behind a disk. *AIAA J.*, 46(5):1118–1134, 2008.

[282] A. Unnikrishnan, S. Shahane, V. Narayanan, and S. P. Vanka. Shear-driven flow in an elliptical enclosure generated by an inner rotating circular cylinder. *Phys. Fluids.*, 34(1), 2022.

[283] J. L. Van Ingen. A suggested semi-empirical method for the calculation of the boundary layer transition region. *Rep. UTHL-74. University of Technology, Dept. Aero. Engng.*, 1956.

[284] H. L. Van Trees. *Detection, estimation, and modulation theory, part I.* New York: Wiley, 1968.

[285] R. Vautard and M. Ghil. Singular spectrum analysis in nonlinear dynamics, with applications to paleoclimatic time series. *Phys. D: Nonlin. Phenom.*, 35(3):395–424, 1989.

[286] J.M. Vega and S. Le Clainche. *Higher Order Dynamic Mode Decomposition and Its Applications*. Elsevier Science, 2020.

[287] T. h. Von Karman. Über den mechanismus des widerstandes, den ein bewegter körper in einer flüssigkeit erfährt. *Göttingen Nachr. Math. Phys. Kl.*, 1911:509–517, 1911.

[288] J. G. Wang and G. R. Liu. A point interpolation meshless method based on radial basis functions. *Internat. J. Numer. Methods Engrg.*, 54(11):1623–1648, 2002.

[289] L. Wang. Radial basis functions methods for boundary value problems: Performance comparison. *Eng. Anal. Bound. Elem.*, 84:191–205, 2017.

[290] L. Wang, Y. Liu, Y. Zhou, and F. Yang. Static and dynamic analysis of thin functionally graded shell with in-plane material inhomogeneity. *Int. J. Mech. Sci.*, 193:106165, 2021.

[291] L. Wang, Z. Qian, Y. Zhou, and Y. Peng. A weighted meshfree collocation method for incompressible flows using radial basis functions. *J. Comput. Phys.*, 401:108964, 2020.

[292] T. Warn, O. Bokhove, T. G. Shepherd, and G. K. Vallis. Rossby number expansions, slaving principles, and balance dynamics. *Q. J. R. Met. Soc.*, 121:723–739, 1995.

[293] J. Waters and D. W. Pepper. Global versus localized rbf meshless methods for solving incompressible fluid flow with heat transfer. *Numer. Heat Transf. B: Fundam.*, 68(3):185–203, 2015.

[294] I. Weisbrot and I. Wygnanski. On coherent structures in a highly excited mixing layer. *J. Fluid Mech.*, 195:137–159, 1988.

[295] M. O. Williams, I. G. Kevrekidis, and C. W. Rowley. A data–driven approximation of the koopman operator: Extending dynamic mode decomposition. *J. Nonlinear Sci.*, 25(6):1307–1346, 2015.

[296] M. O. Williams, C. W. Rowley, and I. G. Kevrekidis. A kernel-based method for data-driven koopman spectral analysis. *J. Comput. Dyn.*, 2(2):247–265, 2015.

[297] C. H. K. Williamson. Vortex dynamics in the cylinder wake. *Annu. Rev. Fluid Mech.*, 28(1):477–539, 1996.

[298] B. M. Woodley and N. Peake. Global linear stability analysis of thin aerofoil wakes. *J. Fluid Mech.*, 339:239–260, 1997.

[299] G. B. Wright. *Radial basis function interpolation: numerical and analytical developments*. PhD thesis, University of Colorado at Boulder, 2003.

[300] G. B. Wright, N. Flyer, and D. A. Yuen. A hybrid radial basis function–pseudospectral method for thermal convection in a 3-d spherical shell. *Geophys. Geochem. Geosyst.*, 11(7), 2010.

[301] G. B. Wright and B. Fornberg. Scattered node compact finite difference-type formulas generated from radial basis functions. *J. Comput. Phys.*, 212(1):99–123, 2006.

[302] Y. Xie, X. Zhao, M. Rubinato, and Y. Yu. An improved meshfree scheme based on radial basis functions for solving incompressible navier–stokes equations. *Int. J. Numer. Meth. Fluids.*, 93(9):2842–2862, 2021.

[303] C.-A. Yeh and K. Taira. Resolvent-analysis-based design of airfoil separation control. *J. Fluid Mech.*, 867:572–610, 2019.

[304] R. Zamolo and E. Nobile. Solution of incompressible fluid flow problems with heat transfer by means of an efficient rbf-fd meshless approach. *Numer. Heat Transf. B: Fundam.*, 75(1):19–42, 2019.

[305] A. Zare, M. R. Jovanović, and T. T. Georgiou. Colour of turbulence. *J. Fluid Mech.*, 812:636–680, 2017.

[306] A. Zebib. Stability of viscous flow past a circular cylinder. *J. Engng Math.*, 21(2):155–165, 1987.

[307] Y. Zhang, L. Cattafesta, and L. Ukeiley. Identification of coherent structures in cavity flows using stochastic estimation and dynamic mode decomposition. In *10th International Symposium on TSFP*, page 3, 2017.

[308] Y. Zhang, L. N. Cattafesta, and L. Ukeiley. Spectral analysis modal methods (samms) using non-time-resolved piv. *Exp. Fluids*, 61(11):1–12, 2020.